UNIVERSITY OF CALIFORNIA
SANTA CRUZ

PHOTOPHYSICAL INVESTIGATIONS INTO OPPOSITELY-CHARGED CONJUGATED POLYELECTROLYTE COMPLEXES

A dissertation submitted in partial satisfaction
of the requirements for the degree of

DOCTOR OF PHILOSOPHY

in

CHEMISTRY

by

William Right Hollingsworth IV

June 2019

The Dissertation of William Right Hollingsworth IV is approved:

_____
Professor Alexander Ayzner, Chair

_____
Professor Ilan Benjamin

_____
Professor Jin Zhang

_____
Lori Kletzer
Vice Provost and Dean of Graduate Studies

CONTENTS

FIGURES

ABSTRACT
PHOTOPHYSICAL INVESTIGATIONS INTO OPPOSITELY-CHARGED CONJUGATED POLYELECTROLYTE COMPLEXES

William Right Hollingsworth IV

Conjugated polyelectrolytes (CPE) offer intriguing possibilities as light-harvesting scaffold in artificial photosynthetic systems. They are water soluble, can be modified synthetically to change their optical properties, have facile exciton migration, have a tendency to self-assemble, are relatively low cost, and can be cast into high quality films. However, the structure – function relationship between a CPE's conjugated backbone and its photophysics means that these compounds will necessarily see changes in their optical and electronic properties upon complexation with an oppositely charged partner. The question becomes whether those changes can be understood and controlled in an aqueous environment. This dissertation tackles that question by investigating a model donor-acceptor CPE complex. The principle tools in this work are steady-state optical absorption and fluorescence spectroscopy, time-resolved fluorescence spectroscopy, time-resolved fluorescence anisotropy, and isothermal titration calorimetry. The major findings of this work as it relates to the donor-acceptor complex are as follows: thermodynamically allowed electronic energy transfer (EET) is observed upon complexation; complexation leads to emergent bright states in the donor when excited directly which are not existent outside of the complex; the donor is "unwound" from its native coiled state upon

complexation, and the extent of that unwinding and straightening is dependent on presence of a molar excess of acceptor; EET proceeds on ~240 fs time-scale, comparable to natural photosynthesis; in contrast to non-conjugated polyelectrolytes, heat is at times-required to form CPE complexes; the degree to which heat is needed depends upon the extent of non-covalent *intra*-chain interactions within the complexing CPEs – the larger those interactions the more "protein – like" the CPE behaves.

ACKNOWLEDGEMENTS

I would like to thank several external collaborators for their contributions to this work: Prof. Art Bragg, Dr. Jamie Young, Dr. Tim Magnelli, Prof. Lei Feng, Dr. Jongbok Lee, and Vanessa Williams.

I would also like give thanks to many members of the UC Santa Cruz community: David Klech, Prof. Dave Kliger, Dr. Eefei Chen, Prof. Ilan Benjamin, Prof. Jin Zhang, Alexander Villagran, Jonathan Balderrama, Diego Garcia, Reilly Seban, Melanie Blum, Walter Meier, Christina Palka, Anna Chatenever, Miguel Pinto, Yi Peng, Tianyi Kuo, Steven Perry, John Diniz, Dr. Stacy Adams, Dr. Vincent Duong, Anna Johnston, Stephanie Pitch, Greg Pitch, Michael Roders, Carmen Segura, and Prof. Alexander Ayzner.

Finally, I would like to thank my much-loved family.

For

Jim and Muriel and Holly and Jo

Chapter 1

Introduction

1.0 Background

As global climate change becomes an increasingly pressing issue, a major policy goal of many nations has been a move away from coal and natural gas toward renewable sources of energy for electricity production.[1] This in turn has spurned ongoing research across physics, chemistry, biology, and engineering into novel methods of harvesting energy from wind, sunlight, tides, and microbial systems – both for direct electricity production, and to produce alternative fuels. Amongst these, harvesting energy from sunlight remains one of the most attractive options for wide global adoption – owing to its ubiquity, as well as the long lifetime of solar light generation compared to the human endeavor.[2-8] Research into solar light harvesting typically falls along two paths: direct conversion to electricity via inorganic or organic photovoltaics, or else direct conversion to fuel via, for example, the photochemical water splitting reaction.[9-11] With regards to the latter, a common research focus has been on carefully modulating the energy levels of metal or metal-oxide clusters covalently linked in a larger organometallic framework. The inspiration for this, of course, are the metal centered protein clusters that make up natural photosynthetic machinery. However, in a natural system, these metal clusters are not covalently bonded to a larger organometallic framework but are instead non-covalently linked to a series of organic light-harvesting antenna. It is this structure – a modular, non-covalently linked, self-assembled photosystem – which forms the basic inspiration for the work presented in this thesis.

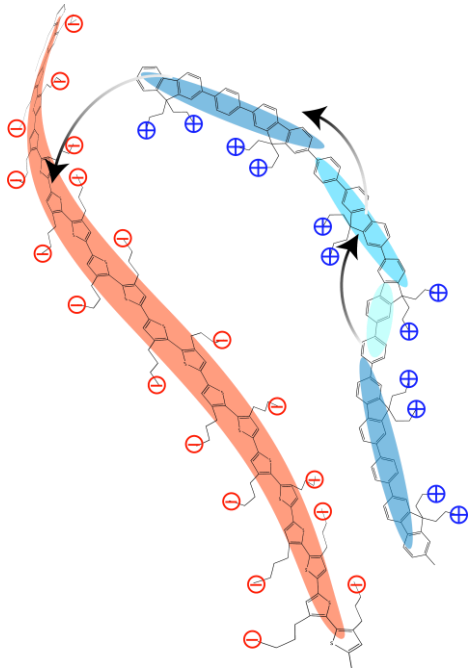

Figure 1.1: Cartoon representation of electronic energy transfer within and between CPEs. Arrows suggest the path of exciton migration, while the red and blue shaded areas imply exciton delocalization along a backbone segment.

If the goal is to more closely mimic a natural photosynthetic system, then the relevant design parameters to consider are as follows: the system should be water soluble, modular, non-covalently self-assembled, broadly light absorbing, and capable to efficient electronic energy transfer. These parameters are largely satisfied by the class of molecules known as conjugated polyelectrolytes (CPEs, **Figure 1.1**). CPEs are a class of synthetic (semi-) conducting polymers that have many properties which make them highly attractive candidates to act as light-harvesting antenna scaffolds in an artificial photosynthetic system[5, 12-14]. CPEs are polymers with fully conjugated backbones, but non-conjugated ionizable side-chains. These ionizable side-chains afford CPEs good water solubility. Because the side-chains are non-conjugated and therefore do not electronically interact with the conjugated backbone, they can be modified significantly without altering the electronic properties of the CPE itself. This further means that the sidechains can be either cationic or anionic in nature, allowing for electrostatically mediated complexation

between oppositely charged CPEs. As will be shown later, complexation can also be mediated by non-ionic π-π interactions, and hydrophobic effects involving the CPE backbone.

Like its sidechains, the backbone of a CPE is amenable to synthetic alterations prior to polymerization. This allows for the electronic properties of a CPE to be carefully modulated by, for example, the inclusion or alteration of hetero atoms such as sulfur or nitrogen, the addition of fused aromatic rings, or the introduction of a second monomer to form block-copolymers.[15-16] While rich synthetic chemistry can be exploited to tune the electronic nature of a CPE, the fundamentals of their electronic properties remain largely the same. In a perfectly linear CPE, the conjugated polymer backbone forms an uninterrupted network of overlapping p_z orbitals, forming a low dimensional conduction band. In intrinsically conducting CPEs this band is partially filled with p_z electrons, while in a semiconducting CPE the band represents the lowest unoccupied molecular orbital (LUMO) of the CPE and is easily accessible by exciting an electron from the highest occupied molecular orbital (HOMO) of the system. In semiconducting CPEs, which form the basis for this work, the language of an inter-band transition is being set aside in favor of a HOMO to LUMO transition, which is more commonly used by chemists, and more accurately reflects the nature of the transition in non-idealized polymers.

The bulk of the work presented in this dissertation was performed in the aqueous phase, and discussions of structural order and electronic properties are largely confined to this regime. This is for good reason. One of the attractive properties of CPEs is water solubility, the principal benefits of which are the avoidance of organic solvents, and potential solution processing. The latter of these is highly desirable from a cost and engineering perspective, but it belies the fact that the ultimate solid-state properties of a system will be tightly coupled to its solution phase properties. Thus, control of fundamental properties in the solid-state must start from understanding and control of the fundamentals of solution phase. Control, in this case, arises from the fact that there is an incredibly strong structure-function relationship between the conformation of a CPE and its electronic properties. In solution conformation can be altered by a wide array of parameters – temperature, ionic strength, solvent polarity, the presence of a complexation partner. Moreover, there are applications for CPEs in biological sensing and as model systems for understanding the formation of membrane-less organelles which are only relevant in solution.

Within this context, the goal of this dissertation is to explore the fundamental photophysical properties of donor-acceptor complexes made of two oppositely-charged conjugated polyelectrolytes. It is envisioned that these complexes, or related structures, can act as the initial light-harvesting units, as well as structural scaffold, for an artificial light-harvesting system. The donor CPE is

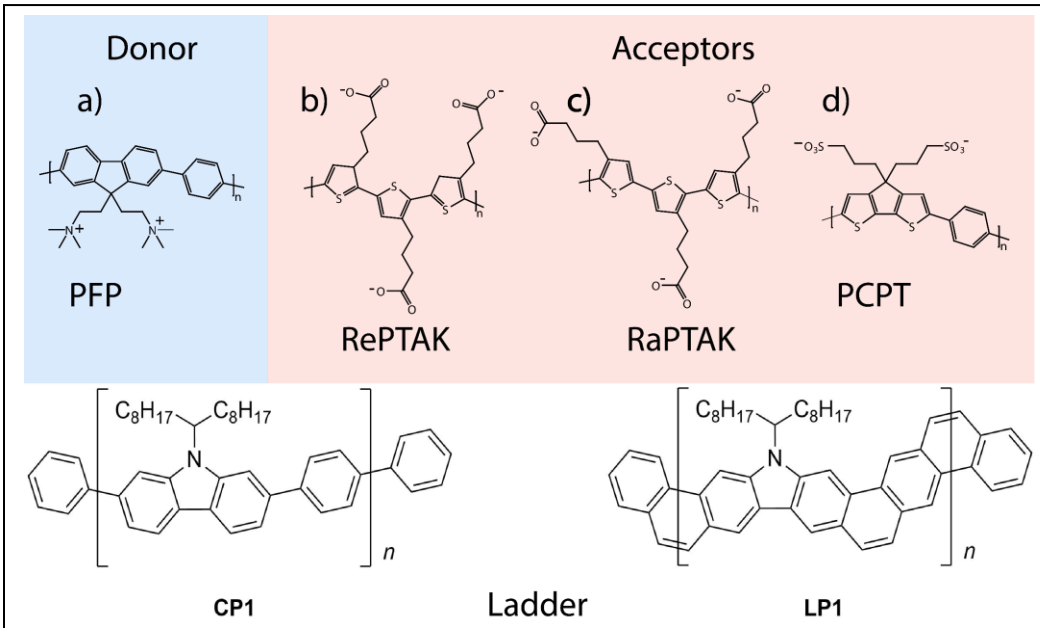

Figure 1.2: Chemical structures of CPEs used in the work.

poly([fluorene]-alt-co-[phenylene]) (PFPI, a doubly cationic polyfluorene derivative) while the acceptor is poly(alkylcarboxythiophene) (PTAK, an anionic polythiophene derivative). This work explores their basic photophysical response and energy transfer dynamics as a function of monomer charge ratio[1], as well as the thermodynamics and kinetics of forming such complexes. The last chapter of this dissertation explores the photophysical characteristics of a novel conjugated ladder polymer poly carbazole (LP1), which represents a growing class of rotationally hindered conjugated polymers which are of interest for their charge transport and photoluminescence properties. Before those results is a discussion of fundamental

[1] IE the ratio, on a monomolar basis, between positively and negatively charged sidechains.

electronic processes in CPEs, and of two experimental techniques which were critical to the work performed. Structures of the CPEs can be seen in **Figure 1.2**.

1.2 Electronic Transitions in Conjugated Polyelectrolytes

ISOLATED CHAINS

In CPEs and other semiconducting polymers, the probability of the HOMO-LUMO transition is governed by Fermi's Golden Rule[17]

$$\lambda_{if} = \frac{2\pi}{\hbar} |M_{if}| \rho_f \qquad (1.1)$$

where ρ_f is the density of final states and M_{if} is the matrix element joining the initial and final states, given as

$$M_{if} = \int \Psi_f^* V \Psi_i \, dv \qquad (1.2)$$

where V is the potential connecting the initial and final states.

The Rule states that the rate of an electronic transition between two eigenstates is proportional to the strength of the coupling between the states as well as their energy density. In semiconducting CPEs the HOMO-LUMO transition rate tends to be quite high, which correspondingly leads them to have high molar extinction coefficients, and hence strong light absorption. Because these are molecular materials, the excited state that is formed is not a free electron and hole, but rather an electron-hole pair which is tightly bound by coulombic interaction.[18] This pair, termed an exciton, does not stay localized to a single atom, but rapidly delocalizes

across the entire conjugated system. This tendency to delocalize is in part responsible for facile exciton diffusion in conjugated polymeric systems.

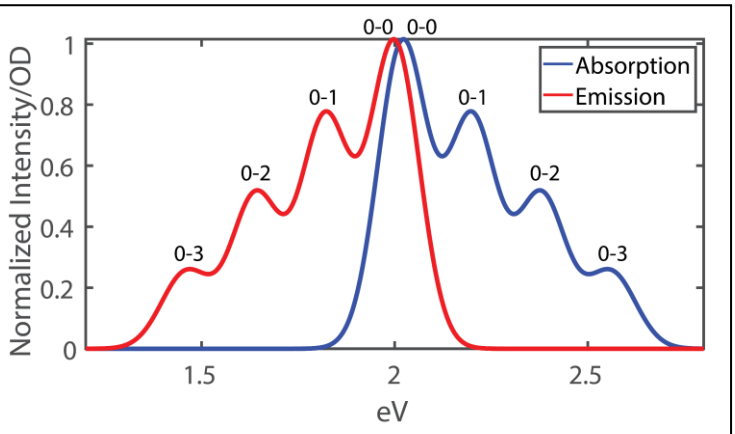

Figure 1.3: Idealized optical absorption and emission spectra for a conjugated molecular system. Peaks are homogeneously broadened, and the vibronic progression is separated by 0.18 eV.

Representative optical absorption and photoluminescence spectra of a hypothetical CPE are shown in **Figure 1.3** (with uniform peak widths due to homogenous broadening) along with actual spectra from a CPE in solution at room temperature. The differences between the representative and actual spectra are illustrative of the close connection between CPE conformational structure and electronic properties. In the idealized case, the absorption and emission spectra will be mirror images of one another, with minimal Stokes shift. The peak progression in each spectrum highlights the fact that the electronic states tend to couple strongly to the vibrational states in these systems, leading to vibronic states. The energies of these vibronic states tends to differ by approximately 0.18 eV[19] and are correlated to the energy of the vinyl stretching mode, which is coupled most strongly. The peaks are labelled as 0 – 0, 0 – 1, etc signifying transitions from S_0, v_0 to S_1, $v_{0,1,2,\ldots}$ as

highlighted in the Jablonski diagram in **Figure 1.4**. In the actual spectra the situation is, understandably, not so neat. Absorption spectra of CPEs in solution are frequently structureless. This is largely because CPEs have high structural disorder in solution, leading to conjugation breaks in the π backbone network that correspondingly give rise to subdomains of the CPE backbone with varying conjugation lengths.[20] In CPEs the conjugation length is of great importance as, to a first approximation, the energy levels of a CPE can be thought of as behaving like the energy levels of a 1 – D particle in a box,

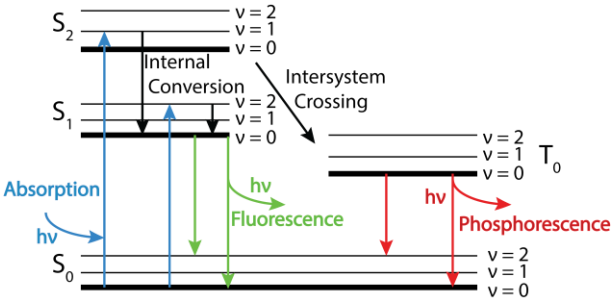

Figure 1.4: Representative Jablonski diagram showing several photophysical processes.

$$E_n = \frac{n^2 h^2}{8mL} \qquad 1.3)$$

with the energies being determined in part by the length of the box. This being the case, the absorption spectrum of a CPE in solution represents the ensemble average of the energy levels of the multiple subdomains and is subsequently broadened as a result. The same broadening is not nearly as pronounced in the emission spectrum, and typically it will show an obvious vibronic progression. This is because the extended π backbone network allows for easy exciton migration. To the extent that conjugation breaks represent tunnelable potential energy barriers, the exciton will

quickly migrate downhill in energy along a chain until it reaches the subunit with the lowest energy[2]. Thus, prior to emission the ensemble average of emitting states is narrowed significantly as the excited state population localizes to the lowest energy (longest) chain segments available.

H-, J-, and HJ-AGGREGATES

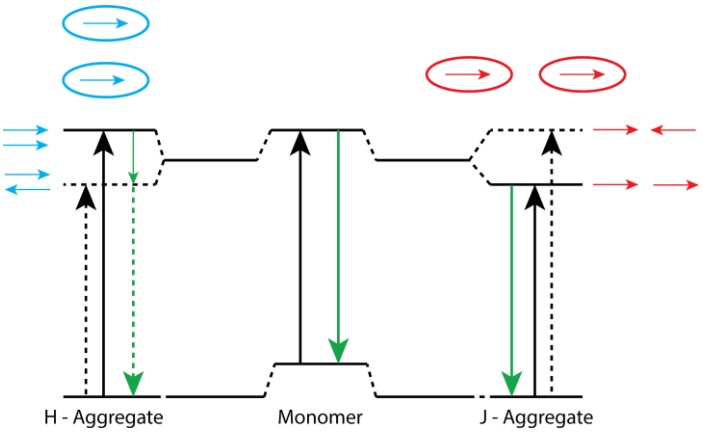

Figure 1.5: Schematic energy level diagrams for the Kasha H- and J-aggregate model. Dashed lines denote disallowed transitions. Black arrows denote absorption events, and green arrows emission events. Red and blue arrows show relative dipole orientations.

Aggregation effects, even absent large changes in conformation, can have a profound impact on the electronic properties of a CPE. The prevailing theory of electronic transitions in aggregated, planar, conjugated molecular systems was put forward by Michael Kasha and co-workers in the mid-1960s.[21] In Kasha's model, aggregates

[2] Subject to certain limitations: The magnitude of the potential energy barrier presented by a conjugation break will be inversely proportional to the degree of overlap between the p_z orbitals of adjacent subunits. In the case where they are perfectly orthogonal, tunneling will be forbidden. It is also conceivable that for a given exciton no migration occurs, either because it has arisen on the global lowest energy subunit or because it is locally surrounded by higher energy subunits. This further assumes that each subunit has relatively little structural disorder. This is generally a good assumption, as the lowest energy geometry of an excited organic chromophore is planar, and the excited state is presumed to be delocalized along the entirety of the chromophore.

classified as either H-aggregates, comprised of co-facially arranged monomers whose transition dipole moments lie in parallel; or J-aggregates[3], comprised monomers whose transition dipole moments are arranged head to tail. A schematic representation is presented in **Figure 1.5**. The framework of Kasha's model is built around intermolecular Coulombic coupling between nearest neighbors, assuming a Frenkel (tightly bound) exciton. The coupling assumes a point-dipole approximation given by

$$J_c = \frac{\mu_1 \cdot \mu_2 - 3(\mu_1 \cdot \hat{R})(\mu_2 \cdot \hat{R})}{4\pi\varepsilon R^3} \quad (1.4)$$

where $\mu_1 \text{and } \mu_2$ are the transition dipole moments for molecules 1 and 2, $\hat{R}$ is the displacement vector between the center of the dipoles, and ε is the dielectric constant of the medium. For identical molecules with dipoles having parallel orientation, the Coulombic coupling term becomes

$$J_c = \frac{\mu^2(1-3\cos^2\theta)}{4\pi\varepsilon R^3} \quad (1.5)$$

where θ is the angle between a dipole and $\hat{R}$. Kasha's designation of H- vs J- depends on θ. In H-aggregates $\theta_M < \theta \leq \pi/2$ and $J_C > 0$, corresponding to aggregates with dipoles aligned side-by-side or cofacially. Here θ_M is the magic angle (≈54.7°) at

[3] In this system "H" stands for hypsochromic, in deference to the characteristic blue-shift of the absorption and emission spectra, whereas "J" stands Edwin E. Jelley who first described them in 1937 while working for the Kodak Research Laboratory. The inconsistency of this nomenclature is a modest ongoing frustration.

which $J_C = 0$. In J-aggregates, $\theta < \theta_M$ and $J_C < 0$, and aggregate dipoles are considered to be aligned head-to-tail.

Kasha and McRae showed that the sign of J_C is meaningful in describing the photophysical response in aggregated systems. Starting with a simple dimer model, they noted that the Coulombic coupling leads to a splitting of the first excited energy level (*a la* Davydov) of $2|J_C|$ forming two possible excited states corresponding to symmetric and anti-symmetric linear combinations of excited states. In H-aggregates, with positive J_C, the symmetric combination occupies the higher energy position, and the anti-symmetric the lower. As only the symmetric state couples to the ground state, it is initially populated upon absorption, and then quickly depopulated by internal conversion to the lower energy anti-symmetric state[4]. The anti-symmetric state, which cannot couple to the ground state, is dark, and the excited state relaxes non-radiatively. In a J-aggregate, with negative J_C, the energetic ordering of symmetric and anti-symmetric states is reversed, with the symmetric state being lower in energy. It is this state which is initially populated upon absorption, and from which emission is allowed. This splitting leads to the classic spectral features which are considered hallmarks of H- and J- aggregation. In H-aggregates the absorption spectrum is blue shifted relative to the monomer

[4] Internal conversion of an initially excited state to the lowest energy excited state is known as Kasha's rule. To very good approximation, it is expected that this process will occur for all excited states on a timescale significantly faster than the radiative lifetime, and hence all emission is expected to occur from the lowest energy excited state. Emission from "hot" excitons is expected to be uncommon.

spectrum, and the rate of emission is greatly suppressed. In J-aggregates the absorption spectrum is red shifted relative to the monomer spectrum and the emission rate is greatly enhanced.

Kasha's dimer model can be reasonably extended[22] to higher order linear aggregates (assuming nearest neighbor interactions and periodic boundary conditions) in which the energy levels of the excitons are presumed to form bands. Here, the energy of the bands depends on *k*, the dimensionless wavevector

$$|k\rangle = \frac{1}{\sqrt{N}}\sum_n e^{ikn}|n\rangle \quad k = 0, \pm\frac{2\pi}{N}, \pm\frac{4\pi}{N}, \ldots, \pi \tag{1.6}$$

such that

$$E_k = E_M + D + J_k \tag{1.7}$$

where E_M is the energy of the monomer, *D* is the gas-to-crystal frequency shift, and J_k is the k-dependent Coulombic coupling

$$J_k = 2J_C\cos(k) \tag{1.8}$$

In this model the oscillator strength is only with the *k = 0* exciton, and the energy splitting in the aggregates is manifest as an upward (H-aggregates) or downward (J-aggregates) deflection of band energy symmetric around *k = 0*. This can be seen schematically in **Figure 1.6** where E_k is plotted as a function of *k*. The linear model

captures the same fundamental aggregation effects as the dimer model, namely that in an H-aggregate the absorption will be blue shifted owing to the upward energetic deflection of the *k = 0* state, and that emission will be forbidden as fast *intra*band relaxation moves the exciton to the *k=π* state[5]. Similarly, J-aggregate absorption and emission both originate at the *k = 0* state, the energy of which has been lowered.

As with isolated molecules, vibronic coupling must be accounted for in aggregated systems. This is done by use of the Frenkel-Holstein Hamiltonian[23], which "dresses" standard Frenkel excitons with intramolecular vibrational modes. Most commonly this is the symmetric C=C stretching mode (the vinyl stretching mode in non-ring systems, or the aromatic stretching mode in ring systems) with energy on the order of 0.17 eV. The Frenkel-Holstein Hamiltonian is of the form

$$H_{FH} = \omega_{0-0} + D + \sum_{m,n} J_{m,n}|m\rangle\langle n| + \omega_{vib}\sum_n b_n^\dagger b_n + \omega_{vib}\sum_n[\lambda(b_n^\dagger + b_n) + \lambda^2]|n\rangle\langle n| \quad (1.9)$$

where the first three terms are the same as in the traditional Frenkel Hamiltonian. ω_{vib} is the energy of the coupled molecular vibration (in inverse centimeters, for the C=C stretch this is ~ 1,400 cm^{-1}), $b_n^\dagger$ and b_n are the raising and lowering operators for vibrational quanta in the ground state (S_0) nuclear potential of a chromophore,

[5] As all the oscillator strength lies in the *k = 0*, a *k = π* transition is symmetry forbidden. Moreover, the selection rule for molecular transitions in this model is that *Δk = 0*, as it must be to conserve momentum. As a practical matter, emission from H-aggregates can be thermally activated, or allowed by symmetry breaking disorder.

and λ^2 is the Huang-Rhys factor. The fourth term represents the energy of the intraband molecular vibration, while the fifth term represents the offset of the first excited state (S_1) nuclear potential assuming all potentials are harmonic oscillators with the same shape. Within the weak and medium coupling limit, this does not greatly change the principle spectroscopic predictions of Kasha's theory; vibronic bands within an energy level are still dispersed upwards in H-aggregates and downwards in J-aggregates symmetric about *k=0*. It does however allow and accurately account for the vibronic progression common to conjugated system.

For transitions from S_1 to vibronic states of S_0 above v=0, the *k=0* selection rule is relaxed. Thus, in H-aggregates, vertical transitions from the low-lying $k=\pi$ states are allowed to the *v = 1,2,3…* vibronic states of S_0, though only the *k=0* transition remains allowed for the *v = 0* state. Because of this, the intensity of the higher order vibronic photoluminescence peaks is invariant with regards to aggregation. Because of this, the main spectroscopic diagnostic for differentiating between H- and J-aggregates is in the change in intensity of the 0-0 photoluminescence peak ($I_{0\text{-}0}$). This is applied practically by taking the ratio $S_R = I_{0\text{-}0}/I_{0\text{-}1}$, where $S_R \geq 1$ is indicative of J-aggregation, and $S_R < 1$ is indicative of H-aggregation[6].

[6] Proper quantitative application of this rule requires converting the photoluminescence spectrum from wavelength space to energy space, and, if there is overlap of the vibronic peaks, fitting the peaks to an appropriate functional to extract their true intensities. This process is applied in detail in Chapter 2.

The utility of the H- and J-aggregate model is that it offers a baseline level of structural information using only standard linear absorption and emission spectroscopy, which is especially attractive when working with systems in solution. However, application of the model to conjugated polymer systems must be considered carefully. In practice, it is nearly impossible to use absorption spectra as an accurate diagnostic of aggregation, since changes in peak position, intensity, and resolution due to aggregation will coincide with changes in the same parameters due to backbone disorder. Only in low disorder (i.e. low temperature crystals) systems can spectroscopic changes in an absorption spectrum due to aggregation be reasonably assigned. Sensitivity of the absorption spectrum to structural disorder highlights the key challenge in treating conjugated polymers under the H- and J-aggregate model. This is namely that the model considers monomeric aggregates in a coupling limit suitable for first order perturbation theory. Because all coupling in monomer aggregates is through-space, this is a reasonable assumption. But, conjugated polymer aggregates will have both through-space *inter*chain coupling[7] as well as through-bond *intra*chain coupling along the backbone. Thus, a perfectly linear conjugated polymer represents a *de facto* J-aggregate[8], while a dimer or higher order cluster of perfectly linear conjugated polymers represents a quandary.

[7] Thought-space coupling may also be between segments of the same polymer chain which are many repeat units apart – and hence isolated through-bond – but which have found themselves in local proximity due to chain bending.

[8] Whether perturbation theory still holds in this regime is an open subject. Spano and co-workers have convincingly modeled the *in situ* polymerized polydiacetylene crystals as J-aggregates using the

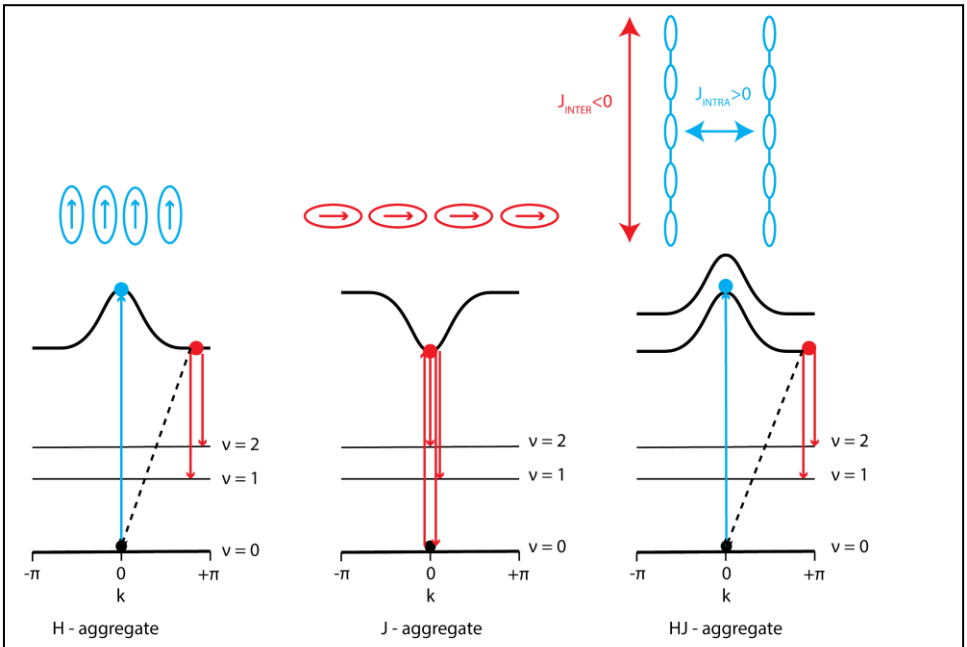

Figure 1.6: Schematics of the linear extension of the Kasha model (first two sections), and Spano HJ-aggregate model (last section).

To solve this, Spano and co-workers[19, 22-33] have worked extensively to re-tool H- and J-aggregate theory to be applicable to conjugated polymers, with significant success. Their model, dubbed the HJ-aggregate model, treats the system as a hybrid, which has H- or J- like spectral response depending on whether the *inter*chain coupling (J_{inter}) or *intra*chain coupling (J_{intra}) is stronger. The Spano model is based on a modified Frenkel-Holstein Hamiltonian and has been successfully used to describe the photophysical response of crystalline poly – 3 – hexylthiophene (P3HT, a canonical conjugated polymer[26]) as well as red and blue phase *in situ* polymerized

Frenkel-Holstein Hamiltonian, suggesting that the designation of extended conjugated polymers as *de facto* J-aggregates is likely appropriate at this level of theory despite the fact that through-bond coupling is presumably stronger than a weak perturbation.

polydiacetylene. In addition to providing predictions for how absorption and photoluminescence spectra will change as a function of $J_{inter/intra}$ the model additionally relates the change in the ratio S_R with changes in temperature, allowing for a quantitative estimation of J_{inter} and J_{intra} according to

$$`S_R = \frac{1}{\lambda^2}\frac{2e^{-2FJ_{inter}/k_bT}}{1+e^{-2FJ_{inter}/k_bT}}\sqrt{\frac{4\pi F|J_{intra}|}{k_bT}} \quad for\ N > \sqrt{4\pi\hbar\omega_c/k_bT} \qquad (1.10)$$

where F is the Frank-Condon factor, k_b is the Boltzman constant, ω_c is the exciton band-width, and N is the number of monomers in the polymer chain. This expression is notable especially insofar as it is valid in the thermodynamic limit for disordered systems. Thus, aggregated conjugated polymers in solution, the HJ-aggregate model can be a powerful tool for gaining initial insight into the structural arrangement of aggregated systems[9]. However, it should be noted that if a quantitative comparison of J_{intra} and J_{inter} is not necessary then whether S_R is greater or less than one is a good first order diagnostic for H- vs J- behavior.

1.3 Electronic Energy Transfer

Electronic energy transfer (EET) is a photophysical process common to many molecular systems. At its most basic level it is the radiation-less transfer of an

[9] A complementary theory has been developed by Barford in the UK with largely similar outcomes. Their work has moreover focused on attempting the model the photophysical response of curved conjugated polymers, with significant focus on the inverse participator number (i.e. the inverse of the chromophore conjugation length). While this has proven successful in a few polymeric test cases, it is finding more use in describing cyclic conjugated polymers.

excited state from a donor molecule to an acceptor molecule.[34] It arises naturally in photosynthetic light-harvesting subunits, and it is responsible for the transfer of energy from those subunits to the photosynthetic reaction center.[35] EET also sees common use in biophysical studies, where the quenching rates of tethered organic dyes can be used to assay changes in protein conformation, for instance, or to determine the distance between protein residues. This is because the rate of energy transfer falls off as a function distance.[36] In the simplest model, EET[10] is described by the Coulombic coupling between two adjacent dipoles. The coupling term is given by

$$V = \frac{\mu_A \cdot \mu_D}{4\pi\varepsilon_0 n^2 R_{AD}^3} - \frac{3(\mu_A \cdot R_{AD})(\mu_D \cdot R_{AD})}{4\pi\varepsilon_0 n^2 R_{AD}^5} \quad (1.11)$$

where μ_A and μ_D are the transition dipole moment vectors of the acceptor and donor, respectively, R_{AD} is the vector which connects the centers of the dipoles of the acceptor and donor, ε_0 is the permittivity of free space, and n is the refractive index of the medium. n^2 gives the dielectric constant of the medium, assumed to be constant. Förster formulated the most familiar model for EET based on the interaction between a single donor and acceptor separated by some distance. Assuming a weak coupling limit, the rate of EET can be calculated using Fermi's Golden Rule as

[10] Otherwise known as RET – Resonance Energy Transfer – or FRET – Förster (Fluorescence) Resonance Energy Transfer.

$$k_t(R) = \frac{Q_D \kappa^2}{\tau_D R^6} \left(\frac{9000(ln10)}{128\pi^5 N n^4}\right) \int_0^\infty F_D(\lambda)\varepsilon_A(\lambda)\lambda^4 d\lambda \qquad (1.12)$$

where Q_D is the donor quantum yield and τ_D is the donor fluorescence lifetime, both in the absence of the acceptor, and N is Avogadro's number. The integral, often shortened to *J(λ)* (see **Figure 1.7**), is the spectral overlap of the area normalized donor fluorescence and acceptor absorption spectra. κ is the orientation factor of the transition dipoles, given as

$$\kappa = \mu_D.\mu_A - 3(\mu_D \cdot R)(\mu_A \cdot R) \qquad (1.13)$$

or

$$\kappa^2 = (\sin\theta_D \sin\theta_A \cos\phi - 2\cos\theta_D \cos\theta_A \qquad (1.14)$$

The orientation factor is often taken to be 2/3 for systems that are dynamically averaged. The Förster model is powerful in applicable circumstances. It allows the rate of EET to be related to easily obtained observables – the donor fluorescence and acceptor absorption spectra, as well as the donor quantum yield and fluorescence lifetime. It

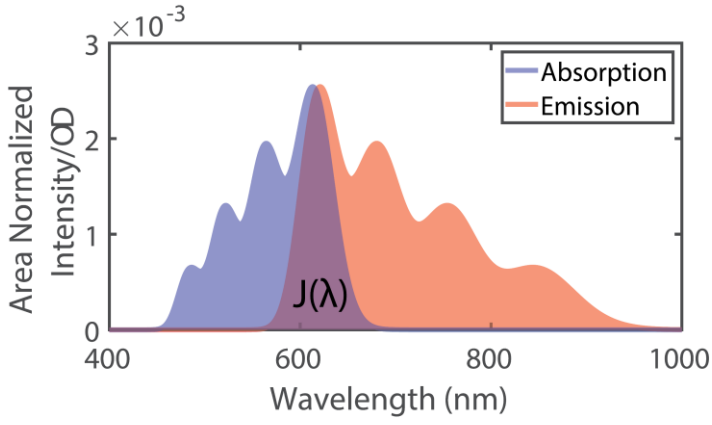

Figure 1.7: Area normalized overlapping absorption and emission spectra of two molecules with the potential for energy transfer. The area of overlap denoted is by *J(λ)*.

guarantees that EET will occur if spectral overlap is non-zero and the dipoles are not orthogonal. The rate equation can be further simplified by establishing the Förster distance R_0 – equal to the distance at which 50% of the decay donor decay is via energy transfer – such that

$$R_0^6 = \frac{9000 \ln(10) \kappa^2 Q_D J(\lambda)}{128 \pi^5 N n^4} \quad (1.15)$$

From this the rate of EET becomes

$$k_t(R) = \frac{1}{\tau_D} \left(\frac{R_0}{R}\right)^6 \quad (1.16)$$

which is the more familiar expression for the Förster rate.

In condensed systems we are less concerned with a singular energy transfer event, and more concerned with a series of energy transfer events resulting in the net directional migration of an excitation. In principle, modelling this should be straight forward: in the case where all surrounding chromophores are isoergic, the excitation will execute a random walk, hopping between chromophores until it relaxes in some way (fluorescence, charge separation and recombination, thermalization etc). In the case where there the chromophores have a distribution of energies, the migration will be a semi-random walk proceeding “downhill’ in energy. In both scenarios the exciton migration will be Markovian I.E. the probability of each hop is independent of the probabilities of the previous hops. In applying Förster theory the model exciton migration however, the results have often badly mis-

estimated the observed rates. This is because the Förster description of EET is only rigorously valid when four assumptions hold true: (1) the donor and acceptor can be treated as point dipoles – I.E. donor-acceptor separation is significantly larger than the donor or acceptor size; (2) neither the donor nor acceptor are significantly self-interacting; (3) the donor and acceptor are free from inhomogeneous broadening; (4) energy transfer is incoherent[36-39]. While these assumptions are good for dilute solutions of dye molecules, or in instances where dyes can be selectively tethered to isolated protein residues, they are not appropriate for considering energy transfer between closely associated molecular systems, I.E. in networks of conjugated polymers or in light-harvesting photosynthetic machinery.

In discussing EET in CPEs, nearly all the above assumptions are violated in some way. Because CPEs tend to complex quite closely, and emission proceeds from the longest chromophores, the interchromophore distance is frequently much smaller than the length of the emitting and absorbing chromophores. As discussed in the previous section, CPEs are also strongly self-interacting, with their photophysical response being greatly dependent on the state of aggregation. Moreover, in solutions and thin films CPEs have high static disorder arising from random conjugation breaks along the CPE backbone. Finally, it has recently been shown by Scholes, Fleming, von Grondelle, and others that EET does not always proceed incoherently in conjugated polymers, or indeed in biological photosynthetic systems[35, 40-44].

Corrections to Förster theory to account for these problems have been proposed with differing degrees of utility. The simplest correction relevant to CPEs is the correction for the point dipole approximation to linear systems.[45] For parallel linear conjugated polymers, the electronic coupling J ~ 1/(RL) for systems where L >> R where L is the extent of exciton delocalization, taken to be over the length of the chromophore in low disorder systems, and R is the interchain distance. Following Barford, the exciton transfer integral in the in the line dipole approximation, J_{ld}, is related to that of the point dipole approximation, J_{pd}, by

$$J_{ld} = fJ_{pd} \tag{1.17}$$

where

$$f = \frac{2R^2}{L^2}\left(1 - \frac{R}{\sqrt{R^2+L^2}}\right) \tag{1.18}$$

and the final Förster rate expression in the L>>R limit is

$$k_{ld} = \frac{1}{\tau_D}\left(\frac{R_0^{ld}}{R}\right)^2 \tag{1.19}$$

The notable result of this correction is that the rate of EET falls off as R^{-2} in the linear dipole approximation as opposed to R^{-6} in the point dipole approximation. This result is in good agreement with measurements in polymer thin films which find that *inter*chain EET can be competitive with *intra*chain EET. A more complete Generalized Förster Theory has been formulated by a large group led by Brédas and Beljonne[46-47]

building on previous recent work by Scholes[46] and Fleming and taking as its starting point the Pauli Master Equation

$$\frac{dP_i(t)}{dt} = \sum_j \left[k_{ij}P_j(t) - \left(k_{ij} + \tau_i^{-1}\right)P_i(t)\right] \quad (1.20)$$

where τ_i is the excited state lifetime, and the rate of exoergic EET is given as

$$k_{ji} = k_{ij}\mathrm{e}^{-\frac{\Delta \mathrm{E_{ij}}}{\mathrm{kT}}} \quad (1.21)$$

where ΔE_{ij} is the energy difference between the donor and acceptor absorption maxima. While this approach has been successful in modelling observed spectra and rates, it requires the calculation of the geometrically relaxed excited state energies and thus losses the practicality and ease of the initial Förster model.

For CPEs specifically, their remains an additional challenge in modelling EET behavior and extracting rates and efficiencies of energy transfer. This is because inherent to the EET models is the assumption that donor and acceptor spectral properties are fixed, even when the donor and acceptor are in close proximity. For dye molecules, light harvesting proteins, and isolated CPEs, this is a relatively safe assumption, but for CPE complexes, where donor and acceptor have oppositely charged sidechains, it is not. CPEs, recall, have a strong structure-function relationship between the conformation of the CPE backbone and the CPE electronic properties. For solutions or films of single component CPE systems it is expected that each CPE will adopt an average back-bone conformation and have some set of

ensemble average spectral properties. Inducing complexation with an oppositely charged partner can radically rearrange a CPE backbone, causing large changes in CPE compaction or extension for instance, and hence radically changes both donor and acceptor spectral properties regardless of EET. Investigations into EET in these systems is frustrated by these conformational rearrangements, and while EET shown to be occurring, its rate and efficiency are not estimable by typical fluorescence quenching experiments. The rate can potentially be determined by careful analysis of transient absorption spectra, which will be discussed in Chapter 3.

1.4 Time – Resolved Photoluminescence & Anisotropy

Time-resolved photoluminescence measurements see wide use when investigating conjugated polymers and other chromophores. These measurements can encode more information about a system than steady-state measurements alone, and differences in lifetimes between chromophore may be resolvable when absorption and photoluminescence differences are not. More importantly, time-resolved measurements lend crucial insight into exciton migration in molecular systems and are necessary for extracting EET rates and modelling EET systems. They can further be used to estimate exciton diffusion lengths, a crucial parameter if one is concerned with harvesting excited states.[34]

The time that an exciton remains in the excited state depends on the rates of radiative and non-radiative decay. These rates are the inverse of the radiative and

non-radiative lifetime (τ_R and τ_{NR}, respectively). The radiative lifetime captures, not surprisingly, the lifetime of radiative decay processes such as fluorescence and phosphorescence, whereas the non-radiative lifetime captures non-radiative decay processes such as collisional quenching, rotational and vibrational relaxation, intersystem crossing, charge-recombination, and singlet – singlet annihilation. These lifetimes are reflective of the various electronic and structural features which give rise to them. For example, a decrease in the radiative lifetime can reflect the creation of low energy exciton traps due to the formation of H-aggregates. In this scenario most excitons are funneled to the low energy traps, and only those which decay most rapidly are seen via fluorescence. Thus, knowledge of the radiative lifetime, which is more easily measure-able than the non-radiative lifetime, can lend crucial insight into structural and electronic changes occurring in a system. For CPEs, which predominantly decay via fluorescence, as opposed to phosphorescence, the relevant parameter is the fluorescence lifetime. A fluorescence lifetime cannot be measured directly but must be calculated from the time it takes for an excited state population to decay. For systems with a single fluorescence decay pathway, the intensity decay takes the form

$$I(t) = I_0 e^{-\frac{t}{\tau}} \tag{1.22}$$

with τ being the fluorescence lifetime, I_0 the initial intensity of the fluoresce, and $I(t)$ the intensity at some time t, where the intensity is proportional to the number of

excited molecules. For systems with multiple independent fluorescence decay pathways, the intensity decay is

$$I(t) = \sum_i \alpha_i e^{-\frac{t}{\tau}} \tag{1.23}$$

where the sum of the pre-exponential constants is unity.

TIME-CORRELATED SINGLE PHOTON COUNTING

A common method for measuring the fluorescence lifetime is time-correlated single photon counting (TCSPC).[48] This is a technique which was first developed in the mid-1960's and is currently enjoying a renaissance as compact electronics, high repetition rate lasers, and highly sensitive photodetectors have transformed it from an experiment requiring a room of electronics and several hours to perform, to one that can be done on a standard optical table in a matter of minutes or seconds. The principle of a TCSPC experiment is as follows: a sample is excited by a pulsed laser, and the time for an emitted photon to reach a

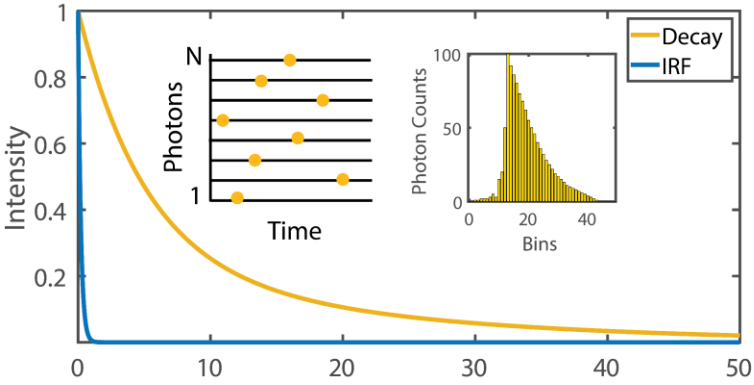

Figure 1.8: Representative time-resolved fluorescence decay curve (yellow) and instrument response function (blue). Insets show the response to photons from a constant fraction discriminator (left) and the way photons are binned in memory (right)

photodetector is recorded in a histogram in memory. If a sufficiently large number of photons are recorded, the photon distribution vs time should accurately reflect the time decay waveform of the fluorophore.

In a standard experiment a signal corresponding to a laser pulse is sent to a constant fraction discriminator (CFD)[11] which measures its arrival time and triggers a time-to-altitude (TAC) converter. The TAC begins a linear voltage ramp which continues until the CFD receives signal due to photon detection at (typically) a photomultiplier tube (PMT). The linear voltage is converted to a time which represents the delay between the start signal and stop signal and is recorded in memory. Ideally, all photons emitted would be collected, however the TAC has a finite, nanosecond, reset time. Because of this, the timing electronics of a TCSPC experiment only measure the first photon after an excitation pulse and cannot measure multiple photons. In order to avoid biasing the distribution toward short-lifetimes, measurements are carried out so that on average only one photon is detected per hundred laser pulses. The TAC reset time also necessitates that TCSPC experiments be run in 'reverse start-stop' configuration, that is that the timing is started with the observation of a photon a stopped by the laser pulse. This avoids

[11] A constant fraction discriminator is typically used in favor equipment which responds to the rising edge of a pulse due to its low timing jitter (on the order of a few ps). A detailed description of the operational of the various electronics in a TCSPC system is somewhat beyond the scope of this work.

the possibility that a high repetition rate pulse keeps the TAC in a perpetual state of reset.

The collected TCSPC decay curve is a discrete statistical distribution[12] (see **Figure 1.8**), and uncertainty can be minimized by collecting a sufficiently large set data. Noise in the experiment arises in two ways: a constant background due to PMT dark counts, and a fundamental counting error within the time channels. This counting error is, to a good approximation, Poisson distributed, and uncertainty in the number of counts in a channel, σ_i, is $\sqrt{N_i}$.[48] Since improvements in precision are inversely proportional to the number of counts in a channel, a high number must be accumulated in the main channel to ensure satisfactory statistics[13].

In an ideal experiment, the collected decay curve would represent response of the sample to a δ-pulse, yielding the true decay curve outright. For samples with long decay times relative to the full-width half-max of the excitation pulse, this an acceptable approximation. If, however, the excitation pulse is on the order of the decay lifetime then then the collected decay curve will be a convolution of the excitation pulse (plus the electronic instrument response) with the true decay curve. The convolution is especially acute at short decay times, where some chromophores

[12] Photon counts are not continuous, but are binned in separate channels in memory, with each channel being of width Δt.

[13] The main channel being the one with the highest counts. 10,000 counts in the main channel is typically considered enough for most experiments. This guarantees a precision of 10% in the channel where the curve has decayed to 1% of its maximum value.

– excited by the early time portion of the excitation pulse – are decaying while others are still being excited by the long-time portion of the excitation pulse. The convolved decay curve takes the form[14]

$$I_0(t) = \int_0^t P_0(t')I(t-t')dt' \tag{1.24}$$

where $P_0(t)$ is the measured instrument response function (IRF), and $I(t)$ is the true decay. There is no exact means of "deconvolving" the measured decay curve, I.E. even if $I_0(t)$ and $P_0(t)$ are known, one cannot directly solve for $I(t)$. In order to obtain $I(t)$, trial functions must be iteratively convolved with the measured IRF until a suitable set of parameters is found. Typically, this is done using least-squares fitting. In this technique, the optimal parameters are found by minimizing the quantity

$$\chi^2_{LS} = \sum_{i=1}^{n} W_i[y(t_i) - Y(t_i)]^2 \tag{1.25}$$

where $y(t_i)$ are the experimental data points, $Y(t_i)$ are the data points of the fitting function, W_i is a weighting factor of ith data point – taken as the reciprocal of $y(t_i)$ – and n is the total number of data points. For TCSPC decay curves this yields

$$\chi^2_{LS} = \sum_{i=1}^{n} \frac{[I_0(t_i) - I(t_i)]^2}{I_0(t_i)} \tag{1.26}$$

[14] The below function approximates the data to be continuous. This is a suitable approximation if the detector has many channels, as modern detectors do. Approximation of the decay as continuous for data analysis purposes should not be taken to disregard the fact that many counts must be accumulated in the main channel to ensure appropriate levels of precision for the experiment.

as the function to be minimized. Function estimation and minimization is carried out computationally using the Levenberg-Marquardt algorithm, a full description of which is beyond this work[15].

Because TCSPC and its fitting are fundamentally statistical in nature, evaluating goodness-of-fit is a high priority in assuring the lifetimes which are ultimately extracted are accurate and therefore physically relevant. This is especially important given that α_i and τ_i are correlated variables. Thus in addition to evaluating the quality of the fit, one must also take care that τ_i *seems reasonable in the context of supporting experiments and published data.* The quality of a fit can be evaluated in several ways, but most commonly it is evaluated by a combination of the reduced chi-square value (χ^2) and examination of the weighted residuals. The reduced chi-square value can be calculated from

$$\chi^2 = \frac{\chi^2_{LS}}{n_2 - n_1 + 1 - p} \tag{1.27}$$

where n_1 and n_2 are the first and last channels which are included in the analysis, and p is the number of free parameters. For Poisson distributed data, χ^2 should be 1 in perfect circumstances. However, the data may not be truly Poisson distributed, nor the fit perfect. There is some debate as to what constitutes an acceptable value

[15] Analysis in this work was carried out in the DecayFit package developed by Søren Preus at the University of Copenhagen. DecayFit allows for the least-squares minimization of up to a four-exponential decay function, with estimated correction parameters for sample scatter and time-shift to account for wavelength-dependent PMT response.

of χ^2, but most agree that values between 0.8 and 1.3 are acceptable. It is possible to achieve an acceptable χ^2 value but for the fit to still be poor. Because of this, a second metric, the weighted residuals, should be inspected. The weighted residuals are calculated as

$$r(t_i) = \frac{I_0(t_i) - I(t_i)}{\sqrt{I(t_i)}} \tag{1.28}$$

and when plotted should be randomly distributed about zero. Checking for a suitable χ^2 value, residuals which appear randomly distributed, as well as reasonable lifetimes should ensure that the fit to data is accurate.

TIME-RESOLVED FLUORESCENCE ANISOTROPY

The usefulness of time-resolved fluorescence data can be extended by considering changes in the polarized emission from the sample – that is, the anisotropy. The use of polarized light to excite a population of chromophores will yield a preferentially excited sub-population with

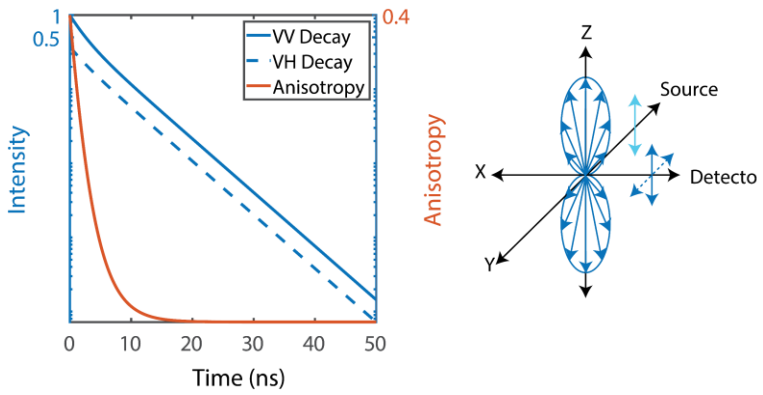

Figure 1.9: Representative time-resolved anisotropy decays (left) and distribution of transition dipoles excited in solution (right). The anisotropy decay starts at 0.4, as for a randomly distributed set of chromophores in solution.

transition dipoles oriented parallel to the excitation polarization (see **Figure 1.9**). This photo-selection phenomenon arises because the transition probability is proportional to $cos^2\theta$, where θ is the angle between the chromophore transition dipole that the polarization of the electric field vector. Over time the fluorescence from this population will depolarize due to molecular motion. The depolarization of an initially photo-selected population over time is reflected in the time-dependent anisotropy[34]

$$r(t) = \frac{I_{\parallel}(t) - I_{\perp}(t)}{I_{\parallel}(t) + 2I_{\perp}(t)} \quad (1.29)$$

where $I_{\parallel}(t)$ and $I_{\perp}(t)$ are the vertical and horizontal time-dependent fluorescence intensities. The anisotropy represents the difference in the vertical and horizontal fluorescence intensities, normalized by the total fluorescence intensity. Anisotropy can be used as a sensitive tool the probe the motion of a chromophore. For simple chromophores treated as ideal spheres or ellipsoids it can provide information about the diffusion and rotational rates in solution. In a biological context it can be used as a probe of segmental motion in long-biopolymers, and to understand denaturation in proteins and membranes.

In most cases, especially if the chromophores are in solution, the entire excited state population will not be perfectly aligned with the excitation polarization but will follow a distribution about it. For a randomly oriented population of

chromophores, $I_{//}$ is proportional to $\langle cos^2\theta \rangle$ and $I_{\perp}$ is proportional to $\langle sin^2\theta \rangle$ such that r, the steady-state anisotropy can be expressed as

$$r = \frac{3\langle \cos^2 \theta \rangle - 1}{2} \quad (1.30)$$

In cases where all transition dipoles are oriented along the excitation polarization, r = 1. For a random distribution however, r < 1. Because of this the fundamental anisotropy, r_0, the anisotropy in the absence of other depolarizing effects in given as

$$r_0 = \frac{2}{5}\left(\frac{3\cos^2 \beta - 1}{2}\right) \quad (1.31)$$

where the two-fifths pre-factor reflects the initial photo-selection of the population, and β is the angle between the absorption and emission dipoles[16]. For time-resolved analysis, the fundamental anisotropy is used as a constant pre-factor to the decay function representing the anisotropy at time-zero.

If one is already equipped to carry out a TCSPC experiment in the L-format orientation, then additional measurement of the anisotropy is relatively straightforward. Whereas a typical TCSPC experiment is carried out with vertically polarized excitation and emission measured at the magic angle[17], an anisotropy measurement is carried out under vertical excitation with emission collected in both vertical and horizontal polarization. The anisotropy can then be calculated from the

[16] Though most emission and absorption dipoles are assumed to be approximately collinear, this is not truly the case, though they may differ by only a few degrees in orientation.
[17] 54.75°. Collecting emission at this angle guarantees spectra will be free from polarization effects.

collected spectra. If the experimental set-up uses a monochromator or similar instrument with a diffraction grating, an additional correction factor, the G-factor, must be calculated. The G-factor accounts for the fact that diffraction gratings have differing quantum efficiencies depending on how the light to be diffracted is polarized. The G-factor is calculated as

$$G = \frac{\int I_{HV}(t)dt}{\int I_{HH}(t)dt} \tag{1.32}$$

where $I_{HV}(t)$ and $I_{HH}(t)$ are the fluorescence vertically and horizontally polarized fluorescence intensities due to horizontally polarized excitation. The G-factor is incorporated into the anisotropy as

$$r(t) = \frac{I_{\parallel}(t) - (G)I_{\perp}(t)}{I_{\parallel}(t) + (2G)I_{\perp}(t)} \tag{1.33}$$

Analysis for a time-resolved anisotropy decay is *highly* system dependent. Whereas a time-resolved fluorescence decay curve can almost always be fit to a sum-of-exponentials model, the same is not true of anisotropy decays. In the very simplest case, for dilute solutions of chromophores assumed to be approximately spherical, the decay can be fit by the exponential model according to

$$r(t) = \sum_j r_0 e^{-\frac{t}{\theta_j}} \tag{1.34}$$

where θ_j is a correlation time. For simple non-spherical systems (oblate or prolate ellipsoids) the rotational diffusion requires five exponentials, which is well beyond

the abilities of most experiments to resolve. Beyond simple systems, the models of depolarization due to chromophore movement will take varied forms and must be chosen based on some physical intuition of the ways chromophore motion might be limited.

ANISOTROPY AND DISPERSIVE TRANSPORT

Molecular motion is not the only process which can depolarize chromophore emission. Depolarization can also be due to exciton migration within a collection of chromophores. For systems where the rotational diffusion time is on the order of the excited state lifetime, rotational diffusion and exciton migration will be "competitive" depolarization processes. However, if rotational diffusion is quite small (due to chromophore size – as in large macromolecules, or solvent viscosity, or because the system is a solid) then exciton migration will be the predominant depolarization process[18]. If the system obeys strict Förster theory, then EET will be between isoergic chromophores[19], and can be modelled as a random walk. As discussed previously, the random chain conformation of CPEs leads to chromophore populations which have significant inhomogeneous broadening. EET in these systems does not proceed as a true random walk, but instead proceeds "downhill" to the lowest energy chain segment, with limited probability of back EET. It can be

[18] Rotational diffusion will dominate in systems where exciton migration is inhibited, as when the concentration of chromophores is quite small.

[19] Or at least between chromophores where the inhomogeneous broadening is significantly less than k_bT.

imagined, that after each EET step, the probability of transfer to another chromophore diminishes as the population of lower energy sites is lowered. Consequently, the rate of transfer, and hence the related rate of depolarization will slow with time. Such transport has been termed “dispersive transport”, and was the subject of significant study by, among others, Fayer, Huber, and Bässler [37-39, 49-51] beginning in the late 1980’s.

Dispersive transport models consider the value $G^s(t)$, which represents the probability that an exciton will be on located on its originating chromophore at some time *t*. Dispersive transport theory was developed specifically for time-resolved anisotropy decays obtained via TCSPC and used dye-labelled polymers as model systems. The basic formulation is seductively straightforward: r*(t)* is taken to be the product of the depolarization due to rotational diffusion the depolarization due to dispersive transport such that

$$r(t) = G^s(t)\phi(t)C \tag{1.35}$$

where C represents time-independent depolarization processes such as the offset between absorption and emission transition dipoles. In optimal cases the ϕ*(t)C* term is negligible, however it can be accounted for directly by measuring the anisotropy in dilute solutions where EET is negligible and anisotropic decay depends only on rotational diffusion and fixed terms

$$r_{dil}(t) = \phi(t)C \tag{1.36}$$

From the dilute measurement and the full concentration measurement, $G^s(t)$ can be calculated directly as

$$G^s(t) = \frac{r(t)}{r_{dil}(t)} \tag{1.39}$$

The full expression[20] for describing $G^s(t)$ is

$$ln\ G^s(t) = -\left(\frac{\rho}{\lambda}\right)\int\left\{1 - e^{-\lambda\omega(r)t}\right\}u(r)dr \tag{1.40}$$

where $u(r)$ is the chromophore pair correlation function, ρ is the chromophore density $\omega(r)$ is the dipole-dipole excitation transfer rate[21]. λ is a scaling factor which accounts for whether the chromophore transfer is donor-donor (IE multiple sequential hops are possible) or donor-trap (IE a single hop is made to the lowest energy state) and can vary between 1 (donor-donor) and 2 (donor-trap). While dispersive transport is an attractive theory, and has been successfully applied in the past, it is limited insofar as exciton migration must be on the order of the fluorescence lifetime. In CPEs, exciton migration is often on the ultra-fast fs time-scale, and so is difficult to model under this formalism.

[20] As formulated by Fayer and Peterson using Huber' first-order cumulant expansion.

[21] $\omega(r) = (1/\tau)(R_0/r)^6\gamma^2$, where τ is the excited state lifetime, R_0 is the Förster radius, and γ = 0.8468 for static randomly oriented dipoles. The model is formulated under the point-dipole approximation, and presumably extension to a line-dipole approximation would see $\omega(r)$ vary as $(1/R)^2$ for L>>R following Barford. To my knowledge no such extension has been made.

AYZNER LAB TCSPC APPARATUS

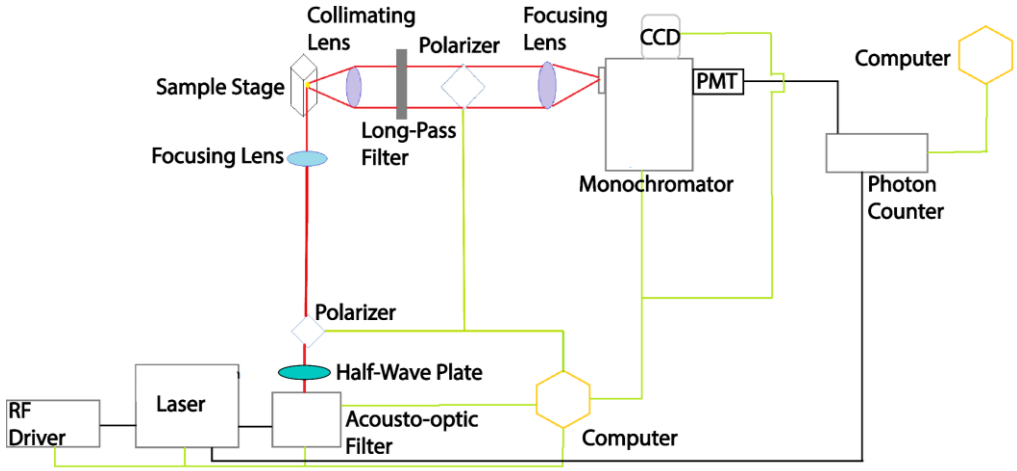

Figure 1.10: Schematic of the Ayzner lab TCSPC. The system is described in detail below.

Time-resolved fluorescence and anisotropy measurements included in this dissertation required the development of a TCSPC apparatus by the author (see **Figure 1.10** for schematic). The system is built in the L-format geometry. The excitation source is a supercontinuum white pulsed laser. Specific excitation wavelengths are selected via a radio-frequency driven piezo-electric crystal prism. Modulation of the radio frequency modulates the refractive index of the prism and directs the desired portion of the spectrum through the excitation aperture. This system has the benefit that excitation can be achieved at multiple pulse frequencies (~5 – 80 MHz), and at wavelengths between 397 nm and 1,400 nm. The large range of accessible excitation wavelengths allows for relatively straightforward interrogation of multiple electronic transitions without the need to recalibrate or realign the system. The cost to this is that the pulse bandwidth is broader than from

a more conventional laser system, and consequently has a broader instrument response function (~120 ps, FWHM). The excitation pulse is natively horizontally elliptically polarized. The beam passes first through an achromatic half-wave plate with its fast axis oriented at 45° from vertical in order to rotate the polarization 90° (vertically elliptically polarized), and then passes through a vertically oriented Glan-Thompson polarizer to provide a vertical linearly polarized beam. The excitation beam passes through an achromatic doublet focusing lens before reaching the sample stage. The sample stage can be arranged for either a traditional cuvette with emitted light collected at 90° relative to the excitation beam, or else a thin-film/1 mm cuvette oriented at 45°[22]. Emitted light is collected and columnated by an achromatic doublet before being passed through a long-pass filter[23] followed by a second Glan-Thompson polarizer set at the magic angle. Beyond the polarizer the emitted light is refocused onto the entrance slit of a monochromator which is used to select exactly which emitted wavelength is to be investigated. The monochromator is equipped with an air-cooled CCD, which allows for capturing steady-state fluorescence spectra, and a hybrid-PMT. When carrying out the TCSPC experiment, the monochromatic emitted light is focused onto the hybrid-PMT which

[22] The former is the traditional L-format orientation and minimizes collection of stray excitation light in the emission path. The latter is useful for films, or for concentrated solutions where non-trivial self-absorption is expected to occur. For the 1 mm cuvette, emitted light is collected "front-face" IE from the top layer of a relatively thin solution volume. The draw-back to this orientation is that a 45° angle maximizes the amount of excitation light reflect along the emission path. As a practical matter, the cuvette or thin film is rotated fractionally away from 45° to diminish laser reflection.
[23] Used to help exclude scatter laser light.

is coupled to a high-performance integrated TCSPC electronics system. The experiment is run in the start-stop configuration with the start pulse originating from the hybrid-PMT and the stop pulse from the NIM pulse of the laser. Both Glan-Thompson polarizers are controlled by motorized systems, allowing for fast re-orientation for anisotropy experiments, while the half-wave plate is re-oriented manually (only when measuring the G-factor). Electronic parameters such as the TAC gain, time-window, and collection time as well as laser wavelength, frequency, and monochromator wavelength are all controlled via computer. Delay between stop and start pulses is controlled by cable length, with 3 ns delay corresponding to 10 cm of cable length. Fundamental parameters such as the zero-crossing level and hybrid-PMT gain were determined when the system was built and are not changed from experiment to experiment[24].

1.5 Isothermal Titration Calorimetry

Insofar as the goal of the work presented herein is to understand the photophysics of oppositely charged conjugated polyelectrolyte complexes and to develop understanding as to how their photophysics might be controlled, a relevant question to ask is what drives the complexation process to begin with? This is in fact

[24] The hybrid-PMT in use has exceptionally low afterpulsing which can routinely be minimized to less than 1% of total IRF peak intensity. Dark counts are on the order of 900 counts-per-second, as compared to ~10^5 counts-per-second for a typical experiment. Characterization of the gain and zero crossing level were done by covering the hybrid-PMT face with a stack of white business cards and illuminating the face directly with a light source. Due to the sensitivity of the hybrid-PMT to light, it was necessary to affix it to the monochromator in the dark. It will be noted that these two operations represented the two most nerve-wracking portions of this work.

a question that extends to general polyelectrolytes more broadly and which remains the subject of ongoing research. The intuitive answer, that complexation is driven by mutual Coulombic attraction between oppositely charged side-chains, is most likely incorrect. Despite several decades of work to model polyelectrolyte complexation using continuum electrostatic models or extensions of Voorn – Overbeek theory, efforts have fallen short to completely capture the process and to describe the solution-phase salt response of these systems. Recent work by Schlenoff[52] has pushed back vigorously on the electrostatic model, arguing instead that complexation is largely driven by the entropically favorable release of counterions, and, to a lesser extent, reordering of the water hydrogen bond network. This work has made extensive use of isothermal titration calorimetry (ITC), a technique developed for determining the thermodynamic properties and rate constants of protein-ligand interactions. Increasingly ITC is being applied to (conjugated) polyelectrolyte complexation in order to asses the thermodynamic driving forces of the complexation process.

Being that it was developed for macromolecule-ligand interactions, this section will hew to the conventions set forth in the biophysics literature in describing the experiment and the associated analysis in terms of macromolecules (M) and ligands (L).[53] In truth, for extended macromolecular systems with multiple points of possible interaction, this description is overly simplistic. However, the M-L formalism is more

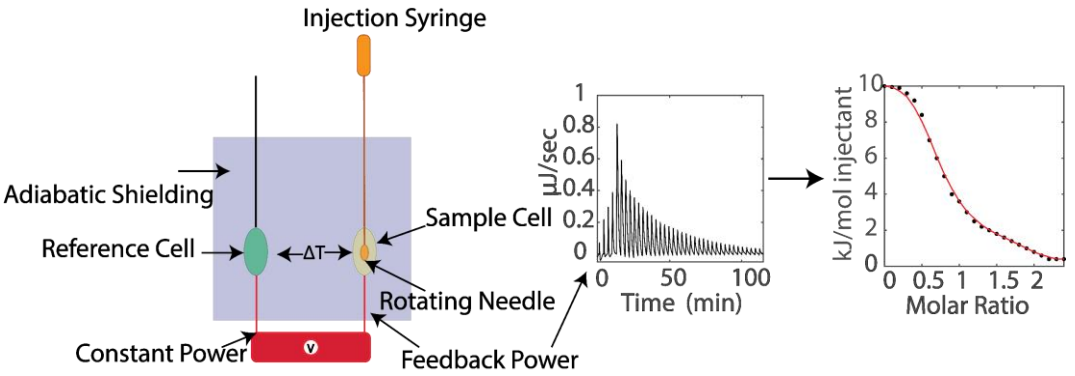

Figure 1.11: Basic schematic for an isothermal titration calorimeter (left). Raw ITC data as it appears on the instrument (middle). Integrated ITC data (with fit), giving heat evolved as a function of molar ratio.

than enough to explain the technique. ITC is one of the few techniques which allows for the direct determination of ΔH. The experiment is carried out in a calorimeter with equipped with a measurement and reference cell. The measurement cell is filled with a low concentration of M, and the reference cell with buffer. High concentration L is titrated into the measurement cell from a high-precision syringe, and the contents are continuously stirred to ensure fast mixing. The heat change is related to the mount of power (in μJ/s or μcal/s) required to maintain a constant temperature differential between the measurement cell and the reference cell. In the initial titrations, it is expected that [M] which is available to bind will be greater than the [L] injected. The first set of injections will all evolve (or consume) approximately the same amount of heat. As the fraction of M available for binding decreases, the heat change will diminish until all sites are occupied. At this point the

heat change from subsequent injections will represent the heat of dilution plus any non-specific heat effects.

Injection of each aliquot of L will change the volume in the measurement cell, displacing a volume of liquid from the cell equal to the volume of the aliquot. The change in volume will cause changes in the concentration of M and L, which can be accounted for as follows

$$[L]_{t,i} = [L]_0 \left(1 - \left(1 - \frac{v}{V_0}\right)^i\right) \quad (1.41)$$

$$[M]_{t,i} = [M]_0 \left(1 - \frac{v}{V_0}\right)^i \quad (1.42)$$

where $[L]_{t,i}$ and $[M]_{t,I}$ are the total concentrations after injection *i,* $[L]_0$ and $[M]_0$ are the initial concentrations, V_0 is the cell volume, and v is the injection volume. The total heat change per injection is found by calculating the area under each injection peak and in total is

$$\Delta Q_i = \Delta q_i + \Delta q_{i,dil} + \Delta q_{i,ns} \quad (1.43)$$

where q_i, $q_{i,dil}$, and $q_{i,ns}$ are the heat due to binding[25], dilution, and non-specific effects, respectively. The heat due to binding can be calculated from

[25] Binding here is generally non-covalent interactions which are assumed to be fixed over the time-scale of the experiment. We have observed a slow (on the order of weeks or months) time evolution of CPEC structure suggesting that these non-covalent interactions are not entirely fixed on long time scales. This evolution may be due to a slow rearrangement of side-chain binding partners, but the phenomenom has not been explored in depth.

$$\Delta q_i = [M]_{t,i} V_0 n \Delta H \Theta \tag{1.44}$$

where n is the number of binding sites on each macromolecule and Θ is the fractional binding of L. Raw ITC data is typically a plot of power vs time. The above expressions allow for this to be converted to a more readily accessible isotherm of heat vs molar ratio ([L]/[M]), where the heat per injection peak can be calculated numerically. Fitting of the isotherm to extract useful thermodynamic parameters is done computationally via the method of least squares. The fitting model used depends heavily on the expected behavior of the system. For a simple one-site binding interaction of the type $M + L \leftrightharpoons ML$, the relevant model is given by Wiseman[54] as

$$\Delta q_i = \frac{n[M]_{t,i} V_0 \Delta H}{2} \left[1 + \frac{[L]_{t,i}}{n[M]_{t,i}} + \frac{1}{c} - \sqrt{\left(1 + \frac{[L]_{t,i}}{n[M]_{t,i}} + \frac{1}{c}\right)^2 - \frac{4[L]_{t,i}}{n[M]_{t,i}}} \right] \tag{1.45}$$

where c is a unitless parameter[26] defined as

$$c = n K_b [M]_{t,i} \tag{1.46}$$

Successful fitting allows the determination of ΔH and K_b as the only free parameters. With these the remaining thermodynamic parameters may be determined following

[26] As a practical matter c controls the "squareness" of the isotherm and [M] is chosen such that c is between 1 and 1000. A large c leads to a square isotherm, with a nearly vertical transition slope, whereas a small c leads to a relatively flat isotherm.

$$\Delta G = \Delta H - T\Delta S = -RT \ln(K_b) \quad (1.47)$$

Further, repeating the experiment at several temperatures allows for the determination of the heat capacity, ΔC_P, from

$$\Delta C_p = \frac{d(\Delta H)}{dT} = T\left(\frac{d(\Delta S)}{dt}\right) \quad (1.48)$$

The heat capacity is of interest with regards to conjugated polyelectrolyte complexes because it can lend insight into hydrophobic effects in the system.

THE BINDING POLYNOMIAL FORMALISM

The necessity to develop independent models for various types of binding activity is an obvious constraint in the analysis of ITC data. Increasingly this is being avoided by use of the binding polynomial formalism[53-55], which allows for a generalized analysis of ITC data. This formalism was initially developed by Wyman and Gill, and its utility has since been extended by Velazquez-Campoy[55] to explain systems which have cooperative/competitive binding. The formalism uses the concept of a binding polynomial which is, for all intents and purposes, a partition function describing the system under study. Establishment of the binding polynomial first begins by considering the binding constants for an association of a macromolecule with *i* ligands such that that total binding event can be described by

$$M + iL \rightarrow ML_i$$

and has an overall association constant of β_i, which is given by

$$\beta_i = \frac{[ML_i]}{[M][L]^i} \tag{1.49}$$

and where β_i relates to K_i, the traditional stepwise binding constant via

$$\beta_i = \prod_{i=1}^{i} K_i \tag{1.50}$$

n, the number of binding sites per macromolecule is given as

$$n = \frac{[L]_B}{[M]_T} = \frac{\sum_{i=0}^{n} i[ML_i]}{\sum_{i=0}^{n}[ML_i]} = \frac{\sum_{i=0}^{n} i\beta_i[L]^i}{\sum_{i=0}^{n}\beta_i[L]^i} \tag{1.51}$$

The binding polynomial itself can be given either in terms of [M] and $[ML_i]$ or else in terms of the overall binding constant such that

$$P = \sum_{i=0}^{n} \beta_i[L]^i \tag{1.52}$$

The fractional saturation related to these terms by

$$\Theta = \frac{[ML_i]}{[M]_T} = \frac{\beta_i[L]^i}{P} \tag{1.53}$$

With these relationships established, the binding polynomial and overall association constant can be related to the integrated heat per injection via

$$\Delta q_i = V_0[M]_{t,i} \langle \Delta H \rangle_i \tag{1.54}$$

where

$$\langle \Delta H \rangle = \frac{\sum_{i=0}^{n} \beta_i[L]^i \Delta H_i}{P} \tag{1.55}$$

and can further be related to the Gibb's free energy by

$$\langle \Delta G \rangle = -RT \ln\left(\sum_{i=0}^{n} \beta_i [L]^i\right) \quad (1.56)$$

Thus, the binding polynomial allows for the determination of the thermodynamic parameters without needing to pre-determine a specific model for the binding interaction. So long as the number of binding sites is known (or can be guessed at) the binding polynomial can be determined and the full thermodynamic profile extracted from the ITC isotherm[27].

An additional correction can be made to the binding polynomial to account for interactions which may occur due to multiple ligands binding to the same macromolecule.[56] In general, if a macromolecule has more than one binding site the ligands which associate with it can behave in three ways toward one another: they can be independent, IE the binding of one ligand has no effect on the other; they can be competitive, IE the binding of one lessens the chance of the binding of another ligand; or they can be cooperative, IE the binding of one ligand increases the chances of binding another ligand[28]. These cooperative or competitive effects can be accounted for in the binding polynomial by inclusion of a pre-factor, α, in the overall binding constant. For independent binding α = 1, and the overall rate is

[27] Note: $[M]_{t,I}$ and $[L]_{t,I}$ are related to how the experiment is carried out, and their functional form does not change in the binding polynomial formalism. Moreover, solving for the ensemble enthalpy and overall binding constant still requires the application of least-squares fitting.

[28] The mechanism of ligand interaction remains a decidedly system specific question. Competition can arise from crowding of closely spaced binding sites, occlusion of a binding site which will accept two different types of ligands, or via allostery wherein binding of one ligand perturbs the macromolecule structure sufficiently to affect the binding site for another ligand. In most cases allostery is the main cooperative mechanism.

unperturbed. For completely competitive binding (IE the binding of one ligand completely precludes binding of another) α = 0. Incomplete competition is inferred when 0 < α < 1, and cooperative binding when α < 1. The inclusion of the α term and subsequent determination of the binding polynomial is best shown by considering a concrete example. In this case we will consider a macromolecule with two binding sites which can accept identical ligands.

$$M + L \overset{K}{\leftrightarrow} ML + L \overset{\alpha K}{\leftrightarrow} ML_2$$

The general binding polynomial is

$$P = \sum_{i=0}^{2} \beta_i [L]^i = 1 + \beta_1 [L] + \beta_2 [L]^2 \quad (1.57)$$

and the binding polynomial in terms of the individual binding constants for each binding event is

$$P = 1 + 2K_b [L] + \alpha K_b^2 [L]^2 \quad (1.58)$$

where each term gives the relative concentration of the un-ligated, singly ligated, and doubly ligated molecule, respectively.

1.6 Description of Chapters to Follow

The following chapters largely concern the fundamental properties of oppositely charged conjugated polyelectrolyte complexes of the model donor-acceptor system of PFPI and PTAK. Chapter 1 deals with the most basic question: given PFPI and PTAK, with thermodynamically allowed EET, do they form stable complexes and are

there signs of EET? The answer to both questions is yes, with the additional finding that PTAK – intrinsically a low quantum yield CPE due to strong J_{intra} – has a dramatically increased quantum yield regardless of EET events occurring. Chapter 2 builds on the preceding chapter and asks: what is the rate of EET between PFPI and PTAK, how is the structural conformation of PTAK changed upon complexation (leading to intrinsically high quantum yield states), and are these factors effected by the ratio of PFPI to PTAK in the complex? It is found that the rate of EET in the complexes is found the be on the order of ~240 fs – commensurate with natural photosynthesis, that PTAK undergoes a significant chain extension upon complexation, and that the highest EET rates and straightest PTAK chains are found when PFPI is in excess on a molar charge basis. Chapter 3 compares the thermodynamics and kinetics of complexation between PFPI and regioregular PTAK (used in Chapters 1 & 2), regiorandom PTAK (which has weaker J_{intra} and an intrinsically higher quantum yield than regioregular PTAK), and a doubly anionic CPE, poly(cyclopentadithieno-alt-phenylene) (PCPT). Here the complexation is found to have slow and fast kinetic components related to the “unravelling” of PTAK chains (fast) and overall network evolution (slow). Complexation is thermodynamically favored, but there is significant enthalpy-entropy compensation as the temperature is varied. Moreover, it is posited that complexation dynamics fall on a spectrum of protein-like to polyelectrolyte like based on the extent of self-interaction in the un-complexed CPEs. Chapter 4 is a photophysical characterization of a recently

synthesized conjugated ladder polymer, LP1, and comparison to its monomer. The polymer is found to have the longest radiative lifetime of any ladder polymer to date, and to high J_{inter}, both suggesting suitability for efficient charge transport and exciton migration.

REFERENCES

1. Parliament, T. E., Directive of the European Parliament of the Council on the promotion of the use of energy from renewable sources. *Official Journal of the European Parliament* **2018**.

2. Aresta, M.; Dibenedetto, A.; Angelini, A., The use of solar energy can enhance the conversion of carbon dioxide into energy-rich products: stepping towards artificial photosynthesis. *Philos Trans A Math Phys Eng Sci* **2013,** *371* (1996), 20120111.

3. Blankenship, R. E.; Tiede, D. M.; Barber, J.; Brudvig, G. W.; Fleming, G.; Ghirardi, M.; Gunner, M. R.; Junge, W.; Kramer, D. M.; Melis, A.; Moore, T. A.; Moser, C. C.; Nocera, D. G.; Nozik, A. J.; Ort, D. R.; Parson, W. W.; Prince, R. C.; Sayre, R. T., Comparing Photosynthetic and Photovoltaic Efficiencies and Recognizing the Potential for Improvement. *Science* **2011,** *332* (6031), 805-809.

4. Brotosudarmo, T. H. P.; Prihastyanti, M. N. U.; Gardiner, A. T.; Carey, A.-M.; Cogdell, R. J., The Light Reactions of Photosynthesis as a Paradigm for Solar Fuel Production. *Energy Procedia* **2014,** *47*, 283-289.

5. Cogdell, R. J.; Gardiner, A. T.; Molina, P. I.; Cronin, L., The use and misuse of photosynthesis in the quest for novel methods to harness solar energy to make fuel. *Philos Trans A Math Phys Eng Sci* **2013,** *371* (1996), 20110603.

6. Frischmann, P. D.; Mahata, K.; Wurthner, F., Powering the future of molecular artificial photosynthesis with light-harvesting metallosupramolecular dye assemblies. *Chem Soc Rev* **2013,** *42* (4), 1847-70.

7. Fukuzumi, S., Development of bioinspired artificial photosynthetic systems. *Phys Chem Chem Phys* **2008,** *10* (17), 2283-97.

8. Garg, V.; Kodis, G.; Liddell, P. A.; Terazono, Y.; Moore, T. A.; Moore, A. L.; Gust, D., Artificial photosynthetic reaction center with a coumarin-based antenna system. *J Phys Chem B* **2013,** *117* (38), 11299-308.

9. Francàs, L.; Richmond, C.; Garrido-Barros, P.; Planas, N.; Roeser, S.; Benet-Buchholz, J.; Escriche, L.; Sala, X.; Llobet, A., Ru–bis(pyridine)pyrazolate (bpp)-Based Water-Oxidation Catalysts Anchored on TiO2: The Importance of the Nature and Position of the Anchoring Group. *Chemistry – A European Journal* **2016,** *22* (15), 5261-5268.

10. Tachibana, Y.; Vayssieres, L.; Durrant, J. R., Artificial photosynthesis for solar water-splitting. *Nature Photonics* **2012,** *6* (8), 511-518.

11. Weston, M.; Handrup, K.; Reade, T. J.; Champness, N. R.; O'Shea, J. N., Experimental observation of sub-femtosecond charge transfer in a model water splitting dye-sensitized solar cell. *J Chem Phys* **2012,** *137* (22), 224706.

12. Concepcion, J. J.; House, R. L.; Papanikolas, J. M.; Meyer, T. J., Chemical approaches to artificial photosynthesis. *Proc Natl Acad Sci U S A* **2012,** *109* (39), 15560-4.

13. Croce, R.; van Amerongen, H., Natural strategies for photosynthetic light harvesting. *Nat Chem Biol* **2014,** *10* (7), 492-501.

14. Ghosh, P. K.; Smirnov, A. Y.; Nori, F., Artificial photosynthetic reaction centers coupled to light-harvesting antennas. *Physical Review E* **2011,** *84* (6).

15. Andrew, T. L.; Swager, T. M., Structure-Property relationships for exciton transfer in conjugated polymers. *Journal of Polymer Science Part B: Polymer Physics* **2011,** *49* (7), 476-498.

16. Thomas, S. W. I.; Joly, G. D.; Swager, T. M., Chemical Sensors Based on Amplifying Fluorescent Conjugated Polymers. *Chemical Reviews* **2007,** *107*, 1339-1386.

17. Kelley, A. M., *Condensed-Phase Molecular Spectroscopy and Photophysics*. Wiley: 2012.

18. Brazovskii, S.; Kirova, N., Physical theory of excitons in conducting polymers. *Chem Soc Rev* **2010,** *39* (7), 2453-65.

19. Spano, F. C.; Silva, C., H- and J-Aggregate Behavior in Polymeric Semiconductors. *Annual Review of Physical Chemistry* **2014,** *65* (1), 477-500.

20. Schwartz, B. J., CONJUGATED POLYMERS AS MOLECULAR MATERIALS: How Chain Conformation and Film Morphology Influence Energy Transfer and Interchain Interactions. *Annual Review of Physical Chemistry* **2003,** *54* (1), 141-172.

21. Kasha, M.; Rawls, H. R.; Ashraf El-Bayoumi, M., The exciton model in molecular spectroscopy. *Pure and Applied Chemistry* **1965,** *11* (3-4), 371-392.

22. Hestand, N. J.; Spano, F. C., Molecular Aggregate Photophysics beyond the Kasha Model: Novel Design Principles for Organic Materials. *Acc Chem Res* **2017,** *50* (2), 341-350.

23. Hestand, N. J.; Spano, F. C., Expanded Theory of H- and J-Molecular Aggregates: The Effects of Vibronic Coupling and Intermolecular Charge Transfer. *Chem Rev* **2018,** *118* (15), 7069-7163.

24. Clark, J.; Chang, J.-F.; Spano, F. C.; Friend, R. H.; Silva, C., Determining exciton bandwidth and film microstructure in polythiophene films using linear absorption spectroscopy. *Applied Physics Letters* **2009,** *94* (16), 163306.

25. Hestand, N. J.; Spano, F. C., Determining the spatial coherence of excitons from the photoluminescence spectrum in charge-transfer J-aggregates. *Chemical Physics* **2016,** *481*, 262-271.

26. Niles, E. T.; Roehling, J. D.; Yamagata, H.; Wise, A. J.; Spano, F. C.; Moulé, A. J.; Grey, J. K., J-Aggregate Behavior in Poly-3-hexylthiophene Nanofibers. *The Journal of Physical Chemistry Letters* **2012,** *3* (2), 259-263.

27. Spano, F. C., The fundamental photophysics of conjugated oligomer herringbone aggregates. *The Journal of Chemical Physics* **2003,** *118* (2), 981.

28. Spano, F. C.; Clark, J.; Silva, C.; Friend, R. H., Determining exciton coherence from the photoluminescence spectral line shape in poly(3-hexylthiophene) thin films. *The Journal of Chemical Physics* **2009,** *130* (7), 074904.

29. Spano, F. C.; Yamagata, H., Vibronic coupling in J-aggregates and beyond: a direct means of determining the exciton coherence length from the photoluminescence spectrum. *J Phys Chem B* **2011,** *115* (18), 5133-43.

30. Yamagata, H.; Norton, J.; Hontz, E.; Olivier, Y.; Beljonne, D.; Bredas, J. L.; Silbey, R. J.; Spano, F. C., The nature of singlet excitons in oligoacene molecular crystals. *J Chem Phys* **2011,** *134* (20), 204703.

31. Yamagata, H.; Spano, F. C., Interplay between intrachain and interchain interactions in semiconducting polymer assemblies: the HJ-aggregate model. *J Chem Phys* **2012,** *136* (18), 184901.

32. Yamagata, H.; Spano, F. C., Vibronic coupling in quantum wires: Applications to polydiacetylene. *The Journal of Chemical Physics* **2011,** *135* (5), 054906.

33. Yamagata, H.; Spano, F. C., Strong Photophysical Similarities between Conjugated Polymers and J-aggregates. *J Phys Chem Lett* **2014,** *5* (3), 622-32.

34. Lakowicz, J. R., *Principles of Fluorescence Spectroscopy*. 3 ed.; Springer Science+Business Media, LLC: New York, NY, 2006.

35. Chenu, A.; Scholes, G. D., Coherence in energy transfer and photosynthesis. *Annu Rev Phys Chem* **2015,** *66*, 69-96.

36. Olaya-Castro, A.; Scholes, G. D., Energy transfer from Förster–Dexter theory to quantum coherent light-harvesting. *International Reviews in Physical Chemistry* **2011,** *30* (1), 49-77.

37. Peterson, K.; Zimmt, M.; Fayer, M.; Jeng, Y.; Frank, C., Fluorescence Depolarization of Chromophores in Polymeric Solids. *Macromolecules* **1989,** *22*, 5.

38. Stein, A.; Peterson, K.; Fayer, M., Dispersive Electronic Excitation Transport in Polymeric Solids at and Near Room Temperature. *Chem Phys Lett* **1989,** *161* (1), 7.

39. Stein, A.; Peterson, K.; Fayer, M., Dispersive Excitation Transport at Elevated Temperatures (50-298K): Experiments and Theory. *J Phys Chem* **1990,** *92* (9), 14.

40. Arpin, P. C.; Turner, D. B.; McClure, S. D.; Jumper, C. C.; Mirkovic, T.; Challa, J. R.; Lee, J.; Teng, C. Y.; Green, B. R.; Wilk, K. E.; Curmi, P. M.; Hoef-Emden, K.; McCamant, D. W.; Scholes, G. D., Spectroscopic Studies of Cryptophyte Light Harvesting Proteins: Vibrations and Coherent Oscillations. *J Phys Chem B* **2015,** *119* (31), 10025-34.

41. Collini, E.; Scholes, G. D., Coherent Intrachain Energy Migration in a Conjugated Polymer at Room Temperature. *Science* **2009,** *323* (5912), 369-373.

42. Collini, E.; Scholes, G. D., Electronic and Vibrational Coherences in Resonance Energy Transfer along MEH-PPV Chains at Room Temperature. *The Journal of Physical Chemistry A* **2009,** *113* (16), 4223-4241.

43. Fassioli, F.; Dinshaw, R.; Arpin, P. C.; Scholes, G. D., Photosynthetic light harvesting: excitons and coherence. *J R Soc Interface* **2014,** *11* (92), 20130901.

44. Hwang, I.; Scholes, G. D., Electronic Energy Transfer and Quantu-Coherence in π-Conjugated Polymers†. *Chemistry of Materials* **2011,** *23* (3), 610-620.

45. Barford, W., Beyond Forster resonance energy transfer in linear nanoscale systems. *J Phys Chem A* **2010,** *114* (43), 11842-3.

46. Beljonne, D.; Curutchet, C.; Scholes, G. D.; Silbey, R. J., Beyond Forster resonance energy transfer in biological and nanoscale systems. *J Phys Chem B* **2009,** *113* (19), 6583-99.

47. Gierschner, J.; Huang, Y. S.; Van Averbeke, B.; Cornil, J.; Friend, R. H.; Beljonne, D., Excitonic versus electronic couplings in molecular assemblies: The importance of non-nearest neighbor interactions. *J Chem Phys* **2009,** *130* (4), 044105.

48. Becker, W., *The bh TCSPC Handbook*. Becker & Hickl GmbH: 2012.

49. Mahrt, R. F.; Pauck, T.; Lemmer, U.; Siegner, U.; Hopmeir, M.; Hennig, R.; Bassler, H.; Gobel, E. O.; Haring Bolivar, P.; Wegman, G.; Kurz, H.; Scherf, U.; Mullen, K., Dynamics of optical excitation in a ladder-type pi-conjugated polymer containing aggregate states. *Physical Review B* **1996,** *54* (3), 1759-1765.

50. Meskers, S. C. J.; Hubner, J.; Oestreich, M.; Bassler, H., Dispersive Relaxation Dynamics of Photoexcitations in a Polyfluorene Film Involving Energy Transfer: Experiment and Monte Carlo Simulations. *J Phys Chem B* **2001,** *105*, 9139-9149.

51. Movaghar, B.; Grünewald, M.; Ries, B.; Bassler, H.; Würtz, D., Diffusion and relaxation of energy in disordered organic and inorganic materials. *Physical Review B* **1986,** *33* (8), 5545-5554.

52. Fu, J.; Schlenoff, J. B., Driving Forces for Oppositely Charged Polyion Association in Aqueous Solutions: Enthalpic, Entropic, but Not Electrostatic. *J Am Chem Soc* **2016,** *138* (3), 980-90.

53. Freire, E.; Schön, A.; Velazquez-Campoy, A., Chapter 5 Isothermal Titration Calorimetry. In *Biothermodynamics, Part A*, 2009; pp 127-155.

54. Herrera, I.; Winnik, M. A., Differential binding models for isothermal titration calorimetry: moving beyond the Wiseman isotherm. *J Phys Chem B* **2013,** *117* (29), 8659-72.

55. Vega, S.; Abian, O.; Velazquez-Campoy, A., A unified framework based on the binding polynomial for characterizing biological systems by isothermal titration calorimetry. *Methods* **2015,** *76*, 99-115.

56. Brown, A., Analysis of cooperativity by isothermal titration calorimetry. *Int J Mol Sci* **2009,** *10* (8), 3457-77.

Chapter 2

Exciton Transfer and Emergent Excitonic States in Oppositely-Charged Conjugated Polyelectrolyte Complexes

Acknowledgements: This chapter was originally published in the Journal of Physical Chemistry B with the following authorship: William R. Hollingsworth,[≠] Carmen Segura,[≠] Jonathan Balderrama, Nathaniel Lopez, Pamela Schleissner, Alexander L. Ayzner. WRH carried out time-resolved spectroscopy and analysis thereof; CS carried out dynamic light scattering, small angle x-ray scattering, and analysis thereof; JB, NL and PS assisted with sample preparation and steady-state spectroscopy. WRH and CJ principally wrote the manuscript. ALA edited the manuscript and oversaw the project.

Abstract: Photosynthetic organisms have mastered the use of "soft" macromolecular assemblies for light absorption and concentration of electronic excitation energy. Nature's design centers on an optically-inactive protein-based backbone that acts as a host matrix for an array of light-harvesting pigment molecules. The pigments are organized in space such that excited states can migrate between molecules, ultimately delivering the energy to the reaction center. Here we report our investigation of an artificial light-harvesting energy transfer antenna based on complexes of oppositely charged conjugated polyelectrolytes (CPEs). The conjugated backbone and the charged sidechains of the CPE lead to an architecture that simultaneously functions as a structural scaffold and an electronic energy "highway". We find that the process of ionic complex formation leads to a

remarkable change in the excitonic wavefunction of the energy acceptor, which manifests in a dramatic increase in the fluorescence quantum yield. We argue that the extended backbone of the donor CPE effectively templates a planarized acceptor polymer, leading to excited states that are highly delocalized along the polymer backbone.

2.1 INTRODUCTION

Over billions of years, natural organisms such as bacteria and plants have evolved the exceedingly complex, supramolecular light-harvesting machinery to ensure efficient conversion of sunlight to chemical potential energy.[1-4] Given the nearly inexhaustible source of solar photons and the success of natural photosynthesis, light-harvesting architectures based on the general principles employed by Nature are attractive for solar generation of chemical fuels. This involves directionally funneling photogenerated electronic excited states (excitons) to a molecular interface, where generation of electron/hole pairs and their subsequent spatial separation takes place. Upon separation, charges cascade down an electron transport chain to the protein assemblies that subsequently drive fuel-generating biochemical reactions.[5]

The elegance of natural supramolecular organization and its associated efficiency of light harvesting inspires us to mimic this photosynthetic machinery in the laboratory. We seek to construct a *modular*, "soft" artificial photosystem capable of efficient light absorption, electronic energy transfer (EET) and long-lived charge generation. This goal requires creating a supramolecular assembly with subunits capable of carrying out the above photophysical processes. To increase the effective absorption cross-section of the photosystem, Nature uses an array of peripheral proteins that serve as an optically-inactive structural scaffolding for pigment molecules. These complexes are collectively known as light-harvesting

antennae (LHA). Excitons generated in pigments within LHA are directionally funneled via a combination of coherent and incoherent EET to a “reaction center”, where the exciton is energetically trapped prior to generation of electron/hole pairs via electron transfer. Thus, efficient EET is of paramount importance for LHA function.[4, 6-9]

A large body of work exists describing the synthesis of covalently-linked LHA and reaction centers. Fairly large porphyrin arrays coupled to fullerene electron acceptors,[10-13] as well as more exotic systems containing built-in energy gradients have been prepared to date,[14] among many others. However, it has been recognized that modularity in Nature is key for successful photosystem function.[2] Thus, self-organization appears to be a more attractive avenue for construction of “soft” photosystems. This is because assembly of modular subunits allows for greater flexibility and optimization of the individual parts, as opposed to the need to synthesize the entire collection “from scratch” if the system must be altered in one or more of its functions to suit a particular energetic, structural or stability requirement.

A particularly attractive candidate to serve as the cornerstone for a supramolecular LHA assembly is the conjugated polyelectrolyte (CPE) – an amphiphilic polymer with a conjugated backbone and ionized (or ionizable) sidechains.[15] Due to their π-electron-rich backbones and ionic sidechains, CPEs hold

great promise as electronic energy highways and macromolecular scaffolds.[16-19] The electrostatic coupling leads to strong interactions, while controlling the charge density allows for tuning the cooperative strength of this interaction. Furthermore, the strong influence of the backbone microstructure on its optoelectronic properties, as well as sensitivity to the local electric field, allows one to tune the environment to control EET, akin to how the polypeptide scaffolding environment can tune the energy levels of natural pigments. Using CPEs in light-harvesting assemblies largely obviates the need for an optically inactive scaffolding, thereby raising the density of subunits that directly contribute to excited state generation.

In this manuscript, we describe assembly of oppositely charged CPEs as LHA with complementary electronic absorption and emission spectra, resulting in thermodynamically-allowed EET between the complexed CPEs. To the best of our knowledge, this is the first time that a multi-CPE complex assembly in solution has been studied. We show that both in solution and the solid state, oppositely-charged CPEs readily form ionic complexes that undergo inter-CPE EET. Further, we show that complex formation drastically modulates the nature of the emitting excitonic wavefunction relative to isolated CPEs. Our results demonstrate that oppositely charged complexes of donor/acceptor CPEs display rich photophysics and intriguing assembly behavior, underscoring the potential of these materials to function as tunable exciton relays for LHA applications.

2.2 RESULTS AND DISCUSSION

This investigation focuses on an oppositely charged pair of CPEs, the chemical structures of which are shown in **Figure 2.1A**. The iodide salt of the cationic poly(fluorene-co-phenylene) (PFPI) derivative serves as the excitonic donor, and the potassium salt of an anionic, regioregular poly(thiophene) (PTAK) derivative acts as the energy acceptor. **Figure 2.1B** shows that the emission spectrum of PFPI spectrally overlaps the optical density (OD) of PTAK, indicating that energy transfer is thermodynamically allowed. Since both CPEs emit readily detectable photoluminescence (PL), and because the chain microstructure is strongly coupled to the polymer photophysics, PL spectroscopy forms the basis for this investigation. Aqueous CPE concentrations were chosen to

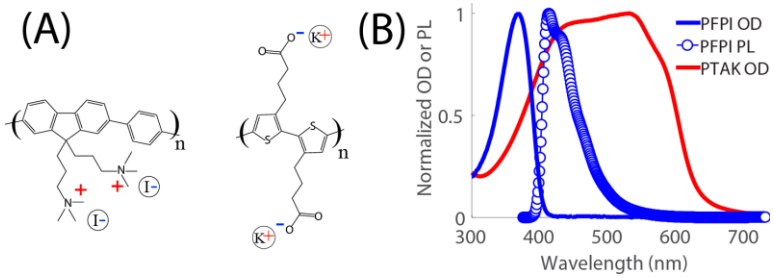

Figure 2.1. (A) Chemical structures of PFPI (left) and PTAK (right). (B) Optical density (OD) and photoluminescence (PL) of PFPI and PTAK solutions. The overlap of PFPI PL with OD of PTAK indicates that excitons can undergo energy transfer from the excited PFPI donor to the PTAK acceptor.

be large enough so as to observe phase separation beyond a critical polycation/polyanion charge ratio, allowing us to compare the photophysics of the liquid and solid phases.

Figure 2.2 shows steady-state PL contour maps with excitation and emission wavelengths plotted vertically and horizontally, respectively, of both isolated CPE solutions and their mixed solutions. The PL map of 1 mg/mL PFPI is shown in **Figure 2.2A**. As expected, the PL intensity is concentrated in the region that corresponds to

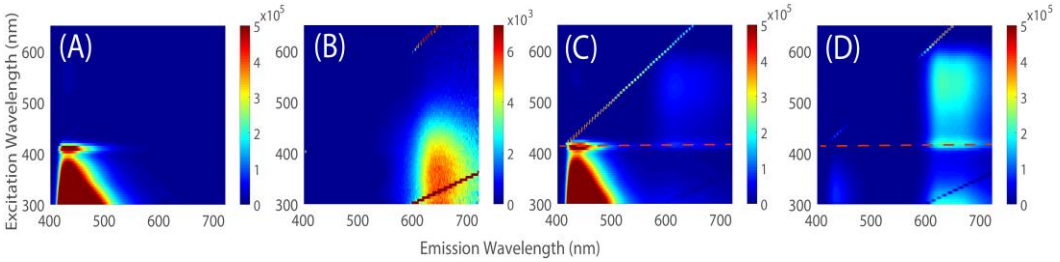

Figure 2.2. Aqueous solution 2D PL maps of (A) PFPI at 1 mg/mL, (B) PTAK mole-matched to the 1:0.25 charge ratio CPEC, (C) 1:0.01 PFPI:PTAK CPEC, and (D) 1:0.25 CPEC. The bright pixels falling on a diagonal line in the upper left corner are due to reflections of the excitation wavelength. The red dashed, horizontal line in (C) and (D) indicates the excitation wavelength that gives rise to PFPI emission and to simultaneous PTAK emission. The sharp enhancement of the latter cannot be explained by the PTAK absorption spectrum, indicating evidence of EET from PFPI to PTAK. The same enhancement is seen at lower excitation wavelengths as well. Though isolated PTAK emits in this region as well, in a CPEC this PTAK PL is drastically more intense, as indicated by the change in scale between (B) and (D).

strong PFPI absorption, as shown in **Figure 2.1**. However, because of the very large extinction coefficient of PFPI, at these concentrations the PL map appears as two PL bands as a function of excitation wavelength (λ_{ex}). This is a consequence of the fact

that PL intensity was collected at 90° with respect to the excitation beam, resulting in imperfect spatial overlap of PL signal due to excitations near the OD peak with the capture cross-section of the detector.

Figure 2.2B shows PL due to an aqueous PTAK solution at a concentration matched to the PFPI:PTAK complex at the 1:0.25 molar charge ratio (**Figure 2.2D**). A contrast scale that was different from the rest of the samples had to be used for this particular sample due its very low PL intensity; in fact, at these instrumental parameters, PL from lower concentration solutions was barely measurable. In addition to the observation that PTAK solutions fluoresce weakly, it is important to note that there is negligible PL arising at λ_{ex} that give rise to peak absorption. In this context, it is worth mentioning that the *solution* absorption spectrum of PTAK is quite similar to that of a *thin film* of neutral, regioregular poly(3-hexylthiophene) – a well-studied poly(thiophene) derivative, P3HT – which is also known to have low PL quantum yields.[20-23]

Figures 2C and **2D** show PL maps from solutions of oppositely-charged CPE complexes (CPECs) at the specified polycation:polyanion molar charge ratios. Here, the PFPI concentration has been fixed at 1 mg/mL, and the charge ratio is varied by varying the concentration of PTAK. The 2D PL map for the 1:0.01 CPEC (**Figure 2.2C**) shows the characteristic PFPI emission band, but in addition, the PTAK region at emission wavelengths (λ_{em}) > 550 nm now also shows several PL bands. First, there is

PTAK PL peaked in a narrow λ_{ex} range corresponding to the excitation of low-energy PFPI chromophores; as such, this PTAK band falls on the same horizontal line (λ_{ex} = constant) as PFPI, labeled with a red dashed line. Second, there is measurable PL coming from PTAK throughout its absorption band. Control PTAK solution at this concentration do not show any intensity on this contrast scale.

When the charge ratio is further increased to 1:0.25, the solution phase separates into a liquid phase and a dense CPE network phase, which resembles a loose precipitate. The PL map of the solid phase is shown in Appendix I. **Figure 2.2D** shows the PL of the solution phase at this charge ratio. The figure shows that PFPI PL has been substantially quenched. Concomitantly, PTAK PL is substantially enhanced both over the λ_{ex} that give rise to PFPI PL. Additionally, PTAK PL arising from the bulk of its absorption (λ_{ex} > 450 nm) is now quite strong, in stark contrast to the weak PL from the control PTAK solution at the same nominal concentration (**Figure 2.2B**).

To understand the difference between the steady-state PTAK photophysics in isolation vs. as part of a CPEC, we have displayed representative OD spectra of PTAK

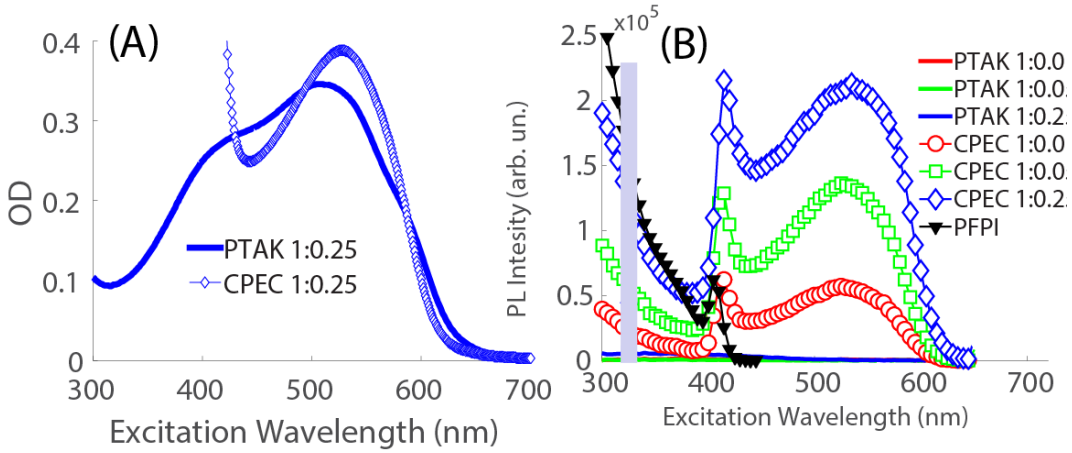

Figure 2.3. (A) OD of isolated PTAK and PTAK complexed to PFPI (CPEC) at the same nominal PTAK concentrations. (B) PL excitation (PLE) spectra collected at an emission wavelength that exclusively corresponds to PTAK PL. For comparison, PLE of PFPI in a CPEC (collected near PFPI PL peak and scaled for clarity) is also shown with black filled diamonds. The PLE intensity of PTAK complexed to PFPI is orders of magnitude larger than that of PTAK on its own. The enhancement in complexed PTAK's PL at wavelengths that correspond to PFPI PL yet do not correspond to sharp PTAK OD features is strong evidence of inter-CPE EET from photoexcited PFPI to PTAK. The grey bar masks the specular reflection of the excitation light.

in isolation vs. in the complexed state in **Figure 2.3A**. Both samples show comparable OD magnitudes; however, there are notable differences. The isolated PTAK spectrum is slightly red-shifted relative to the CPEC, and the latter has enhanced oscillator strength over the main excitonic absorption band.

To quantify differences in PL intensities between the different PTAK samples, **Figure 2.3B** shows the PL excitation (PLE) spectrum for different charge ratios *exclusively in the PTAK emission region*, generated by plotting the PL intensity at λ_{em} close to the peak of the PTAK emission spectrum as a function of λ_{ex}. In the CPEC, there is clear enhancement in PTAK PL precisely at λ_{ex} that give rise to strong PL from

PFPI (black diamonds; also seen in **Figures 2A** and **2C**), both at the relatively sharp band at λ_{ex} ~ 420 nm and at lower wavelengths. This enhancement in PTAK's PL precisely at λ_{ex} that give rise to strong PFP PL is even more clear at lower concentrations, due to a more uniform spatial distribution of excited states; this is shown in Appendix I. The combination of the following observations constitutes strong evidence of EET from PFPI to PTAK: a) PTAK PL enhancement tracks the PFPI PLE intensity as a function of λ_{ex}; b) PFPI emission is progressively quenched with increasing PTAK concentrations. This then directly implies that oppositely-charged PFPI and PTAK readily form a supramolecular complex in aqueous solution, leading to efficient EET from the donor to the acceptor CPE. Photoexcited electron transfer from PFPI to PTAK can be ruled out as a primary quenching mechanism for PFPI PL, as this would produce electron polarons on PTAK that would not give rise to enhanced PL.

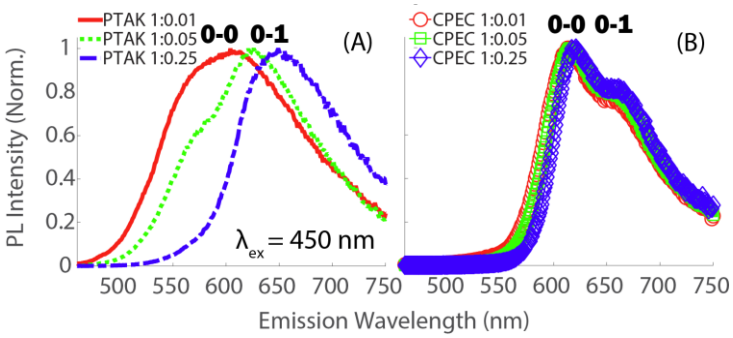

Figure 2.4. Normalized PL of PTAK in isolated aqueous solution (A) vs. that of the CPEC (B) exciting at 450 nm. The data show that the apparent 0-0/0-1 vibronic ratio differs substantially between the same CPE in different environments: < 1 in isolation and > 1 in the CPEC.

Closer inspection of **Figure 2.3B** shows a striking result: The PTAK PL intensity in isolation is approximately two orders of magnitude lower than that of PTAK in a

CPEC solution. To elucidate what is responsible for such a drastic difference in PL quantum yields, in **Figure 2.4** we have plotted normalized PTAK emission spectra exciting at λ_{ex} = 450 nm. This λ_{ex} was chosen because at longer wavelengths, the very weak PL signal to noise ratio of isolated PTAK becomes too low for quantitative analysis, though the same trends persist regardless of λ_{ex}.

Figure 2.4A shows PL spectra of control PTAK solutions, and **Figure 2.4B** shows emission spectra from CPEC solutions corresponding to the same nominal PTAK concentrations as the controls in (A). 0-0 and 0-1 vibronic peak positions are labeled in bold. **Figure 2.4A** demonstrates that the apparent 0-0/0-1 peak ratio is less than unity for all three PTAK concentrations (corresponding to the three CPEC charge ratios), and the ratio progressively decreases with concentration. We interpret the peak red shift with increasing concentration as a signature of enhanced inter-chain π-stacking. In stark contrast, the apparent 0-0/0-1 ratio is larger than unity for PTAK when it is complexed to PFPI (**Figure 2.4B**), with a negligible change as the PTAK concentration is increased.

To understand emission spectra from conjugated polymers, the molecular exciton model, developed for dye aggregates by Kasha[24] and extended to polymers by others has been found to be particularly useful. Within this model, the 0-0/0-1 vibronic ratio < 1 in chromophore aggregates is associated with H-type excitons, which have low emission quantum yields. We interpret the weak emission from

isolated PTAK solutions with a 0-0/0-1 ratio < 1 as arising from predominantly H-like emitting states, which are primarily physically associated with π-stacked inter-chain species.[25] The latter might arise due to interactions between separate chains or between two or more distinct segments of the same coiled chain. This interpretation is consistent with the observation that the absorption spectrum of isolated PTAK is similar to that of a P3HT film. Such absorption in P3HT has previously been shown to give rise to H-like emitting states.[23, 26]

On the other hand, a 0-0/0-1 ratio approximately equal to or greater than unity is primarily associated with excitons having substantial J-like character, and which give rise to strongly allowed light emission.[27] When complexed to PFPI, the fact that PTAK PL spectra show nominal 0-0/0-1 ratios ~ 1, and the fact that the PL intensity is several orders of magnitude larger in the complexed state, leads us to conclude that within a CPEC, PTAK excitons are primarily J-like. Thus, oppositely-charged complex formation leads to *emergent excitonic states* in the regioregular PTAK that are wholly absent for the EET acceptor CPE in isolation.

To further test this interpretation, we have measured time-resolved PL (TRPL) via time-correlated single-photon counting. **Figure 2.5A** shows the TRPL decays on a semi-logarithmic scale of a pure PFPI solution along with CPECs and PTAK controls excited at 420 nm with emission collected at 442 nm, which corresponds to the peak of the PL spectrum of PFPI. We find that for the lowest

charge ratio CPEC, there is a moderate yet significant drop in intensity, which tracks the steady state PL. A blowup of this data on a linear scale is shown in the inset.

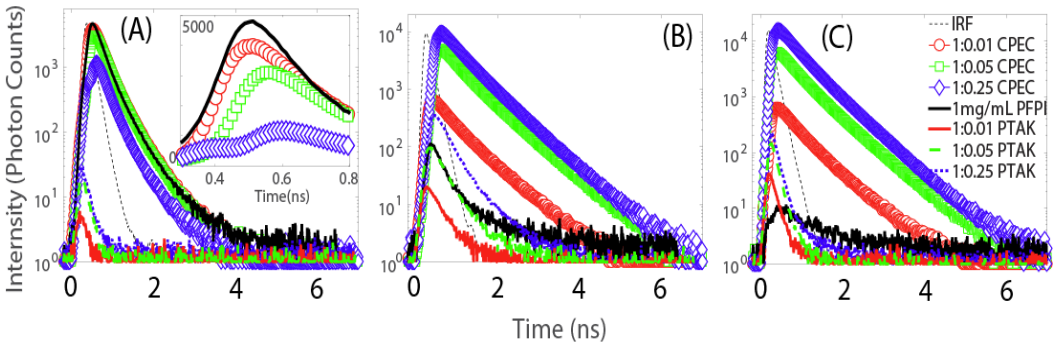

Figure 2.5. Time-resolved PL decays (collected for the same duration) of CPECs at varying polyion charge ratios as well as pure CPE solution controls prepared at concentrations corresponding to their respective CPEC solutions. The legend is shown on the far right; pure PTAK controls are labeled with the corresponding CPEC chare ratio. The instrument response function (IRF) is shown as a thin dashed line in all panels. (A) λ_{ex} = 420 nm and λ_{em} = 442 nm. Emission is collected near the peak of PFPI PL. The inset shows PFPI and CPEC solutions plotted on a linear scale. The data show that PFPI PL is progressively quenched with increasing relative charge ratio, which we attribute to EET from PFPI to PTAK. (B) λ_{ex} = 420 nm and λ_{em} = 615 nm. Emission at the latter comes overwhelmingly from PTAK. The curves show that upon complexation with PFPI, PTAK emission intensity increases by ~ two orders of magnitude and lasts substantially longer than that of pure PTAK. We attribute this to emergence of extended, J-like excitonic states largely delocalized over the conjugated PTAK backbone. (C) λ_{ex} = 600 nm and λ_{em} = 680 nm. In this case, the lowest-energy excitons of PTAK are excited with vanishing PFPI excitation. Similar to the data shown in (B), the decays display long-lived PL and are due to delocalized J-like excitons.

At the two higher ratios, there is pronounced quenching of the PFPI emission, consistent with steady-state results. **Figure 2.5B** shows TRPL decays excited at the same λ_{ex} but with emission detected at 615 nm, strictly corresponding to PTAK PL. This panel shows that across all PTAK concentrations, there is a drastic increase in the intensity of emission from the CPEC relative to the corresponding PTAK controls. The increase in fluorescence is several times greater than what would be expected just from the increase in total polymer concentration in solution. While this change in total fluorescence intensity tracks the decrease in CPEC fluorescence

at 442 nm (quenching of PFPI emission), the fractional changes in the magnitudes are not similar. In fact, the increase in fluorescence at 615 nm between concentrations is approximately 5-10 times larger than the associated decrease in PFPI emission, depending on the sample. Thus, in addition to EET, the increase in the PL lifetime of PTAK bound to PFPI is again consistent with emission from J-like states.

Finally, to better understand the PL that comes from PTAK excitons generated in the red tail of the CPEC absorption - corresponding to the most delocalized excited states - **Figure 2.5C** displays TRPL curves collected at λ_{ex} = 600 nm and λ_{em} = 680 nm. As in **Figure 2.5B**, we again see that the total fluorescence of the CPECs far exceeds what would be expected just by increasing the total polyelectrolyte concentration. This suggests that whether excited by energy transfer from PFPI or excited directly, PTAK excitons are relaxing through the same highly emissive J-like excitons. Therefore, complexation appears to preclude strong formation of intra- and inter-chain H-aggregation, leading to J-like states instead.

In an effort to connect the photophysics to the physical structure of the complexes, we have characterized CPECs at varying charge ratios using both dynamic (visible) light scattering (DLS)[28-30] and small-angle X-ray scattering[31-32] (SAXS). In DLS measurements, we collected self-beating intensity autocorrelation functions[33] (ACFs) $g^1(t)$ at scattering angles of 20°. **Figure 2.6** shows a composite ACF plot of CPEC solutions at varying charge ratios, as well as relaxation time distribution functions obtained using the CONTIN algorithm, which performs a regularized inverse Laplace transform.[34]

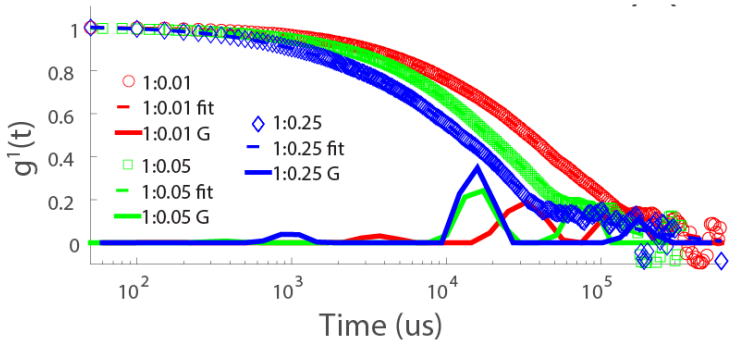

Figure 2.6. Normalized DLS electric field autocorrelation functions for CPEC solutions collected at a 20° scattering angle. Circles correspond to data, dashed lines to CONTIN-generated fits, and solid lines to relaxation time distribution times obtained from CONTIN, labeled in the legend as G.

DLS relaxation times, associated diffusion coefficients and mean hydrodynamic radii are summarized in **Table 2.1**. Inspection of **Figure 2.6** demonstrates that the mean relaxation time for the lowest charge ratio is longest, which means that the mean size is largest. The 1:0.01 charge ratio yielded a predominantly bimodal distribution with two characteristic particle sizes, the smaller of which was 87 nm. Particles corresponding to the smaller of the two sizes shrank progressively with increasing charge ratio to 46 nm at 1:0.05 and 42 nm at 1:0.25.

Additionally, we find that for all three charge ratios, we observe large particle sizes in excess of 100 nm. These results imply that as more PTAK is added to PFPI, the mean complex size progressively shrinks as charges on one polymer are compensated by its oppositely charged partner. This is possibly due to a propensity to lower the interfacial area between the hydrophobic conjugated backbones of the CPEs and the highly polar solvent as the effective charge density of the complex diminishes. The decrease in size is consistent with a slight red shift in PTAK PL when complexed to PFPI (**Figure 2.4B**), which we attribute with a mild increase in inter-chain π-stacking.

Table 2.1. CONTIN fit results of DLS autocorrelation functions from CPEC solutions at two scattering angles.

PFP3I:PTAK Molar Charge Ratio	Relaxation time (us)	R_H (nm) [a]	Relative Size Distribution (%)
1:0.01	3.3×10^4	87	47.4
	3.7×10^3	10	7.9
	1.3×10^5	342	44.7
1:0.05	1.7×10^4	46	55.6
	6.8×10^4	180	44.4
1:0.25	1.6×10^4	42	76.4
	1.7×10^5	462	23.7

[a] Intensity-weighted hydrodynamic radius from dynamic light scattering.

To characterize the electron density contrast between water and CPECs as a function of charge ratio, we carried out synchrotron solution SAXS measurements. These results are shown in **Figure 2.7** on a double logarithmic plot, where we compare pure PFPI to that of the CPECs for both addition orders. We find that all the curves except the 1:0.25 CPEC exhibit similar limiting power law exponents at high *Q*, suggesting that interfaces internal to the CPE coil do not differ substantially between pure PFPI and CPECs at the lower charge ratio. At 1:0.25, the decrease in the slope could possibly be due to a more fractal internal geometry, though a more systematic investigation of this observation is beyond the scope of this paper.

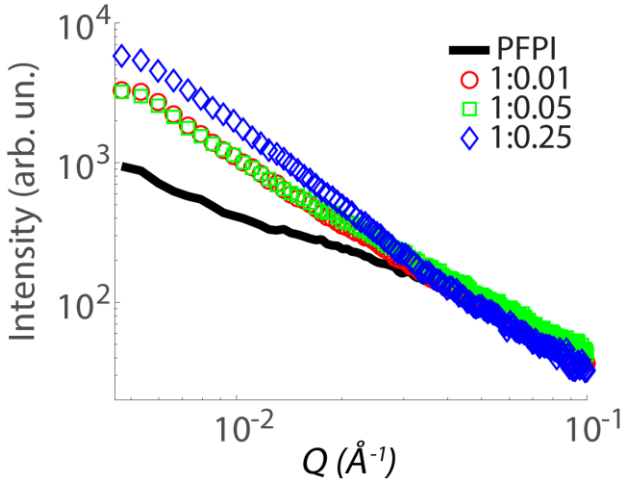

Figure 2.7. SAXS intensities vs. scattering vector *Q* for 1 mg/mL PFPI solution (solid black) and CPEC solutions at 1:0.01 (red circles), 1:0.05 (green squares) and 1:0.25 (blue diamonds) charge ratios.

At low *Q*, however, all CPEC curves show an excess in scattering intensity relative to pure PFPI. This is reasonable, since when the oppositely charged CPEC forms, we expect that the electron density contrast between pure solvent and the complex will be larger than that of the isolated CPE. Curves for 1:0.01 CPECs can be roughly captured with a single power law decay. In 1:0.05 CPECs curves begin to depart from a power law as they show signs of a developing (yet relatively poorly-

defined) Guinier region at low *Q*. At the 1:0.25 ratio, the SAXS curve displays a hint of Guiner behavior, indicating formation of a more well-defined CPEC particle shape relative to pure PFPI and the lowest charge ratio complex. Taken together with DLS results, this suggests that the decrease in mean particle size at larger charge ratios leads to solution complexes with greater packing density, as implied by the rise in scattering intensity at low *Q*.

Having characterized CPEC solutions, we now turn to examining the dense CPEC network phase. Phase separation occurs at charge ratios exceeding 1:0.05. The dense phase was spread on a glass substrate as a paste and allowed to dry prior to collecting PL, which is shown in **Figure 2.8** for two charge ratios. The first striking feature is that PL from PFPI is effectively absent, save for a weak band at the PFPI:PTAK charge ratio of 1:0.25. There is a pronounced enhancement in PL from PTAK when exciting between ~ 320 and 420 nm. This corresponds well to the OD of PFPI; however, PTAK has (relatively low) absorption in this region as well, and isolated PTAK solutions also showed PL when exciting in this region. It is worth noting that a pure spin-coated PTAK film does not give rise to measurable PL (not shown), which is in contrast to the CPEC films shown in **Figure 2.8**.

Although we cannot rule out direct excitation of PTAK and its subsequent emission as contributing to PTAK's PL in the 320-420 nm excitation region, there are several observations that suggest that this PL at least partially contains emission

from PTAK excitons that are populated directly as a result of EET from PFPI in the solid state. First, the enhancement of PTAK PL at these λ_{ex} differs qualitatively from the solution PL shown in **Figure 2.3**. Second, if this PL was simply due to pure PTAK, we would expect strong self-quenching, as we observed in spin-coated PTAK films; this is not the case. Third, **Figure 2.8A** shows that there is an additional enhancement in PTAK PL in the 1:0.063 ratio film at λ_{ex} ~ 410 nm, which resembles solution behavior. Taken together, we believe that a fairly significant fraction of PTAK PL originating from λ_{ex} between 320 nm and 420 nm is due to direct EET from PFPI to PTAK.

In both films shown in **Figure 2.8**, λ_{ex} between 450 nm and 600 nm corresponds to a PL band that appears to roughly track the absorption spectrum of CPEC thin films. The fact that this PL persists for both charge ratios suggests that these PTAK chains are strongly associated with PFPI. These observations again suggest that PTAK chains preferentially associate with PFPI, and inter-PTAK π-stacking is not prevalent.

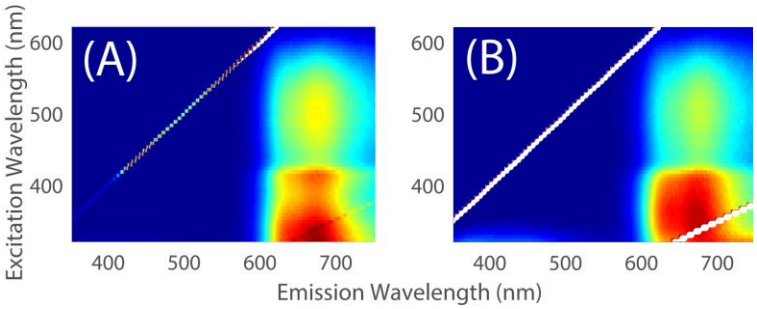

Figure 2.8. 2D PL maps of the solid CPEC dense phase isolated from CPEC solutions of varying polycation/polyanion charge ratios: (A) 1:0.063; (B) 1:0.25. The solid was spread on a substrate as a paste and allowed to dry. PFPI PL is nearly completely quenched, and PTAK PL is enhanced in the excitation region corresponding to strong PFPI emission when PFPI is in isolation.

Thus, it is clear that both solution and the solid state, PFPI and PTAK readily form ionically bound complexes, which exhibit EET from PFPI to PTAK. We have also shown that in solution,

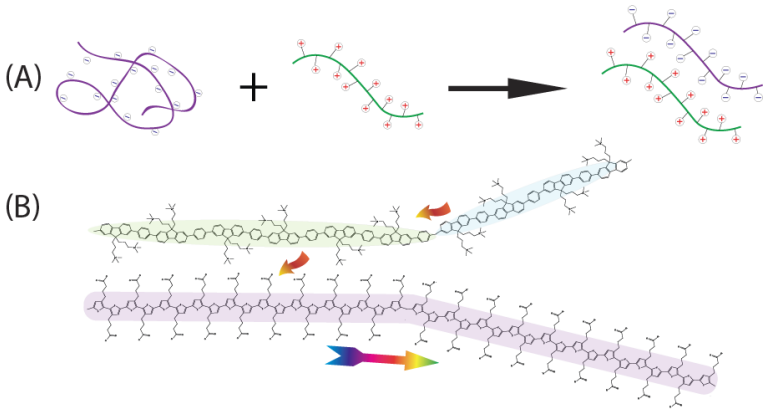

Figure 2.9. (A) Cartoon illustrating the change in PTAK chain microstructure going from isolated solution to the CPEC. The result is a planarization of the PTAK backbone relative to isolated solutions. (B) Cartoon of PFPI and PTAK chains in a solution-phase CPEC. The backbones of both CPEs are fairly extended, leading to coherent excitonic wavefunction delocalization over a large backbone segment. One consequence of this backbone planarization due to CPEC formation is a drastic increase in the PL quantum yield of PTAK (bottom CPE), consistent with emission from J-like excitonic states. Arrows indicate directional transfer of electronic energy.

PTAK excitons are converted from H-like to J-like in the process of complexation with PFPI. With increasing charge ratio, the average complex size shrinks, but the primary J-like excitonic states remain. According to work by Spano *et al.* and Barford *et al.*, J-like excitons in conjugated polymers are primarily viewed as arising from head-to-tail arrangements of transition dipoles localized on each monomer unit, which together add in phase.[22, 24, 27, 35-36] In the limit of vanishing disorder, this leads to excitons highly delocalized over a single polymer chain. If multiple relatively straight chains are in proximity, excitons are expected to exhibit both J-like and H-like character. In the context of this model, we interpret J-like emission from PTAK within a CPEC as arising from excitons largely delocalized over a single chain akin to

a 1D molecular wire in the low disorder limit. A cartoon of this is shown in **Figure 2.9**. This result is very intriguing, as the highly delocalized nature of the intra-chain J-like exciton will lead to facile electronic energy migration down the chain and may additionally result in an interplay between coherent and incoherent EET. The former has been observed for conjugated polymers in room temperature solution.[37] Such a combination of EET mechanisms has been invoked as possibly being essential for efficient directional funneling of excitons in natural light harvesting systems.[5] These observations underscore the potential that CPEs and their complexes have for light-harvesting antenna applications.

2.3 CONCLUSIONS

To conclude, to the best of our knowledge we have reported on the very first preparation and characterization of an oppositely charged conjugated polyelectrolyte complex in aqueous solution capable of electronic energy transfer. We found that the oppositely-charged complex undergoes EET both in solution and the solid state. Importantly, we have also found that the excitonic wavefunction of the accepter polyelectrolyte changed qualitatively in the complex compared to the polyelectrolyte in isolation. This work highlights the fact that a) conjugated polyelectrolyte complexes present highly intriguing photophysics that are in need of fundamental investigation, and b) that modular assemblies of excitonic

donor/acceptor conjugated polyelectrolytes hold substantial promise for artificial light harvesting applications.

REFERENCES

1. Barter, L. M.; Durrant, J. R.; Klug, D. R., A Quantitative Structure-Function Relationship for the Photosystem Ii Reaction Center: Supermolecular Behavior in Natural Photosynthesis. *Proc Natl Acad Sci U S A* **2003**, *100*, 946-51.

2. Croce, R.; van Amerongen, H., Natural Strategies for Photosynthetic Light Harvesting. *Nat Chem Biol* **2014**, *10*, 492-501.

3. McConnell, I.; Li, G.; Brudvig, G. W., Energy Conversion in Natural and Artificial Photosynthesis. *Chem Biol* **2010**, *17*, 434-47.

4. Scholes, G. D.; Fleming, G. R.; Olaya-Castro, A.; van Grondelle, R., Lessons from Nature About Solar Light Harvesting. *Nat Chem* **2011**, *3*, 763-74.

5. Blankenship, R. E., *Molecular Mechanisms of Photosynthesis*; Wiley, 2014.

6. Fassioli, F.; Dinshaw, R.; Arpin, P. C.; Scholes, G. D., Photosynthetic Light Harvesting: Excitons and Coherence. *J R Soc Interface* **2014**, *11*, 20130901.

7. Olaya-Castro, A.; Scholes, G. D., Energy Transfer from Förster–Dexter Theory to Quantum Coherent Light-Harvesting. *International Reviews in Physical Chemistry* **2011**, *30*, 49-77.

8. Scholes, G. D., Long-Range Resonance Energy Transfer in Molecular Systems. *Annu Rev Phys Chem* **2003**, *54*, 57-87.

9. Stirbet, A., Excitonic Connectivity between Photosystem Ii Units: What Is It, and How to Measure It? *Photosynth Res* **2013**, *116*, 189-214.

10. Bhosale, S. V.; Bhosale, S. V.; Shitre, G. V.; Bobe, S. R.; Gupta, A., Supramolecular Chemistry of Protoporphyrin Ix and Its Derivatives. *European Journal of Organic Chemistry* **2013**, *2013*, 3939-3954.

11. Bottari, G.; Trukhina, O.; Ince, M.; Torres, T., Towards Artificial Photosynthesis: Supramolecular, Donor–Acceptor, Porphyrin- and Phthalocyanine/Carbon Nanostructure Ensembles. *Coordination Chemistry Reviews* **2012**, *256*, 2453-2477.

12. Elemans, J. A. A. W.; van Hameren, R.; Nolte, R. J. M.; Rowan, A. E., Molecular Materials by Self-Assembly of Porphyrins, Phthalocyanines, and Perylenes. *Advanced Materials* **2006**, *18*, 1251-1266.

13. Fukuzumi, S., Development of Bioinspired Artificial Photosynthetic Systems. *Phys Chem Chem Phys* **2008**, *10*, 2283-97.

14. Hayashi, H.; Sobczuk, A.; Bolag, A.; Sakai, N.; Matile, S., Antiparallel Three-Component Gradients in Double-Channel Surface Architectures. *Chem. Sci.* **2014**, *5*, 4610-4614.

15. Jiang, H.; Taranekar, P.; Reynolds, J. R.; Schanze, K. S., Conjugated Polyelectrolytes: Synthesis, Photophysics, and Applications. *Angew Chem Int Ed Engl* **2009**, *48*, 4300-16.

16. Costa, T.; Garner, L. E.; Knaapila, M.; Thomas, A. W.; Rogers, S. E.; Bazan, G. C.; Burrows, H. D., Aggregation Properties of P-Phenylene Vinylene Based Conjugated Oligoelectrolytes with Surfactants. *Langmuir* **2013**, *29*, 10047-58.

17. Evans, R. C.; Knaapila, M.; Willis-Fox, N.; Kraft, M.; Terry, A.; Burrows, H. D.; Scherf, U., Cationic Polythiophene-Surfactant Self-Assembly Complexes: Phase Transitions, Optical Response, and Sensing. *Langmuir* **2012**, *28*, 12348-56.

18. Knaapila, M.; Evans, R. C.; Garamus, V. M.; Almasy, L.; Szekely, N. K.; Gutacker, A.; Scherf, U.; Burrows, H. D., Structure and "Surfactochromic" Properties of Conjugated Polyelectrolyte (Cpe): Surfactant Complexes between a Cationic Polythiophene and Sds in Water. *Langmuir* **2010**, *26*, 15634-43.

19. Pinto, S. M.; Burrows, H. D.; Pereira, M. M.; Fonseca, S. M.; Dias, F. B.; Mallavia, R.; Tapia, M. J., Singlet-Singlet Energy Transfer in Self-Assembled Systems of the Cationic Poly{9,9-Bis[6-N,N,N-Trimethylammonium)Hexyl]Fluorene-Co-1,4-Phenylene} with Oppositely Charged Porphyrins. *J Phys Chem B* **2009**, *113*, 16093-100.

20. Guo, S.; Ruderer, M. A.; Rawolle, M.; Korstgens, V.; Birkenstock, C.; Perlich, J.; Muller-Buschbaum, P., Evolution of Lateral Structures During the Functional Stack

Build-up of P3ht:Pcbm-Based Bulk Heterojunction Solar Cells. *ACS Appl Mater Interfaces* **2013**, *5*, 8581-90.

21. Roehling, J. D.; Arslan, I.; Moulé, A. J., Controlling Microstructure in Poly(3-Hexylthiophene) Nanofibers. *J. Mater. Chem.* **2012**, *22*, 2498-2506.

22. Yamagata, H.; Spano, F. C., Interplay between Intrachain and Interchain Interactions in Semiconducting Polymer Assemblies: The Hj-Aggregate Model. *J Chem Phys* **2012**, *136*, 184901.

23. Clark, J.; Chang, J.-F.; Spano, F. C.; Friend, R. H.; Silva, C., Determining Exciton Bandwidth and Film Microstructure in Polythiophene Films Using Linear Absorption Spectroscopy. *Applied Physics Letters* **2009**, *94*, 163306.

24. Spano, F. C.; Silva, C., H- and J-Aggregate Behavior in Polymeric Semiconductors. *Annual Review of Physical Chemistry* **2014**, *65*, 477-500.

25. Schwartz, B. J., Conjugated Polymers as Molecular Materials: How Chain Conformation and Film Morphology Influence Energy Transfer and Interchain Interactions. *Annual Review of Physical Chemistry* **2003**, *54*, 141-172.

26. Spano, F. C.; Clark, J.; Silva, C.; Friend, R. H., Determining Exciton Coherence from the Photoluminescence Spectral Line Shape in Poly(3-Hexylthiophene) Thin Films. *The Journal of Chemical Physics* **2009**, *130*, 074904.

27. Yamagata, H.; Spano, F. C., Vibronic Coupling in Quantum Wires: Applications to Polydiacetylene. *The Journal of Chemical Physics* **2011**, *135*, 054906.

28. Chu, B.; Wang, Z.; Yu, J., Dynamic Light Scattering Study of Internal Motions of Polymer Coils in Dilute Solution. *Macromolecules* **1991**, *24*, 6832-6838.

29. Tsunashima, Y.; Nemoto, N.; Kurata, M., Dynamic Light Scattering Studies of Polymer Solutions. 2. Translational Diffusion and Intramolecular Motions of Polystyrene in Dilute Solutions at the Θ Temperature. *Macromolecules* **1983**, *16*, 1184-1188.

30. Sedlák, M. n., The Ionic Strength Dependence of the Structure and Dynamics of Polyelectrolyte Solutions as Seen by Light Scattering: The Slow Mode Dilemma. *The Journal of Chemical Physics* **1996**, *105*, 10123.

31. Combet, J.; Lorchat, P.; Rawiso, M., Salt-Free Aqueous Solutions of Polyelectrolytes: Small Angle X-Ray and Neutron Scattering Characterization. *The European Physical Journal Special Topics* **2012**, *213*, 243-265.

32. Glatter, O.; Kratky, O., *Small Angle X-Ray Scattering*; Academic Press, 1982.

33. Berne, B. J.; Pecora, R., *Dynamic Light Scattering: With Applications to Chemistry, Biology, and Physics*; Dover Publications, 2013.

34. Scotti, A.; Liu, W.; Hyatt, J. S.; Herman, E. S.; Choi, H. S.; Kim, J. W.; Lyon, L. A.; Gasser, U.; Fernandez-Nieves, A., The Contin Algorithm and Its Application to Determine the Size Distribution of Microgel Suspensions. *The Journal of Chemical Physics* **2015**, *142*, 234905.

35. Barford, W.; Marcus, M., Theory of Optical Transitions in Conjugated Polymers. I. Ideal Systems. *The Journal of Chemical Physics* **2014**, *141*, 164101.

36. Marcus, M.; Tozer, O. R.; Barford, W., Theory of Optical Transitions in Conjugated Polymers. Ii. Real Systems. *The Journal of Chemical Physics* **2014**, *141*, 164102.

37. Collini, E.; Scholes, G. D., Coherent Intrachain Energy Migration in a Conjugated Polymer at Room Temperature. *Science* **2009**, *323*, 369-373.

Chapter 3

Polyion Charge Ratio Determines Transition Between Bright and Dark Excitons in Donor/Acceptor Conjugated Polyelectrolyte Complexes

Acknowledgements: This chapter was originally published in the Journal of Physical Chemistry C with the following authorship: William R. Hollingsworth,[≠] Timothy J. Magnanelli,[≠] Carmen Segura, Jamie D. Young, Arthur E. Bragg, Alexander L. Ayzner. WRH carried out sample preparation, time-resolved and steady-state photoluminescence spectroscopy, time-resolved anisotropy and analysis thereof; TJM carried out transient absorption spectroscopy and analysis thereof; CS carried out dynamic light scattering, small angle x-ray scattering, and analysis thereof; JDY assisted with transient absorption analysis. WRH and TJM principally wrote the manuscript. AEB and ALA edited the manuscript and oversaw the project. TJM, JDY, and AEB were affiliated with Johns Hopkins University at the time of publication. WRH, CS, and ALA were affiliated with UC Santa Cruz at the time of publication.

Abstract: There is substantial urgency to create artificial light-harvesting systems that are relatively inexpensive and capable of absorbing a significant fraction of the solar spectrum. Molecular materials possess a number of attractive characteristics for this purpose, such as their light weight, spectral tunability and the potential to use self-assembly to form large structures capable of executing multiple photophysical processes required for photoelectric energy conversion. In this work, we demonstrate that ionically assembled complexes composed of oppositely charged conjugated polyelectrolytes (CPEs) that function as excitonic donor/acceptor pairs possess significant potential as artificial energy transfer antennae. We find that upon complexation in water, excitation energy is transferred from the donor to the acceptor CPE in less than 250 femtoseconds – a timescale that is competitive with natural

light-harvesting antennae. We further find that the state of CPE chain extension and thus spatial delocalization of the excited-state wavefunction can be readily manipulated using the relative polyion charge ratio, allowing us to tune the emission quantum yield of the CPE in a straight-forward manner. Collectively, our results point towards the fact that the extension of a CPE chain upon complexation is a cooperative phenomenon between multiple chains even at dilute polymer concentrations.

3.1 Introduction

The pressing need to convert sunlight to electrochemical potential energy for a broad range of renewable energy applications has led to a comprehensive effort aimed at discovering materials that can be used as inexpensive, environmentally benign light harvesters. Inspired by Nature's elegant photosynthetic machinery, artificial light harvesting based on soft, molecular materials continues to be an active research area.[1-13] Central to light harvesting based on soft materials – whether natural of artificial – is the ability to directionally transfer the energy of electronic excited states over large distances relative to molecular scale. In natural systems, this process occurs on ultrafast timescales and is characterized by very high efficiencies approaching unity.[14-19]

The quest to create artificial molecular systems capable of efficient electronic energy transfer has led to a significant library of organic materials, including large covalent molecules that incorporate energy gradients and molecular self-assemblies.[1, 7, 20-27] The latter, in principle, avoid difficulties associated with intricate covalent engineering and processing issues associated with very large molecules. Self-assembled systems are also attractive due to the possibility of manipulating their excited-state dynamics by changing the state of noncovalent spatial organization.[28] When the chromophore unit composing the assembly is an organic dye molecule, energy migration in realistic systems, i.e. subject to disorder, is primarily associated

with excited-state (exciton) hopping from one molecule to the next.[29] Thus, an exciton may need to execute a large number of hops to cover an appreciable distance.

Conjugated polyelectrolytes (CPEs) – conjugated polymers bearing ionic sidechains – possess several distinct advantages that make them promising molecular candidates to serve as artificial light-harvesting antennae.[30-31] First, electronic delocalization along the CPE backbone allows excitons to very rapidly move along the polymer chain, as well as to hop between chains or multiple segments of the same chain. Thus, instead of a sequence of hops between small-molecule pigments that most commonly communicate electronically via relatively weak π-electron interactions, a significant fraction of exciton migration in a CPE occurs through-bond along the chain and is thus characterized by a stronger electronic coupling. Second, the electronic (backbone) and ionic (sidechain) degrees of freedom of a CPE are strongly coupled, leading to sensitivity to the local electrostatic environment. The latter has been previously leveraged in charge-transport,[32] sensing[33-36] and biomedical applications.[37-41] However, the strong electron-ion interaction can also be used via ionic self-assembly to create artificial light-harvesting structures in water that support spatially delocalized electronic states and thus the possibility of efficient and rapid electronic energy transfer upon assembly. Furthermore, should CPE excitons be ultimately converted to electronic charges, the combination of backbone electronic delocalization and ionic stabilization will in principle assist in lowering the charge recombination rate.

We previously showed for the first time that aqueous, ionic assembly of oppositely charged CPEs resulted in substantial modification of the native CPE electronic wavefunctions.[42-43] This led to a large enhancement in the photoluminescence quantum yield of one of the CPEs upon complexation. Our prior work focused on a single donor/acceptor composition, and thus we were unable to elucidate under what conditions such a substantial photophysical change took place. Furthermore, though we showed that there were clear signatures of electronic energy transfer between the two CPEs, we could not comment on the specific timescale over which excitation energy was transferred from the donor to the acceptor.

In this manuscript, we answer two questions. First, how does the relative polyion charge ratio influence the photophysics and solution microstructure of oppositely charged CPEs that function as an exciton donor/acceptor pair? Second, on what timescales do the inter-CPE exciton transfer and intra-CPE exciton diffusion dynamics occur as a function of CPE complex (CPEC) composition? To do this, we combine multiple spectroscopic and scattering probes. We find that inter-CPE energy transfer occurs on ultrafast timescales, and that most of the energy is transferred in less than 250 fs. Additionally, we show that the relative polyion charge ratio plays a very large role in determining CPEC photophysics, leading to stretched out, brightly emissive acceptor CPE chains when the donor CPE is in excess. In contrast, when the acceptor CPE is in excess, the assembly emission is weak due to the presence of exciton traps characterized by π-π interactions between chain segments. This leads to

qualitatively different exciton dynamics as a function of CPEC composition and allows us to propose a mechanism for CPE complexation that involves collective chain interactions even at dilute concentrations. Our results highlight the fact that inter-monomer correlations that fundamentally arise due to the connectivity of the CPE chain lead to a unique sensitivity to assembly stoichiometry that is absent in small-molecule assemblies. This leads to the ability to use relative CPEC mole fractions in a manner that broadly tunes the temporal evolution of CPE excited states.

3.2 Results

In this manuscript, we build on our previous work and focus on the following CPE pair: an iodine salt of a polycation with a poly(fluorene-co-phenylene) backbone and propylammonium sidechains (PFPI), and a potassium salt of a polyanion with a regioregular poly(thiophene) backbone and a butylcarboxylate-terminated sidechain (PTAK). The chemical structures of both CPEs are shown in the inset to **Figure 3.1**. PFPI functions as the excited-state (exciton) donor, and PTAK functions as an exciton acceptor in the energy transfer process. We aim to characterize the exciton dynamics over multiple timescales (100s of fs to 10s of ns) and thereby relate inter-CPE energy transfer and intra-CPE exciton diffusion to the solution complex morphology. To do this, we combine time-resolved pump probe and photoluminescence spectroscopy with small-angle X-ray and dynamic light scattering (DLS).

Throughout this manuscript, we define the ionic charge ratio, *R*, as the ratio of cationic PFPI charges to anionic PTAK charges. The PFPI:PTAK per-monomer charge stoichiometry is 2:1; thus, a solution containing equal concentrations of cationic and anionic CPE charges does not correspond with equal donor and acceptor monomer concentrations. As *R* is varied via stoichiometry, the relative CPE concentrations are varied in a manner that keeps the nominal solution ionic strength constant. This ensures that if the fraction of condensed counterions on each CPE is similar, the solution ionic strength and thus the Debye screening length is nearly constant. The latter characterizes the average distance over which screened electrostatic interactions decay. At *R* = 50:50, corresponding to ionic CPE charge equivalence, the CPEC is unstable with respect to phase separation. Thus, we focus on *R* values that bracket charge equivalence, including those that correspond to excess PFPI (90:10 through 60:40) and excess PTAK (40:60 through 10:90). Below, we first examine the steady-state photophysics as a function

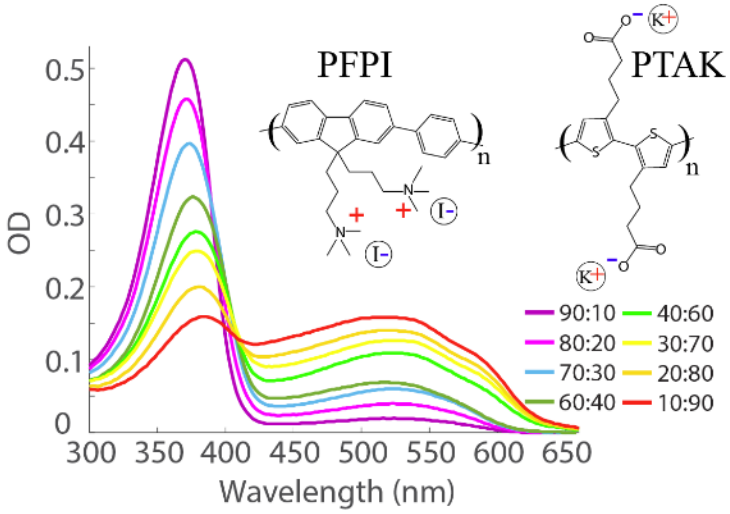

Figure 3.1. Optical density of CPEC solutions at various charge ratios *R*. The sharp peak is due to PFPI, and the broad peak at longer wavelengths is due to PTAK. Chemical structures are shown in the inset.

of *R* before proceeding to time-resolved exciton dynamics. We then discuss scattering measurements, which allow us to form a coherent picture of complex formation and its structural and electronic ramifications.

Steady-State Photophysics

Figure 3.1 shows the ground-state absorption, or optical density (OD), spectra of CPECs prepared with different *R* values. PFPI absorption shows a fairly narrow peak around 365 nm, whereas the relatively broad PTAK OD has an onset around 620 nm and peaks around 525 nm. The anticorrelated behavior of the peaks reflects the constraint of keeping the ionic strength approximately constant as the composition of CPEC solutions is varied. **Figure 3.1** shows that the PTAK OD shape differs on both sides of the 50:50 boundary.

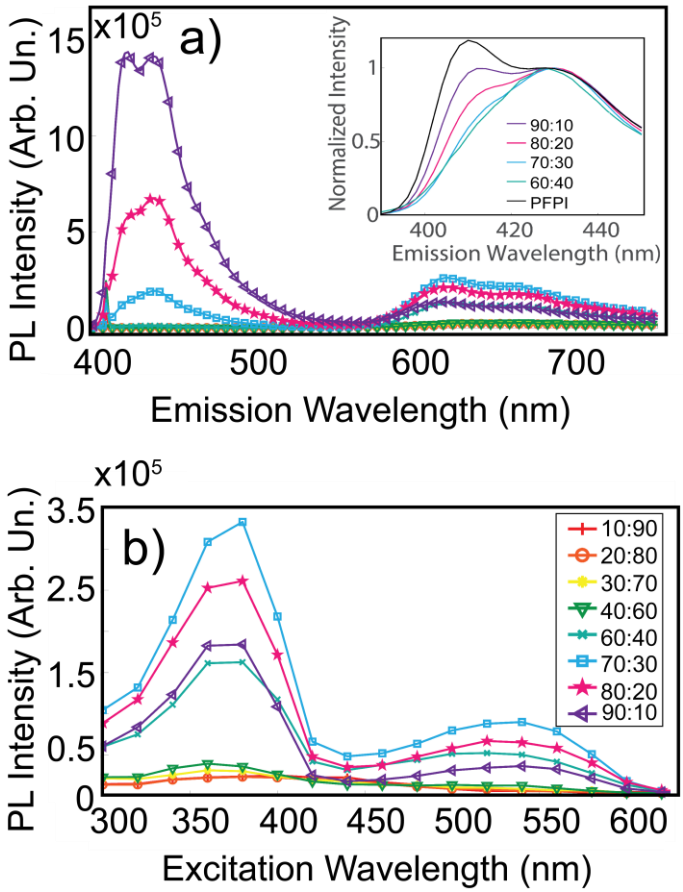

Figure 3.2. a) Steady-state PL spectra of CPEC solutions as a function of charge ratio. b) PL excitation spectra collected at a wavelength that corresponds to PTAK emission only. The inset in a) shows the PFPI PL spectrum normalized to the 0-1 vibronic peak.

Specifically, when *R* > 50:50, the PTAK spectrum looks relatively featureless. However, when *R* < 50:50 the long-wavelength absorption starts to exhibit some structure. In our previous work, we showed that the structure arises due to the presence of π-stacking regions either within a single chain or between multiple chains. This is also characteristic of PTAK solutions in the absence of PFPI. Given the relatively low concentrations (~2 x 10^{-4} M) used in this work, we believe the π-stacking regions are largely intramolecular, i.e. they belong to two or more regions of the same PTAK chain. However, since the hydrophobic interaction may lead to aggregation of more than one like-charged chain even at dilute concentrations, we cannot completely rule out the possibility of some intermolecular interaction.

With the distribution of ground-state CPE states in mind, we have used photoluminescence (PL) spectroscopy to interrogate CPEC formation. The PL intensity and spectrum shape are sensitive to the chain conformation, owing to the tightly coupled relationship between CPE structural and electronic properties, as well as the correlation between the PL quantum yield and the spatial extent of the exciton wavefunction. This fact allows us to gain substantial insight into the ionic assembly process. **Figure 3.2a** shows PL spectra of CPEC solutions prepared at different *R* following excitation at 400 nm. The spectra of the two CPEs are well-separated, allowing us to track emission from both components independently.

Several important features can be immediately observed. First, as *R* decreases, which corresponds with progressively more PTAK relative to PFPI, the PFPI PL –

centered about 425 nm – monotonically decreases. This is primarily due to energy transfer from PFPI to PTAK, and, given sufficient PTAK (*R* < 70:30), all emission due to PFPI is quenched. Second, the 0-0/0-1 vibronic peak ratio, S_R, of PFPI PL progressively decreases with increasing PTAK concentration. The 0-0 peak corresponds to a pure electronic downward transition near the onset, and the longer-wavelength 0-1 peak corresponds to an electronic ground state with one remaining vibrational quantum. Prior theoretical and experimental work has shown that S_R reports on the electronic interactions that determine the nature of the emitting exciton wavefunction.[44-51] In the context of conjugated polymer solutions, S_R > 1 corresponds to excitons delocalized over relatively extended single chains, whereas S_R < 1 corresponds to emission originating from relatively coiled states characterized by intra- (or inter-) chain π-stacked regions.

Third, just as ionic charge equality (*R* = 50:50) forms a demarcation line for the appearance of structure in the PTAK absorption spectrum, evidently the PL quantum yield of PTAK (centered about 530 nm) follows a similar trend. Specifically, CPECs with *R* < 50:50 exhibit low PTAK quantum yields across all wavelengths – a well-known characteristic of π-stacked polymer chains, which lead to the formation of low-energy exciton traps.[52] As the fraction of PFPI is increased past *R* = 50:50, the PL quantum yield of PTAK rises significantly, and concomitantly its S_R increases towards unity. Thus, relative to the two CPEs in isolation, complexation in the regime where *R* > 50:50

leads to a decrease in S_R for PFPI and an increase in S_R for PTAK as *R* is lowered from 90:10 to 60:40.

Direct evidence of inter-CPE energy transfer comes from **Figure 3.2b**, which shows PL excitation spectra collected at an emission wavelength centered about the PL due to PTAK only. Thus, the PL excitation spectrum reflects those excited states that ultimately lead to intensity at the fixed emission wavelength. In the absence of energy transfer, the excitation spectrum of a CPE tends to roughly track its OD. When the energy acceptor (PTAK) becomes excited by means of energy transfer from the exciton donor (PFPI), the shape of PTAK's PL excitation spectrum changes qualitatively. Specifically, **Figure 3.2b** shows that for *R* > 50:50, the excitation spectrum of PTAK resembles a linear combination of the PFPI and PTAK absorption spectra. This constitutes direct evidence of energy transfer from PFPI to PTAK, which can only take place in solution to any appreciable extent if the two CPEs are within a distance at which the rate of resonant energy transfer is competitive with radiative relaxation.

Though tempting, quantifying energy transfer efficiencies using the PL excitation spectrum in CPECs is quite challenging. Traditionally, the intensity of the acceptor PL excitation spectrum upon excitation in the region *where the donor absorbs* in the presence and absence of the donor is compared. The change in acceptor PL intensity is then related to the energy transfer efficiency. The quenching of the donor PL can often similarly be related to the energy transfer efficiency.[53-54]

Unfortunately, both methods break down for CPECs. This is because both methods critically rely on the assumption that the donor and acceptor PL quantum yields are unchanged when the two are brought in proximity. The steady-state photophysics described above preclude such a calculation, as the PL quantum yields of both components evidently do not stay constant upon complexation. Nevertheless, the quenching of the donor PL can be used as an approximation of the energy-transfer efficiency, which shows that for $R \leq 60{:}40$, the upper limit is effectively 100%, as the donor PL is completely quenched. At $R = 80{:}20$, the spectrally integrated donor PL is quenched by 49%, and when $R = 70{:}30$, 79% of donor PL is quenched. This CPEC ratio corresponds to a total CPE monomer concentration of 0.19 mM.

Ultrafast Energy Transfer Dynamics

Although our emission results indicate that energy transfer between the ionically complexed CPEs must be fairly efficient, the timescale for energy transfer is unclear. Our previous time-resolved PL results suggested that the relevant timescale for this process is shorter than the time resolution of those measurements (i.e. sub-50 ps). To further address this question, we have performed ultrafast pump-probe transient absorption experiments. Global analysis was performed on each set of transient absorption data to extract spectral components associated with each of the spectral relaxation timescales observed. Details of the global analysis fitting

procedure are included in the SI; all fitting parameters obtained are summarized in **Table AII.1**.

Figure 3.3 displays contour maps plotting time-resolved, wavelength-dependent transient absorption signals collected with pure PTAK (a), CPEC 60:40 (b) and pure PFPI (c) samples following low-fluence excitation at 360 (a, c) or 600 (b) nm. Although both CPEs absorb at 360 nm, absorption at this wavelength is dominated by PFPI in complexes (**Figure 3.1**); it is thus convenient to use this wavelength to study energy transfer from photoexcited PFPI to PTAK. In contrast, 600 nm light exclusively excites PTAK even when it is bound within a CPEC; this wavelength can be used to isolate spectral features of PTAK for a given CPEC composition that should be anticipated due to energy transfer and to further examine how PTAK photophysics correlates with PTAK morphology when complexed with PFPI.

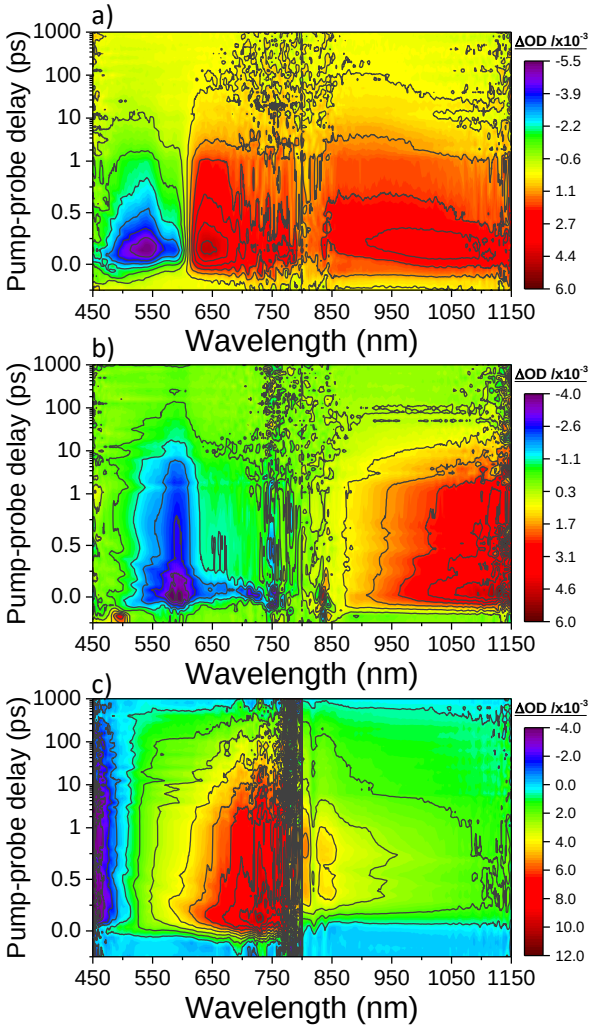

Figure 3.3. Transient absorption signals obtained from a) pure PTAK excited at 360 nm, b) CPEC 60:40 excited at 600 nm and c) pure PFPI excited at 360 nm. All data was smoothed in the spectral dimension using a 20-point Savitsky-Golay filter.

Transient spectra collected with pure PTAK samples (**Figure 3.3a**) excited at 360 nm exhibit a bleaching of the steady-state absorption ("ground-state" bleach, a negative signal) with vibronic features appearing below 600 nm, as well as absorption features at 650 nm and in the near-IR. The latter are similar to transient absorption features observed for □-stacked P3HT films and aggregates:[55-61] Careful wavelength, pulse fluence, and temperature dependent studies with regioregular-P3HT concluded that the feature at 650 nm arises from coupled electron/hole-pair ("polaron pair") states that dissociate into free charges at higher temperatures. In contrast the broad absorption in the near-IR arises from singlet excitons and some free charges (i.e. polarons). Global analysis with a two-state (i.e. two-spectrum) model reveals an initial spectral relaxation timescale

of 430 fs, followed by the triexponential decay of all remaining transient features on timescales of 0.38, 7.9, and 220 ps (**Figure AII.1**). We also collected spectral transients with pure PTAK using 600 nm excitation (**Figure AII.2**); excitation at 600 nm results in similar spectral features as those observed with 360 nm but with slightly different spectral intensities and relaxation timescales (biexponential decay lifetimes of 0.55 and 16 ps). These differences most likely reflect energy-dependence in exciton and charge-pair formation as well as energy-dependence in charge-pair recombination.

Direct excitation of PTAK within CPEC 60:40 at 600 nm (**Figure 3.3b**) yields only the bleaching of the PTAK ground state and the broad absorption of the singlet exciton peaking above 1100 nm (global analysis results shown in **Figure AII.3**). This is similar to transient spectral features of single-strand polythiophene,[62-64] such that the stark difference between the spectral dynamics observed for pure PTAK and PTAK within a 60:40 CPEC is consistent with a change in PTAK morphology when complexed with PFPI as discussed further below. Transient spectra collected with pure PFPI excited at 360 nm (**Figure 3.3c**) reveal a ground-state bleach below 500 nm, a sharp transient absorption peak and shoulder at 725 and 550 nm, respectively, and significantly weaker and relatively unstructured absorption across the near-IR. The time-dependent spectral data could only be fit with a single spectral component (**Figure AII.4**), with absorption features arising from the singlet excited state of PFPI. The fit yields a triexponential decay of all transient features with associated decay lifetimes of 1.7, 17, and 430 ps.

Figure 3.4 displays transient absorption data obtained from various CPECs following low-fluence excitation at 360 nm. The transient absorption from the 60:40 complex (**Figure 3.4a**) reveal clearly discernible signatures of excited PFPI, appearing as a short-lived absorption band (positive signal) between 600 and 800 nm in the few hundred fs following excitation. Interestingly, despite the fact that PFPI accounts for ~94% of the absorption cross section at 360 nm in the 60:40 CPEC, transient absorption of the PFPI singlet excited state is a minor component of the overall transient spectrum; furthermore, the PFPI signal is quenched very rapidly, leaving behind only bleach, stimulated emission and absorption bands due to PTAK. By contrast, transient spectral features in the visible recorded with direct, 600-nm excitation of the PTAK domain of the 60:40 CPEC exhibit a strong bleach and yield a negative signal in this region at all delays (see **Figure 3.3b**).

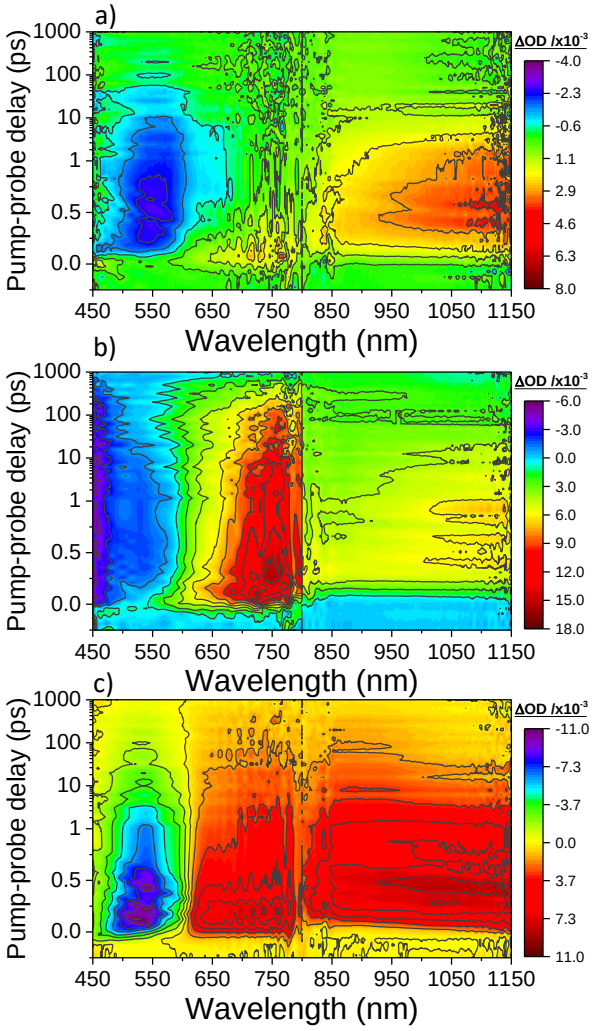

Figure 3.4. Transient absorption data collected with 360 nm excitation of CPEC mixtures at the following PFPI:PTAK ratios: a) 60:40, b) 80:20, and c) 20:80. All data was smoothed in the spectral domain by passing through a 20-point Savitsky-Golay filter.

Visual inspection and comparison of the time-resolved data presented in **Figures 4a** and 3b already provides qualitative support for ultrafast PFPI-to-PTAK energy transfer. If no such transfer occurred, one could expect that the contribution of PFPI and PTAK transient signals would be controlled by the relative absorption cross-sections (**Figure 3.1**) of the PTAK and PFPI components at the excitation wavelength. Specifically, based on decomposition of the CPEC OD spectrum into PFPI and PTAK contributions, PFPI should be expected to absorb 73, 85, 94, and 99% of the excitation for *R* = 20:80 through 80:20 respectively. Therefore, the intensity of the PTAK ground-state bleach, stimulated emission and transient absorption signals should be expected to be minor since fewer PTAK chains can be excited directly at this wavelength. Rather, PTAK signal disproportionally dominates the transient spectra (e.g. 60:40

CPEC, **Figure 3.4a**), indicating that PTAK transients are excited by means other than direct photoexcitation, namely energy transfer from excited PFPI.

To confirm this assertion, we applied global spectral analysis to extract species-associated spectra and their accompanying time-dependence for each species/state that contributes to the transient spectral dynamics of the CPECs. When compared with transient spectra of the pure CPEs, species-associated spectra obtained from CPEC data offer far clearer spectral signatures of energy transfer whilst also providing kinetic information for each of the components, allowing us to quantify the rate for energy transfer.

Figure 3.5 plots species-associated spectra (**Figure 3.5a**) and their time-dependence (**Figure 3.5b**) for the 60:40 CPEC excited at 360 nm (**Figure 3.4b**) extracted using a three-state kinetic model (A → B → C). Here, A represents the species populated initially upon excitation that subsequently relaxes to populate state

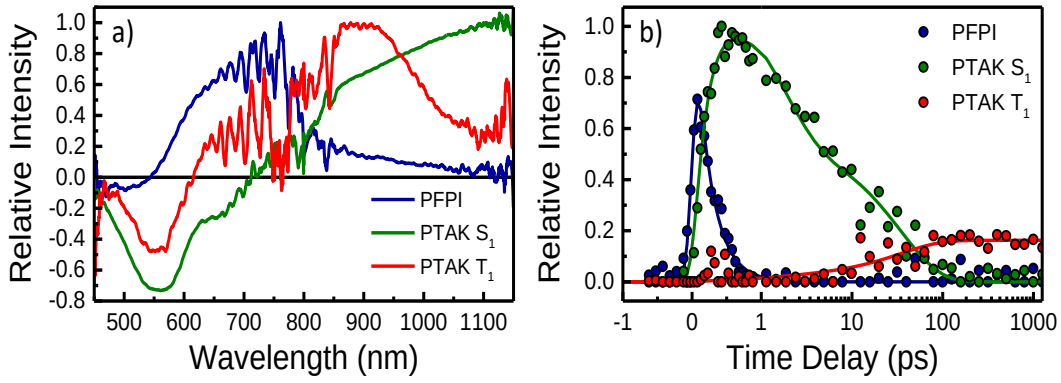

Figure 3.5. Results of global analysis of spectral transients collected from 60:40 CPEC samples pumped with 360-nm light. a) Species-associated spectra for PFPI (blue), PTAK singlet (green) and PTAK triplet (red) obtained from the three-state kinetic model described in the text. b) Time-dependence of the three spectral components shown in panel a). Points correspond to the relative weight of each spectrum from a), the solid lines represent the kinetic model fit.

B and similarly C from B. The species associated spectrum of A (blue) closely matches the transient spectrum of the PFPI excited singlet state (**Figure AII.4**); similarly, B (green) and C (red) closely match transient absorption of the singlet and triplet excited states of PTAK in the 60:40 complex when directly excited at 600 nm (**Figure AII.3**). The time-dependence associated with component A reveals that the initial population of PFPI decays with a 240 fs lifetime to populate the PTAK singlet. The PTAK singlet subsequently deactivates with a significant PTAK triplet yield. The fit to the time-dependent deactivation of the PTAK singlet population is improved using a bi-exponential decay with timescales of 1.6 and 34 ps, although we note that the appearance of the triplet population is dominated only by the slower of these timescales. The complete list of fitting parameters (including relaxation lifetimes) is included in **Table AII.1**. The 40:60 CPEC sample exhibits qualitatively similar behavior, as illustrated in **Figure AII.5**, although the PFPI lifetime extracted approaches the temporal response of our experiment (i.e. <100 fs).

Increasing the PFPI:PTAK charge ratio of the CPEC to 80:20 (**Figure 3.4b**) results in spectral transients dominated by features from PFPI. In addition to the transient absorption of excited PFPI, contributions from the ground-state bleach (500-600 nm) and singlet excited PTAK are also apparent within a few hundred fs of excitation. Absorption of the excited PTAK singlet dominates the red edge of the near-IR region and persists for 10s of ps, while the spectrum in this region begins to resemble a

combination of remaining excited PFPI singlet absorption and the PTAK triplet spectrum at later delays (>100 ps).

Global analysis of 80:20 CPEC transients reveals the species-associated spectra and their time-dependence as shown in **Figure 3.6a** and **6b**, respectively. The

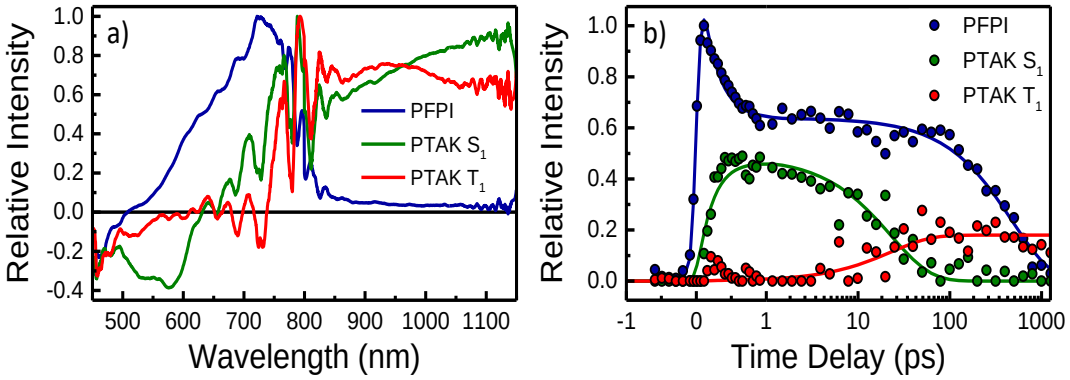

Figure 3.6. Results of global analysis of transient absorption data collected from the 80:20 CPEC following 360-nm excitation. a) Species-associated spectra for PFPI (blue), PTAK singlet (green) and PTAK triplet (red) obtained from the three-state kinetic model described in the text. b) Time-dependence of the three spectral components shown in panel a). Points correspond to the relative weight of each spectra from a), the solid lines represent the kinetic model.

component spectra are similar to those obtained for the 60:40 CPEC. However, the time-dependence of these components (**Figure 3.6b**) are quite different (*cf*. **Figure 3.5b**): Approximately half of the PFPI transients relax with a 220-fs lifetime to generate excited PTAK singlets (a lifetime in accord with PFPI deactivation in the 60:40 complex), which then decays exponentially with a lifetime of 23 ps to populate the PTAK triplet with a significant quantum yield. However, the other half of the excited PFPI population relaxes over a much longer timescale, 480 ps, comparable to the slowest lifetime for the singlet excited-state decay observed with pure PFPI. Based on

the applied model and time-dependence of spectral components, this prolonged decay of the PFPI absorption appears to occur *without* any additional population of PTAK singlet excited state, implying either that this fraction of the excited PFPI is effectively too far-removed spatially from PTAK chains for energy transfer to occur or that there are too few PTAK energy acceptors available for the density of excited PFPI. We believe the former possibility is more likely. These kinetics are consistent with observation of PFPI emission with ~50% PL quantum yield at *R* = 80:20 (**Figure 3.2b**).

Comparisons between transient spectra obtained with pure PTAK (**Figure 3.3a**, **Figure AII.1**) and 20:80 CPEC (**Figure 3.4c, Figures AII.6**) samples reveal only minor differences, with the ground-state bleach shifted to slightly shorter wavelengths and the visible transient absorption band lower in overall intensity for the latter. PFPI accounts for roughly 70% of the CPEC absorption cross section at 360 nm in the 20:80 composition. The transient spectra collected with the 20:80 CPEC exhibit no clear signatures of excited PFPI despite the fact that PFPI dominates absorption at the

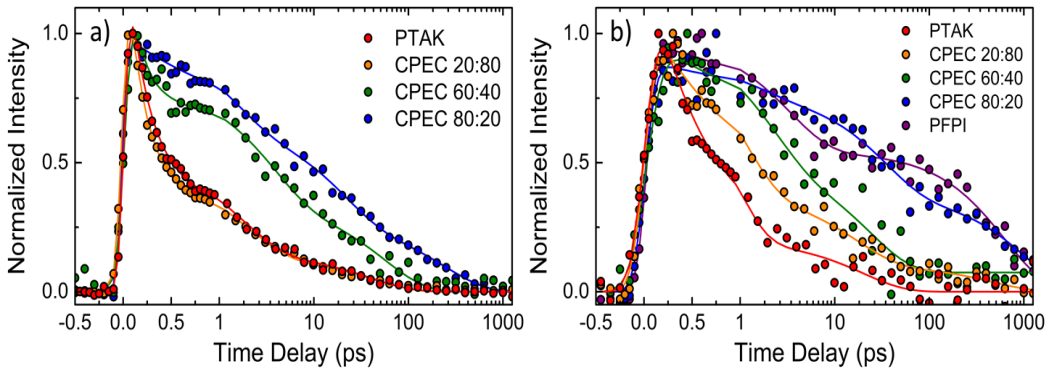

Figure 3.7. Normalized near-IR absorption (integrated 1050-1125 nm) and associated fits for samples excited at a) 600 nm and b) 360 nm illustrate dependence of PTAK photophysics with CPEC composition.

excitation wavelength, suggesting that PFPI relaxation likely occurs considerably faster than the instrument response of our measurements. This could be expected at lower charge ratios, as there are statistically more PTAK acceptors available to receive energy from excited PFPI energy donors. We note that the differences in PTAK spectral dynamics for these two samples at 360 nm are comparable to what is observed with 600 nm excitation of the PTAK control and 20:80 CPEC (**Figures AII.2** and **AII.7**, respectively). Therefore, we expect that the minor differences in transient spectral features observed with 360-nm excitation are associated principally with morphological changes in PTAK when complexed with PFPI rather than contributions from excited PFPI itself or from PFPI to PTAK energy transfer.

In addition to providing definitive signatures of energy-transfer dynamics and its dependence on CPEC composition, ultrafast time-resolved spectral data provides an additional window into morphological changes of PTAK in CPECs of various compositions, as illustrated in **Figures 3a** and 3b. **Figure 3.7** plots the normalized time-dependent transient absorbance measured at the long-wavelength edge of the photoinduced near-IR absorption (integrated 1050-1125 nm) for pure PTAK, pure PFPI and each CPEC composition excited at 600 nm (**Figure 3.7a**) and 360 nm (**Figure 3.7b**). Absorption in this probe window is dominated by transient signals from PTAK rather than PFPI and allows us to monitor how relaxation of excited PTAK is impacted when complexes are formed with PFPI. Traces collected with 600 nm excitation were fit with a triexponential decay; parameters from these fits are presented in **Table AII.2**.

Transients collected with pure PTAK or CPECs with low-PFPI mole percent are dominated by ultrafast (< 200 fs) absorption decay with slower decay occurring on ps to 10s of ps timescales. In general, the fraction of ultrafast absorption decay drops significantly with increasing PFPI fraction, whereas the lifetimes associated with absorption decay on >1 ps timescales increases significantly. A similar trend is observed with composition for 360 nm excitation (**Figure 3.7b**) although the ultrafast component of the PTAK decay is washed out, which could arise from the combination of lower temporal resolution at this excitation wavelength and PFPI-to-PTAK energy-transfer kinetics; parameters from bi- (where applicable) and triexponential fits of these traces are given in **Table AII.2**. The close similarity between the 60:40 traces collected with 600 and 360 nm excitation implies that PFPI transients have a negligible contribution to this spectral region at this composition. In contrast, the 80:20 trace collected with 360 nm persists on timescales considerably longer than the trace collected when the PTAK component of the CPEC is excited directly with 600 nm, reflecting that excited PFPI signals contribute significantly in this region at this composition (**Figure 3.4b**).

Nanosecond Exciton Diffusion Dynamics

Having established that energy transfer in a CPEC composed of a PFPI exciton donor and PTAK exciton acceptor is ultrafast, we go on to interrogate the dynamics of exciton diffusion within the PTAK component of the CPEC following rapid energy transfer from PFPI. The radiative dynamics of PTAK excitons within the CPEC assembly indirectly report on the local PTAK density of electronically coupled exciton states. The intra-chain and inter-chain excitonic couplings that characterize the network of PTAK chains in the complex cause transitions within the density of states. As a result, radiative exciton dynamics carry information about the distribution of chain conformations.

To characterize the dynamics of PTAK exciton diffusion and the state of chain extension as a function of *R*, we measured the PL anisotropy dynamics. The time-dependent anisotropy is defined as

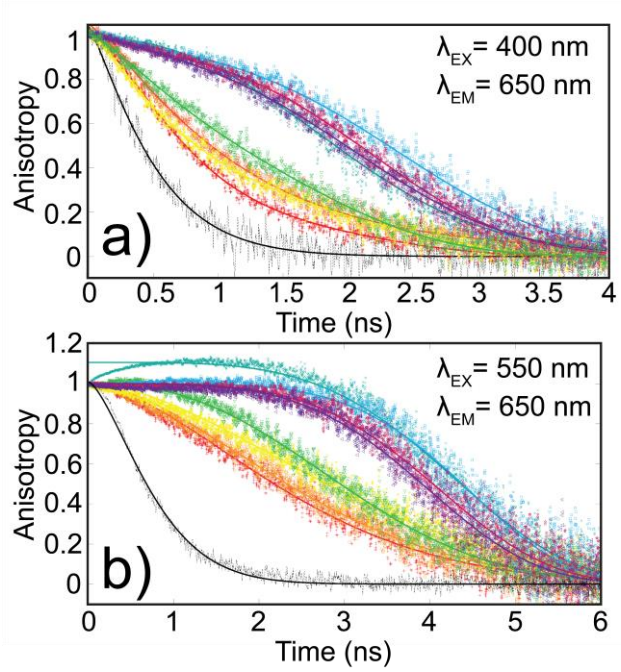

Figure 3.8. Normalized time-resolved PL anisotropy decays exciting at a) 400 nm and b) 550 nm. The PL wavelength was fixed at 650 nm for both, corresponding to PL from PTAK only. Smoothed data (symbols) is shown with respective stretched exponential fits (solid lines). Both figures follow the legend in **Figure 3.2**, with data in black corresponding to pure PTAK.

$$r(t) = \frac{I_{\parallel}(t) - GI_{\perp}(t)}{I_{\parallel}(t) + 2GI_{\perp}(t)} \quad (1)$$

where $I_{\parallel}$ is the emission component parallel to the (vertical) polarization of the exciting light, $I_{\perp}$ is the component corresponding to the perpendicular (horizontal) component, and G corrects for the difference in detectivity of the two polarization components.[65] $r(t)$ is particularly sensitive to the coupling between excited states both on the same chain and between separate chains. Specifically, after a population of excitons is formed by excitation with linearly polarized light, at early times emission from these states will have nearly the same polarization as the excitation. However, emission can quickly depolarize due to energy transfer between chromophores with slightly misoriented transition dipole moments.[66-69] Furthermore, motion of chain segments that localize the excited state can also rotate the transition dipole, leading to PL depolarization and thus additional decay of the PL anisotropy. Both intra-chain segmental motion and rotational diffusion of the overall complex may lead to depolarization. As discussed further below, due to the size of the CPEC we expect that rotational motion of the complex as a whole is effectively frozen out on the time scale of this experiment.

Figures 3.8a and **3.8b** show anisotropy decays normalized at early times as a function of *R* exciting at both 400 nm and 550 nm, respectively, and monitoring PL at

650 nm from PTAK excited states only. The measured fundamental anisotropy values are summarized in the SI. We find that the anisotropy decays are described well by a stretched-exponential model:[70]

$$r(t) = \sum_i \alpha_i e^{-\left(\frac{t}{\tau_i}\right)^{\beta_i}} \quad (2)$$

A single term was necessary to capture the curves excited at 550 nm, whereas two terms were required for satisfactory agreement when exciting at 400 nm. The stretching exponent β has previously been related to an underlying distribution of emitting states.[71] The fact that decays excited at 400 nm require two stretched exponentials to fit the data suggests that there may be two distinct depolarization processes. The fitting parameters are given in **Tables AII.4** and **AII.5** of Appendix II.

Both sets of data show a trend that is qualitatively similar to that of the steady-state PL. All the CPEC decay curves effectively fall into two categories, one with *R* > 50:50 and one with *R* < 50:50. Decays excited at 550 nm show the starkest evolution, with the depolarization time of pure PTAK of ~800 ps increasing to ~3.3 ns for the 10:90 CPEC and ultimately increasing to ~4.4 ns for the 90:10 CPEC. In fact, when the concentration of cationic PFPI charges exceeds that of anionic PTAK charges, the anisotropy becomes effectively flat, meaning that negligible depolarization occurs during the excited-state lifetime. We note that depolarization after ~3 ns accounts for only ~5% of remaining emitting species (see Appendix II). This means 95% of directly excited PTAK chromophores experience very little depolarization. This is particularly

notable given how rapidly the emission of pure PTAK is depolarized. We hypothesize that the eventual decay of the anisotropy for CPECs with *R* > 50:50 is due to rotational motion of chain segments as the complex diffuses. We note that the initial rise of the 60:40 sample is not well-understood and is likely artifactual.

When *R* < 50:50, the depolarization time drops significantly, though it always exceeds that of pure PTAK solutions. Between *R* = 10:90 and *R* = 40:60, β progressively increases from 1.6 to 2.4 before sharply rising to ~4 for *R* > 50:50 along with a concomitant increase in the depolarization time. The apparent effect of increasing the PFPI mole fraction on radiative PTAK dynamics is to substantially slow down the initial decay of the anisotropy, with a sharp transition occurring in the vicinity of the *R* = 50:50 composition. This transition across the ionic charge equivalence condition is consistent with the change in steady-state photophysics discussed above.

Relative to the mean size of an exciton created with 500 nm light, exciting at 400 nm additionally generates excitons on relatively short chain segments. Exciton diffusion within its density of states is not a random walk, as excitons localized on short chain segments are preferentially funneled to longer chain segments. We believe the reason that the anisotropy decay appears to have an additional fast component upon 400 nm excitation relative to 500 nm is because of exciton migration from, on average, shorter to longer chain segments. This evidently occurs on a ~0.5 – 1 ns timescale, which appears too long to be fully explained by intrachain exciton migration. It is feasible that PFPI may be assembling more than one PTAK chain – possibly of varying length – and excitons localized on shorter regions eventually migrate to longer PTAK chains in the assembly.

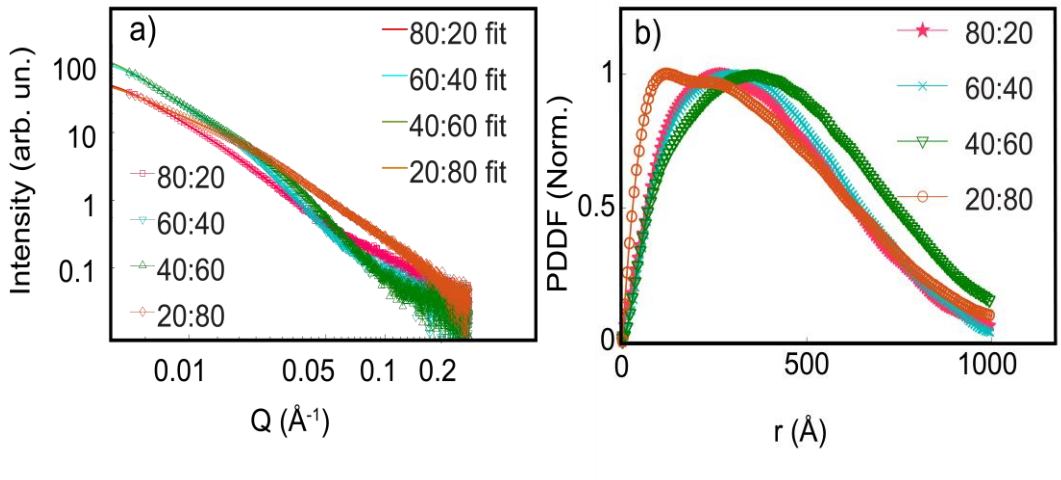

Figure 3.9. a) SAXS curves for CPECs at various charge ratios. Symbols correspond to data and lines to fits with the indirect Fourier transform. b) Corresponding PDDFs for the same samples.

Complex Solution Morphology

Our spectroscopic characterization of CPECs has collectively revealed the fact that as *R* passes through 50:50, photophysical properties change significantly. To relate these properties to the hierarchical, nanoscale solution morphology of the CPEC, we first discuss small-angle X-ray scattering (SAXS) measurements that probe the 1 to 10s of nm length scales. Due to the relatively low X-ray scattering power of CPEC solutions at concentrations used for spectroscopy, the SAXS signal-to-noise ratio was too low for quantitative analysis. Thus, we also interrogated complexes prepared at a total polymer concentration one order of magnitude greater (of order 1 mg/mL PFPI) than what was used in experiments described above. However, we verified that the overall trend persisted, both in scattering measurements and in steady-state spectroscopy. Given this observation, we present the larger-concentration set for SAXS analysis only. The scattering intensities as a function of scattering vector length, Q, are plotted in **Figure 3.9a**. The curves at the extremes of *R* differ qualitatively from each other and from the curves for the ratios near charge equivalence at all Q, including in the limiting slopes at high Q. Thus, over this Q range, the 60:40 and 40:60 microstructure appears similar. The SAXS intensity in the low-Q limit for these samples is larger than that of those with more extreme values of *R*, which reflects an increase in the average electron density contrast near ionic charge equivalence.

We have used the indirect Fourier transform to obtain orientationally averaged pair-distance distribution function (PDDF) as a function of *r*, where *r* is the

radial intraparticle coordinate.[72-74] The PDDF is a spatial correlation function that is related to the probability of observing two intraparticle points characterized by some electron density contrast a distance *r* apart.[75] **Figure 3.9b** shows the calculated PDDFs. We note that the PDDF in the limit of large *r* must be interpreted with care. It may be the case that the minimal experimentally accessible Q is insufficient to observe the onset of a Guinier plateau. In such a circumstance, the uncertainty in indirect Fourier transform due to interpolation to zero Q may lead to some inaccuracies in PDDF at large *r*. We see that for the 20:80 CPEC, there is more amplitude at short *r*, leading to an apparent shoulder around 10 nm that is absent for the other three samples. We associate this with π-stacked PTAK chain aggregates either on the same chain or between proximal chains. We note that we have observed a similar PDDF shape in pure PTAK solutions. Among these four samples, the 20:80 CPEC displays the most pronounced spectroscopic signatures indicative of π-stacking, which is consistent with our assignment.

To examine the overall hydrated complex size over larger dimensions, we turned to dynamic light scattering. **Figure AII.11** shows autocorrelation functions of the scattered light intensity, while the relaxation time distributions obtained via the regularized least-squares CONTIN algorithm are shown in **Figure 3.10**.[76] The distribution abscissa is also shown on a size scale using the Stokes-Einstein relation. The mean relaxation times of the 90:10, 80:20, 70:30 and 60:40 complexes are all quite similar – 1.2 x 10^4 μs – corresponding to a hydrodynamic radius of ~32 nm. As *R* is decreased to 40:60, the relaxation time (radius) undergoes a substantial increase to 5.1 x 10^4 μs (126 nm). Further decreasing *R* leads to a monotonic decrease in size; the 10:90 CPEC relaxation time becomes very similar to CPECs with *R* > 50:50. **Table AII.7** summarizes the mean relaxation times of the dominant peaks in the distribution, along with their corresponding complex sizes.

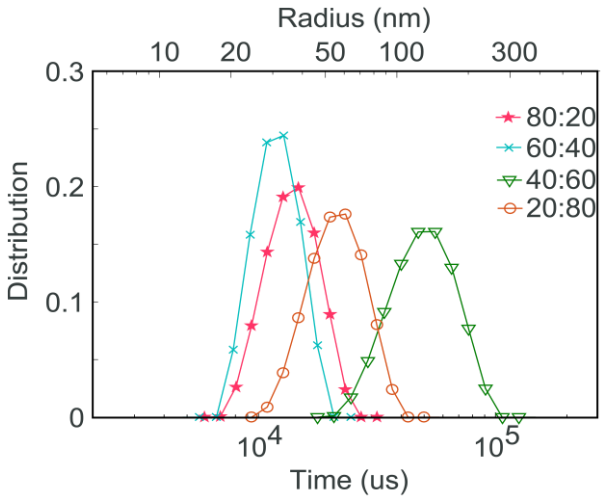

Figure 3.10. Relaxation time distributions obtained from DLS measurements via the CONTIN algorithm.

The observation that the average hydrodynamic size is comparable for CPECs with *R* from 90:10 to 60:40 is interesting, particularly in light of the SAXS results. We found that the SAXS intensities of the 60:40 and 40:60 samples were larger than the

80:20 and 20:80 samples. The fact that the hydrodynamic sizes of the 80:20 and 60:40 CPECs are similar suggests that as *R* decreases towards charge equivalence, the CPEC network becomes denser.

3.3 DISCUSSION

To synthesize together the results described above, it is helpful to summarize our main findings. First, we have shown that the energy transfer rate between PFPI and PTAK in the CPEC is ultrafast; we observe clearly that PFPI excitons transfer to PTAK in 250 fs or faster. Second, the PTAK PL quantum yield undergoes a substantial drop when *R* is lowered below 50:50 and begins to approach that of pure PTAK solutions; this is consistent with what is observed in the ultrafast dynamics of the PTAK component (**Figure 3.7b**). Conversely, for *R* > 50:50, the PTAK quantum yield is larger than that of pure PTAK solutions by approximately a factor of 20 – a fact that we also observed in our prior work. We find that for *R* < 50:50, the OD spectrum of PTAK acquires a well-defined shoulder near its red edge, while the PTAK PL anisotropy begins to decay rapidly. For *R* > 50:50, the anisotropy is remarkably flat up to several ns. Similarly, both time-resolved PL and transient absorption decays exhibit a significant contribution from a fast component that is also seen in pure PTAK (see SI). Furthermore, the transient spectral features associated with the PTAK phase observed in ultrafast TA measurements for CPECs with low *R* are similar to those

previously associated with □-stacking in polythiophene films and aggregates, whereas features observed for CPECs with high R are more similar to those observed for isolated polymer strands. Finally, we have found structural signatures of enhanced π-stacking for *R* < 50:50 and its near absence for *R* > 50:50. The overall complex size grows significantly as *R* is lowered below 50:50, ultimately becoming fairly compact again for the lowest *R* value (10:90).

The picture that emerges from these findings is summarized in the cartoon in **Figure 3.11**. In its native aqueous state, PTAK is strongly coiled, leading to significant π-stacking. Introduction of PFPI at *R* < 50:50 results in a partial uncoiling of the PTAK chain. When *R* > 50:50, PFPI is able to largely unwind the PTAK chain; this minimizes the number of π-stacking contacts between PTAK chromophores and leads to formation of bright excitons delocalized over significant regions of the PTAK chain. Our results underscore the fact that *only* when the cationic PFPI charge concentration

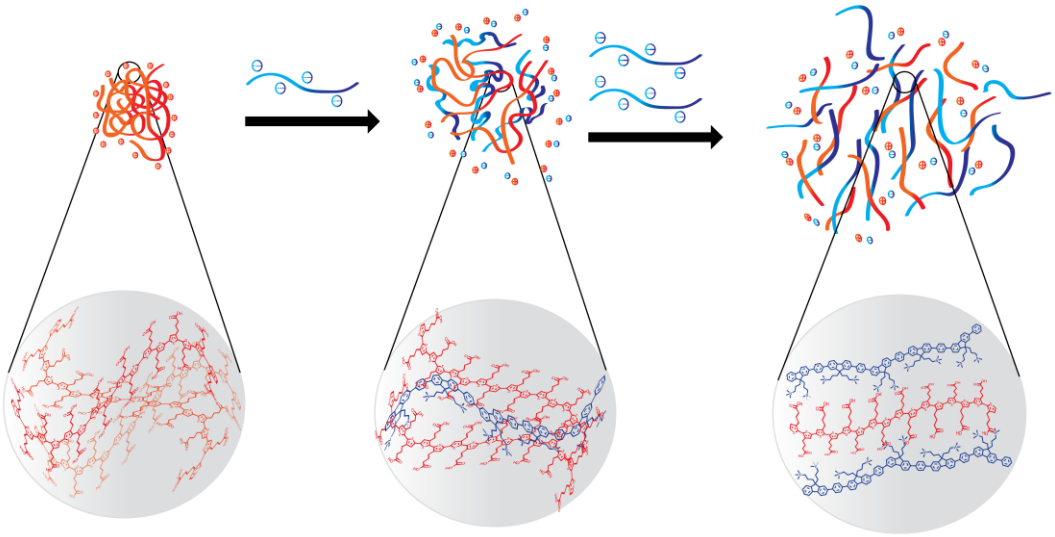

Figure 3.11. Cartoon of CPE complexation as a function of relative ionic charge ratio *R*. PTAK chains are shown as orange curves with positive counterions, and PFPI chains are indicated by blue chains with negative counterions. The top shows the unwinding of coiled PTAK states upon introduction of PFPI. When PFPI charges are in molar excess relative to PTAK, PTAK chains undergo a substantial straightening, leading to a substantial rise in the PL quantum yield and depolarization time, as well as transient absorption lifetime. In so doing, the PFPI chain must evidently contort to accommodate the straightening of PTAK. Circles show cartoon representations of the hypothesized molecular-level changes.

exceeds that of the anionic PTAK charges does the PTAK chain largely unwind and straighten from its native coiled state in water. This leads to a substantial change in the PL anisotropy and the PL quantum yield, consistent with excited states becoming much more delocalized along the PTAK backbone. Though there are quantitative differences in emission depolarization lifetimes and stretching exponents between CPECs in the range of 90:10 to 60:40, qualitatively the large transformation in the PTAK chain microstructure is seen for all these samples, so long as *R* exceeds 50:50. What does appear to change fairly significantly is the importance of π-interactions in PFPI, as judged by its vibronic PL ratio S_R (inset of **Figure 3.2**). We interpret this as

being due to the PFPI chain becoming progressively more coiled or contorted as the PTAK mole fraction increases. When $R < 50{:}50$, we observe the prominent appearance of PTAK π-stacking interactions. At the same time, the PL dynamics, its anisotropy and the transient exciton absorption begin to decay more rapidly. In particular, comparison of the PL anisotropy decays for 60:40 and 40:60 ratios – characterized by very different complex sizes – shows that even at these relatively close compositions, there are significant, qualitative differences in the exciton dynamics. We have in fact observed that the 40:60 ratio, which gives rise to the largest complexes, appears least stable with respect to eventual phase separation.

It is intriguing that the temporal evolution of CPEC excited states can be manipulated via the relative polyion charge ratio. The question that remains is, why does it take an excess of PFPI charges to unwind the PTAK chain sufficiently so as to yield electronic states that are largely delocalized over stretched-out chains? We hypothesize that a PTAK chain must be unwound by the action of more than one PFPI chain; that is, the complexation and the extension of the PTAK chain is a cooperative phenomenon. In such a model, PTAK effectively bridges vicinal PFPI chains in a manner that extends its backbone. In the process, the PFPI backbone becomes somewhat contorted to accommodate this geometric distortion of the PTAK chain. The logical extension of this hypothesis is that, even at these relatively low CPE concentrations, CPEC solutions effectively resemble ionically assembled networks. This would allow

PFPI excitons to diffuse along this network and possibly find a PTAK chain to which to transfer its energy.

For compositions limited by the acceptor concentration (e.g., *R* = 80:20), though the acceptor CPE chains straighten, not all donor excitons can be harvested. What, then, is the influence of PFPI on PTAK when PTAK is in excess, i.e. when *R* < 50:50 and all donor excitons transfer to acceptor CPE states? Based on the relative PL quantum yields and the long-wavelength OD structure observed in these CPEC samples, PTAK displays evidence of π-stacking interactions analogous to that of pure PTAK solutions. However, the PL anisotropy dynamics show that pure PTAK solutions are characterized by a more rapid depolarization time, which appears to be too fast to be explained by differences in overall complex size. This implies that when *R* < 50:50, PFPI is unable to fully uncoil PTAK chains; nevertheless, binding to PFPI progressively "opens up" the originally coiled PTAK state, which leads to an increase in the PL depolarization lifetime. This may proceed by PFPI binding to the outside of the PTAK coil, partially uncoiling peripheral PTAK chain segments. The result would be that the core of the PTAK coil retains some amount of π-stacking, though at a smaller number density of backbone contacts than the native coiled state. However, given the substantial increase in size for the CPECs at the 30:70 and 40:60 compositions, we believe it is challenging to explain this based on interactions between two oppositely charged chains, even at this dilute total polymer concentration. We hypothesize that as *R* approaches 50:50 from below, increasing concentrations of PFPI begin to bind

multiple partially coiled PTAK chains, leading to progressively longer-lived exciton dynamics.

Our fluorescence excitation and ultrafast pump probe results for the 80:20 CPEC show that energy transfer is not complete at large *R*, indicating one of two possibilities relating to CPEC structure: Either some PFPI excitons are incapable of migrating to sites from which energy transfer to PTAK can occur, or the energy-harvesting potential is limited by the PTAK density. In the case of the former, PTAK sites could be thought of as effectively "saturated" with donors, such that excess PFPI excitations can only transfer once initial excitations of PTAK have relaxed. For the latter case, a fraction of PFPI is distant enough from PTAK so as to lead to substantial radiative relaxation of PFPI excitons and an inability to transfer energy over long distances within the molecular network. At the 60:40 ratio, the mean separation between PFPI and PTAK chains decreases and the acceptor density increases. Concurrently, complete energy transfer from PFPI to PTAK is observed, while retaining fairly extended PTAK chains. Contrasting the energy-transfer dynamics observed for 80:20 and 60:40 CPECs and comparison to steady state PL results points to an optimal ratio for complete energy transfer from PFPI to PTAK between 80:20 and 60:40. More specifically, since photoluminescence quenching of PFPI is incomplete at 70:30, one would anticipate that optimal energy harvesting complex occurs between 70:30 and 60:40 and perhaps lies close to the charge ratio that would reflect monomer equivalence, i.e. 67:33. Indeed, in utilizing CPECs for energy harvesting and transfer,

the ideal system would be one in which complete energy transfer occurs from PFPI to PTAK, as seen in 60:40, but does so with the highest possible fraction of PFPI to absorb more radiation and thereby minimize losses from PFPI emission.

It is interesting to note that, quite generally, we expect the assumptions intrinsic to the commonly used Förster energy transfer model to break down within an exciton donor/acceptor CPEC. This is because the distance between the two CPE chains is comparable to the mean spatial extent of the exciton wavefunction, which is delocalized along the CPE backbone. Exciton transfer within a CPEC must instead be described within a generalized Förster formalism based on transition densities that reflect the underlying chain microstructure.[17] This suggests that beyond spectral overlap considerations, the donor/acceptor excitonic interaction may be chemically tuned via the CPE electronic structure; this presents a potentially fruitful avenue to control the energy transfer rate.

3.4 CONCLUSION

We have shown that complexation between oppositely charged exciton donor/acceptor CPEs leads to ultrafast energy transfer. We also found that the evolution in the CPE chain microstructure and thus its exciton dynamics changed qualitatively across the polyion charge equivalence point. The extent to which the chain microstructure is “patterned” from one CPE to the other appears to be

proportional to the relative amounts of each CPE in the complex, with the major component determining whether the CPEC is dominated by extended (bright) or coiled (dark) chain conformations. The fact that oppositely charged CPEs can be readily assembled in water to yield an ultrafast exciton transfer antenna, whose photophysics can be manipulated via the polyion charge ratio, temperature and ionic strength, is attractive for soft-matter light-harvesting applications. The energy transfer rate is in fact comparable to what is seen in natural photosynthesis; this makes the ionically assembled CPEC an efficient self-assembled energy-transfer antenna. Questions remain as to how the mutual chain extension may be further increased, as well as what the roles of rigidity and charge density along the backbone are in determining the degree of chain extension and the associated exciton transfer dynamics.

REFERENCES

1. Wasielewski, M. R. Self-Assembly Strategies for Integrating Light Harvesting and Charge Separation in Artificial Photosynthetic Systems. *Accounts of Chemical Research* **2009,** *42* (12), 1910-1921.

2. Albinsson, B.; Hannestad, J. K.; Börjesson, K. Functionalized DNA Nanostructures for Light Harvesting and Charge Separation. *Coordination Chemistry Reviews* **2012,** *256* (21-22), 2399-2413.

3. Andreiadis, E. S.; Chavarot-Kerlidou, M.; Fontecave, M.; Artero, V. Artificial Photosynthesis: From Molecular Catalysts for Light-driven Water Splitting to Photoelectrochemical Cells. *Photochemistry and Photobiology* **2011,** *87* (5), 946-964.

4. Hansen, M.; Troppmann, S.; König, B. Artificial Photosynthesis at Dynamic Self-Assembled Interfaces in Water. *Chemistry – A European Journal* **2016,** *22* (1), 58-72.

5. Bottari, G.; Trukhina, O.; Ince, M.; Torres, T. Towards Artificial Photosynthesis: Supramolecular, Donor–Acceptor, Porphyrin- and Phthalocyanine/Carbon Nanostructure Ensembles. *Coordination Chemistry Reviews* **2012,** *256* (21-22), 2453-2477.

6. Frischmann, P. D.; Mahata, K.; Wurthner, F. Powering the Future of Molecular Artificial Photosynthesis with Light-Harvesting Metallosupramolecular Dye Assemblies. *Chem Soc Rev* **2013,** *42* (4), 1847-70.

7. Hayashi, H.; Sobczuk, A.; Bolag, A.; Sakai, N.; Matile, S. Antiparallel Three-Component Gradients in Double-Channel Surface Architectures. *Chem. Sci.* **2014,** *5* (12), 4610-4614.

8. Olivier, J.-H.; Barberá, J.; Bahaidarah, E.; Harriman, A.; Ziessel, R. Self-Assembly of Charged Bodipy Dyes To Form Cassettes That Display Intracomplex Electronic Energy Transfer and Accrete into Liquid Crystals. *Journal of the American Chemical Society* **2012,** *134* (14), 6100-6103.

9. Ziessel, R.; Harriman, A. Artificial Light-Harvesting Antennae: Electronic Energy Transfer by Way of Molecular Funnels. *Chemical Communications* **2011,** *47* (2), 611-631.

10. Haycock, R. A.; Yartsev, A.; Michelsen, U.; Sundström, V.; Hunter, C. A. Self-Assembly of Pentameric Porphyrin Light-Harvesting Antennae Complexes. *Angewandte Chemie* **2000,** *112* (20), 3762-3765.

11. Faul, C. F. J. Ionic Self-Assembly for Functional Hierarchical Nanostructured Materials. *Accounts of Chemical Research* **2014,** *47* (12), 3428-3438.

12. Stupp, S. I.; Palmer, L. C. Supramolecular Chemistry and Self-Assembly in Organic Materials Design. *Chemistry of Materials* **2014,** *26* (1), 507-518.

13. Sancho Oltra, N.; Browne, W. R.; Roelfes, G. Hierarchical Self-Assembly of a Biomimetic Light-Harvesting Antenna Based on DNA G-Quadruplexes. *Chemistry* **2013,** *19* (7), 2457-61.

14. Blankenship, R. E.; Tiede, D. M.; Barber, J.; Brudvig, G. W.; Fleming, G.; Ghirardi, M.; Gunner, M. R.; Junge, W.; Kramer, D. M.; Melis, A. et al. Comparing Photosynthetic and Photovoltaic Efficiencies and Recognizing the Potential for Improvement. *Science* **2011,** *332* (6031), 805-809.

15. Croce, R.; van Amerongen, H. Natural Strategies for Photosynthetic Light Harvesting. *Nat Chem Biol* **2014,** *10* (7), 492-501.

16. Scholes, G. D.; Fleming, G. R.; Olaya-Castro, A.; van Grondelle, R. Lessons from Nature About Solar Light Harvesting. *Nat Chem* **2011,** *3* (10), 763-74.

17. Beljonne, D.; Curutchet, C.; Scholes, G. D.; Silbey, R. J. Beyond Förster Resonance Energy Transfer in Biological and Nanoscale Systems. *The Journal of Physical Chemistry B* **2009,** *113* (19), 6583-6599.

18. Chenu, A.; Scholes, G. D. Coherence in Energy Transfer and Photosynthesis. *Annu Rev Phys Chem* **2015,** *66*, 69-96.

19. Scholes, G. D. Long-Range Resonance Energy Transfer in Molecular Systems. *Annu Rev Phys Chem* **2003,** *54*, 57-87.

20. Kelley, R. F.; Lee, S. J.; Wilson, T. M.; Nakamura, Y.; Tiede, D. M.; Osuka, A.; Hupp, J. T.; Wasielewski, M. R. Intramolecular Energy Transfer within Butadiyne-Linked Chlorophyll and Porphyrin Dimer-Faced, Self-Assembled Prisms. *Journal of the American Chemical Society* **2008,** *130* (13), 4277-4284.

21. Li, X.; Sinks, L. E.; Rybtchinski, B.; Wasielewski, M. R. Ultrafast Aggregate-to-Aggregate Energy Transfer within Self-assembled Light-Harvesting Columns of Zinc Phthalocyanine Tetrakis(Perylenediimide). *Journal of the American Chemical Society* **2004,** *126* (35), 10810-10811.

22. V., R. V.; Raanan, C.; M., D. S.; E., B. K.; R., W. M. Photodriven Charge Separation and Transport in Self-Assembled Zinc Tetrabenzotetraphenylporphyrin and Perylenediimide Charge Conduits. *Angewandte Chemie International Edition* **2014,** *53* (13), 3457-3461.

23. Garg, V.; Kodis, G.; Liddell, P. A.; Terazono, Y.; Moore, T. A.; Moore, A. L.; Gust, D. Artificial Photosynthetic Reaction Center With a Coumarin-Based Antenna System. *J Phys Chem B* **2013,** *117* (38), 11299-308.

24. Gust, D.; Moore, T. A.; Moore, A. L. Realizing Artificial Photosynthesis. *Faraday Discuss.* **2012,** *155*, 9-26.

25. Ardoña, H. A. M.; Draper, E. R.; Citossi, F.; Wallace, M.; Serpell, L. C.; Adams, D. J.; Tovar, J. D. Kinetically Controlled Coassembly of Multichromophoric Peptide Hydrogelators and the Impacts on Energy Transport. *Journal of the American Chemical Society* **2017,** *139* (25), 8685-8692.

26. Métivier, R.; Kulzer, F.; Weil, T.; Müllen, K.; Basché, T. Energy Transfer Rates and Pathways of Single Donor Chromophores in a Multichromophoric Dendrimer Built around a Central Acceptor Core. *Journal of the American Chemical Society* **2004,** *126* (44), 14364-14365.

27. Samorì, P.; Yin, X.; Tchebotareva, N.; Wang, Z.; Pakula, T.; Jäckel, F.; Watson, M. D.; Venturini, A.; Müllen, K.; Rabe, J. P. Self-Assembly of Electron Donor−Acceptor Dyads into Ordered Architectures in Two and Three Dimensions: Surface Patterning and Columnar "Double Cables". *Journal of the American Chemical Society* **2004,** *126* (11), 3567-3575.

28. Kundu, S.; Patra, A. Nanoscale Strategies for Light Harvesting. *Chemical Reviews* **2017,** *117* (2), 712-757.

29. Wiesenhofer, H.; Beljonne, D.; Scholes, G. D.; Hennebicq, E.; Brédas, J. L.; Zojer, E. Limitations of the Förster Description of Singlet Exciton Migration: The Illustrative Example of Energy Transfer to Ketonic Defects in Ladder-type Poly(para-phenylenes). *Advanced Functional Materials* **2005,** *15* (1), 155-160.

30. Jiang, H.; Taranekar, P.; Reynolds, J. R.; Schanze, K. S. Conjugated polyelectrolytes: synthesis, photophysics, and applications. *Angew Chem Int Ed Engl* **2009,** *48* (24), 4300-16.

31. Liu, B.; Bazan, G. C. *Conjugated Polyelectrolytes: Fundamentals and Applications*. Wiley: 2013.

32. Hoven, C.; Yang, R.; Garcia, A.; Heeger, A. J.; Nguyen, T.-Q.; Bazan, G. C. Ion Motion in Conjugated Polyelectrolyte Electron Transporting Layers. *Journal of the American Chemical Society* **2007,** *129* (36), 10976-10977.

33. Thomas, S. W.; Joly, G. D.; Swager, T. M. Chemical Sensors Based on Amplifying Fluorescent Conjugated Polymers. *Chemical Reviews* **2007,** *107* (4), 1339-1386.

34. Zhao, X.; Liu, Y.; Schanze, K. S. A Conjugated Polyelectrolyte-Based Fluorescence Sensor for Pyrophosphate. *Chemical Communications* **2007,** (28), 2914-2916.

35. Zhao, X.; Schanze, K. S. Fluorescent Ratiometric Sensing of Pyrophosphate via Induced Aggregation of a Conjugated Polyelectrolyte. *Chemical Communications* **2010,** *46* (33), 6075-6077.

36. Wang, D.; Gong, X.; Heeger, P. S.; Rininsland, F.; Bazan, G. C.; Heeger, A. J. Biosensors from Conjugated Polyelectrolyte Complexes. *Proceedings of the National Academy of Sciences* **2002,** *99* (1), 49.

37. Calver, C. F.; Schanze, K. S.; Cosa, G. Biomimetic Light-Harvesting Antenna Based on the Self-Assembly of Conjugated Polyelectrolytes Embedded within Lipid Membranes. *ACS Nano* **2016,** *10* (11), 10598-10605.

38. Ji, E.; Parthasarathy, A.; Corbitt, T. S.; Schanze, K. S.; Whitten, D. G. Antibacterial Activity of Conjugated Polyelectrolytes With Variable Chain Lengths. *Langmuir* **2011,** *27* (17), 10763-9.

39. Wang, D.; Gong, X.; Heeger, P. S.; Rininsland, F.; Bazan, G. C.; Heeger, A. J. Biosensors from Conjugated Polyelectrolyte Complexes. *Proc Natl Acad Sci U S A* **2002,** *99* (1), 49-53.

40. Wang, X.; He, F.; Tang, F.; Li, L. Optically Amplified DNA Detection on Self-Assembled Solid Films Using Conjugated Polyelectrolytes. *Journal of Materials Chemistry* **2012,** *22* (30), 15303.

41. Wang, Y.; Schanze, K. S.; Chi, E. Y.; Whitten, D. G. When Worlds Collide: Interactions at the Interface Between Biological Systems and Synthetic Cationic Conjugated Polyelectrolytes and Oligomers. *Langmuir* **2013,** *29* (34), 10635-47.

42. Hollingsworth, W. R.; Segura, C.; Balderrama, J.; Lopez, N.; Schleissner, P.; Ayzner, A. L. Exciton Transfer and Emergent Excitonic States in Oppositely-Charged Conjugated Polyelectrolyte Complexes. *The Journal of Physical Chemistry B* **2016,** *120* (31), 7767-7774.

43. Schleissner, P.; Ayzner, A. L. Effects of pH on the Photophysics of Conjugated Polyelectrolyte Complexes. *Polymer* **2018,** *136*, 114-120.

44. Clark, J.; Chang, J.-F.; Spano, F. C.; Friend, R. H.; Silva, C. Determining Exciton Bandwidth and Film Microstructure in Polythiophene Films Using Linear Absorption Spectroscopy. *Applied Physics Letters* **2009,** *94* (16), 163306.

45. Hestand, N. J.; Spano, F. C. Molecular Aggregate Photophysics beyond the Kasha Model: Novel Design Principles for Organic Materials. *Accounts of Chemical Research* **2017**.

46. Spano, F. C.; Clark, J.; Silva, C.; Friend, R. H. Determining Exciton Coherence from the Photoluminescence Spectral Line Shape in Poly(3-hexylthiophene) Thin Films. *The Journal of Chemical Physics* **2009,** *130* (7), 074904.

47. Yamagata, H.; Norton, J.; Hontz, E.; Olivier, Y.; Beljonne, D.; Bredas, J. L.; Silbey, R. J.; Spano, F. C. The Nature of Singlet Excitons in Oligoacene Molecular Crystals. *J Chem Phys* **2011,** *134* (20), 204703.

48. Yamagata, H.; Spano, F. C. Vibronic Coupling in Quantum Wires: Applications to Polydiacetylene. *The Journal of Chemical Physics* **2011,** *135* (5), 054906.

49. Barford, W. Exciton Transfer Integrals Between Polymer Chains. *J Chem Phys* **2007,** *126* (13), 134905.

50. Barford, W.; Marcus, M. Theory of Optical Transitions in Conjugated Polymers. I. Ideal Systems. *The Journal of Chemical Physics* **2014,** *141* (16), 164101.

51. Marcus, M.; Tozer, O. R.; Barford, W. Theory of Optical Transitions in Conjugated Polymers. II. Real Systems. *The Journal of Chemical Physics* **2014,** *141* (16), 164102.

52. Spano, F. C.; Silva, C. H- and J-Aggregate Behavior in Polymeric Semiconductors. *Annual Review of Physical Chemistry* **2014,** *65* (1), 477-500.

53. Clegg, R. M.; Murchie, A. I.; Lilley, D. M. The Solution Structure of the Four-Way DNA Junction at Low-Salt Conditions: a Fluorescence Resonance Energy Transfer Analysis. *Biophysical Journal* **1994,** *66* (1), 99-109.

54. Clegg, R. M. Fluorescence Resonance Energy Transfer and Nucleic Acids. In *Methods in Enzymology*, Academic Press: 1992; Vol. Volume 211, pp 353-388.

55. Guo, J.; Ohkita, H.; Benten, H.; Ito, S. Near-IR Femtosecond Transient Absorption Spectroscopy of Ultrafast Polaron and Triplet Exciton Formation in

Polythiophene Films with Different Regioregularities. *Journal of the American Chemical Society* **2009,** *131*, 16869-16880.

56. Gao, B.-R.; Wang, H.-Y.; Wang, H.; Yang, Z.-Y.; Wang, L.; Jiang, Y.; Hao, Y.-W.; Chen, Q.-D.; Sun, H.-B. Investigation of Polaron Pair Dynamics in Poly(3-hexylthiophene) Film by Time-Resolved Spectroscopy. *IEEE J. Quantum Elec.* **2012,** *48*, 425-432.

57. Magnanelli, T. J.; Bragg, A. E. Time-Resolved Raman Spectroscopy of Polaron Pair Formation in Poly(3-hexylthiophene) Aggregates. *Journal of Physical Chemistry Letters* **2015,** *2015*, 438-445.

58. Ogata, Y.; Kawaguchi, D.; Tanaka, K. An Effect of Molecular Motion on Carrier Formation in a Poly(3-hexylthiophene) Film. *Scientific Reports* **2015,** *5*, 8436.

59. Piris, J.; Dykstra, T. E.; Bakulin, A. A.; van Loosdrecht, P. H. M.; Knulst, W.; Trinh, M. T.; Schins, J. M.; Siebelies, L. D. A. Photogeneration and Ultrafast Dynamics of Excitons and Charges in P3HT/PCBM Blends. *Journal of Physical Chemistry C* **2009,** *113*, 14500-14506.

60. Reid, O. G.; Pensack, R. D.; Song, Y.; Scholes, G. D.; Rumbles, G. Charge Photogeneration in Neat Conjugated Polymers. *Chemistry of Materials* **2014,** *26*, 561-575.

61. Martin, T. P.; Wise, A. J.; Busby, E.; Gao, J.; Roehling, J. D.; Ford, M. J.; Larsen, D. S.; Moule, A. J.; Grey, J. K. Packing Dependent Electronic Coupling in Single Poly(3-hexylthiophene) H- and J- Aggregate Nanofibers. *Journal of Physical Chemistry B* **2013,** *117*, 4478-4487.

62. Busby, E.; Carroll, E. C.; Chinn, E. M.; Chang, L.; Moulé, A. J.; Larsen, D. S. Excited-State Self-Trapping and Ground-State Relaxation Dynamics in Poly(3-hexylthiophene) Resolved with Broadband Pump–Dump–Probe Spectroscopy. *The Journal of Physical Chemistry Letters* **2011,** *2* (21), 2764-2769.

63. Tapping, P. C.; Kee, T. W. Optical Pumping of Poly(3-hexylthiophene) Singlet Excitons Induces Charge Carrier Generation. *The Journal of Physical Chemistry Letters* **2014,** *5* (6), 1040-1047.

64. Yu, W.; Zhou, J.; Bragg, A. E. Exciton Conformational Dynamics of Poly(3-hexylthiophene) (P3HT) in Solution from Time-Resolved Resonant-Raman Spectroscopy. *The Journal of Physical Chemistry Letters* **2012,** *3* (10), 1321-1328.

65. Lakowicz, J. R. *Principles of Fluorescence Spectroscopy*. Springer US: 2007.

66. Stein, A. D.; Peterson, K. A.; Fayer, M. D. Dispersive Electronic Excitation Transport in Polymeric Solids at and Near Room Temperature. *Chemical Physics Letters* **1989,** *161* (1), 16-22.

67. Stein, A. D.; Peterson, K. A.; Fayer, M. D. Dispersive Excitation Transport at Elevated Temperatures (50–298 K): Experiments and Theory. *The Journal of Chemical Physics* **1990,** *92* (9), 5622-5635.

68. Gochanour, C. R.; Andersen, H. C.; Fayer, M. D. Electronic Excited State Transport in Solution. *The Journal of Chemical Physics* **1979,** *70* (9), 4254-4271.

69. Colby, K. A.; Burdett, J. J.; Frisbee, R. F.; Zhu, L.; Dillon, R. J.; Bardeen, C. J. Electronic Energy Migration on Different Time Scales: Concentration Dependence of the Time-Resolved Anisotropy and Fluorescence Quenching of Lumogen Red in Poly(methyl methacrylate). *The Journal of Physical Chemistry A* **2010,** *114* (10), 3471-3482.

70. Kohlrausch, R. Theorie des Elektrischen Rückstandes in der Leidener Flasche. *Annalen der Physik* **1854,** *167* (2), 179-214.

71. Berberan-Santos, M. N.; Bodunov, E. N.; Valeur, B. Mathematical Functions for the Analysis of Luminescence Decays with Underlying Distributions 1. Kohlrausch Decay Function (Stretched Exponential). *Chemical Physics* **2005,** *315* (1), 171-182.

72. Brunner-Popela, J.; Glatter, O. Small-Angle Scattering of Interacting Particles. I. Basic Principles of a Global Evaluation Technique. *Journal of Applied Crystallography* **1997,** *30* (4), 431-442.

73. Ehmann, H. M. A.; Spirk, S.; Doliška, A.; Mohan, T.; Gössler, W.; Ribitsch, V.; Sfiligoj-Smole, M.; Stana-Kleinschek, K. Generalized Indirect Fourier Transformation as a Valuable Tool for the Structural Characterization of Aqueous Nanocrystalline Cellulose Suspensions by Small Angle X-ray Scattering. *Langmuir* **2013,** *29* (11), 3740-3748.

74. Fukasawa, T.; Sato, T. Versatile Application of Indirect Fourier Transformation to Structure Factor Analysis: from X-ray Diffraction of Molecular Liquids to Small Angle Scattering of Protein Solutions. *Physical Chemistry Chemical Physics* **2011,** *13* (8), 3187-3196.

75. Glatter, O.; Kratky, O. *Small Angle X-ray Scattering*. Academic Press: 1982.

76. Scotti, A.; Liu, W.; Hyatt, J. S.; Herman, E. S.; Choi, H. S.; Kim, J. W.; Lyon, L. A.; Gasser, U.; Fernandez-Nieves, A. The CONTIN Algorithm and its Application to Determine the Size Distribution of Microgel Suspensions. *The Journal of Chemical Physics* **2015,** *142* (23), 234905.

Chapter 4

Activation and Formation of Aqueous Exciton Transport Networks

Acknowledgements: When published, this chapter will have the following authorship: William R. Hollingsworth, Vanessa Williams, Alexander L. Ayzner. WRH prepared regioregular and regiorandom complexes, performed time-resolved and steady-state spectroscopy/anisotropy and analysis thereof, and performed isothermal titration calorimetry and analysis thereof. VW prepared PCPT samples and carried out steady-state spectroscopy of the same. WRH wrote the manuscript. ALA edited the manuscript and oversaw the project. At the time of publication VW will be associated with UC Berkeley, WRH and ALA with UC Santa Cruz.

Abstract: Conjugated polyelectrolytes (CPEs) have emerged as attractive building blocks for artificial light-harvesting complexes and as precursors for the formation of membrane-less organelles due to their light weight, solution processability, spectral tunability, and potential for self-assembly. Oppositely charged CPEs have been shown to form stable donor-acceptor complexes in solution, however what drives that formation is not well understood. Here we show that the formation of aqueous exciton transport networks made up of oppositely charged CPEs is an activated process, requiring heat. We find that the need for activation is driven by the strength of hydrophobic and π-π interactions relative to hydrophilic side-chain interactions. For CPEs dominated by the former, complexation kinetics resemble protein-ligand interactions around the protein glass transition while

thermodynamics reveal a switch from an endothermic complexation process at low temperatures to an exothermic process at high temperatures.

4.1 INTRODUCTION

Conjugated polyelectrolytes (CPEs) have recently emerged as materials of interest for the formation of artificial light-harvesting complexes. Much like natural photosynthetic subunits, CPEs are “soft” water soluble materials capable of harvesting energy from a large portion of the solar spectrum and transferring it spatially between donor-acceptor pairs. This makes them attractive materials to act as the primary light-harvesting components in artificial photosynthetic systems. The formation of these systems may be aided by the fact that CPEs can, under specific conditions, form complex coacervates[1-5] – a potentially necessary precursor for the formation of memebraneless organelles. In contrast to the robust theoretical and experimental literature[6-8] devoted to non – conjugated polyelectrolyte (PE) complexation, the mechanisms underlying CPE complexation remain under studied. In standard PEs complexation is dominated by entropy – driven by the release of counterions into solution when oppositely charged sidechains associate with one another. However, the nature of the extended π – network along a CPE backbone all but guarantees that the mechanisms of CPE complexation will differ significantly from those for PE complexation as the backbone π – network introduces strong hydrophobic and π-π interactions which are not present in standard PEs. This can be seen readily by the observation that PE complex formation is amenable to “dump – and – mix” techniques, wherein complexation is guaranteed when oppositely charged PEs are mixed, whereas CPE complex formation is not always amenable to

the same technique. In fact, our prior work has found that CPE complexation is an *activated* process, requiring an input of heat before complexation can occur. The need for a heat input represents a possible avenue to tune and control the CPE formation process, but it cannot be realized without developing an understanding of what causes it to arise in the first place.

In this manuscript we begin addressing the origin and mechanism of the activated network formation process by examining the kinetics and thermodynamics of complexation between a donor CPE and three different acceptor CPEs with varying extents of π-π interactions in their native state. We propose that disrupting these interactions is necessary for complexation to occur and for efficient electronic energy transfer between donor and acceptor to be possible. Acceptors were selected to span a range from strong to weak π-π interactions, largely moderated by the extent to which ionic class between like sidechains precluded intrachain coiling and the formation of close π – stacking arrangements. Kinetics were probed by tracking the increase in donor CPE fluorescence when excited directly over a range of temperatures using steady-state fluorimetry. The kinetics show a distinct two rate process: the “fast” rate we associate with initial complexation and the disruption of the acceptor π-π network, while the “slow” rate we associate with continued evolution of the overall network structure. Upon applying the Arrhenius equation, we find that the acceptor with the most π-π interactions natively has a convex Arrhenius curve with two distinct activation energies, while the other acceptors have

effectively barrierless complexation. Thermodynamics were probed using isothermal titration calorimetry, which is sensitive to the heat change arising from complexation and allows for the determination of the complexation enthalpy, entropy, and Gibbs Free Energy. We find that complexation endo/exothermicity and enthalpic/entropic driving forces are extremely sensitive to the temperature at which the complexes form, likely due to the large changes in hydrobic surface area exposed to water as more π – stacked acceptors are "unraveled". Our results highlight the important role that hydrophobic and π-π interactions play in directing CPE complexation, and the potential use of heat to mediate and control those effects.

4.2 RESULTS AND DISCUSSION

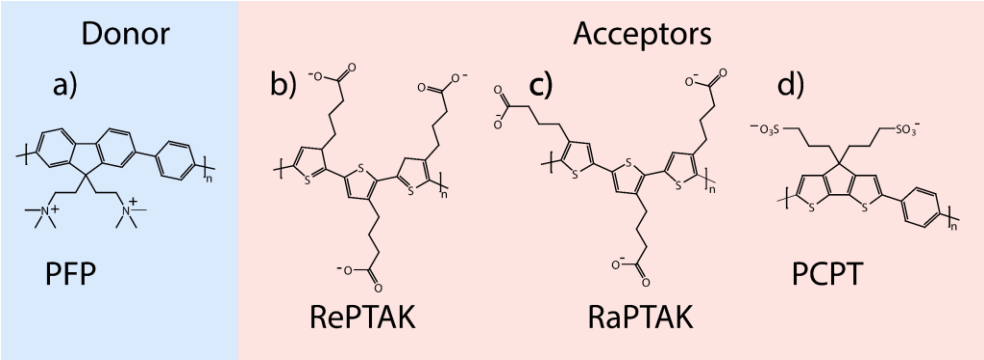

Figure 4.1: Chemical structures of conjugated polyelectrolytes used in this study: Poly([fluorene] -*alt*-co-[phenylene]) (PFP, a), regioregular (RePTAK, b) and regiorandom (RaPTAK c) poly – (butylcarboxythiophene), poly(cyclopentadithieno-alt-phenylene) (PCPT, d).

Our goal in this study was to better understand the fundamental kinetic and thermodynamic forces driving CPEC formation. Our previous work[9-10] on binary systems of PFP and RePTAK found that upon complexation RePTAK transitions from a natively self-coiled, low quantum yield state with traditional photoluminescence

signatures of H-like aggregation, to an extended, high quantum yield state with traditional signatures of J-like aggregation. Notably, PTAK only undergoes this transition when PFP is present and the sample is heated – neither element on its own is sufficient to notably perturb the RePTAK backbone. This stands in contrast to traditional PEC formation where a "dump and mix" approach readily forms complexes, driven largely by the increase in entropy related to counterion release from PE sidechains.[6] To probe the cooperative nature of the PFP-RePTAK-temperature interaction, we studied the kinetics of formation of three different donor:acceptor CPECs – PFP:RePTAK, PFP:RaPTAK, and PFP:PCPT (**Figure 4.1)** – over a range of temperatures in solution. Complexes were prepared at a 70:30 monomolar charge ratio, which our previous work has shown to form stable complexes, with RePTAK completely extended. RaPTAK was chosen with the expectation that regiorandom sidechain orientation would minimize close intrachain π-π interactions owing to mutual electrostatic repulsion of similarly charged sidechains in proximity, and thus inhibit adoption of a self-coiled native state. PCPT was chosen in order to probe the effects of sidechain density on CPEC formation, as it has two anionic sidechains per monomer in comparison to one per monomer for RePTAK and RaPTAK. Absorption and emission spectra for all four CPEs can be found in **Figure AIII.1**. Like RePTAK, both RaPTAK and PCPT show signs of H-like aggregation in their native states ($\frac{I_{0-0}^{Pl}}{I_{0-1}^{Pl}} < 1$)[11-13], suggesting that some π-π interactions are present. However, RaPTAK and PCPT are highly responsive to temperature in

isolation, showing ~ 4X increases in quantum yield when heated to 95 °C as compared to 5 °C (see **Figure AIII.2)**. This indicates that what π-π interactions are present are easily disrupted by increasing temperature, in contrast to RaPTAK which has only weak temperature response. PFP also has a weak temperature response, as it readily adopts an extended J-like conformation in solution due to electrostatic repulsion between sidechains.

Complexation kinetics for all three complexes were probed by following the change in donor and acceptor photoluminescence quantum yield as a function of time, at temperatures between 20 °C and 90 °C. It is possible to follow the changes in donor and acceptor quantum yield separately, as their photoluminescence spectra are well separated energetically. The resulting kinetic spectra are presented

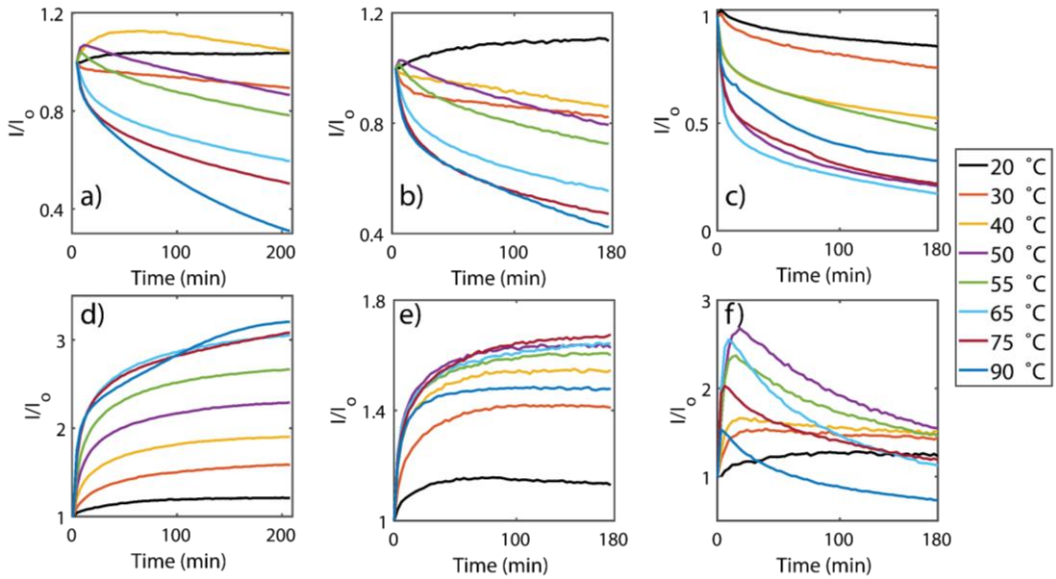

Figure 4.2: Steady-state kinetics for formation of all three CPECs from 20 °C to 90 °C. Kinetics were collected by exciting at the λ_{MAX} of the chosen polymer at 3-minute intervals and integrating the area of the resulting photoluminescence spectrum. TOP: Donor (PFP) kinetics. BOTTOM: Acceptor kinetics. PFP:RePTAK – a, d. PFP:RePTAK – b, e. PFP:PCPT – c, f.

in **Figure 4.2.** Panels a), b), and c) capture the kinetics of PFP in each complex, while panels d), e), and f) capture the kinetics of the donor CPE (RePTAK, RaPTAK, and PCPT – respectively). Because changes in PFP quantum yield due to structural reorganization cannot be separated from changes due to electronic energy transfer (which is expected to dominate), PFP kinetics are a complicated probe of complexation phenomenon we are trying to observe. On the other hand, all three acceptor CPEs can be excited directly, and changes in their photoluminescence quantum yield should directly reflect only their structural reorganization due to complexation. Because of this, while we have presented both donor and acceptor kinetics for completeness, we chose to draw structural inference only from the simpler, structure dominated, acceptor kinetics.

Both RePTAK and RaPTAK have qualitatively comparable kinetics. At a given temperature, both exhibit an initial fast rise in photoluminescence quantum yield, followed by a slower steady rise throughout the duration of the experiment. We attribute the increase in photoluminescence quantum yield to the disruption of *intra*chain π-π interactions as the respective PTAK chains are "uncoiled" and adopt a largely extended linear conformation.[10] This uncoiling leads to a transition from a largely H-like state with a suppressed quantum yield, to a more J-like state with an

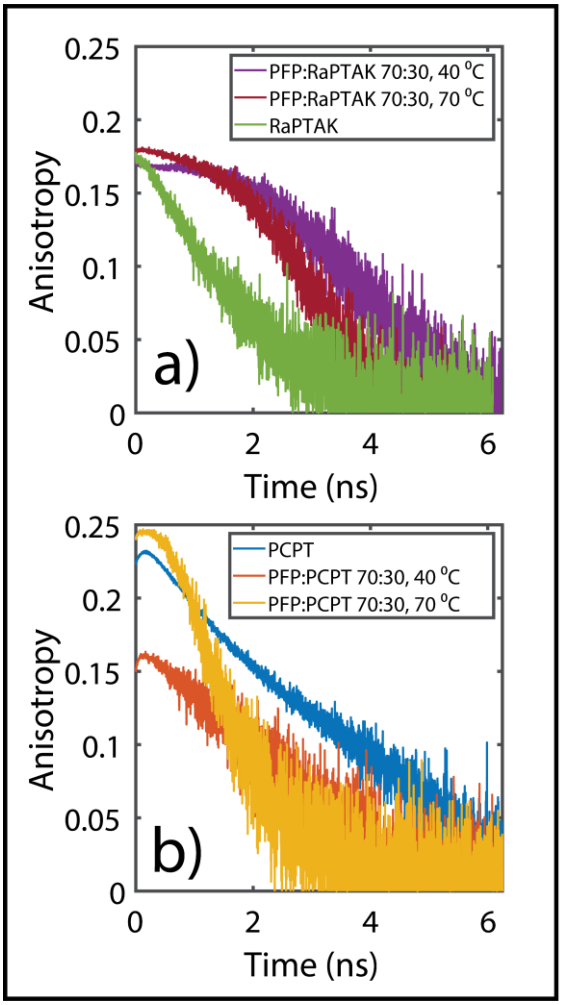

Figure 4.3: Time-resolved photoluminescence anisotropy of RaPTAK (a) and PCPT (b) in isolation and in CPECs prepared at 40 °C and 70 °C. Similar data for PFP:RePTAK CPECs has been published previously.

enhanced quantum yield. The enhancement is not due to electronic energy transfer from PFP, which cannot occur when the acceptors are excited directly. We put forward that the observed fast rise in photoluminescence quantum yield is due to single PTAK chains uncoiling as they complex with and are pulled open by complementary PFP chains. The slow rise may be due to a larger scale macrostructural rearrangement of the overall CPEC network after initial complexation has taken place. It is likely that the energy landscape of the network has many, closely-spaced, thermally accessible local minima which the network probes over time and which leads to continued extension of the PTAK chain. Though they have similarities, RePTAK and RaPTAK differ in their temperature response. RePTAK sees overall photoluminescence quantum yield increase monotonically with temperature, with the sample prepared at 90 °C having the

largest improvement in quantum yield. By contrast, RePTAK, sees a maximum reached monotonically at 75 °C, with a decrease in quantum yield when the sample is prepared at 90 °C. We observe that while the 90 °C sample has the same fast rise as the other samples, it does not appear to have a subsequent slow rise. This may imply that for RePTAK, too high a preparation temperature inhibits the formation of a larger scale network. The PCPT complex kinetics do not follow the same trajectory as the PTAK complexes. While PCPT has an initial fast rise in photoluminescence quantum yield that is indicative of decreased *intra*chain π-π interactions, the subsequent slow component corresponds with a *decrease* in quantum yield. This would suggest that while initial complexation favors the extension of PCPT chains, the formation of the overall network structure causes PCPT chains to collapse back in on themselves. This is consistent across all preparation temperatures except for 20 °C, which sees a modest increase in photoluminescence quantum yield over the timespan investigated.

Our general assessment, that PTAK chains adopt a relatively linear extended conformation when complexed while PCPT adopts a coiled state, is supported by time-resolved photoluminescence anisotropy (TRPLA) shown in **Figure 4.3**. TRPLA tracks the change in anisotropy over time due to depolarization of initially aligned electronic transition dipoles which have been preferentially excited by vertically polarized light.[14] Rapid depolarization due to exciton hopping and localization leads to fundamental anisotropy values (anisotropy at $\tau = 0$) well below the theoretical

value of 0.4 and is not captured in the time window of our experiment. Rather we capture the depolarization subsequent to localization of the exciton. TRPLA of RePTAK (reported previously) and RaPTAK (**Figure 4.3a**) show a clear slowing and eventual flattening of the decay with temperature relative to the native state in which anisotropy tends to decay quickly. This indicative of RePTAK and RaPTAK adopting a highly extended chain microstructure as they complex. PCPT (**Figure 4.3b**) on the other hand shows a significant increase in anisotropic decay rate when complexed at higher temperatures, indicating a highly disordered and self-coiled state.[15-16]

To more quantitatively address the energetic barriers associated with complexation, Arrhenius plots (**Figure 4.4**) were made by fitting the fast and slow RePTAK and RaPTAK kinetics to an empirical double exponential model (see Supporting Information, and **Table AIII.3** for fit parameters). Since the PTAK kinetics largely capture the disruption of *intra*chain π-π interactions and the gradual transition to more extended conformations as complexation progresses, in principle these Arrhenius plots capture the ensemble activation energy needed to disrupt PTAK *intra*chain π stacks. Only when this energy barrier is overcome can Re- or RaPTAK complex effectively with PFP to form long range electronic energy transport networks. The plots reveal two key insights: as expected due to its weaker π-π interactions, RaPTAK has a lower activation energy (effectively zero), as compared to RePTAK. This makes sense given that the regiorandom backbone is expected to

introduce significant coulombic clash between sidechains, precluding tight self-coiling. While steady-state data (see **Figure AIII.2**) suggests RaPTAK adopts an – on average – π-stacked state with signs of H-like aggregation, that state is readily disrupted with or without any thermal input. By contrast, we have seen previously that heating is a necessary, though not sufficient, pre-condition for RePTAK uncoiling and subsequent network formation. This suggests that the relative strength of π-π interactions in the native state of a CPE determines whether it will have barrier to complexation which must be overcome.

The second insight is related to shape of the RePTAK Arrhenius plot. The plot deviates from the expected linear behavior, instead adopting a convex shape. This convexity reveals two distinct regimes, each of which can be fit to extract a relevant activation energy: 71.5 kJ/mol below ~35 °C, 12.3 kJ/mol above ~35 °C. To our knowledge such a shape has not been observed in the polyelectrolyte literature, as complexation is typically presumed to be barrier-less. It has however been observed in the biophysics literature in the context of the so-called protein “glass”

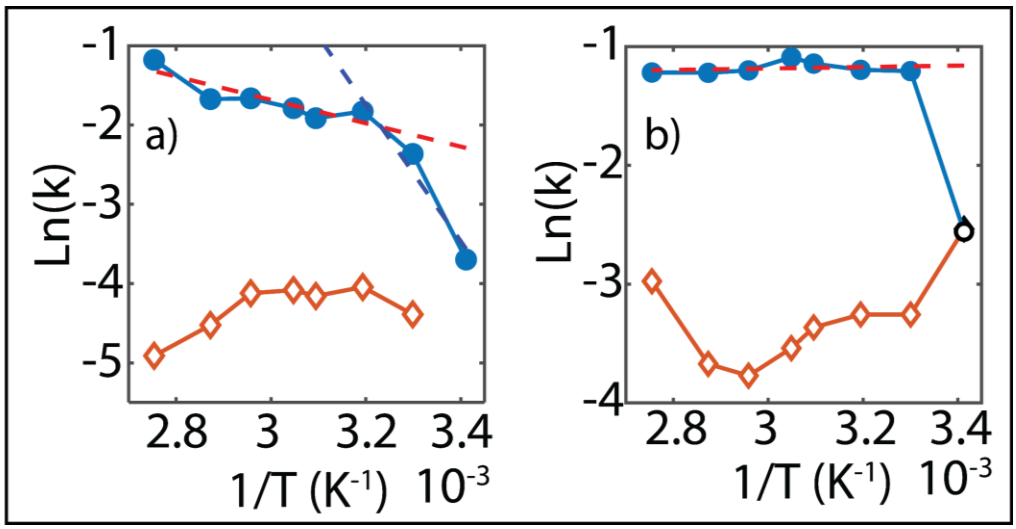

Figure 4.4: Arrhenius plots of PFP:RePTAK (a) and PFP:RaPTAK (b) complexation kinetics. The fast kinetics (blue, closed circles) correlating with PTAK chain uncoiling were fit to the Arrhenius equation to extract activation energies, while the slow kinetics (orange, open diamonds) corresponding to bulk structural reorganization, were not.

transition.[17-20] Here it is known that the catalytic turnover of a protein will decrease with temperature, and that the rate of that decrease accelerates below the protein "glass" transition. The transition does not seem to signify the formation of a true glass. Rather it signifies the loss of allowed collective motion amongst the protein subunits. While vibrational and librational modes of individual bonds within a protein are observed below this temperature, what is not observed is the collective reorientation of interconnected subunits necessary to accept and turnover a binding partner.[19] This transition is typically observed at low temperatures (~ 220 K), it has been observed at higher temperatures for thermophilic proteins with strong hydrogen bonding networks. This similarity between proteins and strongly π-stacking RePTAK suggests that the reason both heat and a complexation partner (PFP) are needed to uncoil RePTAK is because the uncoiling phenomenon requires

the cooperative motion of multiple monomers in tandem. Much the same way that a protein will not spontaneously adopt the conformation is does when turning over a ligand *without* that ligand, so too RePTAK will not spontaneously adopt the extended conformation of a CPEC without an appropriate complexation partner.

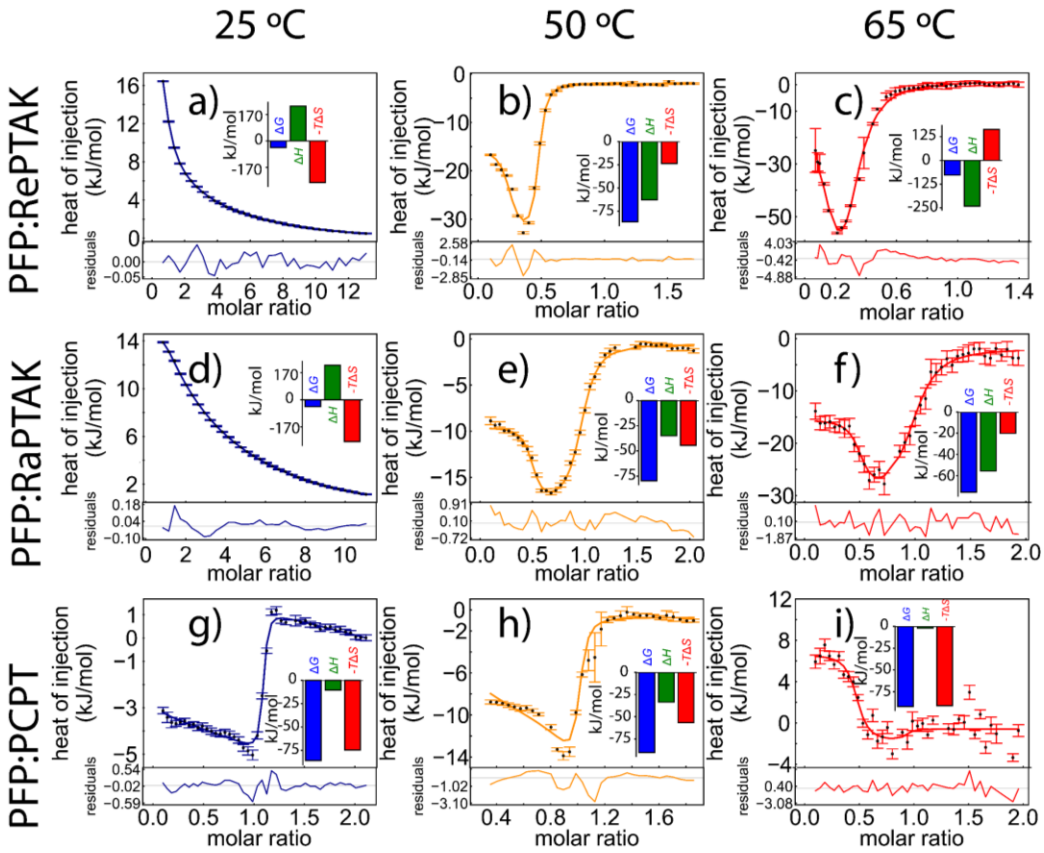

Figure 4.5: Isothermal titration calorimetry data (dots) and fits (solid lines) to a symmetric two-site binding model for three CPEC donor:acceptor complexes formed at three different temperatures. Each row corresponds to a single donor:acceptor pair (Top: PFP:RePTAK, Middle: PFP:RaPTAK, Bottom: PFP: PCPT) while each column corresponds to the temperature the measurement was taken at (from left to right: 25 °C, 50 °C, 65 °C). Insets are net thermodynamic parameters for the formation of a ternary ABB complex with cooperativity taken into account.

In order to better understand the thermodynamic driving forces of the CPEC formation process, we turned to isothermal titration calorimetry (ITC). ITC is more commonly employed by biochemists to determine the binding affinities between ligands and macromolecules, however it has recently been adapted to study the interactions between oppositely charged polyelectrolytes in solution.[3, 6, 21] These studies are notable for showing that polyelectrolyte complexation is largely entropy driven[6], with no enthalpic contribution from electrostatic sidechain pairing, and limited enthalpic contribution due to disruption in the water hydrogen bonding network. In an ITC experiment, microliter aliquots of a ligand (in our case 0.288mM PFP) are injected into a continually stirred solution of a macromolecular binding partner (0.0288mM Re/RaPTAK or PCPT) and the heat required to maintain a constant temperature is recorded as a function of time. This data can then be transformed to give the heat released or absorbed per mole of injectant as a function of molar ratio. The basic thermodynamic parameters (ΔG, ΔH, and ΔS) can be derived from these thermograms. The results of these measurements are show in **Figure 4.5**. All data was fit to a symmetric two-site binding model (see Supporting Information) using the SEDPHAT package, with the general interaction outlined in **Scheme 1**. There are inherent limitations to

$$A + B \overset{k_1}{\longleftrightarrow} AB + B \overset{\alpha k_2}{\longleftrightarrow} ABB$$

Scheme 1: General scheme for the reversible binding of two symmetric ligands. Each binding event has a related association constant, k_i, with the second event having a pre-factor, α, accounting for cooperativity. For our purposes we assume A and B to be the sidechains of the relevant donor CPE and PFP, respectively.

using a model developed to describe small molecule/macromolecule interactions to model complexes of two macromolecules with multiple interacting subunits. It is not immediately clear what constitutes the interacting species, nor is it possible to separate the enthalpic and entropic energies of direct subunit interaction from the energies needed to allow those interactions to occur. For instance, how much of an observed enthalpy change is due to direct subunit interactions and how much is due to the structural reorganization that allowed them to occur? With this is mind, we found the two-site model[22-25] to capture the data well in almost all instances, though simpler and more complex models did not. We assigned A to be the sidechain of the relevant donor CPE and B to be a sidechain of PFP, based on the 1:2 stoichiometric ratio between the PTAK and PFP sidechains. Despite a 1:1 stoichiometric sidechain ratio between PCPT and PFP, the two-site model was employed for these complexes both for consistency across experiments and because the thermograms bear strong qualitative resemblance to the PTAK complexes, however the fits at 25 ºC and 50 ºC are notably worse than their PTAK counterparts. A simpler single site binding model, which might be assumed due to the 1:1 sidechain ratio, produce significantly worse fits. This highlights the need to develop more specific models for these sorts of highly coupled systems, especially as ITC becomes more common in investigating CPE and PE complexes.

Complexes formed with RePTAK (**Figure 4.5 a-c**) and RaPTAK (**Figure 4.5 d-f**) show similar thermodynamic profiles. Insets in each panel show thermodynamic

signatures for the formation of the ABB complex, accounting for possible cooperativity/competition (full thermodynamic parameters for the AB complex, as well as the cooperativity parameters, can be found in **Tables AIII.1** and **AIII.2**). At room temperature complexation is endothermic and is entropically driven. As the temperature is raised, the process becomes exothermic, and is increasingly driven by enthalpy. Complexes formed with PCPT (**Figure 4.5 g-i**) follow the opposite trend, with the process being exothermic at 25 ºC and 50 ºC and endothermic at 65 ºC, though it remains entropically driven at all temperatures. It is notable that even at 25 ºC complexation has a favorable free energy across the series.

A possible explanation for these results can be derived from thermodynamic studies of protein denaturation.[26] Here, changes in enthalpy are related to changes in heat capacity, ΔC_P. In these studies, a positive ΔC_P is characteristic of the hydration of apolar groups, whereas a negative ΔC_P term is characteristic of the hydration of polar groups. For both PTAK complexes, ΔH, and hence ΔC_P, decreases with increasing temperature, whereas for PCPT it is flat. The polar-apolar hydration paradigm is imperfect, but useful. The negative ΔC_P for Re- and RaPTAK would indicate that the negative enthalpy change is driven by the exposure of previously solvent inaccessible sidechains to the bulk solvent as the chain unwinds. However, any such unwinding would also be accompanied by exposure of the highly hydrophobic backbone to water, which should correspond with an *increase* in enthalpy. Added to this, backbone extension also has enthalpically favorable

component as it allows electrons to de-localize over a larger area, lowering their energy. These three terms – sidechain hydration, backbone hydration, and backbone extension – are, alone, insufficient to explain Re- and RaPTAK extension during complexation at elevated temperatures, as neither CPE adopts an extended structure in isolation. Additional favorable enthalpy of complexation must come from PFP, which favors a highly extended conformation in isolation.

In traditional PEC formation the entropy is dominated by the translational entropy of sidechain counterions as they are released into solution upon complexation. The change in configurational and translational entropy of the polyelectrolytes themselves is thought to be a minority component of the overall entropy change. A different landscape emerges in CPEC formation, especially at elevated temperatures. While the favorable entropy of counterion release is maintained at all temperatures, its magnitude decreases when complexes are formed at higher temperatures as the net change in translational entropy is lessened. Moreover, unlike PEs which adopt a relatively linear conformation in solution, the CPEs here are in various states of compaction. The net change in configurational entropy must then be quite large (and favorable) as PTAK transitions from a compacted to extended state. As stated above the extension of the backbone coincides with significant solvent interactions. These interactions are thought to be entropically unfavorable due to the water ordering effects of the backbone – that is, water will self-organize to form a solvent cavity which minimizes solvent-backbone

interactions. It is reasonable to expect that the more hydrophobic the backbone is, the stronger this effect will be. It has been observed in protein denaturation experiments that this effect becomes more pronounced at higher temperatures. Similarly, hydration of the sidechains will lead to a weak ordering effect, which is enthalpically favorable, and becomes less pronounced as temperature increases. With regards to the two PTAK complexes, the relative magnitudes of the enthalpy and entropy changes at 50 ºC and 65 ºC (generally much larger for RePTAK than RaPTAK) may be a function of the initial degree of compaction. For RePTAK, which is tightly coiled, the net change in sidechain- and backbone-solvent interactions as well as in the structural disorder, can be expected to be larger than for RaPTAK, which is much less tightly coiled.

4.3 CONCLUSION

These results allow us to loosely classify CPEs on a continuum scale from protein-like (PL; RePTAK, RaPTAK) to polyelectrolyte-like (PEL; PCPT, PFP), and to correlate their thermodynamics accordingly. At the protein-like end, the coiled native state of a CPE in solution is dominated by π-π interactions, which are considerably stronger than the solvent-sidechain interactions which would otherwise lead to extension. In this state, the thermodynamics of CPEC formation bear strong resemblance to thermal protein denaturation: the enthalpy change is determined by favorable solvent-sidechain interactions relative to unfavorable

solvent-backbone interactions and the entropy is determined by favorable gains in translational entropy of counterions and configurational entropy of the backbone vs unfavorable solvent ordering effects due to backbone-solvent and sidechain-solvent interactions. As π-π interactions become weaker relative to sidechain-solvent interactions, the CPE adopts a looser coil (PCPT) or extended structure (PFP) and becomes more polyelectrolyte-like. This is reflected in complexation which more closely resembles traditional a PEC and is largely driven the increase in translational energy of free counterions in solution. In this paradigm, we expect the initial CPEC formation kinetics to be controlled by the more PL CPE. The barrier to starting complexation involving a very PL CPE will be the disruption of strong π-π interactions, which is expected to involve both thermal activation and the complementary CPE. Assigning control of the secondary kinetics – the slow kinetics of network evolution – is less obvious. One possibility is that is driven by the strength of the electrostatic interactions between the CPEs. The network structure of a CPEC is metastable, and it can be expected that after initial complexation, sidechains may sample multiple partners in their local area, leading to overall network evolution over long time scales. As the strength of the electrostatic interaction is increased (either by introducing multivalent sidechains, or increasing the number of sidechains per monomer), a sidechain will be rigidly locked in place, and will sample fewer local connections. We can expect then, that the structure of a CPEC involving relatively strong electrostatic interactions will be “set” more quickly

than those with weak interactions. The structure may also be larger and less stable with regards to solubility. We have observed that while Re- and RaPTAK complexes will pass through a 450 micron filter, PCPT complexes will not. PCPT complexes are also more prone to precipitation during centrifugation than are PTAK complexes.

With the foregoing, we would suggest some basic principles to guide CPEC formation: 1) As mentioned above, the rate of initial complexation and the trajectory of network formation will be determined by the most PL CPE, with the strength of π-π interactions dominating; 2) Overall network qualities will likely be a function of the strength of electrostatic interactions between the two CPEs; 3) The intermediate regime between PL and PEL is delineated by native CPE temperature response. PL CPEs are expected to be unresponsive to temperature due to the strength of their π-π interactions. Similarly, PEL CPEs will also be unresponsive to temperature because their backbones are already largely extended in solution. We would categorize RaPTAK and PCPT as falling at the PL and PEL ends of this regime, respectively.

REFERENCES

1. Perry, S.; Li, Y.; Priftis, D.; Leon, L.; Tirrell, M., The Effect of Salt on the Complex Coacervation of Vinyl Polyelectrolytes. *Polymers* **2014,** *6* (6), 1756-1772.

2. Chollakup, R.; Beck, J. B.; Dirnberger, K.; Tirrell, M.; Eisenbach, C. D., Polyelectrolyte Molecular Weight and Salt Effects on the Phase Behavior and Coacervation of Aqueous Solutions of Poly(acrylic acid) Sodium Salt and Poly(allylamine) Hydrochloride. *Macromolecules* **2013,** *46* (6), 2376-2390.

3. Priftis, D.; Megley, K.; Laugel, N.; Tirrell, M., Complex coacervation of poly(ethylene-imine)/polypeptide aqueous solutions: thermodynamic and rheological characterization. *J Colloid Interface Sci* **2013,** *398*, 39-50.

4. Priftis, D.; Xia, X.; Margossian, K. O.; Perry, S. L.; Leon, L.; Qin, J.; de Pablo, J. J.; Tirrell, M., Ternary, Tunable Polyelectrolyte Complex Fluids Driven by Complex Coacervation. *Macromolecules* **2014,** *47* (9), 3076-3085.

5. Qin, J.; Priftis, D.; Farina, R.; Perry, S. L.; Leon, L.; Whitmer, J.; Hoffmann, K.; Tirrell, M.; de Pablo, J. J., Interfacial Tension of Polyelectrolyte Complex Coacervate Phases. *ACS Macro Letters* **2014,** *3* (6), 565-568.

6. Fu, J.; Schlenoff, J. B., Driving Forces for Oppositely Charged Polyion Association in Aqueous Solutions: Enthalpic, Entropic, but Not Electrostatic. *J Am Chem Soc* **2016,** *138* (3), 980-90.

7. Markarian, M. Z.; Hariri, H. H.; Reisch, A.; Urban, V. S.; Schlenoff, J. B., A Small-Angle Neutron Scattering Study of the Equilibrium Conformation of Polyelectrolytes in Stoichiometric Saloplastic Polyelectrolyte Complexes. *Macromolecules* **2012,** *45* (2), 1016-1024.

8. Wang, Q.; Schlenoff, J. B., The Polyelectrolyte Complex/Coacervate Continuum. *Macromolecules* **2014,** *47* (9), 3108-3116.

9. Hollingsworth, W. R.; Segura, C.; Balderrama, J.; Lopez, N.; Schleissner, P.; Ayzner, A. L., Exciton Transfer and Emergent Excitonic States in Oppositely-Charged Conjugated Polyelectrolyte Complexes. *The Journal of Physical Chemistry B* **2016,** *120* (31), 7767-7774.

10. Hollingsworth, W. R.; Magnanelli, T. J.; Segura, C.; Young, J. D.; Bragg, A. E.; Ayzner, A. L., Polyion Charge Ratio Determines Transition between Bright and Dark Excitons in Donor/Acceptor-Conjugated Polyelectrolyte Complexes. *The Journal of Physical Chemistry C* **2018,** *122* (39), 22280-22293.

11. Hestand, N. J.; Spano, F. C., Expanded Theory of H- and J-Molecular Aggregates: The Effects of Vibronic Coupling and Intermolecular Charge Transfer. *Chem Rev* **2018,** *118* (15), 7069-7163.

12. Spano, F. C.; Silva, C., H- and J-Aggregate Behavior in Polymeric Semiconductors. *Annual Review of Physical Chemistry* **2014,** *65* (1), 477-500.

13. Yamagata, H.; Spano, F. C., Interplay between intrachain and interchain interactions in semiconducting polymer assemblies: the HJ-aggregate model. *J Chem Phys* **2012,** *136* (18), 184901.

14. Lakowicz, J. R., *Principles of Fluorescence Spectroscopy*. 3 ed.; Springer Science+Business Media, LLC: New York, NY, 2006.

15. Cross, A.; Fleming, G., Analysis of Time-Resolved Fluorescence Anisotropy Decays. *Biophys J.* **1984,** *46*, 11.

16. Muller, J.; Atas, E.; Tan, C.; Schanze, K.; Kleiman, V., The Role of Exciton Hopping and Direct Energy Transfer in Efficient Quenching of Conjugated Polyelectrolytes. *J Am Chem Soc* **2006,** *128*, 9.

17. Doster, W., The protein-solvent glass transition. *Biochim Biophys Acta* **2010,** *1804* (1), 3-14.

18. Jansson, H.; Swenson, J., The protein glass transition as measured by dielectric spectroscopy and differential scanning calorimetry. *Biochim Biophys Acta* **2010,** *1804* (1), 20-6.

19. Ringe, D.; Petsko, G. A., The 'glass transition' in protein dynamics: what it is, why it occurs, and how to exploit it. *Biophysical Chemistry* **2003,** *105* (2-3), 667-680.

20. Zhang, Y.; Batys, P.; O'Neal, J. T.; Li, F.; Sammalkorpi, M.; Lutkenhaus, J. L., Molecular Origin of the Glass Transition in Polyelectrolyte Assemblies. *ACS Cent Sci* **2018,** *4* (5), 638-644.

21. Vitorazi, L.; Ould-Moussa, N.; Sekar, S.; Fresnais, J.; Loh, W.; Chapel, J. P.; Berret, J. F., Evidence of a two-step process and pathway dependency in the thermodynamics of poly(diallyldimethylammonium chloride)/poly(sodium acrylate) complexation. *Soft Matter* **2014,** *10* (47), 9496-505.

22. Brautigam, C. A., Fitting two- and three-site binding models to isothermal titration calorimetric data. *Methods* **2015,** *76*, 124-136.

23. Brown, A., Analysis of cooperativity by isothermal titration calorimetry. *Int J Mol Sci* **2009,** *10* (8), 3457-77.

24. Herrera, I.; Winnik, M. A., Differential binding models for isothermal titration calorimetry: moving beyond the Wiseman isotherm. *J Phys Chem B* **2013,** *117* (29), 8659-72.

25. Vega, S.; Abian, O.; Velazquez-Campoy, A., A unified framework based on the binding polynomial for characterizing biological systems by isothermal titration calorimetry. *Methods* **2015,** *76*, 99-115.

26. Prabhu, N. V.; Sharp, K. A., Heat capacity in proteins. *Annu Rev Phys Chem* **2005,** *56*, 521-48.

Chapter 5

Exciton Relaxation in Highly Rigid Conjugated Polymers: Correlating Radiative Dynamics with Structural Heterogeneity and Wavefunction Delocalization

Acknowledgements: This chapter was original published in ACS Energy Letters with the following authorship: William R. Hollingsworth, Jongbok Lee, Lei Fang, Alexander L. Ayzner. WRH prepared all samples and carried out all spectroscopy and analysis thereof. JL synthesized LP1 and CP1. WRH wrote the manuscript. LF and ALA edited the manuscript and oversaw the project. JL and LF were affiliated with Texas A&M University at the time of publication. WRH and ALA were affiliated with UC Santa Cruz at the time of publication.

Abstract: Conjugated polymers are promising materials for solar cells and other electronic applications due to facile charge and electronic energy migration along the conjugated backbone. Torsional defects due to rotation around single bonds on the backbone are known to decrease the effective conjugation length of these materials, limiting their ability to shuttle charge and electronic energy. We investigated the radiative emission dynamics of a recently synthesized rigid conjugated ladder polymer (LP1) and non-rigid control (CP1), with a similar carbazole backbone moiety.. LP1 was prepared using a recently reported synthesis under thermodynamic control, leading to a low backbone defect density. We find the singlet emission lifetime of LP1 is longer than any previously reported ladder conjugated polymer, which we attribute to its low defect density. Further, the emission contains a large-amplitude long component with a lifetime that lasts as long as 5 ns. Our results imply that careful control of defects at the synthesis level can lead to processable polymers with large electronic wavefunction delocalization and correspondingly long fluorescence lifetimes. This indicates an avenue to further tune the rapid solid-state energy transport rate along the polymer backbone.

5.1 INTRODUCTION

Conjugated polymers (CPs) have been the subject of intense research over the last few decades owing to the strong coupling between their chain microstructure and their optoelectronic properties. The delocalization of electronic states along the backbone due to extensive π-conjugation results in large extinction coefficients, making these materials highly attractive for solar cell applications. Their fluorescence is very sensitive to the conformation of the polymer chain, thus allowing them to act as sensors.[1-3] Furthermore, electronic delocalization leads to facile charge and electronic energy migration along the chain, provided that the chain is relatively straight, as torsional defects are known to limit the effective delocalization length and thus act as traps and scattering centers.[4-5] Indeed, CPs polymerized in a solid matrix have been shown to exhibit macroscopic exciton coherence over the polymer backbone when the chain length becomes extremely large.[6-7] In order to take the intrinsic advantages of solution processability of polymer materials to serve as active components in optoelectronic devices, however, their backbones are often designed to possess torsional flexibility. Unfortunately, these torsional motions meanwhile shorten the effective conjugation length of CPs, limiting both the charge mobility and exciton delocalization.[8]

We have recently reported the synthesis of a new, highly rigid ladder-type CP, which is amenable to facile processing despite the rigid coplanar backbone and low level of constitutional defects.[9] Ring-closing olefin metathesis was employed under thermodynamic control to facilitate the construction of the fused-ring ladder-type backbone, leading to minimal unreacted defects and thus allowing us to investigate the intrinsic photophysical

properties of this type of coplanar conjugated ladder polymer. Such a rigid backbone results in strongly delocalized electronic states and thereby the potential for rapid intra-chain migration of electronic excited states – a property that is extremely important for artificial light harvesting antenna applications. Moreover, recent work has shown that electronic quantum coherence may play a role in enhancing energy transfer along a single polymer chain in solution.[10] To this end, ladder-type CPs, in which the entire backbone of the polymer is made up of fused conjugated rings, are attractive due to their inherently low torsional disorder; thus, such CPs possess significant potential to function as efficient energy relays[10-11]. In this manuscript, we use steady-state and time-resolved photoluminescence spectroscopy to interrogate the nature and dynamics of electronic excited states of this new ladder polymer.

We find that both the steady-state photophysics and the radiative relaxation rates exhibited by the two polymers differ substantially. First, the fluorescence spectral width of the ladder polymer is approximately a factor of two smaller than that of the control polymer, indicating that the ladder polymer gives rise to a significantly smaller structural heterogeneity, which is consistent with its highly extended nature. As the linewidths maintain this ratio across a temperature range of 263-323 K, it is unlikely that their relative sizes are due to thermal effects. Second, the long-lived fluorescence of the ladder polymer is comparable to that of common laser dyes, whereas the control polymer shows much faster dynamics, presumably due to a higher density of torsional defects. The average fluorescence lifetime is significantly longer than the singlet emission lifetimes of previously characterized ladder polymers such as MeLPPP, and the long-lifetime component is significantly larger

than the recently synthesized Me-LPyP, which to date has had the longest lifetime of any known ladder polymer.[12-14] We further find a coexistence of H- and J-like exciton states in solution, with the preponderance of emission arising from the un-aggregated J-like states. Finally, in the solid state, the ladder polymer fluorescence is almost completely quenched, owing to the efficient inter-chain interactions between highly planar backbone regions. This stands in contrast to the control, which exists as a largely disordered coil and hence possesses relatively inefficient π-stacking and thus a larger fluorescence quantum yield in the solid state. We close by discussing the promise of this novel ladder motif for both energy transfer and charge transport applications.

Taking advantage of the intimate link between backbone structure of conjugated polymers and their photophysics, we have used photoluminescence (PL) spectroscopy to probe electronic delocalization and singlet exciton dynamics in a recently synthesized rigid conjugated polymer, **LP1**. The chemical structure of **LP1** is shown **Figure 5.1b**. We expect that fused benzene rings will lead to enhanced excitonic delocalization relative to a similar polymer with a larger number of readily accessible torsional degrees of freedom. To place in context the changes in exciton behavior that accompany formation of a highly rigid backbone, we have compared the optical properties of **LP1** to that of **CP1**, whose structure is shown in **Figure 5.1a**. The carbazole-based conjugated polymer **CP1** has similar repeating units as **LP1**, but the lack of additional ring closure is expected to lead to greater chain flexibility compared to **LP1**.

5.2 RESULTS AND DISCUSSION

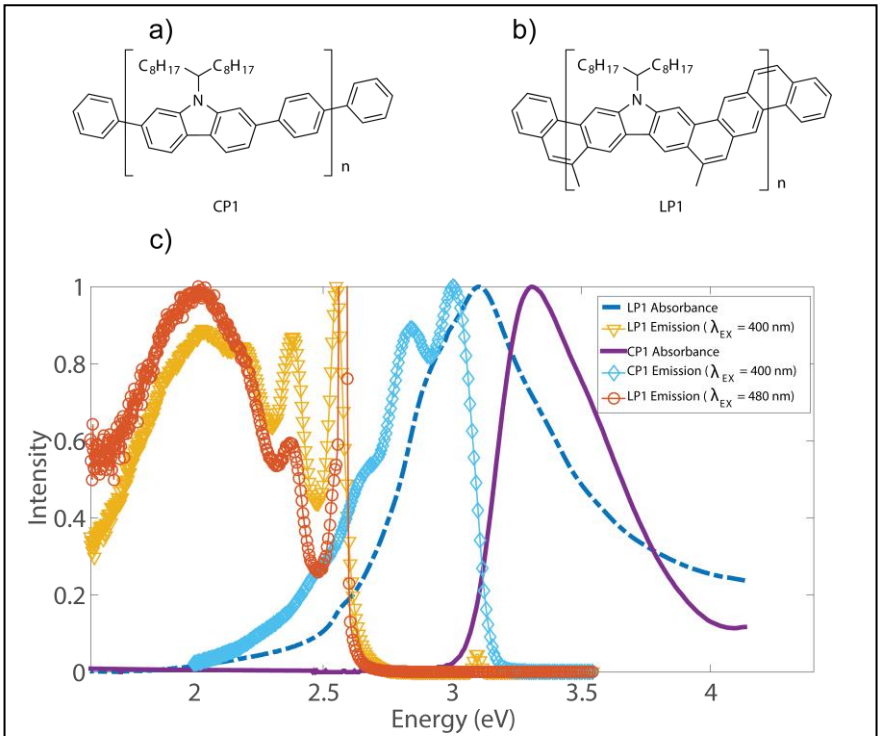

Figure 5.1. a) Chemical structure of CP1, and b) LP1. c) Normalized absorbance and photoluminescence spectra of dilute (0.01 mg/mL) solutions of CP1 and LP1 in chloroform. Spectra have been normalized to their highest intensity peaks.

Although the room-temperature steady-state absorption and PL of **LP1** have been reported previously[9], it is instructive to compare the photophysics of both polymers. **Figure 5.1c** shows the steady-state room-temperature absorption and photoluminescence spectra of **LP1** and **CP1** in $CHCl_3$. **CP1** absorption is relatively featureless, with an absorption maximum (λ_{max}) at 3.32 eV and a slight shoulder evident at approximately 3.54 eV. Emission is shown due to excitation (λ_{EX}) at 3.10 eV, corresponding to the peak of LP1 absorption and the lowest excitation wavelength used for time resolved measurements. At this wavelength, a vibronic progression and a Stokes shift of 0.45 eV are clearly visible. **LP1** shows noticeable shoulders corresponding to a vibronic progression in its absorption spectrum, in addition to

well-separated vibronic peaks in its PL spectrum, and along with a large red-shift in absorption (0.21 eV) and PL (0.45 eV) relative to **CP1**.

Additionally, there are two notable features displayed in **Figure 5.1c**. First, if we associate the small peak near the absorption onset of **LP1** (2.56 eV) with the true 0-0 vibronic transition of the low-energy singlet, the Stokes shift for **LP1** is only ~0.01 eV, which is consistent with other conjugated ladder polymers[15-18] and with a generally rigid structure. The low oscillator strength of the 0-0 absorption is possibly related to the formation of strongly coupled H-like aggregates in solution, which have been proposed to shift oscillator strength from the 0-0 transition into higher lying transitions. However, previous theoretical calculations at the time-dependent density functional level of theory of the **LP1** monomer electronic structure have made a strong argument that the low-lying transitions have relatively low oscillator strength due to the symmetry of the involved wavefunctions. It is likely that these considerations extend to the polymer, thus partially explaining the low 0-0 absorption. Thus, the spectrum shape reflects both the monomer electronic structure and the perturbation to it due to the excitonic coupling; this fact makes it challenging to disentangle the relative spectral contributions. That the PL in the steady-state limit at this concentration does not show a diminution of the 0-0 peak suggests that the lowest-energy emissive states are largely un-aggregated, intrachain excitons characterized by an increased 0-0/0-1 peak ratio relative to that seen in the absorption spectrum[18-19].

The second notable feature is the significant broadening of the **LP1** PL spectrum beyond the 0-1 transition. While the 0-0 and 0-1 transitions are well resolved and are of comparable widths, the subsequent transitions – to the extent that they can be

distinguished – appear to be broad and overlapping. As excitation at longer wavelengths is probed (λ_{EX} = 480 nm; 2.58 eV), this broad feature grows in intensity relative to the sharp lower-energy features. This PL behavior of **LP1** differs qualitatively from **CP1**, which retains a well-defined vibronic progression across the entire emission spectrum, with no indication of a broad emission feature at redder emission wavelengths. We interpret the shape of the **LP1** spectrum as arising due to a coexistence of excitonic states that are either primarily delocalized over a single polymer chain or over multiple chromophores[18]. Owing to the relatively low solution concentration, we might expect that the latter are caused by interaction between multiple segments on the same polymer chain[20-23].

To help further investigate the nature of emissive **LP1** states in solution, we collected PL spectra of both **LP1** and **CP1** as a function of temperature over the 263-323 K range and as a function of concentration. We note that mild sonication was necessary to access the highest nominal **LP1** concentration shown below. **Figure 5.2** shows PL at 293 K as a function of polymer concentration. Both **CP1** and **LP1** show more H-like emissive states at the highest polymer concentrations, as evidenced by the diminution of the 0-0 peak

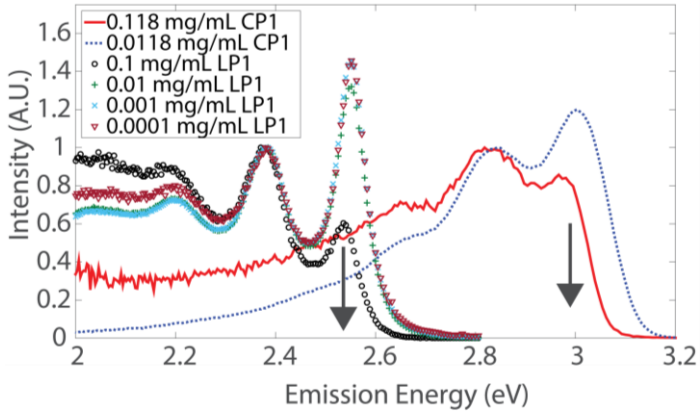

Figure 5.2: Photoluminescence spectra at 293 K of **LP1** and **CP1** as a function of concentration. The spectra are normalized to the 0-1 peak. As concentration increases, the 0-0 emission peak of both polymers diminishes, implying a change to more H-like aggregates in the emissive population.

and the 0-0/0-1 intensity ratio, $S_R = \frac{I_{0-0}^{PL}}{I_{0-1}^{PL}}$, which drops below 1 at high concentration.

To better characterize this transition, we attempted to analyze the temperature dependence of S_R for the three highest **LP1** and **CP1** concentrations within the framework of the HJ-aggregate model due to Spano and Yamagata.[23-25] In the thermodynamic (high temperature) limit, the vibronic ratio is determined by an interplay between the intrachain coupling that favors J-aggregate-like states, and the interchain coupling, which favors H-aggregate-like states. Within this model, the vibronic ratio is given by

$$S_R = \frac{1}{\lambda_0^2}\frac{2e^{-2FJ_{inter}/k_bT}}{1+e^{-2FJ_{inter}/k_bT}}\sqrt{\frac{4\pi F|J_{intra}|}{k_bT}} \quad (1)$$

F is the Franck-Condon factor, λ_0^2 is the Huang-Rhys factor, J_{inter} and J_{intra} are the respective *inter*- and *intra*- chain coupling strengths in cm^{-1} and k_b is Boltzman's constant. The full results of this fitting are presented in **Table 6**. For the highest concentration samples of **CP1** and **LP1**, $|J_{inter}| > |J_{intra}|$, consistent with the formation of predominantly H-like emissive states. At lower concentrations, the situation is the opposite, consistent with more J-like emissive states. Thus, at low concentrations of **LP1**, it appears that while the ensemble absorption spectrum reflects significant H-like aggregation, excitons can clearly migrate to un-aggregated, largely J-like, states from which emission originates. Furthermore, we find that $|J_{intra}|$ is substantially larger for LP1 relative to CP1 (as is $|J_{inter}|$ at the highest concentration), further underscoring the increased strength of the inter-monomer interactions that, on average, tend to keep the LP1 backbone substantially more planar than CP1. This leads to a greater extent of excitonic wavefunction delocalization, which is further supported by time-resolved measurements described below. Although the multi-parameter

fits outlined in the Supporting Information are expectedly quite sensitive to fitting constraints, we believe that we have qualitatively captured trend between the two polymers.

Having established the nature of the primary excitations that give rise to observed emission behavior, we can then compare the temperature dependence of the peak full width at half-max (σ) of the 0-0 transitions for both **CP1** and **LP1**, with the hope of gaining insight into the relative microstructural heterogeneity of the CPs. We find that $<\sigma_{LP1}>$ = 0.050 ± 0.002 eV and $<\sigma_{CP1}>$ = 0.080 ± 0.002eV in the temperature range from 273-323 K for 0.01 mg/mL **LP1** an 0.0118 mg/mL **CP1**. We note that both peaks broaden with increasing temperature by 6.25% and 7.8%, respectively (see **Table AIV.5**). It is understood that the backbones of excitedstate conjugated polymers undergo rapid (~ <10 ps) planarization, and that fluorescence is presumed to originate from these relatively planar, low-energy regions.[26-29] That we observe a relatively weak temperature dependence suggests that, within this regime, the peak width is dominated by the distribution of polymer chromophore lengths. As such, the data indicate that **LP1** has less structural disorder in its emissive states than **CP1**, as the difference in linewidth primarily arises from broadening of the conformational density of states.[30]

Across the concentration range we observe a modest blue-shift of the 0-0 peak of **LP1** of with increasing temperature. For the three lowest concentrations the average shift is 8.3×10^{-5} eV/K, while for 0.1 mg/mL **LP1** it is 1.7×10^{-4} eV/K. A similar magnitude blue shift has been observed in thin films of MeLPPP.[31-32] This blue-shift at higher temperatures has been attributed to a decrease in available low-energy exciton states, which tend to serve as

exciton sinks. **CP1** shows different behavior, with low concentration **CP1** having no observable shift within our limits of detection, and with high concentration **CP1** displaying a red shift of 1.2×10^{-4} eV/K. This last finding stands in contrast to behavior observed in other conjugated polymers and large oligomers, where a blue-shift is also expected.[33-34] Although we do not yet fully understand the difference in the high-concentration temperature-dependent peak shifts between the two CPs, the difference in the low-concentration behavior can be rationalized on the basis of the polymers' average single-chain conjugated lengths. Since at these concentrations, minimal inter-polymer coil interactions are expected, it is plausible that the lack of a temperature-dependent blue-shift in **CP1** and its observation in **LP1** are further evidence for enhanced intra-coil interactions in the native **LP1** chain due to the enhanced backbone planarity.

To gain a more thorough understanding of **LP1** and **CP1** emission, **Figure 5.3** shows steady-state 2D PL maps of **LP1** and **CP1** in dilute solution, which display emission spectra collected at a series of excitation wavelengths. We have marked each polymer's PL map to show the excitation/emission pairs used for time-resolved PL measurements below. In general, points were chosen to correspond to the 0-0 and 0-1 transitions of **LP1** (λ_{EM} = 485 nm (2.56 eV) and 520 nm (2.38 eV), respectively) arising from excitation at the first three absorption peaks (λ_{EX} = 480 nm (2.58 eV), 450 nm (2.76 eV), and 400 nm (3.10 eV), respectively). Additionally, λ_{EM} = 565 nm (2.19 eV) was probed in order to gain insight into the broad feature on the red side of the **LP1** emission. For reference, the same points were probed for **CP1**, as well as the λ_{EX} = 400 nm (3.10 eV) / λ_{EM} = 435 nm (2.85 eV) point, which

lies in the spectral vicinity of the **CP1** absorption onset. PL decays of **CP1** collected using this wavelength pair should be compared to the corresponding red-edge excitation point in **LP1**

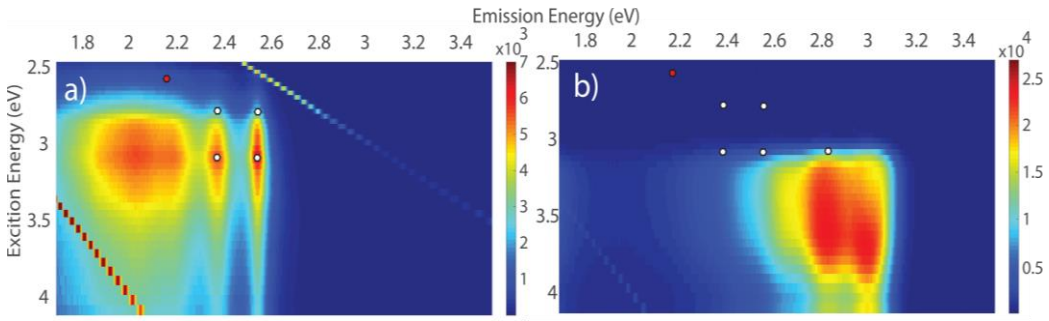

Figure 5.3. 2D steady-state PL maps of 0.01 mg/mL **LP1** (left) and 0.0118 mg/mL **CP1** (right), which compile PL spectra as a function of excitation wavelength. Diagonal lines across the **LP1** spectrum are due to first and second order reflections of the excitation source. Black and white hexagons mark excitation-emission combinations which were used for time-correlated single photon counting measurements. Vibronic progression is present or both samples, though it is significantly better resolved in **LP1** due to its substantially narrower PL linewidth. A faint, broad feature is present in the **LP1** spectrum centered on the upper-rightmost hexagon. No such feature is present in **CP1**. The excitation and emission wavelengths used for **Figure 5.4** have been highlighted in red. Note the differences in scale: The peak of LP1 photoluminescence is approximately an order of magnitude lower than that of CP1.

at λ_{EX} = 480 nm (2.58 eV). Because our laser excitation wavelength is limited to 400 nm (3.1 eV) and above, we were unable to measure **CP1** emission decays at its λ_{max}.

Representative PL decay traces and fits for **CP1** and **LP1** at their second highest concentrations are shown in **Figure 5.4**, with decay times and parameters for all fits summarized in **Tables 5.1** and **5.2**, respectively. The chosen excitation and emission wavelengths reflect similar regions of the absorption and PL spectrum of each compound – both corresponding to the red edge near the absorption onset. Excitation in this region interrogates **CP1** excitons with the longest delocalization lengths, making them more comparable to **LP1**. Generally, we found that **CP1** and **LP1** were well-fit (χ^2_{CP1} = 0.956, χ^2_{LP1} = 0.993) by a bi-exponential decay model (see Supporting Information).

The stark observation is that compared to **CP1**, **LP1** has much longer decay components ($\tau_{1,\,LP1}$ = 1.14 ns vs. $\tau_{1,\,CP1}$ = 0.47 ns and $\tau_{2,\,LP1}$ = 4.91 ns vs. $\tau_{2,\,CP1}$ =2.24 ns – where τ_1 and τ_2 are the short and long decay lifetimes, respectively.), with a greater part of the PL attributable to the long decay component in **LP1** ($\alpha_{2,\,LP1}$ = 0.207 vs $\alpha_{2,\,CP1}$ = 0.007). We interpret these differences as arising due to the substantial difference in the backbone rigidity of each polymer. The long-time component of **LP1** is likely due to excitons largely delocalized along a single polymer chain, states which have been shown previously to have large PL quantum yields.[35] Thus, excited states are rapidly delocalized through the backbone π-electron network due to a long effective conjugation length, while minimizing the likelihood of encountering trap states possibly arising from torsional defects. That a larger portion of the decay is attributable to the long lifetime component in **LP1** as compared to **CP1** is likely due to the loss of torsional defects and a larger intrachain coupling in **LP1**.

Interestingly, when exciting deep in the red tail of **CP1** absorption where extinction coefficients become negligible (λ_{EX} > 400 nm (3.1 eV)), there is a small population of **CP1** chains that have long decay components that are comparable to **LP1**. Given that the number density of such emissive states is very low, such states are likely not statistically significant when considering the average exciton migration behavior of **CP1**. It is also worth noting the possibility that the long lifetimes of **LP1** are being depressed by the formation of aggregates, as the steady-state spectra show a coexistence of single-chain and inter-chain states. States delocalized over multiple chains or multiple segments of the same chain are H-aggregate-like excitons that can function as exciton sinks for intra-chain excitons; such inter-chain states are characterized by small PL quantum yields[35]. This would result in a nominal

lowering of the observed **LP1** radiative lifetime, potentially suggesting that pure intra-chain **LP1** excitons likely have even longer lifetimes. However, analysis of our highest concentration **LP1** and **CP1** (see **Tables AIV.1** and **AIV.3**, respectively) showed no significant lifetime shortening, despite clear evidence that the emissive states of the polymers have adopted a more H-like conformation. It is possible that the emissive chains at these concentrations are only weakly H-like (a reasonable conclusion given that the 0-0 PL peaks are diminished, but not totally absent) and thus their lifetimes are only weakly affected. Lifetime measurements of more dilute solutions of LP1 (below 0.01 mg/mL) were inconclusive, as the low PL intensity did not allow for the collection of decays with sufficient signal for analysis. That the lifetime of the long component does not change significantly at higher concentration, even after a clear increase in the concentration of H-like states,

suggests that it is an inherent molecular backbone property and not simply a chromophore aggregation effect.

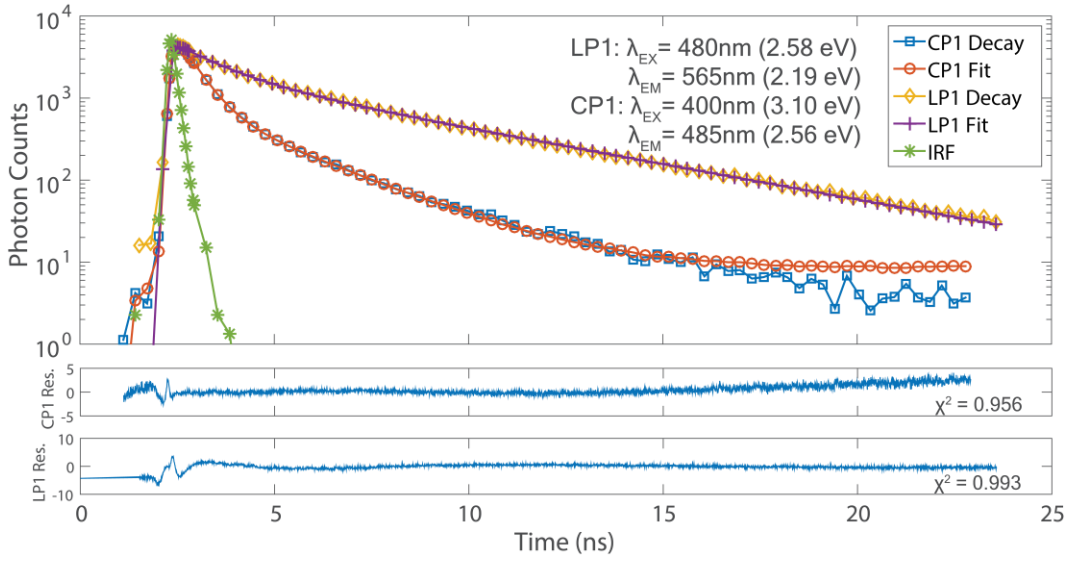

Figure 5.4. Time-resolved PL decay traces of 0.01 mg/mL LP1 and 0.0118 mg/mL CP1. Excitation for both was at the red edge of their respective absorption spectra. Included is the instrument response function (IRF), which determines the absolute time resolution of the fit and is representative of all of the IRFs for the measurements. The data has been down-sampled for legibility.

At the concentrations presented here, both compounds exhibit longer lifetimes and a larger weighting toward the long lifetime component when measuring emission at longer wavelengths while keeping the excitation wavelength constant. In accord with the dispersive transport model[4], this shift is expected, as longer emissive wavelengths correspond to lower-energy excitons, which have a limited population of sites to which they can migrate. While the lifetime of the longest component increases with increasing excitation wavelength for **CP1** (likely due to probing the small populations of progressively straighter **CP1** chains), it remains approximately fixed for **LP1** ($\tau_{2,AVG}$ = 4.953 ns ± 0.049 ns).

However, we do not observe a comparable trend for the shorter lifetime component. For both **CP1** and **LP1**, the lifetime of the shorter component lengthens with increasing excitation wavelength. One potential reason for this could be that the polymer chains comprising the red edge of the absorption spectrum are less closely aggregated than those excited close to λ_{max} and so have fewer inter-chain states in spatial proximity to quench fluorescence. That is, this relatively narrow distribution of chromophores with exciton energies close to the bandgap is characterized by a smaller interchain excitonic coupling. While the life-time of **CP1** at λ_{EX} = 400 nm (3.1 eV) is consistent with other similar polycarbazoles [36], both the average and the shortest life-time components of **LP1** are longer than those exhibited by other known ladder polymers including MeLPPP, as well rigid non-ladder poly-carbazoles[12-13, 36]. In the thin film state, highly delocalized electronic states of LP1 characterized by these relatively long fluorescence lifetimes lead to very efficient inter-chain interactions, resulting in very low fluorescence quantum yields even when deposited from high-vapor pressure solvents. This is in contrast to CP1, which continues to emit relatively strongly (see Supporting Information).

We note that the lifetimes presented here are potentially lower bounds of the true **LP1** lifetime. As mentioned above, solutions of **LP1** were sonicated to reach the largest concentrations explored herein. This process can introduce defects into the polymer backbone, which may partially quench emission.[37] Indeed, lifetimes of non-sonicated **LP1** at λ_{EX} = 400 nm (3.1 eV)/ λ_{EM} = 485 nm (2.56 eV) are presented in **Table AIV.4**, which shows that the average fluorescence lifetimes increases to 4.62 ns, with the long component (5.51 ns) fraction increasing to 0.451. Both the average lifetime and longest component are

longer lived than the recently synthesized Me-LPyP, which to date is the ladder polymer with the longest fluorescence lifetime.[14]

Table 5.1. Decay lifetimes and amplitudes for a dilute solution of 0.0118 mg/mL **CP1**.

λ_{EX}	λ_{EM}	α_1	τ_1 (ns)	α_2	τ_2 (ns)	<τ> (ns)	χ^{2*}
400 nm (3.10 eV)	435 nm (2.85 eV)	1.000	0.49	---	---	0.49	0.857
	485 nm (2.56 eV)	0.993	0.47	0.007	2.24	0.53	0.956
	520 nm (2.38 eV)	0.958	0.52	0.042	2.42	0.84	0.957
450 nm (2.76 eV)	485 nm (2.56 eV)	0.768	1.14	0.232	5.06	3.39	1.001
	520 nm (2.38 eV)	0.760	1.34	0.240	5.29	3.53	0.992
480 nm (2.58 eV)	565 nm (2.19 eV)	0.857	1.87	0.143	6.94	3.80	0.993

*Residuals can be found in **Figure AIV.2**.

Table 5.2. Decay lifetimes and amplitudes for a dilute solution of 0.01 mg/mL **LP1**.

λ_{EX}	λ_{EM}	α_1	τ_1 (ns)	α_2	τ_2 (ns)	<τ>(ns)	χ2*
400nm (3.10 eV)	485 nm (2.56 eV)	0.906	0.65	0.094	4.91	2.52	0.985
	520 nm (2.38 eV)	0.759	0.70	0.241	4.97	3.66	1.207

450nm (2.76 eV)	485 nm (2.56 eV)	0.834	0.68	0.166	4.95	3.20	1.017
	520 nm (2.38 eV)	0.771	0.84	0.229	5.03	3.51	1.015
480nm (2.58 eV)	565 nm (2.19 eV)	0.793	1.14	0.207	4.91	3.14	0.993

*Residuals can be found in **Figure AIV.2**.

5.3 CONCLUSIONS

To conclude, we have found that PL lifetimes of our new ladder polymer are consistently longer than those of its non-rigid control polymer in solution. To the best of our knowledge, solution lifetimes of **LP1** are longer than any ladder polymer synthesized to date. This is consistent with the rigid nature of the **LP1** backbone, which substantially lowers the density of torsional defects, thus allowing for efficient exciton migration through a long effective conjugation length. At the same time, this backbone rigidity corresponds with an increased tendency to form H-like aggregated states in the solid state, which decrease the quantum yield of the polymer relative to **CP1**. While this decrease is only mild in solution, it is drastic in thin films, leading to nearly total PL quenching (see **Section S6** in **Appendix IV**). **CP1** itself has relatively little spectral or intensity change from solution to thin film due to its substantially diminished propensity to form inter-chain states. Our results indicate that the highly delocalized states of the solution-processable **LP1** hold promise for rapid excitonic delocalization and energy transfer. This is attractive for light-harvesting applications, where exciton mobilities are direct functions of the electronic wavefunction delocalization extent.

REFERENCES

(1) Rochat, S.; Swager, T. M. Conjugated Amplifying Polymers for Optical Sensing Applications. *ACS Appl. Mater. Interfaces.* **2013,** *5*, 4488-502.

(2) Satrijo, A.; Swager, T. M. Anthyrl-Doped Conjugated Polyelectrolytes as Aggregation-Based Sensors for Nonquenching Multicationic Analytes. *J. Am. Chem. Soc.* **2007,** *129*, 16020-16028.

(3) Thomas, S. W. I.; Joly, G. D.; Swager, T. M. Chemical Sensors Based on Amplifying Fluorescent Conjugated Polymers. *Chem. Rev.* **2007,** *107*, 1339-1386.

(4) Meskers, S. C. J.; Hubner, J.; Oestreich, M.; Bassler, H. Dispersive Relaxation Dynamics of Photoexcitations in a Polyfluorene Film Involving Energy Transfer: Experiment and Monte Carlo Simulations. *J. Phys. Chem. B.* **2001,** *105*, 9139-9149.

(5) Hwang, I.; Scholes, G. D. Electronic Energy Transfer and Quantum-Coherence in π-Conjugated Polymers†. *Chemistry of Materials* **2011,** *23*, 610-620.

(6) Dubin, F.; Melet, R.; Barisien, T.; Grousson, R.; Legrand, L.; Schott, M.; Voliotis, V. Macroscopic Coherence of a Single Exciton State in an Organic Quantum Wire. *Nat. Phys.* **2006,** *2*, 32-35.

(7) Guillet, T.; Berréhar, J.; Grousson, R.; Kovensky, J.; Lapersonne-Meyer, C.; Schott, M.; Voliotis, V. Emission of a Single Conjugated Polymer Chain Isolated in Its Single Crystal Monomer Matrix. *Phys. Rev. Lett.* **2001,** *87*, 087401.

(8) Zahn, S.; Swager, T. M. Three-Dimensional Electronic Delocalization in Chiral Conjuagted Polymers. *Angew. Chem. Int. Ed.* **2002,** *41*, 6.

(9) Lee, J.; Rajeeva, B. B.; Yuan, T.; Guo, Z.-H.; Lin, Y.-H.; Al-Hashimi, M.; Zheng, Y.; Fang, L. Thermodynamic Synthesis of Solution Processable Ladder Polymers. *Chem. Sci.* **2016,** *7*, 881-889.

(10) Collini, E.; Scholes, G. D. Coherent Intrachain Energy Migration in a Conjugated Polymer at Room Temperature. *Science* **2009,** *323*, 369-373.

(11) Collini, E.; Scholes, G. D. Electronic and Vibrational Coherences in Resonance Energy Transfer along MEH-PPV Chains at Room Temperature. *J. Phys. Chem. A.* **2009,** *113*, 4223-4241.

(12) Laquai, F.; Mishra, A. K.; MArcos, R. R.; Petrozza, A.; Jacob, J.; Akcelrud, L.; Müllen, K.; Friend, R. H.; Wegner, G. Photophysical Properties of a Series of Poly(ladder-type phenylene)s. *Adv. Funct. Mater.* **2007,** *17*, 3231-3240.

(13) Moscatelli, A.; Livingston, K.; So, W. Y.; Lee, S. J.; Scherf, U.; Wildeman, J.; Peteanu, L. A. Electric-Field-Induced Fluorescence Quenching in Polyfluorene, Ladder-Type Polymers, and MEH-PPV: Evidence for Field Effects, on Internal Conversion Rates in the Low Concentration Limit. *J. Phys. Chem. B.* **2010,** *114*, 14430-14439.

(14) Rudnick, A.; Kass, K.-J.; Preis, E.; Scherf, U.; Bassler, H.; Kohler, A. Interplay of localized pyrene chromophores and pi-conjugation in novel poly(2,7-pyrene) ladder polymers. *J. Chem. Phys.* **2017,** *146*, 9.

(15) Patil, S. A.; Scherf, U.; Kadashchuk, A. New Conjugated Ladder Polymer Containing Carbazole Moities. *Adv. Funct. Mater.* **2003,** *13*, 609-614.

(16) Dierschke, F.; Grimsdale, A. C.; Müllen, K. Novel Carbazole-Based Ladder-Type Polymers for Electronic Applications. *Macromol. Chem. Phys.* **2004,** *205*, 1147-1154.

(17) Mahrt, R. F.; Pauck, T.; Lemmer, U.; Siegner, U.; Hopmeir, M.; Hennig, R.; Bassler, H.; Gobel, E. O.; Haring Bolivar, P.; Wegman, G.; Kurz, H.; Scherf, U.; Mullen, K. Dynamics of Optical Excitation in a Ladder-Type Pi-Conjugated Polymer Containing Aggregate States. *Phys. Rev. B.* **1996,** *54*, 1759-1765.

(18) Cocherel, N.; Poriel, C.; Jeannin, O.; Yassin, A.; Rault-Berthelot, J. The Synthesis, Physicochemical Properties and Anodic Polymerization of a Novel Ladder Pentaphenylene. *Dyes Pigm.* **2009,** *83*, 339-347.

(19) Spano, F. C. Spectral Signatures of Frenkel Polarons in H and J Aggregates. *Acct. Chem. Res.* **2009,** *32*, 429-439.

(20) Schwartz, B. J. Conjugated Polymers as Molecular Materials: How Chain Conformation and Film Morphology Influence Energy Transfer and Interchain Interactions. *Annu. Rev. Phys. Chem.* **2003,** *54*, 141-172.

(21) Niles, E. T.; Roehling, J. D.; Yamagata, H.; Wise, A. J.; Spano, F. C.; Moulé, A. J.; Grey, J. K. J-Aggregate Behavior in Poly-3-hexylthiophene Nanofibers. *J. Phys. Chem. Lett.* **2012,** *3*, 259-263.

(22) Spano, F. C.; Clark, J.; Silva, C.; Friend, R. H. Determining Exciton Coherence from the Photoluminescence Spectral Line Shape in Poly(3-hexylthiophene) Thin Films. *J. Chem. Phys.* **2009,** *130*, 074904.

(23) Spano, F. C.; Yamagata, H. Vibronic Coupling in J-Aggregates and Beyond: a Direct Means of Determining the Exciton Coherence Length from the Photoluminescence Spectrum. *J. Phys. Chem. B.* **2011,** *115*, 5133-43.

(24) Yamagata, H.; Spano, F. C. Strong Photophysical Similarities between Conjugated Polymers and J-aggregates. *J Phys Chem Lett* **2014,** *5*, 622-32.

(25) Yamagata, H.; Spano, F. C. Interplay between intrachain and interchain interactions in semiconducting polymer assemblies: the HJ-aggregate model. *J Chem Phys* **2012,** *136*, 184901.

(26) Zhou, J.; Yu, W.; Bragg, A. E. Structural Relaxation of Photoexcited Quaterthiophenes Probed with Vibrational Specificity. *J Phys Chem Lett* **2015,** *6*, 3496-502.

(27) Gallaher, J. K.; Chen, K.; Huff, G. S.; Prasad, S. K.; Gordon, K. C.; Hodgkiss, J. M. Evolution of Nonmirror Image Fluorescence Spectra in Conjugated Polymers and Oligomers. *J Phys Chem Lett* **2016,** *7*, 3307-12.

(28) Clark, J.; Nelson, T.; Tretiak, S.; Cirmi, G.; Lanzani, G. Femtosecond Torsional Relaxation. *Nat Phys* **2012,** *8*.

(29) Parkinson, P.; Muller, C.; Stringelin, N.; Johnston, M. B.; Herz, L. M. Role of Ultrafast Torsional Relaxation in the Emission from Polythiophene Aggregates. *J Phys Chem Lett* **2010,** *1*, 2788-2792.

(30) Thiessen, A.; Vogelsang, J.; Adachi, T.; Steiner, F.; Vande Bout, D.; Lupton, J. M. Unraveling the Chromophoric Disorder of Poly(3-hexylthiophene). *Proc. Natl. Acad. Sci. U. S. A.* **2013,** *110*, 3550-3556.

(31) Snedden, E. W.; Thompson, R.; Hintshich, S.; Monkman, A. P. Fluorescence vibronic analysis in a ladder-type conjugated polymer. *Chemical Physics Letters* **2009,** *472*, 80-84.

(32) Guha, S.; Rice, J. D.; Yau, Y. T.; Martin, C. M.; Chandrasekhar, M.; Chandrasekhar, H. R.; Guentner, R.; Scanduicci de Freitas, P.; Scherf, U.

Temperature-dependent photoluminescence of organic semiconductors with varying backbone conformation. *Physical Review B* **2003,** *67*, 125204-1 - 125204 - 7.

(33) Kanemoto, K.; Akai, I.; Sugisaki, M.; Hashimoto, H.; Karasawa, T.; Negishi, N.; Aso, Y. Temperature effects on quasi-isolated conjugated polymers as revealed by temperature-dependent optical spectra of 16-mer oligothiophene diluted in a sold matrix. *J Chem Phys* **2009,** *130*, 234909.

(34) Panzer, F.; Bassler, H.; Kohler, A. Temperature Induced Order-Disorder Transition in Solutions of Conjugated Polymers Probed by Optical Spectroscopy. *J Phys Chem Lett* **2017,** *8*, 114-125.

(35) Spano, F. C.; Silva, C. H- and J-Aggregate Behavior in Polymeric Semiconductors. *Annu. Rev. Phys. Chem.* **2014,** *65*, 477-500.

(36) Belletete, M.; Bouchard, J.; Leclerc, M.; Durocher, G. Photophysics and Solvent-Induced Aggregation of 2,7-Carbazole-Based Conjugated Polymers. *Macromolecules* **2005,** *38*, 880-887.

(37) Caruso, M. M.; Davis, D. A.; Shen, Q.; Odom, S. A.; Sottos, N. R.; White, S. R.; Moore, J. S. Mechanically-Induced Chemical Changes in Polymeric Materials. *Chem. Rev.* **2009,** *109*, 44.

(38) Nguyen, T.-Q.; Martini, I. B.; Liu, J.; Schwartz, B. J. Controlling Interchain Interactions in Conjugated Polymers: The Effects of Chain Morphology on Exciton-Exciton Annihilation and Aggregation in MEH-PPV Films. *J. Phys. Chem. B.* **2000,** *104*, 237-255.

(39) Schwartz, B. J. Cojugated Polymers as Molecular Materials: How Chain Conformation and Film Morphology Influence Energy Transfer and Interchain Interactions. *Annu. Rev. Phys. Chem.* **2003,** *54*, 141-172.

(40) Pope, M.; Swenberg, C. E., *Electronic Properties in Organic Crystals and Polymers*. 2 ed.; Oxford University Press: New York, New York, 1999.

APPENDIX I

Supporting Information for

Exciton Transfer and Emergent Excitonic States in Oppositely-Charged Conjugated Polyelectrolyte Complexes

S1. Experimental

S1.1 *Sample Preparation*

The cationic conjugated polyelectrolyte poly([fluorene]-alt-co-[phenylene]) (PFPI) with an average molecular weight (MW) of 21,000 Da and polydispersity index (PDI) of 1.2 was obtained from Solaris Chem Inc. The anionic conjugated polyelectrolyte poly(alkylcarboxythiophene) derivative (PTAK) with an MW of 16,000 Da and a PDI of 2.2 was obtained from Rieke Metals. Both materials were used as received.

Stock Solutions of PFP3I and PTAK (10.0 mg/mL) were prepared in Milli-Q water and then mixed in desired molar ratios to form CPECs. The PTAK stock solution was stirred at ~ 70 °C for 24 hours. The PFPI stock solution was stirred at ~ 70 °C for 72 hours. Care was taken to minimize exposure to ambient lights. CPEC solutions with PFPI:PTAK charge ratios of PFP3I to PTAK (1 : 0.01, 1 : 0.05, 1 : 0.25) were

prepared based on the number of chargers per monomer unit. The PFPI monomer carries a charge of 2+, and the ionized PTAK monomer carries a 1- charge. The PFPI concentration was fixed at 1 mg/mL for all CPEC solutions. The forward addition method is as follows. PFPI from the stock solution was added to Milli-Q water, after which PTAK stock was added dropwise to the solution while stirring at room temperature to achieve the desired charge ratio. The order of CPE addition is switched in the reverse order. CPEC solutions were then stirred at ~ 70 °C for 24 hours. In solutions with a solid/liquid phase coexistence, mixtures were centrifuged at 3400 rpm for 30 minutes, after which the phases were separated for further measurements.

S1.2 *Steady-State Spectroscopy*

Optical density measurements were taken in 1.0 nm increments with a Shimadzu UV-2700 Spectrophotometer with an integration time of 0.1 seconds and a 2.0 nm slit width over the range of 300-800 nm. Photoluminescence measurements were taken using a Horiba Fluromax-4 spectrofluorometer in a right-angle geometry in cuvettes with 2 mm pathlengths, with excitation wavelengths scanned in 5.0 nm increments and emissions measured in 1.0 nm increments over the range of 300-800 nm. Liquid samples were measured with a Rayleigh masking slit width of 5.0 nm and an integration time of 0.1 seconds. Solid samples were placed at an 87° angle relative

to the incident beam and measured with a Rayleigh masking slit width of 2.0 nm and an integration time of 0.05 seconds.

S1.3 *Dynamic Light Scattering (DLS)*

Solutions were filtered using 0.65 μm Millipore filter directly into borosilicate glass test tubes. Samples were immersed in decalin to match the index of refraction of glass (n ~ 1.33). All DLS measurements were made on a Brookhaven BI-200SM goniometer system using a TurboCorr Photon Counter and digital correlator at room temperature. The light source was a CW Mini-L30 solid-state diode laser outputting 637 nm light with adjustable power limited to 35 mW. The laser power and optical density filter were adjusted in order not to exceed a signal intensity of 200 kilocounts per second. Scattered photons were detected by an avalanche photodiode detector. The normalized intensity correlation functions were transformed to the normalized electric-field field correlation function using the Siegert regulation. The field correlation functions were analyzed using CONTIN, which is a regularized inverse Laplace transform algorithm originally written in FORTRAN by Provencher and since emulated by Marino in MATLAB. Distribution of relaxation times were obtained for scattering angles of 20 and 90 degrees with the regulation parameter (α) set to 0.1. Various choices for α as well as various grid densities for the relaxation time space were explored. We found that relaxation times obtained with different choices of α

were similar. A larger value of α was avoided so as to not overly smooth the relaxation time distribution. Hydrodynamic radius values were obtained using the Stokes-Einstein equation.

S1.4 *Small-Angle X-ray Scattering (SAXS)*

SAXS measurements were performed at beam line 4-2 at the Stanford Synchrotron Radiation Laboratory (SSRL) using a Rayonix MX225-HE detector. Samples in thin-wall quartz capillary cell were irradiated by a 11 keV X-ray (1.17 Å) at a sample to detector distance of 3.5m. A set of 10 consecutive 1 second X-ray exposures were made on each sample at room temperature. The scattering of the background (Milli-Q water) was subtracted from solution scattering. To avoid degradation, the samples were oscillated during data collection. SasTool, a software package developed at SSRL, was used to convert collected 2D TIFF images to intensity vs scattering vector and to subtract solvent scattering.

S1.5 *Time-Resolved Photoluminescence Spectroscopy*

Time-correlated single photon counting (TCSPC) was carried out on a home-built apparatus. The excitation source was a pulsed Super K EXTREME (NKT Photonics) supercontinuum laser coupled to a Super K SELECT (NKT Photonics) acousto-optic filter and external RF driver (NKT Photonics) to select the wavelength

of the excitation pulse. Measurements were carried out at a 78MHz pulse repetition rate with either 15.4µW (420nm) or 97.6µW (600nm) power, as measured near the sample. Both excitation and emission beams were horizontally polarized by mounted Glan-Thompson polarizers (Thorlabs). Emission light was collimated and refocused by a set of achromatic doublets (Thorlabs). Long pass filters were used to minimize the influence of the reflected excitation beam. Emission wavelengths were selected by an Acton Spectra Pro SP-2300 monochromator (Princeton Instruments), on which two detectors were mounted for steady-state and time-resolved measurements. An air-cooled PIXIS 100 CCD (Princeton Instruments) was used to record the steady-state spectra on the fly. A hybrid PMT with minimal after-pulsing (Becker and Hickl) was used to record the time-resolved fluorescence decay. An SPC-130 photon counting module (Becker and Hickl) coupled to a Simple-Tau 130 table top TCSPC system was used for photon counting. Emitted photons were collected for 5 seconds, and each measurement was repeated 50 times prior to averaging and subsequent analysis.

S2. Photoluminescence Excitation of a Dilute CPEC Solution.

Figure AI.1 show photoluminescence excitation (PLE) plots for a 1:0.25 charge ratio CPEC at a PFPI concentration of 0.1 mg/mL. At this concentration, the PFPI exciton density as a function of position in the cuvette along the beam direction is significantly more uniform relative to the 1 mg/mL solution. This leads to much improved spatial overlap of emitted light with the cross section of the detector. Black diamonds show the PLE spectrum collected at λ_{em} = 440 nm, which corresponds to PFPI emission. The red curve shows PLE collected at λ_{em} = 660 nm, where PTAK exclusively emits. PFPI PL largely follows its OD (**Figure 2.1** of main text). The fact that PTAK shows substantial enhancement in PL precisely at the wavelengths that give rise to PFPI PL constitutes strong evidence of EET from photoexcited to PFPI to PTAK.

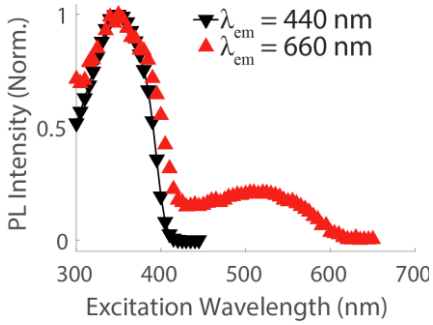

Figure AI.1. Normalized PLE of a 1:0.25 charge ratio CPEC. Black triangles show PL collected at 440 nm, corresponding to PFPI PL. Red upside-down triangles show PL collected at 660 nm, corresponding to PTAK.

S3. Fits to PL Spectra.

In order to put a comparison of PL spectra between isolated PTAK control solutions and the corresponding CPEC solutions on a more quantitative footing, we have fit spectra on a photon energy scale to a vibronic progression. First, spectra

were transformed from wavelength to energy space by scaling the measured intensity with a factor of $1/E^2$, where *E* is the photon energy. Intensities were further divided by a factor of E^3 to eliminate the energy dependence of the photon density of states. The resulting spectral intensities *I* were fit to a sum of Gaussian functions to represent the different vibronic contributions to the PL envelope as

$$I = \sum_{n=0}^{3} a_n \exp[-(E - E_0 + nE_{vib})^2 / \sigma^2)] + const. \qquad \text{(AI.1)}$$

where the *a*'s are the Gaussian amplitudes, E_0 is the electronic origin, E_{vib} is the energy of the vibrational normal mode coupled to the electronic transition, and σ is the width. A constant background offset was also included. The 0-0/0-1 vibronic intensity ratio ($I_{0\text{-}0}/I_{0\text{-}1}$) was calculated as the ratio of the first and second Gaussian amplitudes. The width was constrained to be constant for each vibronic peak but allowed to vary between samples. The fit results are summarized below in **Table AI.1**, along with the goodness-of-fit parameter R^2.

Table AI.1. Gaussian fits to transformed PL spectrum.

Sample	E_0 (eV)	E_{vib} (eV)	σ (eV)	$I_{0\text{-}0} / I_{0\text{-}1}$	R^2
PTAK (1:0.05)	2.16	0.23	0.17	0.26	0.996
CPEC (1:0.05)	2.01	0.13	0.10	0.91	0.999

Symbols are defined above. PTAK corresponds to the control for the corresponding CPEC (the charge ratio is indicated to the right).

It is at the moment unclear why the apparent energy of the vibrational mode coupled to PL transition of PTAK in isolation is substantially larger than that of PTAK complexed to PFPI.

APPENDIX II

Supporting Information for:

Polyion Charge Ratio Determines Transition Between Bright and Dark Excitons in Donor/Acceptor Conjugated Polyelectrolyte Complexes

S1. EXPERIMENTAL METHODS

S1.1 *Ultrafast Transient Absorption Spectroscopy*

Transient absorption spectra were collected as described previously.[1] Laser light necessary for these measurements was generated with the fundamental output from a regeneratively amplified Ti:sapphire laser system (Legend Elite-USP-1K-HE seeded with a Coherent Mantis-5 oscillator; 800 nm fundamental, 4.0 mJ/pulse, 990 Hz repetition rate, <40 fs pulse duration). This output beam was split to drive excitation and probe pulse generation.

A small fraction of the beam, (~several hundred nJ), was focused into a CaF_2 or Sapphire crystal to generate a broadband white light continuum (WLC) to serve as the probe pulse. These pulses are used uncompressed and have an instrument response/temporal resolution of ~100 fs. Data was corrected for temporal chirp of the probe pulses after collection; correction procedures are described elsewhere.[2]

The probe was passed through a wire grid polarizer set to magic angle relative to the excitation polarization immediately before the sample in order to isolate population kinetics of transient states from evolution in transition dipole orientation.

A femtosecond OPA (Coherent OPerA Solo) was utilized to generate the 360 and 600 nm excitation pulses through various non-linear processes; resultant pulses had temporal resolution of 50-70 fs. The pump pulses were attenuated and focused such that the beam spot completely encompassed the probe at the sample (>2x the spot size of the probe) with a pump fluence of ~2.5 $\mu J/cm^2$ to remain in a lower fluence, linear excitation regime.

The pump and probe pulse were overlapped spatially and temporally at the sample, with their relative timing controlled by retroreflecting the pump off a corner-cube mirror positioned on a Newport ILS250CC translation stage. Each beam was selectively blocked prior to the sample at specific frequencies by optical choppers in order to collect four phases of information necessary to calculate transient absorption while removing signals due to pump scatter and sample fluorescence. The probe beam was collimated after the sample, focused through a slit into a Princeton Acton SP2300 spectrograph and dispersed onto a Princeton Pixis 100BR CCD array camera. Each probe pulse produced by the laser was collected individually, and transient spectra were obtained through shot-to-shot signal comparisons.

Following collection, transient absorption data was smoothed in the spectral domain using a Savitsky-Golay filter (using 20 points and 4^{th} order polynomial fits). Spectra were then corrected for temporal chirp by applying a delay offset at each wavelength to a common time delay, identified as t_0. Formally, a time delay of $t_0 = 0$ ps was set as the point midway through a fit to the instrument response signal at each wavelength.

S1.2 *Time-Resolved Photoluminescence*

Time-correlated single photon counting (TCSPC) was carried out on a home-built apparatus. The excitation source was a pulsed Super K EXTREME (NKT Photonics) supercontinuum laser coupled to a Super K SELECT (NKT Photonics) acousto-optic filter and external RF driver (NKT Photonics) to select the wavelength of the excitation pulse. Measurements were carried out at a 78MHz pulse repetition rate. The native horizontally elliptically polarized excitation pulse was first rotated 90° via achromatic ½ λ plate (Thorlabs) before being linearealy polarized via Glan-Thompson polarizer (Thorlabs). Polarization of emitted light was by Glan-Thompson polarizer. For anisotropic experiments, rotation of the polarization stages was controlled via motorized rotational stages (Thorlabs) under computer control. Horizontal excitation polarization was achieved with the ½ λ plate fast axis parallel to the horizontal laser pulse. Emission light was collimated and refocused by a set of

achromatic doublets (Thorlabs). Long pass filters were used to minimize the influence of the reflected excitation beam. Emission wavelengths were selected by an Acton Spectra Pro SP-2300 monochromator (Princeton Instruments), on which two detectors were mounted for steady-state and time-resolved measurements. An air-cooled PIXIS 100 CCD (Princeton Instruments) was used to record the steady-state spectra on the fly. A hybrid PMT with minimal after-pulsing (Becker and Hickl) was used to record the time-resolved fluorescence decay. An SPC-130 photon counting module (Becker and Hickl) coupled to a Simple-Tau 130 table top TCSPC system was used for photon counting. For magic angle measurements, collection was carried out until approximately 10,000 counts were reached in the main channel. For anisotropic experiments, collection was carried out until approximately 10,000 counts were reached in the main channel under vertical-vertical conditions. The vertical-horizontal measurement was then carried out for the same amount of time.

After collection, magic angle data was baselined by subtracting the average of the first 30 collected data points (prior to rise onset). All magic angle spectra were time-shifted such that $\tau = 0$ occurred at the peak of the decay. Anisotropy data were time-shifted such that the half-rise time of respective VV and VH measurements were the same.

S1.3 *Steady – State Spectroscopy*

Optical density measurements were taken in 1.0 nm increments with a Shimadzu UV-2700 Spectrophotometer with an integration time of 0.1 seconds and a 2.0 nm slit width over the range of 300-800 nm. Photoluminescence measurements were taken using a Horiba Fluromax-4 spectrofluorometer in a right-angle geometry in cuvettes with 1 mm pathlengths, with excitation wavelengths scanned in 5.0 nm increments and emissions measured in 1.0 nm increments over the range of 300-800 nm. Excitation and emission slit widths were 1 nm bandpass.

S1.4 *Sample Preparation*

The cationic conjugated polyelectrolyte poly([fluorene]-alt-co-[phenylene]) (PFPI) with an average molecular weight (MW) of 21,000 Da and polydispersity index (PDI) of 1.2 was obtained from Solaris Chem Inc. The anionic conjugated polyelectrolyte poly(alkylcarboxythiophene) derivative (PTAK) with an MW of 16,000 Da and a PDI of 2.2 was obtained from Rieke Metals. Both materials were used as received. Stock solutions of PFP3I and PTAK (10.0 mg/mL) were prepared in HPLC water (Sigma-Aldrich) and then mixed in desired molar ratios to form CPECs. The PTAK stock solution was stirred at ~ 70 °C for 24 hours. The PFPI stock solution was stirred at ~ 70 °C for 72 hours. Care was taken to minimize exposure to ambient lights. CPEC solutions with PFPI:PTAK charge ratios of PFP3I to PTAK (10:90 – 90:10)

were prepared based on the number of chargers per monomer unit. We used 0.1 mg/mL PFPI, and 0.0586 mg/mL PTAK solutions to make our samples. The PFPI monomer carries a charge of 2+, and the ionized PTAK monomer carries a 1- charge. At these concentrations any volume of PFPI solution has the same molar concentration of charges as an equal volume of PTAK solution. PFPI was added directly to PTAK in proportion to the charge ratio desired. CPEC solutions were then stirred at 70 °C for 24 hours. In solutions with a solid/liquid phase coexistence, mixtures were centrifuged at 5000 rpm for 15 minutes, after which the phases were separated for further measurements.

S1.5 *Small-Angle X-ray Scattering (SAXS)*

SAXS measurements were performed at beamline 4−2 at the Stanford Synchrotron Radiation Laboratory (SSRL) using a Rayonix MX225-HE detector. Samples in thin-wall quartz capillary cell were irradiated by a 11 keV X-ray (1.17 Å) at a sample to detector distance of 2.5m and 3.5m. A set of 12 consecutive 1 s X-ray exposures were made on each sample at room temperature. The scattering of the background (HPLC water) was subtracted from solution scattering. To avoid degradation, the samples were oscillated during data collection. SasTool, a software package developed at SSRL, was used to convert collected 2D TIFF images to intensity vs scattering vector and to subtract solvent scattering. The pair distance distribution functions (PDDF) of the corrected scattering data are calculated using the GIFT

analysis package.The GIFT program performs an indirect Fourier trans- formation (IFT) of the scattering profiles to calculate a real-space analogue of the original data. By using the IFT method no model assumption is needed evaluate the scattering the data obtain the PDDF. GIFT uses the Fourier inversion shown below to obtain the PDDF from the scattering data.

S2. GLOBAL ANALYSIS OF TRANSIENT ABSORPTION SPECTRA

A global fitting procedure was applied to each set of transient spectra in order to extract species-specific spectral components based on an assumed kinetic model. Fitting parameters were robust and found to be largely independent of the initial values used to initiate global analysis. The steps used for global analysis were as follows:

1. Define a kinetic model for each anticipated component as a series of exponential decays, rises, and constants with interdependent parameters. Make initial predictions of those parameters and convolute the function associated with each species with a shared instrument response function.
2. Fit the kinetic trace obtained for each wavelength (as a function of pump-probe delay) as a linear combination of each component defined above. The weights of these represent the spectrum associated with each component.

3. Fit the full spectrum of the raw data at each time delay as a linear combination of these spectra to determine the kinetic profile for each component.
4. Optimize the parameters from the initial kinetic model such that it best fits the kinetic profiles extracted by the previous step.
5. Repeat steps 2-4 until the fitting algorithm converges to a consistent solution.

For each progression analyzed, the model with the minimum number for parameters necessary to adequately fit the data, both spectrally and temporally, was the one employed. Specific models and their corresponding converged fitting parameters are included below.

Table AII.1: Global analysis fitting parameters for models applied to pure PFPI, pure PTAK, and CPEC transient absorption data. The model used for each is indicated by the number in brackets (1-6) and defined by the equations below.

	360 nm						600 nm			
	PFPI [1]	80:20 [2]	60:40 [3]	40:60 [4]	20:80 [4]	PTAK [5]	80:20 [6]	60:40 [6]	20:80 [5]	PTAK [7]
IRF_W	0.100	0.089	0.099	0.111	0.084	0.093	0.060	0.095	0.074	0.087
c_1	0.277	0.691	1.19	0.471	1.06	1.22	3.47	6.64	2.38	2.80
τ_1	1.73	0.224	0.234	0.086	0.157	0.428	0.043	0.014	0.086	0.05
c_2	0.228	0.639	0.709	0.303	0.931	0.527	0.369	0.353	1.05	0.578
τ_2	16.6	479	1.59	2.41	0.985	0.379	1.61	1.7	0.306	0.546
c_3	0.519	0.485	0.473	0.112	0.293	0.245	0.436	0.391	0.387	0.224
τ_3	434	22.8	34.4	31.6	26.8	7.9	42.6	20.6	4.57	16.3
c_4	---	0.180	0.019	0.061	0.196	0.092	0.072	0.054	0.138	---
τ_4	---	---	---	1270	691	221	---	---	212	---
c_5	---	---	0.122	0.020	0.008	---	---	---		---

$$A(t) = c_1 e^{-(\frac{t}{\tau_1})} + c_2 e^{-(\frac{t}{\tau_2})} + c_3 e^{-(\frac{t}{\tau_3})} \quad \text{(AII.1)}$$

$$A(t) = c_1 e^{-\left(\frac{t}{\tau_1}\right)} + c_2 e^{-\left(\frac{t}{\tau_2}\right)}$$

$$B(t) = c_3(1 - e^{-(\frac{t}{\tau_1})})e^{-(\frac{t}{\tau_3})} \quad \text{(AII.2)}$$

$$C(t) = c_4(1 - e^{-(\frac{t}{\tau_3})})$$

$$A(t) = c_1 e^{-\left(\frac{t}{\tau_1}\right)}$$

$$B(t) = \left(1 - e^{-\left(\frac{t}{\tau_1}\right)}\right)\left(c_2 e^{-\left(\frac{t}{\tau_2}\right)} + c_3 e^{-\left(\frac{t}{\tau_3}\right)}\right) \quad \text{(AII.3)}$$

$$C(t) = c_4\left(1 - e^{-\left(\frac{t}{\tau_2}\right)}\right) + c_5\left(1 - e^{-\left(\frac{t}{\tau_3}\right)}\right)$$

$$A(t) = c_1 e^{-\left(\frac{t}{\tau_1}\right)}$$
$$B(t) = \left(1 - e^{-\left(\frac{t}{\tau_1}\right)}\right)\left(c_2 e^{-\left(\frac{t}{\tau_2}\right)} + c_3 e^{-\left(\frac{t}{\tau_3}\right)}\right) \quad \text{(AII.4)}$$
$$C(t) = \left(c_4\left(1 - e^{-\left(\frac{t}{\tau_2}\right)}\right) + c_5\left(1 - e^{-\left(\frac{t}{\tau_3}\right)}\right)\right) e^{-\left(\frac{t}{\tau_4}\right)}$$

$$A(t) = c_1 e^{-\left(\frac{t}{\tau_1}\right)}$$
$$B(t) = \left(1 - e^{-\left(\frac{t}{\tau_1}\right)}\right)\left(c_2 e^{-\left(\frac{t}{\tau_2}\right)} + c_3 e^{-\left(\frac{t}{\tau_3}\right)} + c_4 e^{-\left(\frac{t}{\tau_4}\right)}\right) \quad \text{(AII.5)}$$

$$A(t) = c_1 e^{-\left(\frac{t}{\tau_1}\right)}$$
$$B(t) = (1 - e^{-\left(\frac{t}{\tau_1}\right)})(c_2 e^{-\left(\frac{t}{\tau_2}\right)} + c_3 e^{-\left(\frac{t}{\tau_3}\right)}) \quad \text{(AII.6)}$$
$$C(t) = c_4(1 - e^{-\left(\frac{t}{\tau_3}\right)})$$

$$A(t) = c_1 e^{-\left(\frac{t}{\tau_1}\right)}$$
$$B(t) = \left(1 - e^{-\left(\frac{t}{\tau_1}\right)}\right)\left(c_2 e^{-\left(\frac{t}{\tau_2}\right)} + c_3 e^{-\left(\frac{t}{\tau_3}\right)}\right) \quad \text{(AII.7)}$$

$$IRF(t) = e^{-\frac{4\ln(2)*(t-IRF_O)^2}{IRF_W{}^2}} \quad \text{(AII.8)}$$

Each model involved convolution of one of the **Equations A.II1-6** with **Equation AII.8**, a Gaussian instrument response function. In **Equation AII.8**, IRF_O corresponds to a correction in the experimental time zero. Spectral data and kinetic traces presented throughout the manuscript and SI have been shifted to account for this correction. IRF_W corresponds to the full width at half maximum of the instrument

response function. Included below are the spectral and corresponding kinetic outputs for each set of transient spectra referred to in **Table AII.1** above.

S2.1 *PTAK, 360 nm excitation*

Spectral dynamics obtained with pure PTAK excited at 360 nm can be fit using a two-state (two-spectrum) model. Here A corresponds with short-lived population of singlet exciton and polaron-pair features that decay monoexponentially to B. B exhibits signatures of polaron-pair and possibly triplet absorption at 900 nm and is well described by triexponential decay. The same PTAK concentration used in CPEC 40:60 was used for this sample.

$$A(t) = c_1 e^{-\left(\frac{t}{\tau_1}\right)}$$
$$B(t) = \left(1 - e^{-\left(\frac{t}{\tau_1}\right)}\right)\left(c_2 e^{-\left(\frac{t}{\tau_2}\right)} + c_3 e^{-\left(\frac{t}{\tau_3}\right)} + c_4 e^{-\left(\frac{t}{\tau_4}\right)}\right) \quad \text{(AII.9)}$$

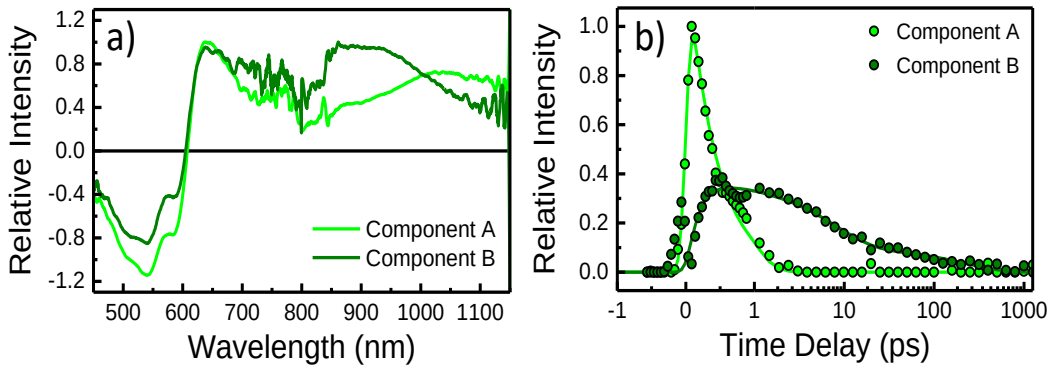

Figure AII.1. Results from global analysis of transient absorption data collected from pure PTAK excited at 360 nm. a) Species-associated spectra obtained from the two-state kinetic model described in the text. b) Time-dependence of the spectral components shown in panel a). Points correspond to the relative weight of each spectrum from a), the solid lines represent the kinetic model fit.

S2.2 *PTAK 600 nm*

Transient absorption collected with pure PTAK excited at 600 nm can be fit using the two-state model shown below. This data is consistent with prior observations of polaron-pair (650 nm) appearing with a delay relative to ground-state bleach at 550 nm and exciton absorption in the near IR.[3] The same PTAK concentration used in CPEC 20:80 was used for this sample and the fits are remarkably similar.

$$A(t) = c_1 e^{-\left(\frac{t}{\tau_1}\right)}$$
$$B(t) = \left(1 - e^{-\left(\frac{t}{\tau_1}\right)}\right)\left(c_2 e^{-\left(\frac{t}{\tau_2}\right)} + c_3 e^{-\left(\frac{t}{\tau_3}\right)}\right) \quad \text{(AII.10)}$$

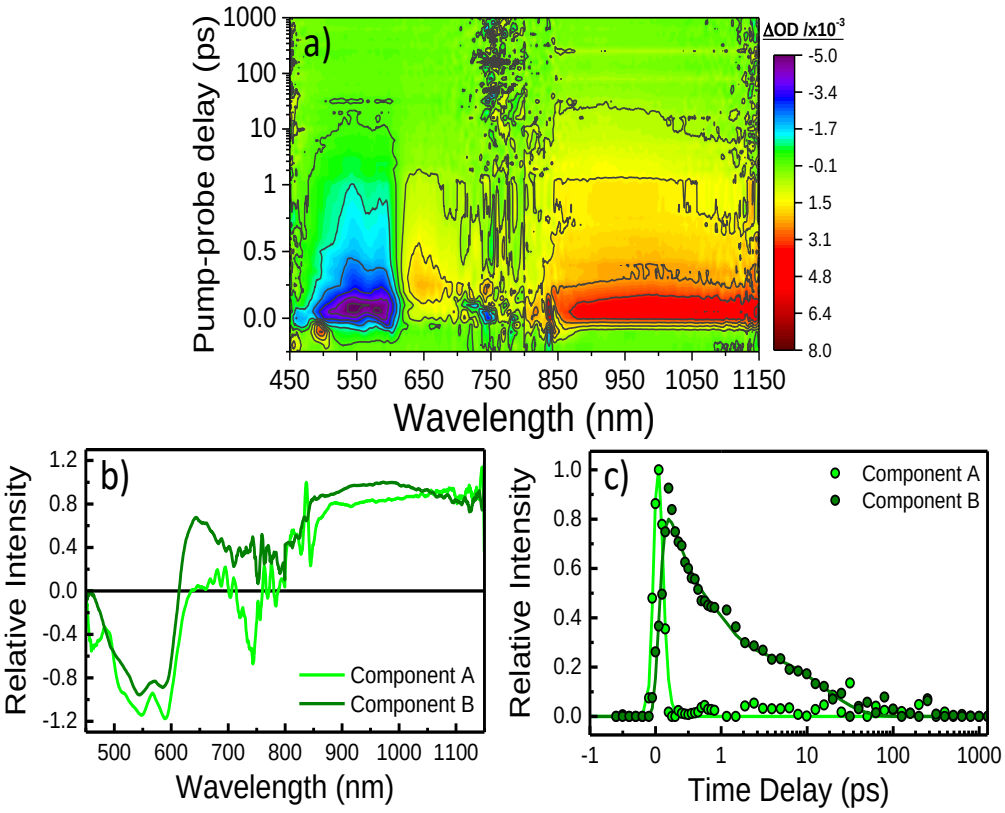

Figure AII.2: a) Transient absorption data collected with 600 nm excitation of pure PTAK. b) Species-associated spectra obtained by global analysis with a two-state kinetic model described in the text. c) Time-dependence of the spectral components shown in panel b). Points correspond to the relative weight of each spectrum from b), the solid lines represent the kinetic model fit.

S2.3 *CPEC 60:40 600 nm excitation*

Transient absorption data obtained with CPEC 60:40 excited at 600 nm was fit using a kinetic model like **Equation AII.11**. B and C correspond with the excited PTAK singlet (B) and triplets (C) states respectively (Component A accounts for spectral artifacts in the pump-probe cross-correlation, as τ_1 is found to be ~14 fs, which is much shorter than the instrument response of our measurements). These

components can be compared directly to those presented in the main text for 360-nm excitation to verify the population of excited PTAK singlet following energy transfer from PFPI.

$$A(t) = c_1 e^{-\left(\frac{t}{\tau_1}\right)}$$
$$B(t) = (1 - e^{-\left(\frac{t}{\tau_1}\right)})(c_2 e^{-\left(\frac{t}{\tau_2}\right)} + c_3 e^{-\left(\frac{t}{\tau_3}\right)}) \quad \text{(AII.11)}$$
$$C(t) = c_4(1 - e^{-\left(\frac{t}{\tau_3}\right)})$$

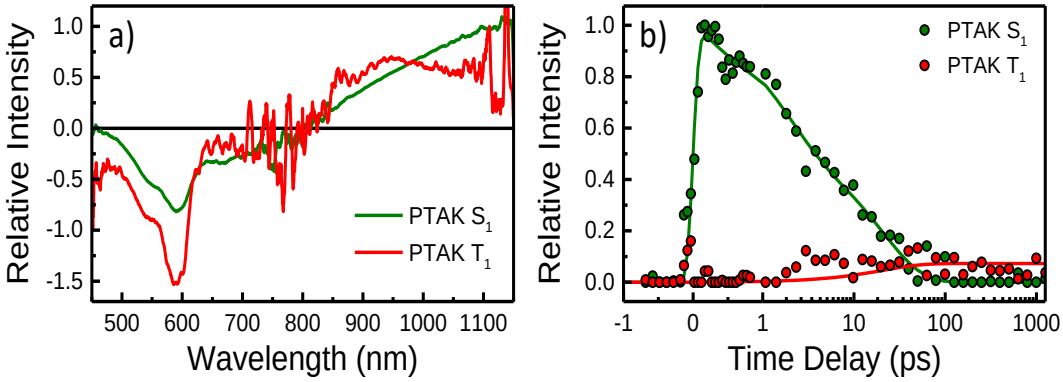

Figure AII.32. Results of global analysis of transient absorption data collected with 60:40 CPEC excited at 600 nm. a) Species-associated spectra correspond to PTAK excited singlet (S_1 - green) and triplet (T_1 - red) obtained from the two-state kinetic model described in the text. b) Time-dependence of the spectral components shown in panel a). Points correspond to the relative weight of each spectrum from a), the solid lines represent the kinetic model fit.

S2.4 *PFPI, 360 nm excitation*

PFPI transient absorption data was best fit with a single spectral component (namely the PFPI S_1 state) evolving in time with a tri-exponential decay in order to capture all time-dependence observed. The same PFPI concentration used in CPEC 40:60 was used for this sample. As can be seen from **Table AII.1**, approximately half

$$A(t) = c_1 e^{-(\frac{t}{\tau_1})} + c_2 e^{-(\frac{t}{\tau_2})} + c_3 e^{-(\frac{t}{\tau_3})} \quad \text{(aII.12)}$$

of the spectral decay occurs on the longest of the tri-exponential decay lifetimes, with approximately a quarter of the population decaying on each of the other two timescales.

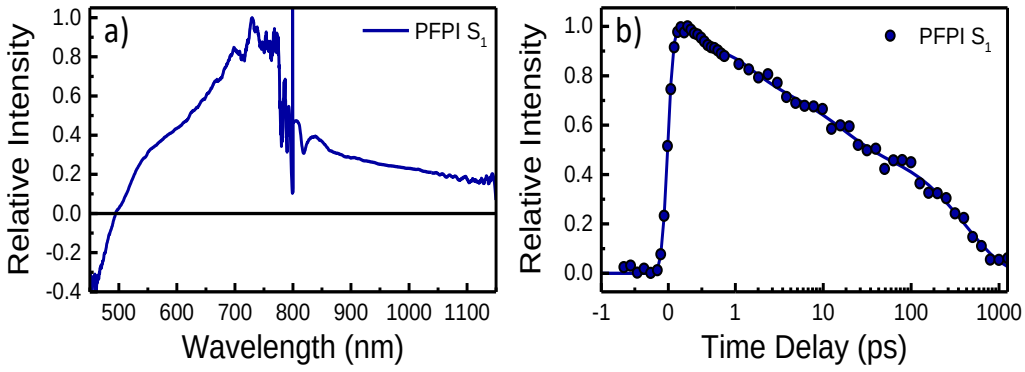

Figure AII.4. Results from global analysis of transient absorption data collected with pure PFPI excited at 360 nm. a) Species-associated spectra corresponding to singlet PFPI. b) Time-dependence of the spectral component shown in panel a).

S2.5 *CPEC 40:60 360nm excitation*

CPEC 40:60 transient data was fit with a similar model used to fit data from CPEC 60:40, with the exception that the triplet population (C) was fit with a decay of

1270 ps. The components appear similar to those of 60:40, though the PFPI (A) component appears to decay more rapidly. This provides reasonable evidence that PFPI is depopulated very rapidly by energy transfer to PTAK (B).

$$A(t) = c_1 e^{-\left(\frac{t}{\tau_1}\right)}$$

$$B(t) = \left(1 - e^{-\left(\frac{t}{\tau_1}\right)}\right)\left(c_2 e^{-\left(\frac{t}{\tau_2}\right)} + c_3 e^{-\left(\frac{t}{\tau_3}\right)}\right) \qquad \text{(AII.13)}$$

$$C(t) = \left(c_4\left(1 - e^{-\left(\frac{t}{\tau_2}\right)}\right) + c_5\left(1 - e^{-\left(\frac{t}{\tau_3}\right)}\right)\right) e^{-\left(\frac{t}{\tau_4}\right)}$$

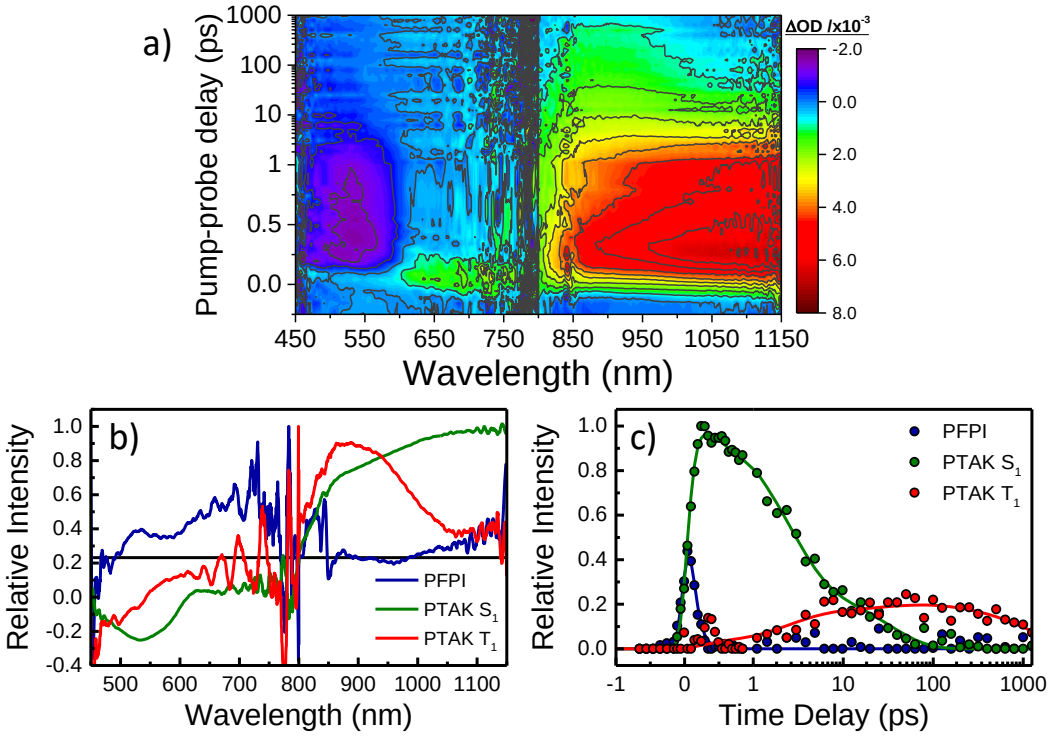

Figure AII.5. a) Transient absorption data collected following 360 nm excitation of the 40:60 CPEC. b) Species-associated spectra for PFPI (blue), PTAK singlet (green) and PTAK triplet (red) obtained from the three-state kinetic model described in the text. c) Time-dependence of the three spectral components shown in panel a). Points correspond to the relative weight of each spectrum from a), the solid lines represent the kinetic model fit.

S2.6 *CPEC 20:80 360 nm excitation*

CPEC 20:80 only exhibits weak evidence of initial PFPI transient state population, as these features appears in the same region where features are observed for pure PTAK domains. This was fit with an identical kinetic model to the 40:60 data above. The inability to extract meaningful spectral components with this model (e.g. the negative intensity for component A in the NIR region) indicates that the minor fraction of PFPI transient signatures are present within the spectra decay within the instrument response.

$$A(t) = c_1 e^{-\left(\frac{t}{\tau_1}\right)}$$

$$B(t) = \left(1 - e^{-\left(\frac{t}{\tau_1}\right)}\right)\left(c_2 e^{-\left(\frac{t}{\tau_2}\right)} + c_3 e^{-\left(\frac{t}{\tau_3}\right)}\right) \quad \text{(AII.14)}$$

$$C(t) = \left(c_4\left(1 - e^{-\left(\frac{t}{\tau_2}\right)}\right) + c_5\left(1 - e^{-\left(\frac{t}{\tau_3}\right)}\right)\right) e^{-\left(\frac{t}{\tau_4}\right)}$$

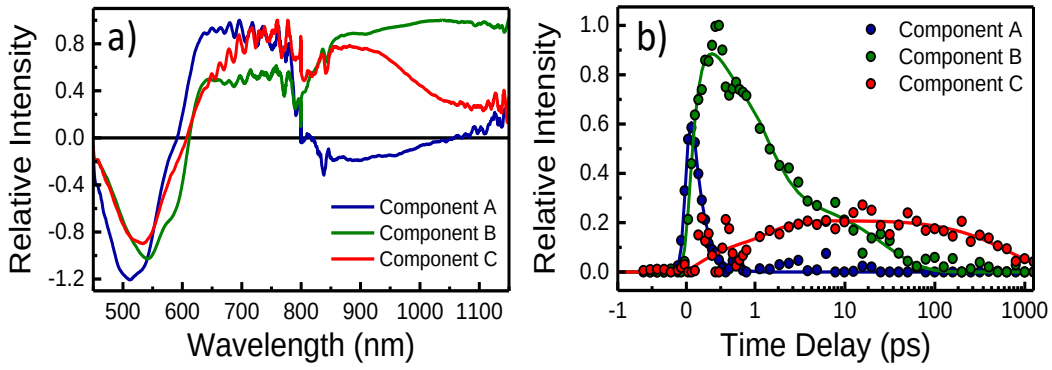

Figure AII.6. Results of global analysis of transient absorption data collected from 80:20 CPEC samples. a) Species-associated spectra obtained from the three-state kinetic model described in the text. b) Time-dependence of the three spectral components shown in panel a). Points correspond to the relative weight of each spectra from a), the solid lines represent the kinetic model fit.

S2.7 *CPEC 20:80 600 nm excitation*

Directly excited at 600 nm, CPEC 20:80 closely resembles the spectrum of pure PTAK (**Figure AII.2**) with only moderate evidence of structural changes brought about by addition of PFPI. The coupled charge transfer state (absorption at ~650 nm) is less intense but the other features persist with similar intensities and almost identical kinetics.

$$A(t) = c_1 e^{-\left(\frac{t}{\tau_1}\right)}$$
$$B(t) = \left(1 - e^{-\left(\frac{t}{\tau_1}\right)}\right)\left(c_2 e^{-\left(\frac{t}{\tau_2}\right)} + c_3 e^{-\left(\frac{t}{\tau_3}\right)} + c_4 e^{-\left(\frac{t}{\tau_4}\right)}\right) \quad (5)$$

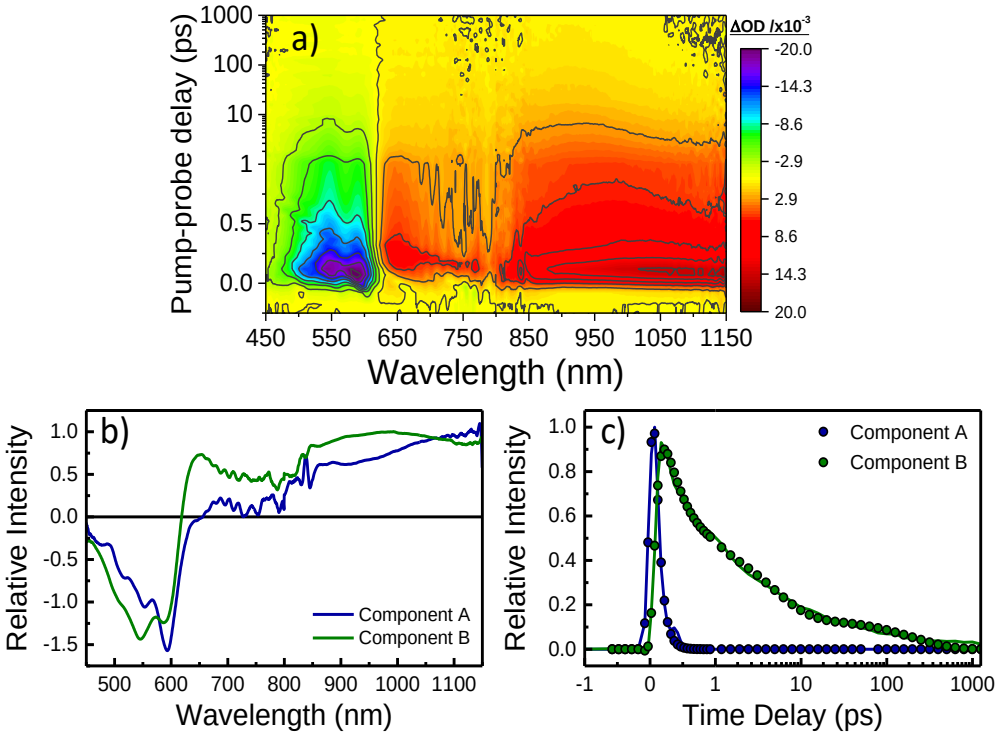

Figure AII.7. a) Transient absorption data collected from the 20:80 CPEC following 600 nm excitation. b) Species-associated spectra obtained from the three-state kinetic model described in the text. c) Time-dependence of the three spectral components shown in panel a). Points correspond to the relative weight of each spectrum from a), the solid lines represent the kinetic model fit.

S3. INSIGHTS ON CPEC MORPHOLOGY FROM ULTRAFAST PTAK SPECTROSCOPY

Figure AII.8 presents transient absorption spectra obtained from the 600 nm excitation of several PTAK and CPEC samples in order to interrogate PTAK photophysics subject to various supramolecular environments. Without or with very little PFPI present (**Figures AII.8a** and **AII.8b**, respectively), the transient spectra obtained are similar to those of polythiophene films and assemblies reported elsewhere. Specifically, transient spectra are dominated by a ground-state bleach with vibronic features below 600 nm, a visible absorption feature at 650 nm arising from coupled charge pair states, and a broad absorbance centered at 1025 nm previously ascribed predominantly to isolated charge carriers (lower wavelength edge) with some overlap from singlet excitons (longer wavelength edge). Only subtle differences in relative peak heights are observed between transient spectra obtained with the PTAK control solution and the 20:80 CPEC. By contrast, 60:40 and 80:20 CPECs (Figures S8c and S8d) exhibit distinctly different transient spectral shapes (**Figure AII.8**) and evolution (**Figure 3.7**): the signatures of charge pair and separated charge carrier transients are no longer present and are replaced by an absorbance peaking further into the near-IR (>1150 nm) consistent with the singlet exciton absorption of polythiophenes in solution. Additionally, the PTAK ground-state bleach signature is blue-shifted by about 10 nm, still exhibits evidence of an underlying vibronic progression, and now shows a stimulated emission band (negative signal) at 650 nm. At the longest pump-probe delays examined, the broad spectrum of the

polythiophene triplet exciton centered at 900 nm appears for 80:20 CPEC (and very weakly for 60:40 and 20:80) and persists onto nanosecond timescales.

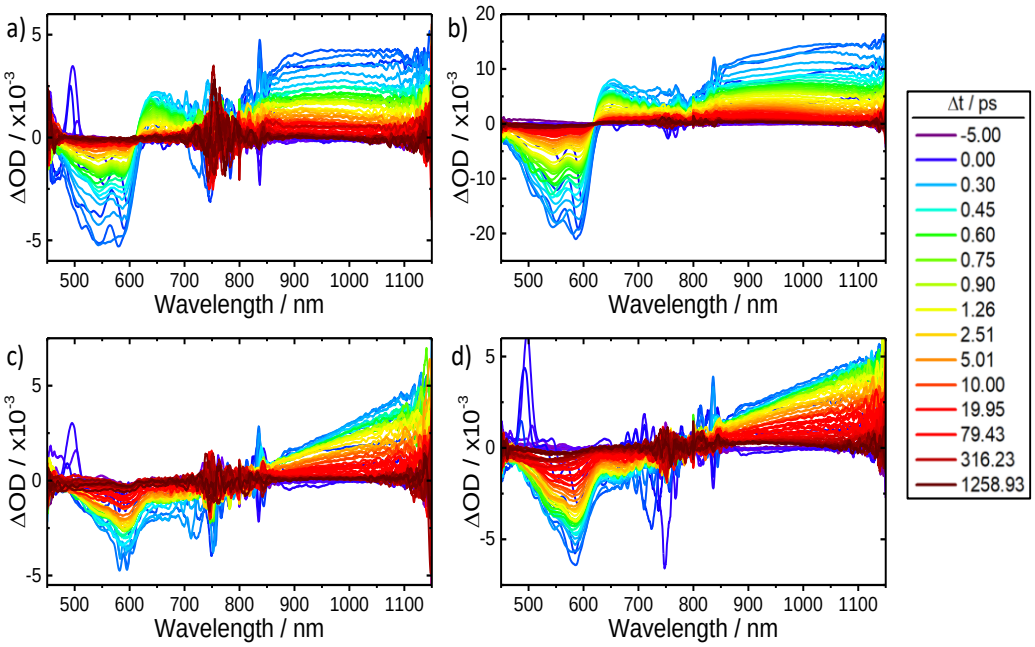

Figure AII.8. Transient absorption spectra of a) PTAK-60, b) CPEC 20:80, c) CPEC 60:40, and d) CPEC 80:20 collected for excitation with 600 nm light.

This comparison illustrates how the change in PTAK chain conformation with increasing PFPI composition impedes the formation of charge-separated species in PTAK that is commonly observed with lamellar-stacked ("H-aggregate") polythiophene domains. The spectra shown in **Figure AII.3a** reflect that changes in thiophene stacking behavior with complex formation favor population of singlet excitons upon photoexcitation. Additionally, the long-lived species absorbing at 900 nm (**Figure AII.8d**) is attributed to the triplet (T_1) absorption of PTAK as this feature appears where triplets have been observed in poly-3-hexylthiophene (P3HT)

films previously. Since this feature appears more prevalently for polythiophene solutions or in films of regiorandom rather than regioregular P3HT in which π-stacked aggregates are typically formed, the absence of this feature in transient spectra of CPECs with high PTAK weight percent is consistent with presence of parallel slip stacked polymer domains at these compositions.

Table AII.2: Parameters obtained from fits to traces collected with 360 and 600 nm excitation presented in **Figures 3.7b** and 3.**7a**, respectively, in the main text. CPEC samples are abbreviated by their PFPI:PTAK charge ratios. "---" indicates an unused parameter, while A_3 represents a constant offset for the 60:40 data set excited at 360 nm. PFPI cannot be directly excited using 600 nm light.

360	***PTAK***	***20:80***	***40:60***	***60:40***	***80:20***	***PFPI***
A_1	1.10	0.712	0.536	0.491	0.136	0.427
τ_1	0.598	0.965	1.48	2.14	1.46	3.32
A_2	0.194	0.273	0.391	0.417	0.390	---
τ_2	20.1	17.2	11.6	21.6	33.4	---
A_3	---	0.102	0.142	0.074	0.372	0.542
τ_3	---	474	412	---	1030	642
600	***PTAK***	***20:80***	***40:60***	***60:40***	***80:20***	***PFPI***
A_1	0.638	0.690	0.853	0.431	0.359	
τ_1	0.21	0.18	0.17	0.13	1.39	
A_2	0.259	0.222	0.411	0.328	0.376	
τ_2	1.86	2.03	5.19	3.61	19.8	
A_3	0.103	0.088	0.040	0.241	0.265	
τ_3	40.7	43.0	118	56.0	244	

S4. TIME-RESOLVED PHOTOLUMINESCENCE SPECTROSCOPY

We performed time-resolved PL (TRPL) measurements to complement the ultrafast measurements described above. **Figure AII.9** displays TRPL decays on a semilogarithmic ordinate scale collected at 650 nm and excited at 550 nm. This corresponds to excitation of PTAK only, allowing us to probe changes in PTAK exciton dynamics as a function of *R*. We find that a biexponential fit with a short and a long component with lifetimes τ_{short} and τ_{long}, respectively, is sufficient to describe the dynamics for all *R*.[4-5] Figure 9 shows that as *R* decreases, τ_{short} decreases, while its contribution to the biexponential decay increases. This observation is consistent with the relatively small steady-state PL quantum yield, as described above. The long component dominates for large *R.* Interestingly, though the long component is the minor contributor at small *R*, τ_{long} is slightly longer for small *R*.

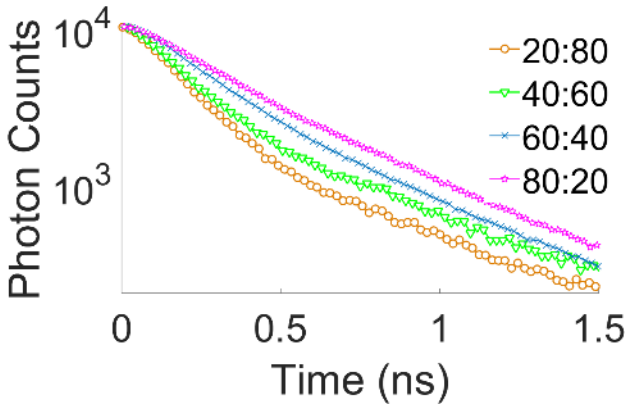

Figure AII.9. Magic-angle time-resolved PL decays as a function of PFPI:PTAK charge ratio (legend). The excitation wavelength is 550 nm, which corresponds to selective PTAK excitation.

We believe that the behavior of τ_{long} can be explained by an increase in the population of highly extended PTAK chains as *R* increases. At low PFPI fraction, PTAK remains largely self-coiled due to π-π interactions, with only a small population being made of up of largely isolated and extended chains. Emission from these extended chains can only occur if they have been excited directly, or else had excitons from neighboring chains diffuse to them. Because the initial population of extended chains is low, this diffusion process is relatively slow and so τ_{long} in the PTAK major regime reflect the intrinsic lifetime of the long-component of an extended chain, in addition to the time is takes an exciton to diffuse to it. As *R* increases, interactions between the natively extended PFPI chains overcomes the π-π interactions between PTAK chains and increase the population of extended PTAK chains, lowering the time needed to diffuse to these extended sites. As mentioned in the manuscript, above the charge neutrality threshold, there is sufficient PFPI to completely disaggregate and straighten nearly all PTAK chains, and so τ_{long} no longer drifts. Under this framework a tightly bound network of largely self-aggregating CPEs slowly gives way to a more open network of largely linearized chains as the inter-CPE interactions over comes the totality of π-π interactions.

Table AII.3: Parameters obtained by fitting magic angle TRPL data to a sum of exponential decays model. For all decays, three exponentials were needed to produce satisfactory residuals and minimize χ^2.

CPEC	α_1	τ_1 *(ns)*	α_2	τ_2 *(ns)*	α_3	τ_3 *(ns)*	$<\tau>$ *(ns)*	$<\tau>_{\tau1, \tau2}$ *(ns)*	χ^2
10:90	0.819	0.131	0.167	0.567	0.014	1.864	0.508	0.336	1.041
20:80	0.830	0.102	0.156	0.556	0.014	1.913	0.543	0.331	1.039
30:70	0.898	0.081	0.091	0.483	0.011	1.515	0.387	0.232	1.061
40:60	0.741	0.116	0.243	0.559	0.015	1.561	0.502	0.387	1.002
60:40	0.680	0.148	0.315	0.519	0.004	1.340	0.398	0.378	1.048
70:30	0.581	0.186	0.416	0.533	0.003	1.406	0.431	0.420	1.098
80:20	0.556	0.180	0.442	0.524	0.002	2.038	0.445	0.420	0.996
90:10	0.566	0.206	0.433	0.550	0.001	2.464	0.456	0.436	1.008

Including the third term, which for all samples accounts for less than 1.5% of the decay, in the average photoluminescence lifetime calculation leads to a trend in lifetimes which does not appear to reflect changes seen in steady-state PL intensity. That is, less quenched samples (such as 90:10) are expected to have longer lived fluorescence than more quenched samples (such as 10:90). In columns 9 and 10 we present the average lifetime (**$<\tau>$**) and average lifetime using only the first two

decay components ($<\tau>_{\tau1,\tau2}$). Because the latter is in agreement with steady-state experiments, we expect that it more accurately reflects the true average lifetimes of the samples.

Table AII.4: Parameters obtained by fitting anisotropy decays (excitation: 400 nm, emission 650 nm) to a sum of two stretched exponential decays.

CPEC	α_1	β_2	τ_1 *(ns)*	α_2	β_2	τ_2 *(ns)*	R^2
10:90	0.871	1.46	0.83	0.133	3.77	2.52	0.95
20:80	0.772	1.23	1.01	0.275	1.21	2.18	0.94
30:70	0.755	1.22	0.76	0.261	3.00	2.47	0.91
40:60	0.590	1.36	0.90	0.411	2.99	2.21	0.94
60:40	0.853	2.55	2.21	0.144	1.12	2.58	0.93
70:30	0.215	0.799	1.50	0.805	3.11	2.75	0.92
80:20	0.102	1.41	0.49	0.900	2.96	2.51	0.94
90:10	0.268	1.04	1.41	0.741	2.92	2.47	0.93

Table AII.5: Parameters obtained by fitting anisotropy decays (excitation: 550 nm, emission 650 nm) to a single stretched exponential decay.

CPEC	α_1	β_2	τ_1 *(ns)*	R^2
10:90	1	1.66	2.72	0.89
20:80	1	1.71	2.88	0.90
30:70	1	1.76	3.44	0.89
40:60	1	2.46	3.42	0.93
60:40	1.11	4.14	4.61	0.92
70:30	1	4.98	4.71	0.87
80:20	1	4.22	4.40	0.91
90:10	1	4.16	4.27	0.87

Table AII.6: Fundamental Anisotropies (r_0) of CPECs exciting at either 400 nm or 550 nm and holding emission wavelength fixed at 650 nm.

CPEC	*400 nm Excitation*	*550 nm Excitation*
10:90	0.271	0.412
20:80	0.244	0.451
30:70	0.193	0.391
40:60	0.259	0.469
60:40	0.280	0.402
70:30	0.256	0.351
80:20	0.311	0.400
90:10	0.256	0.382
PTAK	0.448	0.472

For randomly oriented fluorophores in solution before any depolarization occurs, the fundamental anisotropy, r_0, is expected to 0.4.[6] We may expect this condition to hold when exciting pure PTAK (550 nm excitation). In this regime, $\langle r_0 \rangle = 0.414$, in reasonable agreement with the expected value. $\sigma_{R0} = 0.0413$, and most samples fall within one standard deviation of the mean. Pure PTAK and the 40:60 CPEC lie above, while the 70:30 sample lies below. These deviations represent the natural

uncertainty in our calculations. For samples excited at 400 nm, there is an expected scrambling of transition dipoles due to energy transfer from PFPI to PTAK, requiring that the fundamental anisotropies lie below 0.4.

S5. Zeta Potential Measurements

To measure the zeta potential of the CPEs at different molar charge ratios. All CPEC solutions were filtered through 0.8 um cellulose acetate membrane filters.

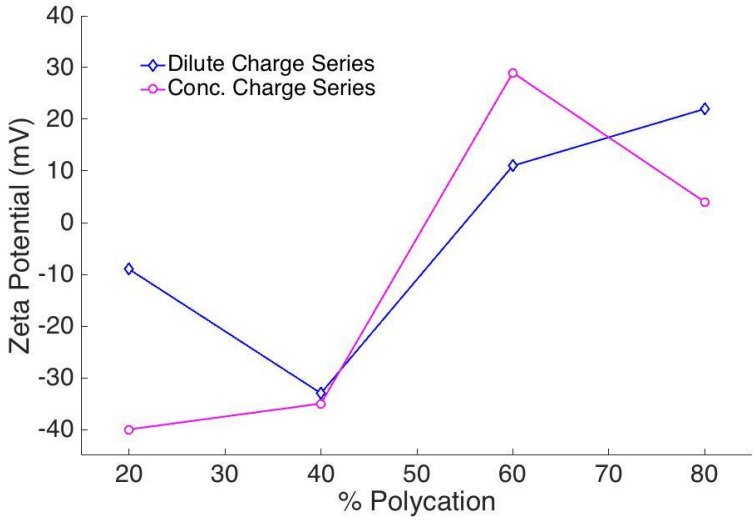

Figure AII.10. Zeta potential of CPECs at varying molar charge ratios for dilute (0.1 mg/mL) and concentrated (1.0 mg/mL) solutions.

The zeta potentials of the complexes were then analyzed by phase analysis light scattering using a Brookhaven ZetaPALS zeta potential analyzer (Brookhaven Instruments Corporation, USA). The Smoluchowski approximation was used. The dielectric constant, refractive index and viscosity were assumed to be the same as for water. Measurements were carried out at room temperature (~22 ^{o}C).

S6. Dynamic Light Scattering

Solutions were filtered using 0.8 µm filters directly into borosilicate glass test tubes. Samples were immersed in decalin to match the index of refraction of glass. All DLS measurements were made on a Brookhaven BI-200SM goniometer system using a TurboCorr photon counter and digital correlator at room temperature. The light source was a CW Mini-L30 solid-state diode laser outputting 637 nm light with adjustable power limited to 35 mW. The incident power was adjusted so as to not to exceed a signal intensity of 200 cps. Scattered photons were detected by an avalanche photodiode detector. The normalized light intensity correlation functions were transformed to the electric-field correlation function using the Siegert relation.[7] The field correlation functions were analyzed using CONTIN,[8] which is a regularized least-squares algorithm originally due to Provencher and since emulated by Marino in MATLAB. Distribution of relaxation times were obtained for scattering angles of 20, 45, 90, 120 and 155 degrees with the regulation parameter

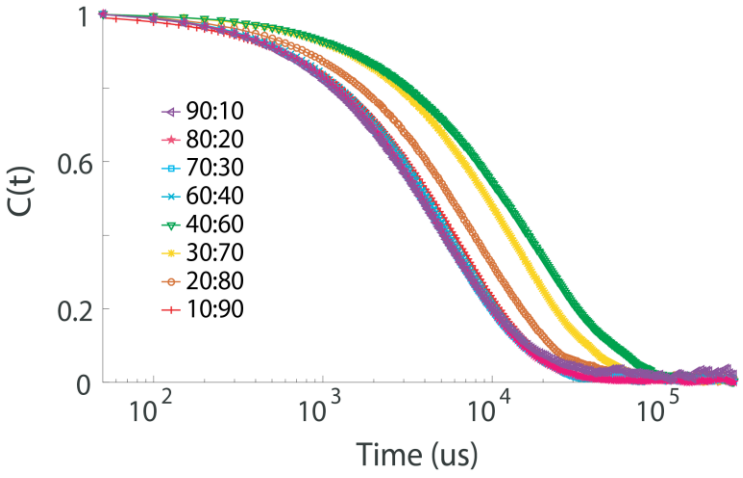

Figure AII.11. Normalized scattered light intensity autocorrelation functions of CPECs at varying molar charge ratios collected at a 20° scattering angle.

(α) set to 0.2. Various choices for α as well as various grid densities for the relaxation time space were explored. We found that relaxation times obtained with different choices of α were similar. A larger value of α was avoided so as to not overly smooth the relaxation time distribution. Hydrodynamic radius values were obtained using the Stokes−Einstein relation.[7]

Table AII.7. CONTIN fit results of DLS autocorrelation functions from CPECs for varying molar charge ratios. Values correspond to mean peak heights of relaxation time distributions.

PFPI:PTAK Molar Charge Ratio	**Relaxation time (us)**	**R_H (nm)** [a]
90:10	10160	27
80:20	13720	36
70:30	9216	24
60:40	11815	31
40:60	51285	136
30:70	31465	83
20:80	21650	57

[a] Intensity-weighted hydrodynamic radius from dynamic light scattering.

REFERENCES

1. Yu, W.; Magnanelli, T. J.; Zhou, J.; Bragg, A. E. Structural Hetrogeneity in the Localized Excited States of Poly(3-hexylthiophene). *Journal of Physical Chemistry B* **2016,** *120*, 5093-5102.

2. Smith, M. C.; Snyder, J. A.; Striefel, B. C.; Bragg, A. E. Ultrafast Excited-State Dynamics of ortho-Terphenyl and 1,2-diphenylcyclohexene: The Role of "Ethylenic Twisting" in the Nonadaibatic Photocyclization of Stilbene Analogs. *Journal of Physical Chemistry Letters* **2013,** *4*, 1895-1900.

3. Bragg, A. E.; Yu, W.; Zhou, J.; Magnanelli, T. Ultrafast Raman Spectroscopy as a Probe of Local Structure and Dynamics in Photoexcited Conjugated Materials. *The Journal of Physical Chemistry Letters* **2016,** *7* (19), 3990-4000.

4. Preus, S. DecayFit - Fluorescence Decay Analysis Software 1.3, FluorTools, www.fluortools.com.

5. O'Connor, D. *Time-Correlated Single Photon Counting*. Elsevier Science: 2012.

6. Lakowicz, J. R. *Principles of Fluorescence Spectroscopy*. Springer US: 2007.

7. Berne, B. J.; Pecora, R. *Dynamic Light Scattering: With Applications to Chemistry, Biology, and Physics*. Dover Publications: 2013.

8. Provencher, S. W.; Štêpánek, P. Global Analysis of Dynamic Light Scattering Autocorrelation Functions. *Particle & Particle Systems Characterization* **1996,** *13* (5), 291-294.

APPENDIX III

Supporting Information for:

Activation and Formation of Aqueous Exciton Transport Networks

S.1 Experimental Methods

S.1.1 Steady-State Photoluminescence/Kinetics

Photoluminescence spectra were collected on a Horiba Fluoromax-4 spectrofluorometer with 1 nm excitation and emission slit widths. Temperature was controlled by a Quantum Northwest TC 1 temperature controller interfaced with a Horiba Peltier Heater. All kinetics measurements were taken in a 1 cm square cuvette, with the solutions stirred at 1200 rpm using an inbuilt stirrer and stir bar in the cuvette.

Kinetics experiments were carried out as follows: The cuvette, with stir bar, was filled with 2.1 mL of 0.100 mg/mL (0.288 mM charged subunit). The cuvette was quickly placed in the Peltier heater in the spectrofluorometer, and 900 µL of the relevant acceptor CPE was added (either 0.059 mg/mL – 0.284 mM charged subunit – RePTAK/RaPTAK or 0.082 mg/mL – 0.0288 mM charged subunit – PCPT) was quickly added. The volumes added correspond to a 70:30 PFP:Acceptor ratio on the basis of charged subunit, IE 70 cationic sidechains: 30 anionic sidechains. Measurements were immediately started, before appreciable complexation could take place. A photoluminescence spectrum for PFP (λ_{EX} = 375 nm) was captured first, immediately followed by an acceptor photoluminescence spectrum (RePTAK λ_{EX} = 550 nm, RaPTAK λ_{EX} = 500 nm, PCPT λ_{EX} = 500 nm). All

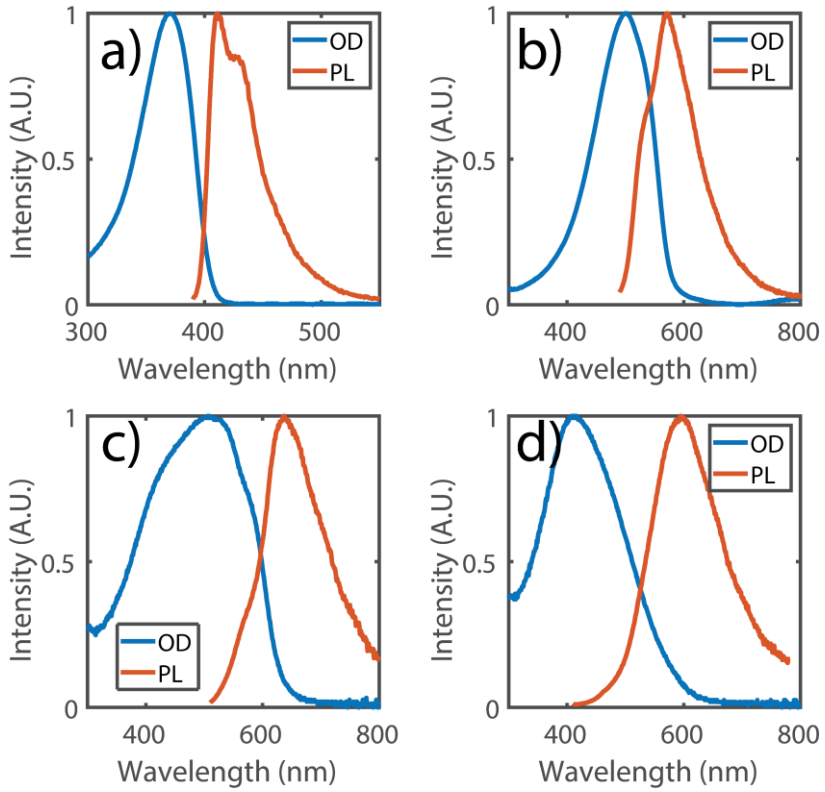

Figure AIII.1: Optical density (OD) and photoluminescence (PL) spectra of PFP (a), PCPT (b), RREG PTAK (c), RRAN PTAK (d).

photoluminescence spectra were captured from 350 nm to 800 nm. Acceptors were excited at higher wavelengths than their λ_{MAX} in order to avoid exciting PFP. This process was carried out 60 times at three-minute intervals at each temperature referenced in **Figure 4.2**. Kinetics curves for a given temperature and CPE were created by integrating the photoluminescence spectra of the relevant CPE at each time point and plotting them against time. The curves were normalized by dividing by the time zero data point in order to show the relative change. All data analysis was carried out in MATLAB 2018a.

The fast and slow rates of complexation for a given kinetics curve were found by fitting the curve to a function of two rising exponentials using the MATLAB Curve Fitting Toolbox. The results of these fits can be found in **Table AIII.1**.

$$a_1 * (1 - e^{-b_1 * t}) + a_2 * (1 - e^{-b_2 * t}) + C \quad \text{(AIII.1)}$$

	a_1	a_2	b_1	b_2	C	R^2
PFP:RePTAK						
20 °C	0.194	0.463	0.025	25.58	0.554	0.9953
30 °C	0.251	0.381	0.094	0.012	0.983	0.9991
40 °C	0.547	0.437	0.018	0.161	0.930	0.9996
50 °C	0.745	0.670	0.148	0.016	0.898	0.9995
55 °C	0.978	0.858	0.167	0.017	0.846	0.9994
65 °C	1.309	0.945	0.190	0.016	0.775	0.9988
75 °C	1.393	0.995	0.188	0.011	0.774	0.9978
90 °C	1.530	1.426	0.007	0.308	0.614	0.9990
PFP:RaPTAK						
20 °C	0.822	-0.683	0.092	0.096	1.007	0.9441
30 °C	0.142	0.277	0.299	0.039	1.000	0.9984
40 °C	0.278	0.268	0.039	0.302	1.000	0.9986
50 °C	0.330	0.305	0.319	0.035	1.001	0.9990
55 °C	0.339	0.266	0.336	0.029	1.002	0.9986
65 °C	0.278	0.360	0.023	0.301	1.004	0.9971
75 °C	0.356	0.313	0.025	0.295	1.002	0.9993
90 °C	0.196	0.283	0.051	0.296	1.001	0.9989

Table AIII.1: Fitting parameters for Equation 1 found using the Curve Fitting Toolbox in MATLAB 2018a.

Arrhenius plots for the fast and slow rates of RaPTAK and RePTAK were formed by plotting the natural logarithm of the respective rate against the inverse of the thermodynamic temperature, following the linearized Arrhenius equation.

$$\ln k = \frac{-E_a}{RT} + \ln A \qquad \text{(AIII.2)}$$

Where k is the rate, E_a is the activation energy, R is the gas constant (8.314 J/mol*K), T is the thermodynamic temperature, and A is the collisional frequency. For RePTAK, the inflection point in the Arrhenius plot was taken to occur at ~35 °C. The fitting range for the high activation energy regime was 20 – 40 °C, while the range for the low activation energy regime was 40 – 90 °C.

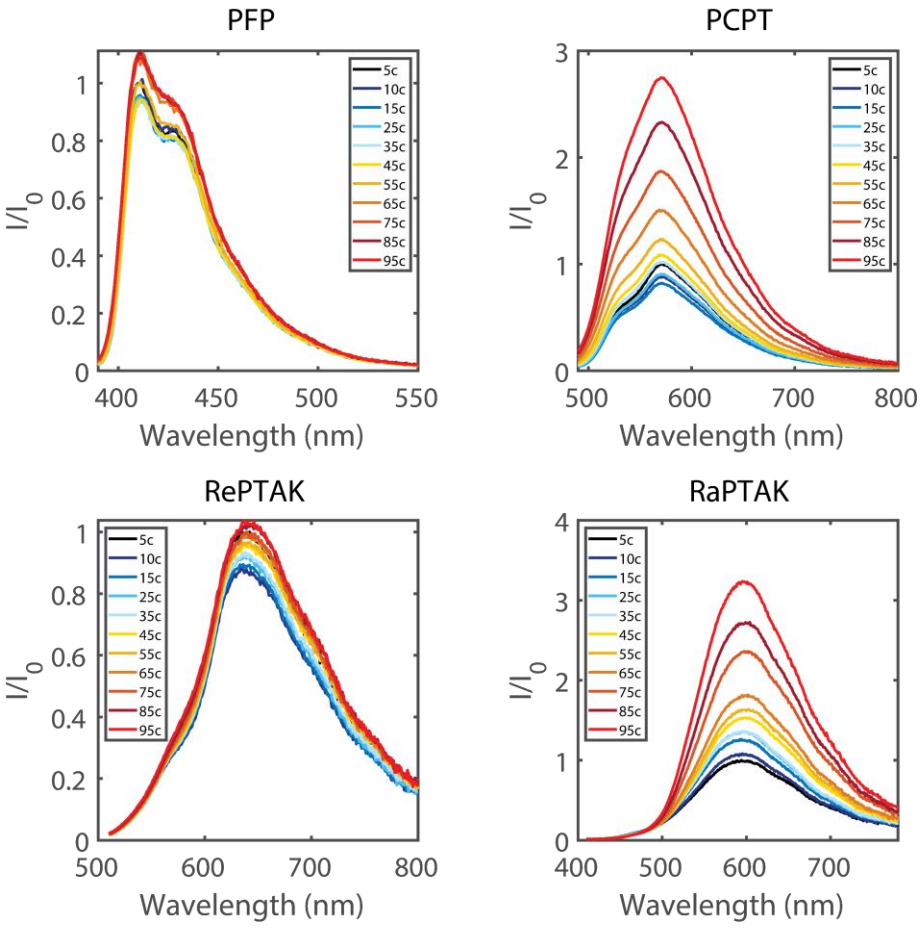

Figure AIII.2: Solution photoluminescence spectra of the four CPEs used in this study, at various temperatures. The figures have been normalized to the maximum intensity of photoluminescence at 5 °C for each CPE. PFP and RePTAK have minimal response to temperature response, while PCPT and RaPTAK enjoy a significant increase in PLQY at elevated temperatures.

Temperature response measurements, **Figure AIII..2**, were taken on the same instrument in a 1 mm rectangular cuvette and were equilibrated for five minutes at each temperature. Owing to the cuvette size, the CPEs were not stirred. The measurements were taken with pure solutions of the four CPEs, at concentrations matching those used to prepare the CPECs for the kinetics experiments. The measurements were taken exciting at the λ_{MAX} for each CPE: PFP λ_{EX} = 375 nm, RePTAK λ_{EX} = 500 nm, RaPTAK λ_{EX} = 400 nm, PCPT λ_{EX} = 480 nm. Emission was collected over the range shown in the figure. For each CPE, the spectra were normalized to the maximum photoluminescence intensity at 5 °C.

S.1.2 Time-Resolved Photoluminescence Anisotropy

Time-correlated single photon counting (TCSPC) was carried out on a homebuilt system, which has been described previously. Our excitation source is a pulsed supercontinuum laser coupled to an acousto-optic filter and external radio frequency driver for wavelength selection. Measurements were carried out at a 78 MHz repetition rate. The output of the laser is inherently elliptically polarized. To carry out anisotropic measurements, the native laser light was first passed through a ½ λ plate to rotate the polarization 90°, then passed through a vertically aligned Glan-Thompson polarizer. This ensured the excitation source was a vertically polarized linear beam. A second Glan-Thompson controlled the polarization of the observed emitted light. Both polarizers were mounted on motorized stages under computer control. Emitted light was passed through a set of achromatic doublets to

a monochromator which allowed us to detect a single wavelength at a time. Detection was via a Becker & Hickl hybrid photomultiplier tube with minimal afterpulsing and photon counter was carried out by a Simple-Tau 130 TCSPC board. Collection times were such that the signal in the main channel reached 10,000 counts under vertical-vertical conditions, and vertical-horizontal measurements were carried out for the same amount of time. Anisotropy data were time-shifted such that the half-rise time of the respective vertical-vertical and vertical-horizontal measurements were the same. The anisotropy calculation was carried out in MATLAB according to:

$$r(t) = \frac{I_{VV}(t) - G * I_{VH}(t)}{I_{VV}(t) - 2G * I_{VH}(t)} \quad \text{(AIII.3)}$$

Where r(t) is the anisotropy at some time t, $I_{\parallel}(t)$ and $I_{\perp}(t)$ are the TCSPC intensities at time t, and G is the G-factor – the system detection efficiency for a given wavelength of light.

$$G = \frac{\int I_{HV}(t)dt}{\int I_{HH}(t)dt} \quad \text{(AIII.4)}$$

Anisotropic decays were collected at 600 nm for PCPT and 650 nm for RaPTAK, with corresponding G-factors of $G_{600\ nm}$ = 0.1742 and $G_{650\ nm}$ = 0.1745.

S.1.3 Isothermal Titration Calorimetry

S.1.3.1 ITC Methods

Isothermal titration calorimetry (ITC) was carried out on a MicroCal VP-ITC calorimeter from Malvern. The instrument has an allowed temperature range of 2°C - 80°C. Before and after each experiment, the sample chamber was thoroughly washed with a 5% detergent solution (CONTRAD 70) followed by MilliQ and HPLC grade water. Opening we covered when the instrument was not in use, to prevent the introduction of dust into the system. Similarly, all needles used to introduce sample or for cleaning were wiped down. The needles and syringes in contact with samples were thoroughly equilibrated with HPLC water before being used. All samples were prepared with HPLC water (Sigma Aldrich) passed through a 0.45 µm glass fiber filter with a polypropylene housing into clean vials. Samples were degassed using the supplied de-gassing unit (a fixed stir plate with an applied vacuum), and care was taken to avoid introducing air bubbles into the instrument. The syringe volume used was 280 µL, and the cell volume was 1400 µL. Injections were allowed to continue until the syringe volume was exhausted. Injection schedules, cell, and syringe volumes can be found in **Table AIII.2**. All measurements were carried out at a stir speed of 177 RPM. Temperature and baseline equilibration were carried out automatically

	# of Pre-Inj.	*Pre-Inj. Vol. (µL)*	*Pre-Inj Time (s)*	*Inj. Vol. (µL)*	*Inj. Time (s)*	*Inj. Wait Time (s)*	*Cell Conc. (mM)*	*Syringe Conc. (mM)*
PFP:RePTAK								
25 °C	4	2	4	8	16	180	0.028	1.68
50 °C	4	2	4	6	12	180	0.028	0.28
65 °C	4	2	4	8	16	180	0.028	0.28
PFP:RaPTAK								
25 °C	4	2	4	8	16	180	0.028	1.44
50 °C	4	2	4	6	12	180	0.028	0.28
65 °C	4	2	4	6	12	180	0.028	0.28
PFP:PCPT								
25 °C	4	2	4	6	12	180	0.028	0.28
50 °C	4	2	4	6	12	180	0.028	0.28
65 °C	4	2	4	6	12	180	0.028	0.28

Table S2: Injection schedule, cell and syringe concentrations for all ITC experiments. All experiments were carried out at a stir rate of 177 RPM, and injections were allowed to continue until syringe volume was exhausted.

S.1.3.2 ITC Analysis

Analysis and plotting of ITC data was carried out using the SEDPHAT package, courtesy of the National Institutes of Health. The SEDPHAT package consists of three standalone cooperative pieces of software: NITPIC, which reads, integrates, and carries out automated peak shape analysis on raw ITC data; SEDPHAT, which carries out global analysis of integrated ITC data; and GUSSI, which is used for data plotting. NITPIC carries out automated integration, with error bars, and peak shape analysis of raw ITC data, as well as an automated baseline correction. Because of this automated baseline correction, we declined to apply a manual correction from measured heat of dilution data. The resulting NITPIC integration tables can be

exported directly into a SEDPHAT readable format, allowing for analysis using models from SEDPHAT's extensive library. A full description of SEDPHAT's capabilities, as well as detailed experimental protocols and examples are outlined in several excellent papers by Zhao, Schuck, and Brautigam.

For our analysis we relied on the in-built symmetric two-site binding model, using the weighted fit from NITPIC. This binding model has a general reaction scheme shown in **Scheme 4.1**

$$A + B \underset{}{\overset{k_1}{\longleftrightarrow}} AB + B \underset{}{\overset{\alpha k_2}{\longleftrightarrow}} ABB$$

in the main text and reproduced here. The experimental parameters for this scheme are $log(K_{AB})$ ΔH_{AB}, $\Delta H_{ABB} - \Delta H_{AB}$, $log(K_{ABB}/K_{AB})$, and the incompetent fraction of A. For our purposes, A is a carboxylate sidechain of PTAK, and B is one of the quaternary ammonium sidechains of PFP or one of the sulfate sidechains of PCPT, where appropriate. In relation to **Scheme 4.1**, subscripts AB refer to equilibrium 1, and subscripts ABB refer to equilibrium 2. The incompetent fraction of A refers to the fraction of sidechains which do not bind to a partner. In general, we expect some fraction of sidechains to remain unbound, in order for the complex to remain soluble. Fitting was carried out using non-linear least squares methods to optimize a global reduced χ^2 parameter. This was done by alternating between the Levenberg – Marquardt and simplex algorithms until no change was observed in the global

reduced χ^2 parameter. The relevant concentration and heat effect data can be evaluated from the following:

$$[A]_T = [A] + K_1[A][B_1] + K_2[A][B_2] + \alpha K_1K_2[A][B_1][B_2]$$
$$[B_1]_T = [B_1] + K_1[A][B_1] + \alpha K_1K_2[A][B_1][B_2]$$
$$[B_2]_T = [B_2] + K_2[A][B_2] + \alpha K_1K_2[A][B_1][B_2] \quad \text{(AIII.5)}$$

$$[A]_{T,I} = [M]_0(1-v/V)^i$$
$$[B_1] = [B_1]_0(1-(1- v/V)^i)$$
$$[B_2] = [B]_0(1- v/V)^I \quad \text{(AIII.6)}$$

$$q_i = V(\Delta H_1([AB_1]_i - [AB_1]_{i-1}(1- v/V)^i) + (\Delta H_2([AB_2]_i - [AB_2]_{i-1}(1- v/V)^i) + (\Delta H_1 + \Delta H_2 + \Delta h)$$
$$X ([AB_1B_2]_I - [AB_1B_2]_{i-1}(1-v/V))) . \quad \text{(AIII.7)}$$

Equations in (**AIII.5**) are derived from the mass action law associated with the kinetic scheme presented above. α is the cooperativity parameter, which can take values ≥ 0. Certain values of α lend themselves to physical interpretation: α = 0, maximally competitive binding; 0 < α < 1, negative competitive binding; α = 1 independent binding; α >1, cooperative binding. In (6), v is the volume of a given injection and V is the total cell volume while $[A]_0$, $[B_1]_0$, $[B_2]_0$ are the initial concentrations of the ligands. In (**AIII.7**) Δh is the enthalpy associated with cooperative/competitive binding effects. A full analysis of these expressions can be found in works by Velazquez-Campoy *et al*, Friere *et al,* Brown, and Brautigam, along with their relations to the more common thermodynamic parameters.

Other groups studying similar systems have elected to employ analytic models, or else to avoid model fitting altogether. Our decision to use a symmetric two-site model is based on what we consider to be the fundamental unit of interaction between the CPEs – that is, the sidechains. While complexation of PEs (and likely CPEs) is not driven by electrostatic interactions – the net favorable change in enthalpy due to sidechain – sidechain interactions versus sidechain – solvent or sidechain – counterion interactions – the CPE complexation is nonetheless mediated primarily through sidechain interconnectivity. In that context it seems reasonable to us to employ a symmetric two-site model for interactions between PFP and either of the PTAKs, owing to the two-to-one ratio between their sidechains. We can envision that between monomers a single carboxylate and single quaternary ammonium can form an interaction pair, AB_1, and that the remaining geminal quaternary ammonium, B_2, can form a ternary interaction complex, AB_1B_2. We would further expect that the binding affinity and thermodynamics of the addition of B_2 to the complex should be modulated via electrostatics and/or sterics of the preexisting AB_1 complex, giving rise to the α term. It is unclear to us whether the geminal quaternary ammoniums can simultaneously interact with the carboxylates on adjoining thiophene monomers (a 1:1 interaction in that case), and whether that specific interaction is common in the system. The use of the two-site model was carried through to the PFP:PCPT complexes, despite a 1:1 sidechain ratio due to the qualitative similarity between PCPT and PTAK thermogram profiles. While

the PCPT thermograms are generally well fit by this model, we note that the fitting is inferior to the PTAK complexes. However, simpler one-site models do a significantly worse job fitting the PCPT complexes, and so we remain satisfied with the use of the two-site model. The full fitting parameters, as well as the extracted thermodynamics parameters for each sample can be found in **Table AIII.3.a, AIII.3.b,** and **AIII.4**.

	ΔG_1 (kJ/mol)	ΔH_1 (kJ/mol)	$-T\Delta S_1$ (kJ/mol)	k_1 (M^{-1})	ΔG_2 (kJ/mol)	ΔH_2 (kJ/mol)	$-T\Delta S_2$ (kJ/mol)	k_2 (M^{-1})
PFP:RePTAK								
25 °C	-30.28	30.36	-60.64	2.02E+05	-21.09	110.29	-131.38	4.98E+03
50 °C	-52.31	-14.08	-38.23	2.85E+08	-43.55	-31.52	-11.83	1.03E+07
65 °C	-43.33	-8.08	-35.25	4.94E+06	-39.01	-121.04	82.07	1.07E+06
PFP:RaPTAK								
25 °C	-31.92	17.16	-49.08	4.21E+05	-21.27	107.74	-129.01	5.35E+03
50 °C	-51.95	-9.1	-42.85	2.50E+08	-39.9	-17.57	-22.33	2.84E+06
65 °C	-51.49	-13.8	-37.69	9.98E+07	-39.61	-29.08	-10.53	1.32E+06
PFP:PCPT								
25 °C	-43.38	-4.07	-38.03	3.97E+07	-43.24	-6.23	-37.01	3.80E+07
50 °C	-44.95	-0.26	-44.67	1.82E+07	-45.32	-16.86	-28.46	2.13E+07
65 °C	-58.12	7.09	-66.3	9.51E+08	-46.1	-1.09	-45.01	1.33E+07

Table AIII.3.a: Thermodynamic parameters for the formation of the binary (AB) and ternary (ABB) complexes. The parameters for the second binding event do not consider any potential cooperativity or competition between the interacting side chains.

	$\Delta G_{co\text{-}op}$ (kJ/mol)	$\Delta H_{co\text{-}op}$ (kJ/mol)	$-T\Delta S_{co\text{-}op}$ (kJ/mol)	$\alpha_{co\text{-}op}$	ΔG_{tot} (kJ/mol)	ΔH_{tot} (kJ/mol)	$-T\Delta S_{tot}$ (kJ/mol)	k_{tot} (M^{-2})
PFP:RePTAK								
25 °C	9.19	79.74	-70.75	0.0246	-42.18	220.39	-262.77	2.47E+07
50 °C	8.94	-17.39	26.32	0.0359	-86.92	-62.99	-23.74	1.05E+14
65 °C	4.23	-113.09	117.256	0.219	-78.11	-242.21	164.076	1.16E+12
PFP:RaPTAK								
25 °C	10.82	90.58	-79.76	0.0127	-42.37	215.48	-257.85	2.86E+07
50 °C	12.03	-8.46	20.5	0.0114	-79.82	-35.13	-44.68	8.09E+12
65 °C	11.85	-15.28	27.14	0.0148	-79.25	-58.16	-21.08	1.95E+12
PFP:PCPT								
25 °C	0.11	-0.89	1.00	0.957	-86.51	-11.19	-74.04	1.44E+15
50 °C	-3.97	-16.58	16.19	1.16	-94.24	-33.7	-56.94	4.50E+14

65 °C	12	-8.18	20.19	0.014	-92.22	-2.18	-91.12	1.77E+14

Table AIII.3.b: Thermodynamic parameters for cooperative and competitive interactions, and for the formation of the ternary complex taking those interactions into account.

	log(K_{AB})	*ΔH_{AB}* (kcal/mol)	*$\Delta H_{ABB} - \Delta H_{AB}$* (kcal/mol)	*log(K_{ABB}/K_{AB})*	*Incompetent Fraction A*
PFP:RePTAK					
25 °C	5.31 (4.94 – 5.58)	7.26 (5.62 – 16.73)	19.10 (14.47 – 42.14)	-1.61 (-1.82 – -1.36)	0.38 (0.26 – 0.69)
50 °C	8.46 (7.51 – 9.44)	-3.37 (-3.95 – -1.88)	-4.16 (-7.17 – -2.96)	-1.44 (-2.31 – -0.54)	0.77 (0.76 – 0.78)
65 °C	6.69 (*)	-1.93 (*)	-27.00 (*)	-0.66 (*)	0.85 (*)
PFP:RaPTAK					
25 °C	5.62 (*)	4.10 (3.65 – 5.74)	(*)	-1.89 (-6.35 – -1.26)	0.00 (0.00 – 0.98)
50 °C	8.40 (7.83 – 9.07)	-2.18 (-2.36 – -1.96)	-2.02 (-2.53 – -1.67)	-1.94 (-2.54 – -1.46)	0.52 (0.51 – 0.53)
65 °C	7.95 (7.13 – 9.08)	-3.30 (-3.79 – -2.70)	-3.65 (-5.19 – -2.56)	-1.83 (-2.83 – -1.05)	0.51 (0.49 – 0.53)
PFP:PCPT					
25 °C	7.49 (1.74 – *)	(-1.26) (*)	-0.24 (*)	0.09 (-2.70 – *)	0.47 (0.46 – 0.48)
50 °C	7.27 (*)	-0.06 (*)	-3.97 (*)	0.06 (*)	0.53 (0.49 – 0.55)
65 °C	8.98 (5.74 – *)	1.69 (* - 3.10)	-1.96 (-4.53 – *)	-1.85 (*)	0.76 (0.65 – 0.91)

Table AIII.4: Values of parameters used to fit ITC data using the SEDPHAT software. Where possible, 95% confidence intervals are included in parenthesis. The confidence intervals are calculated by the software itself. For some parameters only a lower or upper bound could

be found within a reasonable search window, and for others no confidence interval could be found.

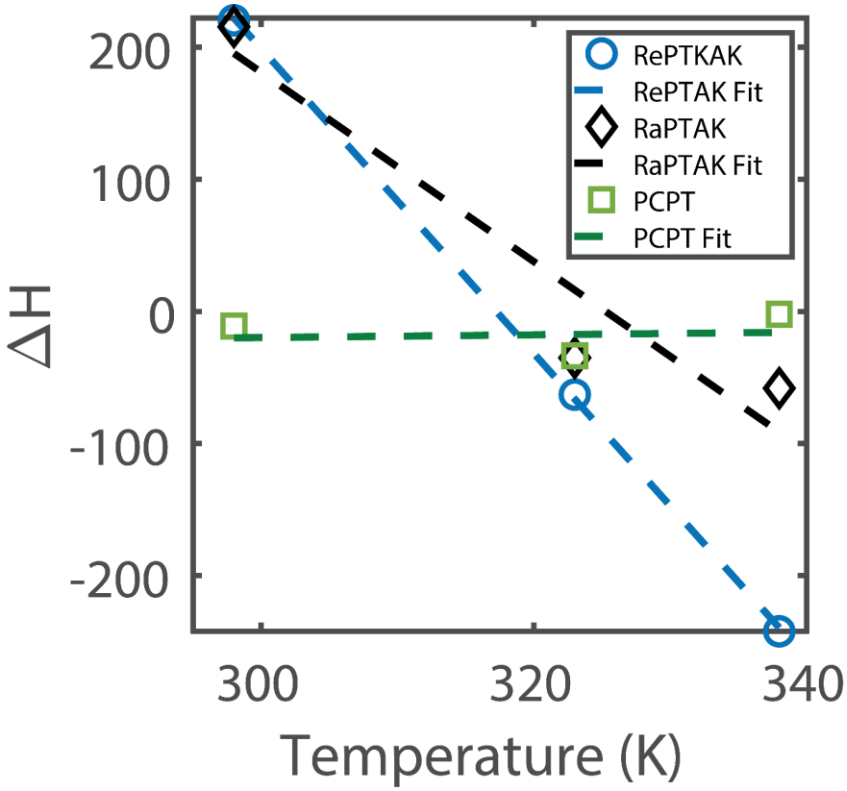

Figure AIII.3: Plot of the net enthalpy for the formation of an ABB complex vs the temperature of complexation. The slope represents the heat capacity, C_p of the system.

S.1.4 Solution Small Angle X-ray Scattering (SAXS)

Solution SAXS was carried out at the Stanford Synchrotron Radiation Laboratory (SSRL) using beamline 4-2 using a Dectris Pilatus3 X 1M photon counting detector. Samples were made prior to experiment and transferred thin-wall quartz capillary cells. Irradiation was via 11 keV X-rays (1.17 Å) with a sample to detector distance of 1.7 meters. All samples were filtered through 0.45 µm Nylon filter prior

to the experiment. For the three PFP:PCPT complexes, this resulted in most of the complex being removed from solution, with little scattering observed. Consequently, the scattering curves from *unfiltered* PFP:PCPT are presented in **Figure AIII.3, C**. For all samples, the scattering of the background solvent (HPLC water) was removed. This subtraction was done using SasTool, a software package developed at SSRL, which also carries out the conversion of the collected 2D TIFF images to traditional intensity vs scattering vector plots. Samples were oscillated during data collection to

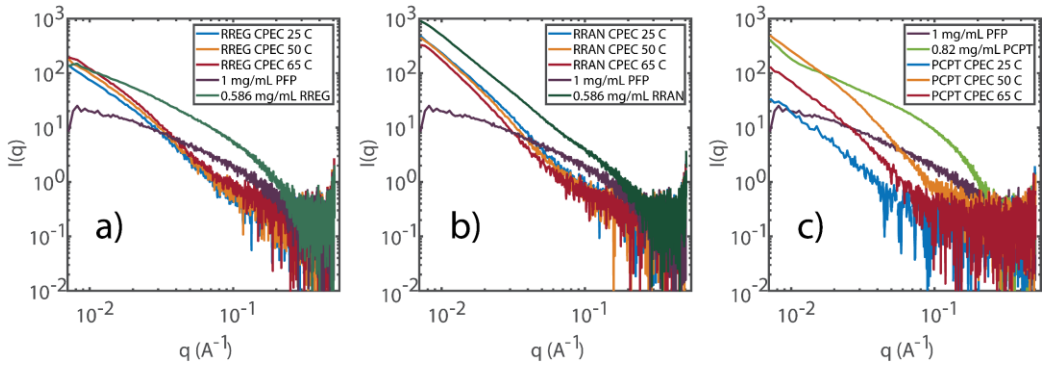

Figure AIII.4: Solution SAXS scattering curves for CPECs made between PFP and RREG PTAK (a), RRAN PTAK (b) or PCPT (c) at 25, 50, and 65 °C. Also included, the scattering curves of the pure CPEs dissolved in water.

avoid beam damage.

S.1.5 Sample Preparation

Conjugated polyelectrolyte poly([fluorene]-alt-co-[phenylene]), PFP, was obtained from Solaris Chem Inc. and had an average molecular weight (MW) of 21 KDa and a polydispersity index (PDI) of 1.2. Regioregular

poly(alkylcarboxythiophene) (RREG PTAK, MW = 16 KDa, PDI = 2.2) and regiorandom poly(alkylcarboxythiophene) (RRAN PTAK, MW = 8 KDa, PDI = 1.8) were obtained from Rieke Metals. Poly(cyclopentadithieno-alt-phenylene) (PCPT, MW = 40 KDa, PDI 3) was obtained from 1-Material. 10 mg/mL stock solutions for all conjugated polyelectrolytes were prepared by dissolving the conjugated polyelectrolytes in HPLC grade water (Fischer) and heating the solution to 70 °C for 24 hours with stirring. The stock solution for PFP was stirred for 72 hours. All materials were used as received, and care was taken to reduce exposure to light using foil.

Samples for steady-state spectroscopy were prepared at a 70:30 cation:anion ratio (PFP:RREG/RRAN/PCPT) based on the monomolar number concentration of sidechains. Solutions of 0.1 mg/mL PFP, 0.0586 mg/mL RREG and RRAN PTAK, and 0.082 mg/mL PCPT were made by dilution of the initial stocks with HPLC water. At these concentrations, all solutions have equal concentrations of charged sidechains on a monomolar basis. CPECs for study were made by mixing PFP with the relevant anionic partner in a 7:3 ratio on a volumetric basis (e.g. 700 µL PFP with 300 µL anionic CPE). The solutions were then heated at 70 °C and stirred for 24 hours. For all solutions the anionic component was added to PFP, and no additional water was used.

APPENDIX IV

Supporting Information for

Exciton Relaxation in Highly Rigid Conjugated Polymers: Correlating Radiative Dynamics with Structural Heterogeneity and Wavefunction Delocalization

S.1 CP1 Synthesis

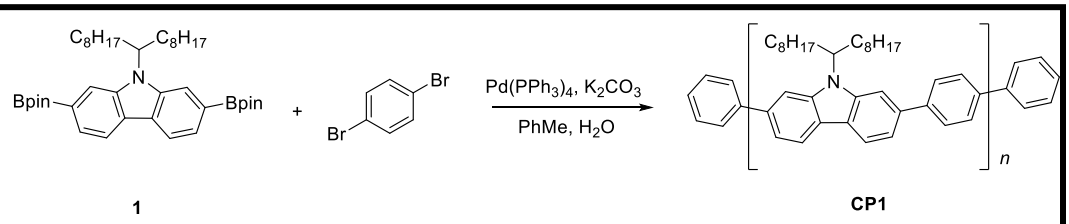

1 CP1

Scheme AIV.1. Synthesis of compound **CP1** from **1** and 1,4-dibromobenzene *via* Suzuki polymerization.

To a 50 mL Schlenk flask was added **1** (183 mg, 0.28 mmol), 1,4-dibromobenzene (66 mg, 0.28 mmol), $Pd(PPh_3)_4$ (32 mg, 10 mol%), K_2CO_3 (230 mg, 1.67 mmol), and Aliquat 336 (32 µL, 0.07 mmol) under N_2. Degassed toluene (5 mL) and water (1 mL) were added and further degassed 3 times by freeze-pump-thaw. The reaction mixture was stirred at 100 ^oC for 24 h, before it was cooled down to room temperature. Bromobenzene (4 equiv.) was added into the flask, and the mixture was stirred at 100 ^oC for 24 h. After 24 h, phenylboronic acid (8 equiv.) was added into the flask, and the mixture was stirred at 100 ^oC for another 24 h. The resulting product was precipitated from methanol, filtered, and washed with acetone. The solid was further washed *via* Soxhlet extraction with acetone, hexane, and chloroform. The chloroform solution

was filtered and condensed under reduced pressure. The desired product was precipitated from methanol. The precipitate was filtered and dried under vacuum to afford **CP1** (67 mg, 50%, M_n = 8 kg/mol, PDI = 1.20 by SEC). ^{1}H NMR (500 MHz, $CDCl_3$): δ 8.15 (m, 2H), 7.80 (br, 4H), 7.64 (m, 2H), 7.51 (m, 2H), 4.66 (br, 1H), 2.35 (br, 2H), 1.96 (br, 2H), 1.10 (m, 24H), 0.74 (t, *J* = 7.0 Hz, 6H).

S.2 Experimental Methods

S2.1 *Sample Preparation*

LP1 stock solution of ~ 0.5mg/mL was prepared by dissolving LP1 in $CHCl_3$ and sonicating for 20 minutes three times. The solution was then filtered twice through 0.45 µm PTFE syringe filters to remove any undissolved particles. The stock was then diluted in $CHCl_3$ to a nominal 0.01mg/mL concentration.

A CP1 stock solution at a concentration of 0.5mg/mL was prepared by stirring polymer powder in $CHCl_3$ for five minutes, as CP1 dissolves quite readily compared to LP1. CP1 was then diluted to a final concentration of 0.0118mg/mL, which represents the concentration at which CP1 and LP1 have equal monomer molar concentrations.

LP1 and CP1 films were prepared by spin coating 5mg/mL stock solutions onto glass microscope slides, which had been successively cleaned with deionized

water, HPLC grade isopropanol and acetone, followed by drying under N_2. The spin speed was 1000rpm, and the spin-coating duration was1 min.

S2.2 *Steady-State Spectroscopy*

Optical density was measured using a 1mm path length cuvette in 1.0nm wavelength increments with a Shimadzu UV-2700 spectrophotometer using an integration time of 0.1s and a 2nm slit width over the range of 300-800nm. Fluorescence measurements were taken in a Horiba Fluoromax-4 spectrofluorometer at right angle geometry in a 1mm cuvette. Excitation was scanned at 5nm intervals from 300nm – 650nm with emission measured at 1nm intervals from 350nm – 800nm. Measurements were made with a Rayleigh masking slit width of 5.0nm and an integration time of 0.1s. No long pass filters were used in this experimental set-up. Thin films were placed 87^o relative to the incident beam.

In order to convert raw signal into a corrected PL spectrum, manufacturer correction factors are applied to the raw data. These factors account for variations in intensity due to the lamp spectrum and due to detector sensitivity. However, the effect of these corrections at low signal intensity is to multiply the spectrum by an

increasing function of wavelength. At the low intensities observed for **LP1** thin films in **Figure AIV.8**, this leads to a noticeable artifact at longer wavelengths.

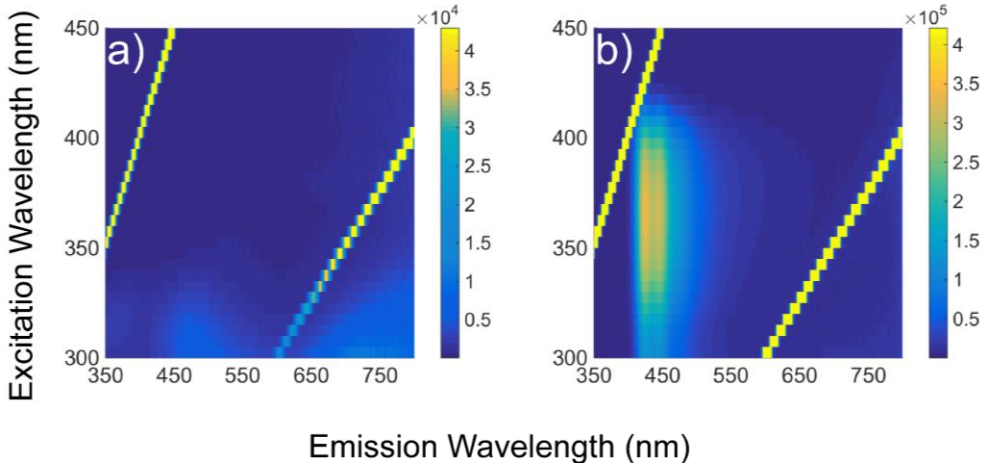

Figure AIV.1. 2D PL maps of LP1 (a) and CP1 (b) thin films. The diagonal lines across the maps are due to the first and second order reflections from the excitation source. Note the large drop in intensity between the two samples, especially as compared to their solution counterparts in Figure 2 in the main text.

S2.3 *Time-Resolved Photoluminescence Spectroscopy*

Time correlated single photon counting (TCSPC) was carried out on a home-built apparatus using a Becker and Hickl Simple-Tau 130 TCSPC system for photon counting and an SPC-130 hybrid photomultiplier tube for detection. The full apparatus has been described elsewhere.[1] All measurements were carried out at 38.9MHz pulse repetition rate except for CP1 thin films, which were carried out at 78MHz, under magic angle conditions. Long pass filters were used to minimize the influence of the reflected excitation beam. For emission at 435 nm and 485 nm a

400 nm filter was used, for emission at 520 nm a 495 nm filter was used, and for emission at 565 nm a 550 nm filter was used. Emission was collected until total peak counts of 8,000-10,000 were measured, depending on sample fluorescence intensity. Measurements in solution were repeated 10-30 times and averaged. Due to the length of the collection needed to achieve the desired peak counts, thin film measurements were only collected once so as to avoid possible photo-degradation.

S3. Fluorescence Decay Lifetime Determination

Fluorescence decay lifetimes were determined by iterative convolution using nonlinear least-squares fitting carried out in DecayFit, a free-ware MATLAB-based program for fluorescence decay fitting.[2] Shift values to correct for spectral shift between the instrument response function (IRF) and decay were selected automatically by DecayFit. When the true decays could be successfully modeled as single exponentials, the initial lifetime τ guess was τ = 4 ns. When single-exponential fits were inadequate, a biexponential model was sufficient, as follows

$$I(t) = \alpha_1 e^{(-t/\tau_1)} + (1-\alpha_1) e^{(-t/\tau_2)} \quad \text{(AIV.1)}$$

with the initial guess parameters as $\alpha_1 = 0.5$, $\tau_1 = 1$ ns, and $\tau_2 = 6$ ns. α_1 was constrained to lie in the 0 – 1 range, and $\tau_{1,2}$ were constrained between 0-25 ns. Additionally, scattered light was modelled by DecayFit by adding a fraction of the

measured IRF to the convoluted decay. Models were chosen on the basis of the χ^2 and visual inspection of the residual matrix. An effort was made to minimize the number of exponential terms used so as to avoid over-fitting. If the addition of another exponential term did not significantly improve the distribution of the residual matrix, or make a marked improvement in the χ^2 value, then a model with fewer exponential terms was used. It is worth noting that there are possible fast decay dynamics <50ps being exhibited in CP1, which we cannot capture due to both restraints on our excitation source (i.e. not being able to excite below 400nm) and due to the width of our IRF (~160ps), which limits our time resolution. As such, an extra exponential term may be appropriate in CP1 fits where λ_{EX} is close to λ_{max}. These dynamics have been seen in structurally similar cationic poly-fluorenes.[3]

Fitting was achieved by iteratively convoluting the measured IRF with trial model functions according to the standard convolution integral:[4]

$$N(t) = \int_0^t L(t')I(t-t')dt' \quad \text{(AIV.2)}$$

Which can be rewritten using $t' = t - u$ such that

$$N(t) = \int_0^t L(t-u)I(u)du \quad \text{(AIV.3)}$$

where $N(t)$ is the measured decay, $L(t')$ is the IRF, and $I(t-t')$ is fluorescence decay of the compound. For each iteration, a trial model function was used for the fluorescence decay and convoluted with the IRF to produce a potential fit of the

decay. The goodness of fit was determined by the reduced χ^2 parameter, with 1.00 being a perfect fit.[4] Optimization of the parameters of the fit was done by DecayFit using MATLAB's inbuilt Trust-Region Reflective algorithm.

Table AIV1. Decay Lifetimes and amplitudes for a solution of (nominal) 0.1 mg/mL **LP1** with minimal sonication.

λ_{EX}	λ_{EM}	α_1	τ_1 (ns)	α_2	τ_2 (ns)	<τ>(ns)	χ^{2*}
400nm	485nm	0.659	1.01	0.341	5.08	3.95	1.692
	520nm	0.612	1.07	0.388	5.29	4.40	1.305
450nm	485nm	0.744	1.12	0.255	5.18	3.66	1.311
	520nm	0.725	1.25	0.275	4.90	3.36	1.284
480nm	565nm	0.734	1.26	0.266	4.83	3.24	1.238

Table AIV2. Decay Lifetimes and amplitudes for a solution of (nominal) 0.01 mg/mL **LP1** with minimal sonication.

λ_{EX}	λ_{EM}	α_1	τ_1 (ns)	α_2	τ_2 (ns)	<τ>(ns)	χ^{2*}
400nm	485nm	0.675	1.02	0.325	5.21	4.07	2.37
	520nm	0.669	0.91	0.331	5.26	4.23	2.35
450nm	485nm	0.723	1.09	0.277	5.22	3.82	1.45
	520nm	0.759	0.95	0.241	5.08	3.55	1.78
480nm	565nm	0.709	1.20	0.291	5.01	3.57	1.90

Table AIV3. Decay lifetimes and amplitudes for a solution of 0.118 mg/mL **CP1**.

λ_{EX}	λ_{EM}	α_1	τ_1 (ns)	α_2	τ_2 (ns)	<τ>(ns)	χ^{2*}
400nm	435nm	1.000	0.51	---	---	0.51	0.735
	485nm	0.998	0.51	0.002	1.89	0.52	1.085
	520nm	0.985	0.51	0.015	1.99	0.59	1.122
450nm	485nm	0.993	0.32	0.007	1.55	0.38	1.253
	520nm	0.967	1.65	0.034	5.34	2.02	1.239
480nm	565nm	0.889	1.51	0.111	7.26	3.64	1.449

Table AIV4. Decay lifetimes for three nominal concentrations of non-sonicated **LP1**. λ_{EM} = 485 nm

λ_{EX}	[LP1] (mg/mL)	α_1	τ_1 (ns)	α_2	τ_2 (ns)	<τ>(ns)	χ^{2*}
400nm	0.1	0.549	1.16	0.451	5.51	4.62	1.188
	0.01	0.849	0.90	0.151	5.18	3.06	1.134
	0.001	0.969	0.71	0.031	4.90	1.47	1.095

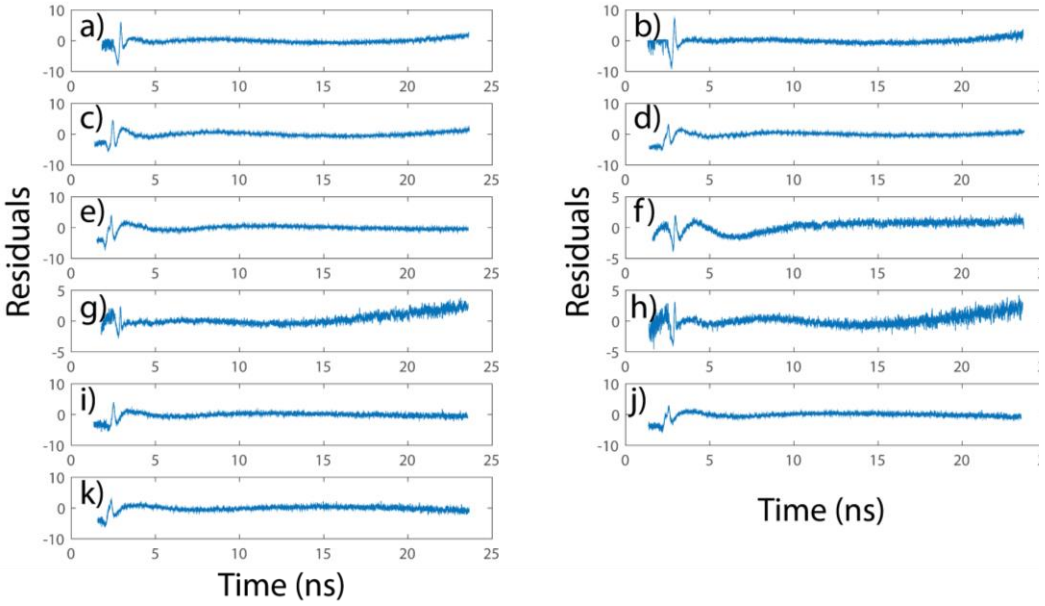

Figure AIV.2. Residuals of fits to LP1 and CP1 fluorescence decay curves. The associated χ^2 values can be found in Tables 1 and 2 in the main text. a) LP1 λ_{EX} = 400 nm, λ_{EM} = 485 nm; b) LP1 λ_{EX} = 400 nm, λ_{EM} = 520 nm; c) LP1 λ_{EX} = 450 nm, λ_{EM} = 485 nm; d) LP1 λ_{EX} = 450 nm, λ_{EM} = 520 nm; e) LP1 λ_{EX} = 480 nm, λ_{EM} = 565 nm; f) CP1 λ_{EX} = 400 nm, λ_{EM} = 435 nm; g) CP1 λ_{EX} = 400 nm, λ_{EM} = 485 nm; h) CP1 λ_{EX} = 400 nm, λ_{EM} = 520 nm; i) CP1 λ_{EX} = 450 nm, λ_{EM} = 485 nm; j) CP1 λ_{EX} = 450 nm, λ_{EM} = 520 nm; k) CP1 λ_{EX} = 480 nm, λ_{EM} = 565 nm. Structure in the early part of the residuals arises from difficulty fitting the rise of the fluorescence decays.

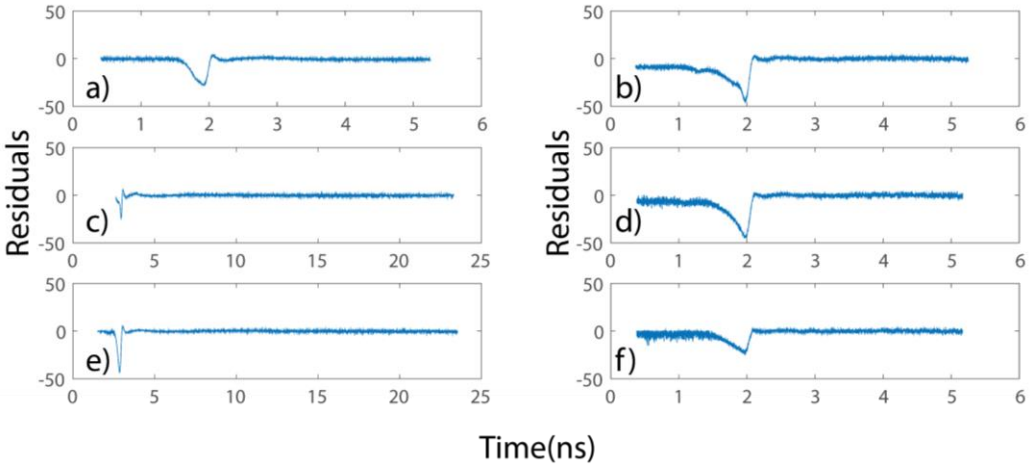

Figure AIV.3. Residuals of fits of LP1 and CP1 thin film fluorescence decay curves. The associated χ^2 values can be found in Tables S7 and S8.a) CP1 λ_{EX} = 400 nm, λ_{EM} = 425 nm; b) LP1 λ_{EX} = 400 nm, λ_{EM} = 520 nm; c) CP1 λ_{EX} = 400 nm, λ_{EM} = 485 nm; d) LP1 λ_{EX} = 400 nm, λ_{EM} = 585 nm; e) CP1 λ_{EX} = 400n m, λ_{EM} = 520 nm; f) LP1 λ_{EX} = 400 nm, λ_{EM} = 680 nm.

S4. Fits of LP1 and CP1 Solution-Phase 0-0 Transition Linewidths

To determine the linewidths of the LP1 and CP1 0-0 vibronic transition linewidths, the respective photoluminescence spectra were converted from wavelength space by scaling by a factor of $1/E^2$. They were further scaled by $1/E^3$ to remove dependence on the photon density of states. The resulting spectra were fit to a sum of Gaussian terms to capture the successive vibronic contributions to the PL using

$$I = \sum_{n=0}^{4} a_n e^{\frac{-(E-E_0+E_{vib})^2}{\sigma_n^2}} \quad \text{(AIV.4)}$$

where a is the Gaussian amplitude, E_0 is the 0-0 transition origin, E_{vib} is the energy of the vinyl stretching normal mode coupled to the electronic transition, and σ is the

linewidth. We found that it was necessary to leave σ unconstrained in order to achieve a high-quality fit. In order to better fit the LP1 spectrum, an additional

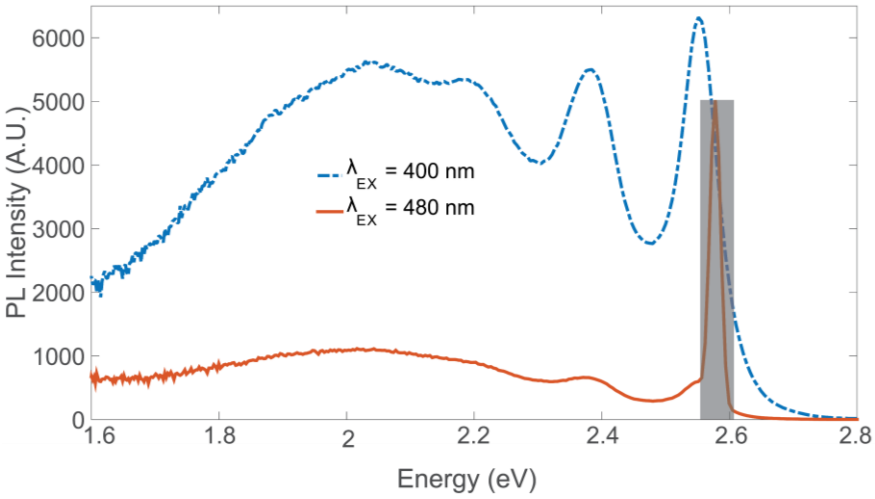

Figure AIV.4. Un-normalized **LP1** PL exciting at 400 nm and 480 nm. The grey box is to delimit the excitation line reflection

Gaussian function was added to the vibronic progression, which helped to capture the broad feature in the low energy part of the spectrum. Tables S5 shows the fit results as well as R^2, the goodness-of-fit parameter.

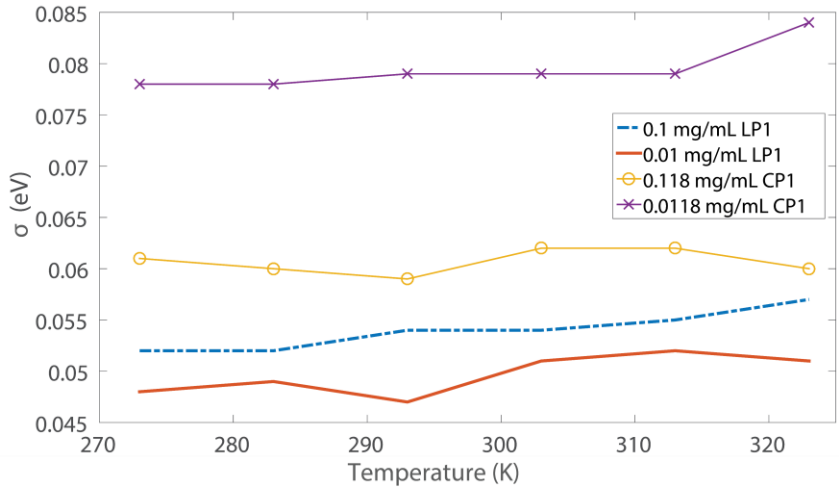

Figure AIV.5: LP1 and **CP1** linewidths as a function of temperature.

Table AIV.5. Gaussian fits to transformed PL spectrum. Symbols are defined in the text

Sample	Temperature (K)	E_0 (eV)	E_{vib} (eV)	σ (eV)	R^2
0.1 mg/mL LP1	0	2.53	0.15	0.052	0.997
	10	2.53	0.15	0.052	0.996
	20	2.53	0.15	0.054	0.996
	30	2.54	0.15	0.054	0.996
	40	2.54	0.15	0.055	0.997
	50	2.53	0.15	0.057	0.997
0.01 mg/mL LP1	0	2.55	0.16	0.048	0.996
	10	2.55	0.16	0.049	0.996
	20	2.55	0.16	0.047	0.994
	30	2.55	0.16	0.051	0.995
	40	2,55	0.16	0.052	0.996
	50	2.55	0.16	0.051	0.996
0.118 mg/mL CP1	0	2.98	0.14	0.061	0.990
	10	2.98	0.13	0.060	0.994
	20	2.98	0.13	0.059	0.994
	30	2.98	0.13	0.062	0.991
	40	2.98	0.13	0.062	0.992
	50	2.98	0.12	0.060	0.996
0.0118 mg/mL CP1	0	3.01	0.16	0.078	0.998
	10	3.01	0.16	0.078	0.999
	20	3.01	0.16	0.079	0.999
	30	3.01	0.16	0.079	0.999
	40	3.01	0.16	0.079	0.999
	50	3.01	0.17	0.084	0.995

S5. Fitting Parameters of the HJ-Aggregate Model

S_R was calculated using the ratio of a_1/a_2 obtained after fitting to the model used in **S4**. These ratios are within <0.1% of the value obtained if the individual Gaussians are plotted and their peak heights are used. We find that the ratios

obtained by first fitting the data to a sum-of-Gaussians model can differ significantly. While the numerical values for **CP1** differ by less than 5% (except for J_{intra} ≈ 11.5% difference) the discrepancy for **LP1** is larger (greater than 10% for all values). Despite this, using fitted or unfitted data produces qualitatively the same result, i.e. $|J_{intra}| > |J_{inter}|$ for J-like aggregates, and the opposite for H-like aggregates.

We calculated the thermal coherence size N_T for the polymers at 293 K using[5]

$$N_T = \sqrt{\frac{4\pi\hbar\omega_c}{k_b T}} \qquad \text{(AIV.5)}$$

with $\hbar\omega_c = F|J_{intra}|$. At most concentrations N_T values for **CP1** and **LP1** are consistent with theory, which expects that at high temperature N_T becomes decoupled from N, the chromophore length, and approaches ≈ 3 at 300 K for J-like emissive aggregates.[6]

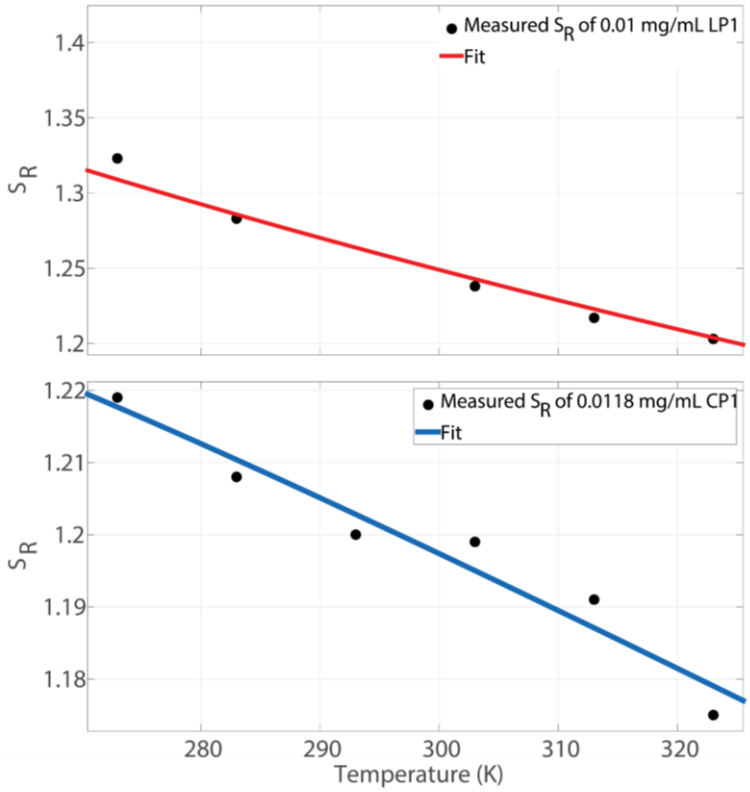

Figure AIV.6: S_R fitted by Spano and Yamagata's model for 0.01 mg/mL LP1 (top) and 0.0118 mg/mL CP1 (bottom)

Table AIV.6. Fitting Parameters from the Spano-Yamagata HJ-aggregate model.

Sample	F	J_{Intra} (cm^{-1})	J_{Inter} (cm^{-1})	λ^2	N_T (293 K)	R^2
0.1 mg/mL LP1	0.1271	-273.7	351.6	1.65	2.15	0.7329
0.01 mg/mL LP1	0.2596	-283.3	0.02	1.376	2.13	0.7220
0.118 mg/mL CP1	0.0836	-51.37	162.3	0.536	0.27	0.8561
0.0118 mg/mL CP1	0.6795	-140.1	75.32	1.453	2.42	0.8672

**Intensity ratios taken from Gaussian fits to PL data.*

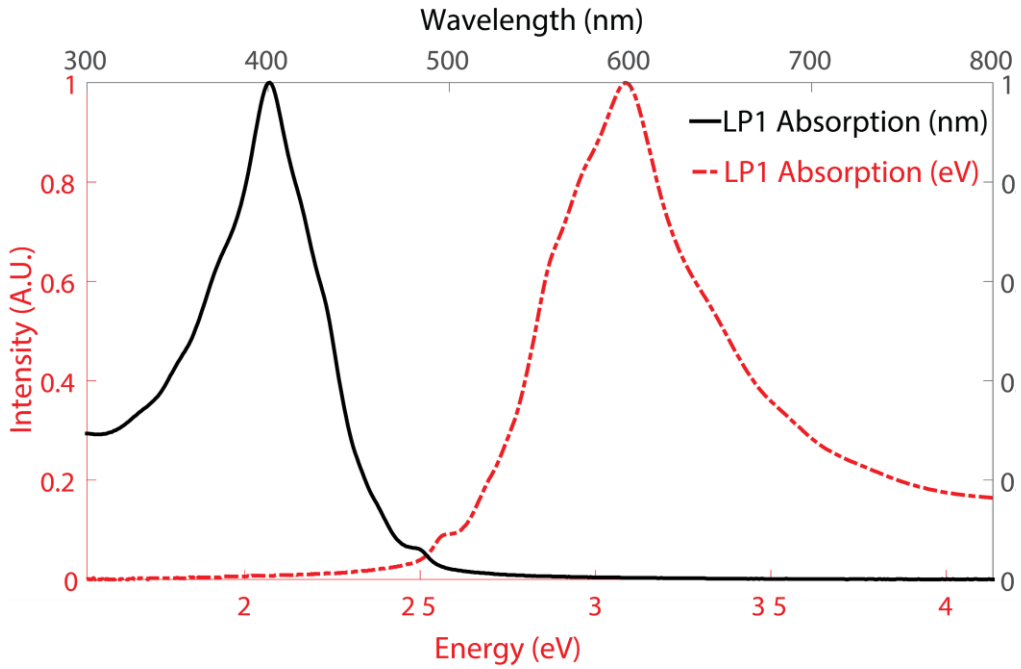

Figure AIV.7: Normalized absorption of LP1 on wavelength and energy scales. The small peak at 484 nm (≈2.51 eV) corresponds to the 0-0 transition of **LP1**.

S6. Thin Film Data

Normalized absorption and PL spectra of thin films are shown in **Figure AIV.8**. The shapes of both absorption profiles are largely unchanged relative to solution, with only a slight sharpening of the vibronic features present in the **LP1** solution

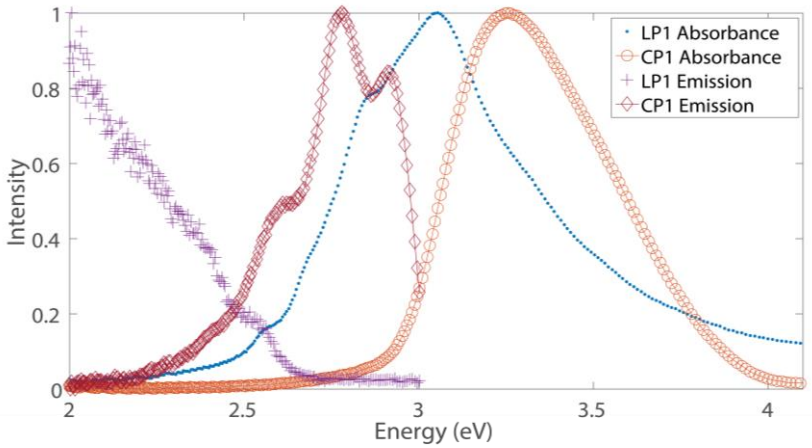

Figure AIV8. Normalized absorption and photoluminescence spectra of LP1 and CP1 thin films deposited on a glass substrate. LP1 and CP1 λ_{max} are red-shifted by 0.05 eV and 0.047 eV, respectively, while the CP1 0-0 transition is red-shifted by 0.08 eV relative to solution. Other than an increase in the CP1 0-1 peak intensity, there is little change in the structure of the CP1 spectrum. This is can be seen as well in the 2D photoluminescence map of the CP1 (see Figure S1). LP1 PL is significantly quenched, and the weak PL is broad and largely featureless. There is a small shoulder at ~2.56 eV which corresponds to the 0-0 transition seen in solution. The diminished 0-0 intensity in relation to other emissive features suggests strong π-π interactions.

absorption spectrum. A minor redshift of 0.047 eV is observed for **CP1**, and of 0.05 eV for **LP1**. Though **CP1** PL is somewhat quenched, it is otherwise qualitatively largely unchanged: There is an ~0.08 eV red shift relative to PL in solution, but the overall shape is very similar. This suggests that **CP1** aggregation does not change substantially when a thin film forms from a relatively rapidly evaporating solvent such as $CHCl_3$. The decrease in PL intensity is likely due to a "tightening" of **CP1** solution aggregates as $CHCl_3$ evaporates. In contrast, **LP1** emission is almost completely quenched in the thin film. We believe this is due to strong inter-chain π-stacking interactions between **LP1** chains in the film[7-8]. Despite these strong local interactions, it is worth noting that **LP1** does not form a semicrystalline solid, except when deposited onto a substrate such as highly ordered pyrolytic graphite.[9]

Tables AIV.7 and **AIV.8** show decay lifetimes for **CP1** and **LP1** thin films excited at 400 nm (3.10 eV). Compared to solution, **CP1** has a comparable average lifetime when collecting emission at 485 nm (2.56 eV) and a moderately longer average lifetime when looking at emission at 520nm (2.38 eV). This is consistent with steady-state PL measurements that suggest that aggregation of **CP1** is not drastically changed between solution and thin film. If this is the case, then the lifetime lengthening can be explained by a decrease in available low-energy sites of suitable energy for exciton migration perhaps due to the frozen film morphology. Though we could not probe the λ_{max} of **CP1** directly, we did probe the red edges of the first and second vibronic peaks of the PL in the thin film and solution,

respectively. These were best fit with a mono exponential decay with lifetimes of ~300 ps – 500 ps.

In contrast, consistent with strong steady-state quenching of **LP1** PL, both the long and short lifetime components are significantly shortened. Strong π-π interactions between rigid backbone regions in the solid state lead to largely nonemissive inter-chain exciton sinks[8, 10]. Thus, in contrast to **CP1**, the increased backbone rigidity of **LP1** promotes facile inter-chain exciton delocalization even when the solvent evaporates rapidly, resulting in short PL lifetimes. Inter-chain π-stacking is known to enhance nanoscale charge connectivity: semicrystalline conjugated polymer films are, on average, known to have much larger field-effect mobilities in the transistor configuration than do those with amorphous chain packing.[11] We note that due to **LP1**'s low PL quantum yield, resulting in moderate-to-poor fits for the **LP1** thin film, it is difficult to determine whether the observed trend among the lifetimes is realistic or an artifact of the data and fitting routine.

Table AIV.7. CP1 thin film emission decay parameters.

λ_{EX}	λ_{EM}	α_1	τ_1 (ns)	α_2	τ_2 (ns)	<τ>(ns)	χ^{2*}
400nm (3.10 eV)	425 nm (2.92 eV)	1.000	0.33	---	---	0.333	0.721
	485 nm (2.56 eV)	0.998	0.50	0.002	2.62	0.52	0.708
	520 nm (2.38 eV)	0.972	0.73	0.028	3.45	1.05	0.792

*Residuals can be found in **Figure AIV.3**.

Table AIV.8. LP1 thin film fluorescence decay parameters.

λ_{EX}	λ_{EM}	α_1	τ_1 (ns)	α_2	τ_2 (ns)	$<\tau>$(ns)	χ^{2*}
400nm	520nm (2.38 eV)	0.989	0.21	0.011	2.04	0.39	1.750
	585nm (2.12 eV)	0.950	0.29	0.050	1.68	0.62	1.360
	680nm (1.82 eV)	0.878	0.32	0.122	1.42	0.74	0.963

*Residuals can be found in **Figure IV3**.

References

(1) Hollingsworth, W. R.; Segura, C.; Balderrama, J.; Lopez, N.; Schleissner, P.; Ayzner, A. L. Exciton Transfer and Emergent Excitonic States in Oppositely-Charged Conjugated Polyelectrolyte Complexes. *The Journal of Physical Chemistry B* **2016,** *120*, 7767-7774.

(2) Preus, S. Spectroscopic Tools for Quantitative Studies of DNA Structure and Dynamics. Doctoral Thesis, University of Copenhagen, Chalmers University of Technology, Copenhagen, Denmark, 2012.

(3) Davies, M. L.; Douglas, P.; Burrows, H. D.; Miguel Mda, G.; Douglas, A. Effect of aggregation on the photophysical properties of three fluorene-phenylene-based cationic conjugated polyelectrolytes. *J Phys Chem B* **2011,** *115*, 6885-92.

(4) Lakowicz, J. R., *Principles of Fluorescence Spectroscopy*. 3 ed.; Springer Science+Business Media, LLC: New York, NY, 2006.

(5) Hestand, N. J.; Spano, F. C. Determining the spatial coherence of excitons from the photoluminescence spectrum in charge-transfer J-aggregates. *Chemical Physics* **2016,** *481*, 262-271.

(6) Spano, F. C.; Yamagata, H. Vibronic Coupling in J-Aggregates and Beyond: a Direct Means of Determining the Exciton Coherence Length from the Photoluminescence Spectrum. *J. Phys. Chem. B.* **2011,** *115*, 5133-43.

(7) Nguyen, T.-Q.; Martini, I. B.; Liu, J.; Schwartz, B. J. Controlling Interchain Interactions in Conjugated Polymers: The Effects of Chain Morphology on Exciton-Exciton Annihilation and Aggregation in MEH-PPV Films. *J. Phys. Chem. B.* **2000,** *104*, 237-255.

(8) Schwartz, B. J. Cojugated Polymers as Molecular Materials: How Chain Conformation and Film Morphology Influence Energy Transfer and Interchain Interactions. *Annu. Rev. Phys. Chem.* **2003,** *54*, 141-172.

(9) Lee, J.; Rajeeva, B. B.; Yuan, T.; Guo, Z.-H.; Lin, Y.-H.; Al-Hashimi, M.; Zheng, Y.; Fang, L. Thermodynamic Synthesis of Solution Processable Ladder Polymers. *Chem. Sci.* **2016,** *7*, 881-889.

(10) Spano, F. C.; Clark, J.; Silva, C.; Friend, R. H. Determining Exciton Coherence from the Photoluminescence Spectral Line Shape in Poly(3-hexylthiophene) Thin Films. *J. Chem. Phys.* **2009,** *130*, 074904.

(11) Pope, M.; Swenberg, C. E., *Electronic Properties in Organic Crystals and Polymers*. 2 ed.; Oxford University Press: New York, New York, 1999.